University of Bergen

Master thesis in petroleum chemistry

Exploration of non-spinning ^{1}H NMR Spectroscopy as a Tool for Determination and Monitoring of Gas Hydrate Formation and Dissociation Processes

Author:

Magnus Rossmann Henrichsen

Supervisors:

Professor Tanja Barth
Professor Per Fotland

Faculty of Mathematics and Natural Sciences

Department of Chemistry

November 2015

Abstract

Natural gas hydrates provide both a flow-assurance hazard and a potential fossil fuel source. In order to face the challenges presented by these scenarios, a greater understanding of the properties of hydrates in a range of environments is required. NMR spectroscopy provides a powerful tool for investigation of such properties; however, most previous studies have involved use of either deuterated components, ^{13}C NMR, magic angle spinning or a combination of these. Proton NMR of static natural-isotope hydrates has therefore received little attention before investigation in this thesis, an important aspect of which is to establish procedures and identify effective NMR experiments. Procedures have therefore been established for the preparation of samples from a cyclopentane hydrate model system, to which ^{1}H, Inverse Recovery, CMPG and NOESY experiments have been applied. The combination of ^{1}H and CMPG experiments was found to quickly and consistently yield information on both sample state and on-going processes, even under rapidly changing conditions. As such, these experiments might be useful for monitoring changing hydrate samples, and can possibly be further applied to hydrates in a range of different environments. The Inverse Recovery and NOESY experiments were found lacking, and will require improvements in order to be useful. Several shortcomings in the established procedures have also been pinpointed, and possible solutions have been outlined.

Acknowledgements

First and foremost I would like to thank my supervisor Professor Tanja Barth for her ideas, advice and words of encouragement and motivation, none of which this thesis would be possible without. I would also like to thank my supervisor Per Fotland, whose knowledge and expertise has contributed immensely to my understanding of natural gas hydrates over the course of two theses, and his help is never more than an email away. On a related note, I also want to thank Statoil for their purchase of the ubiquitous sample rotors. Furthermore, I would like to extend a special gratitude towards Christian Totland, whose interest in my work has been highly appreciated, and his aid and assistance has been absolutely invaluable. I would also like to thank Professor Willy Nerdal for helping me off my feet by aiding in procedure establishment and familiarising me with the spectrometer. I am also grateful for all the work Chief engineer Olav-Audun Bjørkelund has done in order to keep the spectrometer running, both in front of and behind the scenes. It was always nice having our little chats while troubleshooting, even as a runaway temperature control unit reduced my samples to useless liquids. Also, I would like to thank John Georg Seland for providing the spectroscopic tools required for T_2 analysis, as well as helping with setting up the NOESY experiments. I would also like to thank all my friends in Bergen, who more than anyone has made my time as a student in Bergen the fantastic experience that is has been. Honourable mentions go out to Stian, Henrik, Magnus and Sveinung, with whom countless hours have definitely not been wasted over coffee in the cafeteria. Last but not least I would like to thank my family for all their support during my time as a student, as well as in other aspects of life.

Table of Contents

Chapter 1 Introduction

1.1 Background

In the petroleum industry, gas hydrates constitute a considerable risk as well as a potential resource, as they can be found both as natural gas containing reservoirs and as plugs in pipelines containing both water and light hydrocarbons [1]. Whilst natural gas produced from hydrates may aid in powering the world in the future, many challenges still remain as to how these reservoirs can best be tapped, requiring knowledge on how these hydrates behave in the porous geology of their reservoirs. NMR spectroscopy has been a valuable tool in hydrate research for half a century, but as the ever steady march of progress provides better and better NMR technology, the frontier of what is achievable by the technique is expanding. One such technology is magnetic resonance imaging. Requiring the use of gradient pulses, these imaging spectrometers therefore mandate static samples [2]. Therefore, a better understanding of these hydrate systems during static NMR spectroscopy is required in order to fully employ these new techniques.

Before the results are presented and discussed, a basis for the properties and behaviour of gas hydrates is established in the first part of this chapter, followed by theoretical groundwork for the technique of NMR spectroscopy.

1.2 Natural gas hydrates

Gas hydrates are crystalline inclusion compounds, consisting of an ice-like host structure of hydrogen-bonded water molecules stabilised by guest molecules occupying cavities in the host structure [1]. Molecules capable of acting as guests are called hydrate formers, the identity of which influence hydrate thermodynamics, kinetics and morphology. In the presence of water and hydrate former, hydrates form when favourable thermodynamic conditions are met. Although most gas hydrates form at low temperature and high pressure, the hydrates of certain guests are stable at atmospheric pressure and temperatures above the freezing point of water [3]. Examples include cyclopentane and tetrahydrofuran. The hydrate structure is stabilised by intermolecular forces, and as a result their formation and dissociation proceed through first-order phase transitions, not chemical reactions.

1.2.1 Gas hydrate morphology

The hydrogen-bonded H_2O network constitute the framework of hydrate crystals, the principal building blocks of which are square, pentagonal and hexagonal face structures that combine through face-sharing. The hydrate structure is defined by the cavities formed from the combination of these faces using the notation $\boldsymbol{n}_\mathbf{i}^{\boldsymbol{m}\mathbf{i}}$, where $\boldsymbol{n}_\mathbf{i}$ is the number of edges in face type **i**, and $\boldsymbol{m}_\mathbf{i}$ is the number of face type **i** [1].

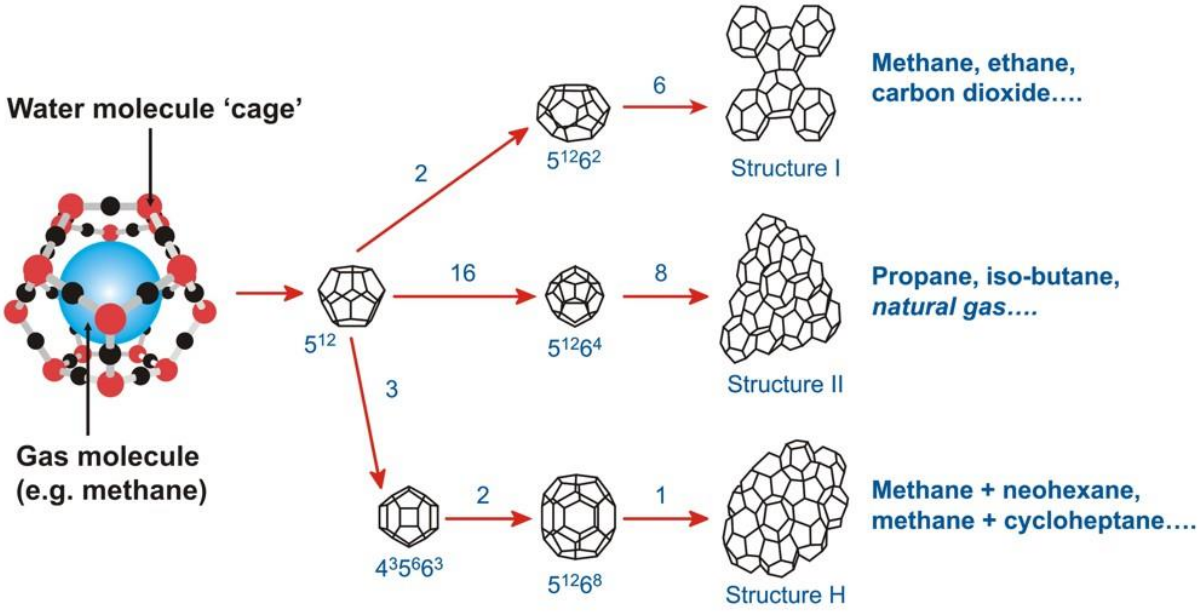

Figure 1.1: Makeup and classification of the three most common hydrate structures, as per the notation described above. The number of each cage type in the unit cell is given above the arrows. As an example, $5^{12}6^2$ signify a water cage consisting of twelve pentagonal and two hexagonal faces. The structure I unit cell is constructed from six of these cages, along with two 5^{12}-cages. Figure taken from [4].

The hydrate structures depicted in figure 1.1 are all naturally occurring, with structure I and II (sI and sII) being most common [1]. At all but very high pressures (>1000 MPa) each cavity can contain only one guest [5]. Structures I and II give rise to a cubic crystal system, while the structure H hydrates adopt a hexagonal crystal system [1]. For a list of the geometries of the three crystal structures, see table 1.1.

Table 1.1: Key geometric properties for hydrates of structure I, II and H. Cavity radius will be influenced by temperature, pressure and guest composition. Radius variation gives the difference in position of oxygen atoms from the cage centre, and thus provides a measure of cage symmetry. From [1].

Crystal structure	**I**		**II**		**H**		
Cavity	Small	Large	Small	Large	Small	Medium	Large
Description	5^{12}	$5^{12}6^2$	5^{12}	$5^{12}6^4$	5^{12}	$4^35^66^3$	$5^{12}6^8$
Number of cavities/unit cell	2	6	16	8	3	2	1
Average cavity radius (Å)	3.95	4.33	3.91	4.73	3.94	4.04	5.79
Variation in radius (%)	3.4	14.4	5.5	1.73	4.0*	8.5*	15.1*
Number of H_2O molecules/cavity	20	24	20	28	20	20	36

Other structure types exist, but are of less importance in natural systems. However, more exotic hydrate lattice types might be key to specialised hydrate applications like gas storage and transport [1].

On a molar basis, approximately 85% of the hydrate structure is composed of water. As a result, hydrates are expected to behave like structure Ih ice in many situations. This assumption does fail for many important properties, for instance thermal conductivity and –expansivity as well as yield strength. [1]

The degree of overall cage occupancy is variable and non-uniform, and several different guests can be present throughout the structure. As such, hydrates are nonstoichiometric compounds. In addition, the hydrate structure will often trap metastable water pockets which lead to difficulties in determining the composition of the hydrate phase [1].

1.2.2 The guest molecule

The gas hydrate structures are stabilised by the balance of attractive and repulsive Van der Waals forces between the guest molecules and host structure [6], with the repulsive force component being of special importance to prevent the collapse of the cavities [1].

For most hydrate formers there are no chemical bonds between guest and host lattice, and the guest is free to rotate within its cage. In addition, the crystal structure of the water framework of hydrates will in most cases remain unchanged as guest identity and level of occupancy is changed. As a result, hydrates can be classified as solid solutions [1, 3]. Some guests are capable of forming hydrogen bonds with the host structure, however, and molecular dynamics simulations indicate that these directional bonds influence guest mobility. Examples are transient hydrogen bonds decreasing the rotational freedom of the guest, and the induction of Bjerrum L defects in the host structure which increase the rate of diffusion of guests between cavities [7].

The size of the guest molecule is seen as the critical parameter for hydrate structure type, as small guests will not be able to sufficiently stabilise larger cavities and large guests will not fit in the smaller ones. As a rule of thumb, guests with diameters between 4.2 and 6 Å form hydrates of structure I, while guests in the 6-7 Å range forms structure II hydrates. Larger guests (7-9 Å) will form structure H hydrates, but require the presence of a help gas to fill the small cavities. Guest shape plays a role as well, especially for sH [1].

1.2.3 Hydrate formation and dissociation

The first step in formation of hydrates involves a stochastic nucleation process. This means that the system experiences an extended period of metastability within the region of thermodynamic stability, before the nucleation event leading to hydrate growth occurs. This time of metastability is called the induction time of the system, which results in a hysteresis loop for the formation-dissociation curve of hydrates. Due to the balance of volume and surface energy terms, the process of nucleation is connected to a critical radius of the hydrate nuclei. At this critical size, thermodynamic stability of the new phase is achieved. During the induction period, clusters of hydrate precursors grow and fall apart by kinetic mechanisms until such a stable nucleus is achieved, and is believed to occur mainly through a heterogeneous nucleation mechanism. Evidence of a so-

called memory effect can be seen for samples not subjected to long times or high temperatures after melting, that indicate the presence of residual structures acting as nuclei for a reformation process. These effects manifest as a considerable decrease in induction time for the system upon re-entry to the region of hydrate stability [1].

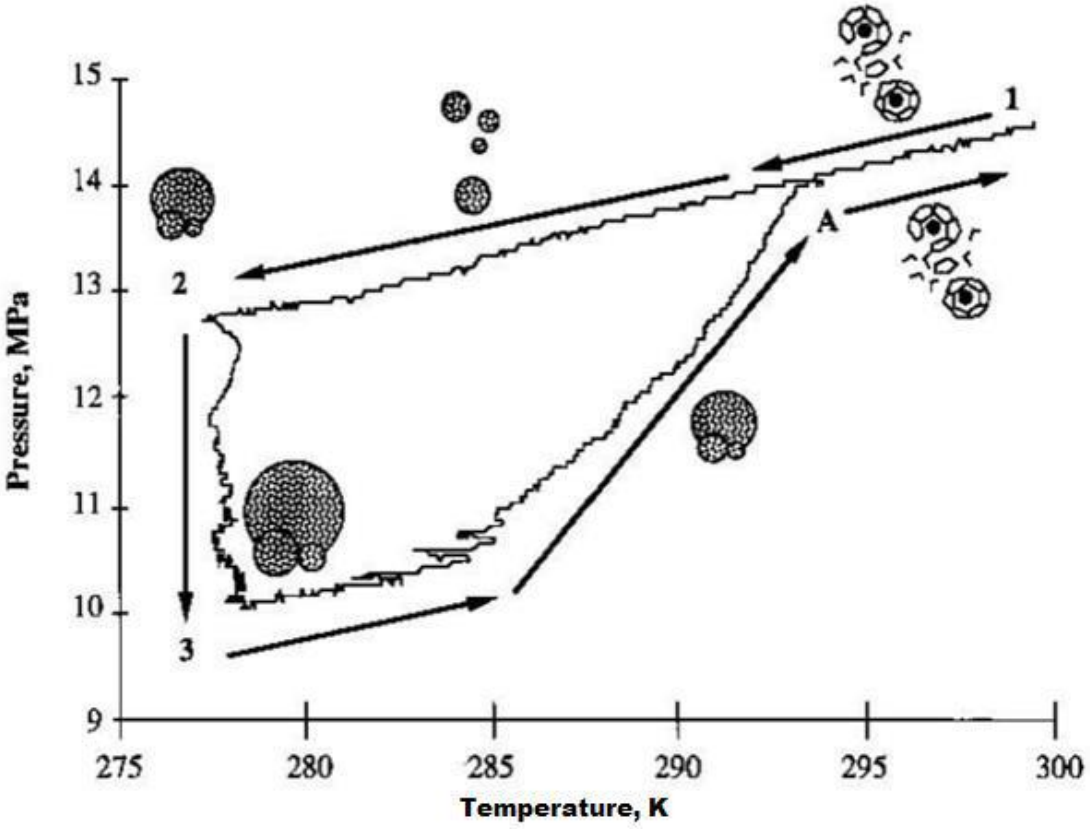

Figure 1.2: Schematic of a pressure-temperature curve obtained for the formation and dissociation of hydrates under agitation in a constant-volume autoclave cell, taken from [8].

After the induction period, a period of rapid hydrate growth ensues. Although the exact mechanisms are a matter of debate, a good starting point can be found in the comprehensive work by Sloan and Koh [1]. The dissociation process of hydrates is an endothermic reaction and is assumed to proceed in gas pipelines by radial melting of the hydrate phase, which would also apply to the cylindrical sample probed in this thesis. It is usually limited by heat-transfer, but situations arise where mass transfer is the limiting process [1].

1.2.4 Hydrates in the petroleum industry

Over a century after their discovery in 1811, gas hydrate research was still done only as a result of academic interest [1]. This changed, however, after Hammerschmidt found these compounds able to accumulate in and block gas pipelines [9], prompting a shift in the research to meet the real world application requirements of the petroleum industry. This resulted, among others, in methods to predict and prevent the formation of gas hydrates [1]. The discovery of natural gas hydrates in permafrost in 1965 gave rise to research into yet another application of these hydrates, namely as an fossil fuel source [1]. This line of research is just now nearing fruition, with methane produced from natural gas hydrate reservoirs during a Japanese test project as recent as 2012 [10]. Clathrate

hydrates might also have applications in the storage and transport of natural gas, and melting of methane gas hydrates in permafrost reservoirs is implicated as a potential mechanism for global warming [1].

As a result, the currently most relevant aspect of hydrates in the petroleum industry is that of flow-assurance, especially as the boundary of hydrocarbon resource production move ever northwards into colder waters. Coupled with the large amounts of natural gas in hydrate reservoirs possibly providing a future fossil fuel resource [11], gas hydrates remain an important field of study in the industry.

1.3 NMR spectroscopy

1.3.1 The basics of NMR spectroscopy

The NMR technique has its basis in in the quantum property of angular momentum for nuclei, and a comprehensive introduction to the technique can be found in the book by Friebolin [2], information from which the following subchapter is closely based upon.

The angular momentum of a particle can be found from the equation:

$$\boldsymbol{P} = \sqrt{I(I+1)}\,\hbar \qquad \textit{Equation 1.1}$$

where *P* is angular momentum, and $\hbar = h/2\pi$ with *h* being Planck's constant. The nuclear spin quantum number *I* can have any integer or half-integer value from 0 to 6, and depends on the nucleus in question. The angular momentum ***P*** further gives rise to a nuclear magnetic moment, $\boldsymbol{\mu}$, and these vectors are related by a proportionality constant called the magnetogyric ratio, γ. For all nuclei considered in this thesis, ***P*** and $\boldsymbol{\mu}$ have the same direction. All different nuclei, including different isotopes, have a specific magnetogyric ratio, and the size of this constant determines the magnitudes of the magnetic moment for different nuclei under equal conditions. This is an important aspect of the technique, as different nuclei will therefore be more or less sensitive to NMR analysis according to their magnetogyric ratio. Substituting ***P*** in Eq. 1.1 with its proportionality equation yields the following:

$$\boldsymbol{\mu} = \gamma\sqrt{I(I+1)}\,\hbar \qquad \textit{Equation 1.2}$$

If an external magnetic field is applied to a nucleus, the direction of the field constituting the z-axis, the nucleus will align itself according to the field so that the P_z component of its angular momentum has a value given by:

$$P_z = m\,\hbar \qquad \textit{Equation 1.3}$$

where *m* is any integer or half-integer from *I* to *-I*. It follows that the orientation of the angular momentum, and therefore also the magnetic moment, is quantified by the application of an external magnetic field. The magnetic moment along the field direction is given by:

$$\mu_z = m\,\gamma\,\hbar \qquad \textit{Equation 1.4}$$

This results in the overall magnetic moment being locked at certain angles to the z-axis. However, it is free to rotate around the magnetic field direction, and according to the classical picture of NMR

spectroscopy this leads to a precession of the magnetic vector around this axis. The frequency of this precession is called the Larmor frequency, and is related to the magnetic flux density by the following equation:

$$\nu_L = B_0 \left|\frac{\gamma}{2\pi}\right| \qquad \textit{Equation 1.5}$$

where ν_L is the Larmor frequency, B_0 is the magnetic flux density and γ is the gyromagnetic ratio. For a given flux density, the energy of a dipole can be found by the following equation:

$$E = -\mu_z B_0 \qquad \textit{Equation 1.6}$$

By combination with Eq. 1.4 this yields:

$$E = -m \gamma \hbar B_0 \qquad \textit{Equation 1.7}$$

The selection rules for the magnetic quantum number m dictate that there must be $(2I + 1)$ different values for m, which also means that $(2I + 1)$ values must exist for E. This in turn means that under the effects of an external magnetic field, the energy levels specified by different magnetic quantum numbers are no longer degenerate, with positive m values aligning the z-component of the magnetic moment parallel to the magnetic field. This gives rise to quantum states lower in energy, whilst negative values of m results in states at higher energy from an antiparallel alignment of μ_z with the magnetic field. In a macroscopic sample, a set of two states corresponding to $m = +½$ and $m = -½$ are populated according to a Boltzmann distribution that can be stated as follows:

$$\frac{N_\beta}{N_\alpha} = 1 - \frac{\gamma \hbar B_0}{k_B T} \qquad \textit{Equation 1.8}$$

where N_α is the number of nuclei with $m = +½$ and N_β is the number of nuclei with $m = -½$, k_b is the Boltzmann constant and T is the temperature in Kelvin. As the energy difference between the levels is miniscule, the corresponding populations of nuclei in the two states are nearly equal. However, this small excess of magnetic moments parallel to the field gives rise to a macroscopic magnetisation vector along the z-axis. Furthermore, irradiating the sample with electromagnetic radiation of a frequency corresponding to the energy difference between the energy levels will induce transitions between them, with excitation and relaxation being equally probable. This frequency is the Larmor frequency of the nucleus in question. If a greater number of nuclei are present in one state, their transition to the other state will be the major process, and this creates a recordable signal. The energy difference, and therefore the population difference, is proportional to the applied magnetic field. It is for this reason powerful cryomagnets are used in modern spectrometers. If both populations are equal a dynamic equilibrium is achieved, quenching the signal. This condition is called saturation.

In real samples, the nuclei will be shielded from the effects of the magnetic field by their chemical environments, meaning that the same nuclei in different molecular configurations will come into resonance at slightly different frequencies. Instead of continuously varying the magnitude of the applied field or the frequency of the irradiating field to bring these into resonance one at a time, modern spectrometers use radiofrequency excitation pulses. These operate on the µs timescale, and their frequency is set according to the spectrometer magnetic field strength and the corresponding resonance condition of the analyte nuclei. Using such short pulses give rise to a distribution of

different frequencies around the centre of the peak, bringing all nuclei into resonance simultaneously. The old field-sweep techniques have left a lasting mark on the nomenclature of NMR spectroscopy, however, with higher chemical shift values referred to as “upfield” and lower values said to be “downfield”, and these expressions are used throughout this thesis.

Although a quantum mechanical approach is necessary for truly explaining these phenomena, such an explanation is outside the scope of this thesis. Instead, the action of these pulses on the macroscopic magnetisation vector can be sufficiently explained by the classical vector model for a range of experiments. In the vector model, a coordinate system is defined with the external magnetic field vector designated as the z-axis. The alternating magnetic field of the pulse is applied along the x-axis, modelled as two magnetic components rotating at the Larmor frequency in the xy-plane, in opposite directions. These are called B_1 and B_2, and interaction between this alternating field and the magnetic vectors of sample nuclei are only possible for components rotating in the same direction. This effecting component is designated as B_1, and the effect of its application is to orthogonally tilt the macroscopic magnetisation vector into the xy-plane. In order to simplify the model, the coordinate system is defined as to rotate around the z-axis at the same frequency as B_1, using primes to designate the axes as rotating. This pins the B_1 component in place at the x’-axis, meaning the tilt of the macroscopic magnetisation vector occurs in the the y’z-plane. The total angle of tilt, or pulse angle, is given by the equation

$$\theta = \gamma\, B_{1i}\, \tau_P \qquad \textit{Equation 1.9}$$

where θ is the pulse angle, γ is the magnetogyric ratio, B_{1i} is the amplitude of the applied pulse and τ_P is the amount of time for which the pulse is applied. A receiver coil is placed over the y-axis, collecting the signal of the magnetic vector at this axis, $M_{y'}$, called the transverse magnetisation. The cause of this transverse magnetisation is the grouping of individual nuclear dipoles by the applied pulse, a condition referred to as phase coherence. Since this means that the signal is at a maximum after being subjected to a $90^{o}_{x'}$ pulse, such pulses can be considered the workhorse of basic NMR spectroscopy.

After the pulse is turned off, the system will undergo relaxation. What this means is that its magnetic component will return to the equilibrium value, which amounts to a recovery of the initial M_z value. Accordingly, any magnetic components introduced to the xy-plane by the applied pulse will decay to zero. Two relaxation processes take place, described by the Bloch equations:

$$\frac{\mathrm{d}M_z}{\mathrm{d}t} = \frac{M_z - M_0}{T_1} \qquad \textit{Equation 1.10}$$

$$\frac{\mathrm{d}M_{x'}}{\mathrm{d}t} = \frac{M_{x'}}{T_2} \qquad \textit{Equation 1.11a}$$

$$\frac{\mathrm{d}M_{y'}}{\mathrm{d}t} = \frac{M_{y'}}{T_2} \qquad \textit{Equation 1.11b}$$

where T_1 is the spin-lattice relaxation time and T_2 is the spin-spin relaxation time. The inverse of these relaxation times are the rate constants of the relaxation processes.

Measurement of the transverse magnetisation vector after an applied pulse returns decay-curves of all applicable sample nuclei superimposed in a time-domain spectrum. Subjecting this spectrum to a

mathematical operation called a Fourier transformation yields the same information in a frequency domain, where individual resonance lines can be seen at their respective frequencies.

1.3.2 Sample inhomogeniety and chemical shifts

For inhomogeneous magnetic fields, otherwise equal nuclei will come into resonance at slightly different frequencies due to the variations in the magnetic field at different locations in the sample [2]. This will result in line broadening in the spectrum, in addition to artefacts if the variation is large. Although small variations in the magnetic field is to be expected even for perfectly shimmed, homogenous samples, the physical-chemical state of a sample can have a profound influence on field homogeneity. Sample inhomogeneity is a common cause of observed artefacts, as unevenly distributed molecules will alter their local magnetic environments [2] and interfaces will carry charges setting up local magnetic fields of their own [12, 13]. Furthermore, magnetic volume susceptibilities of different phases in the sample can lead to large variations in the magnetic field near interfaces [14].

Several techniques for managing the effects of field inhomogeneity exist, the most common being locking and shimming. Locking works by utilising a separate radiofrequency channel in the NMR instrument to continuously measure the signal of a different nucleus than that probed in the main experiment. These measurements are used by the lock unit, which will automatically apply a field correction if the resonance condition of its measured nucleus is lost. This ensures that any eventual instrument drift pertaining to the magnetic field is immediately corrected, under the assumption that the same effect is observed for both the analyte and locking nuclei. Manually tuning this signal to improve field homogeneity is called shimming the sample [2].

Other effects can also influence the resonance frequencies of various compounds, giving rise to peaks of the same molecules lying at different chemical shifts at varying conditions. Water, for instance, is known to display chemical shift changes as a function of temperature [15].

1.3.3 Solid state NMR

The interactions of nuclear spins contain an anisotropic component, resulting in orientation-dependent responses for even otherwise equal spins systems. In liquids, this component is averaged by molecular motions over the timescales of the experiments. For solids, however, the close proximity and rigid configuration of the components preclude such averaging. This results in powder patterns which overlaps due to inequivalent sites in the solid, and therefore broad lines are observed in the NMR spectra of solids [16].

The peak of the ^{1}H spectrum of water ice has previously been determined to have a Gaussian line shape and line width of 72 kHz at 273 K [17]. The water lattice of gas hydrates has a structure related to that of ice, with incomplete filling of water cavities by guest molecules. Therefore, a similar peak is expected to be present in the hydrate spectra.

1.3.4 Magic Angle Spinning NMR

In order to remove the broad patterns in solid NMR spectra, a technique called magic angle spinning (MAS) is used. Here, the sample is spun mechanically at the so-called “magic angle” of 54.7^{o} to the

external magnetic field, usually at a frequency of thousands of Hz. The effect of the rotation is to scale the anisotropic component of the peaks to zero, resulting in peaks approximating that of a liquid sample. Low spinning rates result in spinning sidebands in the spectra, which appear at regular intervals equal to the spin-rate for the sample. These equidistant peaks also include a peak called the isotropic line, which lies at the chemical shift of the analyte being probed. In order to isolate this peak, the MAS rate can be altered, and the peak that remains at the same position for different spin rates is the isotropic line [16].

1.4 Relaxation times

1.4.1 Spin-lattice relaxation (T_1)

The spin-lattice relaxation proceeds through a change in the magnetisation vector in the direction of the applied field. The most important effect is that of dipole-dipole interactions, where the movement of neighbouring magnetic nuclei cause perturbations in the local magnetic field. If these perturbations result in a magnetic field containing components of correct frequency, they can induce the transition between spin states required for relaxation, and as such the T_1 relaxation mechanism is an energy transfer process. For the dipolar relaxation component the following is usually true:

$$\frac{1}{T_1} = \propto \tau_c \qquad \textit{Equation 1.12}$$

τ_c is the correlation time of a molecule, and can be interpreted as the time between two successive changes in position or orientation of the molecule. This means that the greater the mobility of the molecule is, the greater is T_1. This also means that in most cases, T_1 is proportional to temperature. However, the T_1 curve does go through a minimum for a certain range of increasing correlation times [2]. For solid hydrates with nearly all molecules locked in a lattice, this correlation time should correspond to the rotational activation energy of the molecules.

In addition, similar perturbations to the magnetic field can arise whenever interfaces are present in the sample, causes of and potential solutions to which has been detailed by other authors [14, 18]. For the work in this thesis, this means that for a solid hydrate phase with low-mobility components and no interfaces, T_1 times are expected to be low. These values are expected to rise gradually with melting of the sample, as the increased mobility of molecules will originally be offset by the ratio of bulk to interfacial character of any liquid formed. As the amount of liquid increases, so will the number of molecules residing in a homogenous bulk phase. Disregarding the effects of temperature, maximum T_1 values are not expected until all hydrates have melted and any interfacial system has stabilised as to minimise surface area. In addition, any deviations from this expected trend will possibly yield other information on the progression and identity of processes in the sample.

The varying behaviour of T_1 relaxation as a result of the properties of the system which it is in can be used to expand the information attainable from the measurement of the spin-lattice relaxation. For instance, such measurements have been applied to find the presence of exchange phenomena as well as the pore size in cement paste [18]. Furthermore, for ranges where an increase in temperature leads to a decrease in T_1 relaxation time, the correlation time has been found to correlate to the activation energy of an exchange process, and the same applies to the T_2 relaxation time [17].

Another relaxation mechanism worthy of note is that of interaction of the nucleus with electron pairs on paramagnetic species [2]. To avoid confounding of sample-specific relaxation mechanisms with that of paramagnetic contaminants, care must be taken in order to avoid introduction of these by for instance avoiding metal equipment. A similar process of relaxation can also manifest by interactions of the nuclear spins with surfaces, and both phenomena are labelled as the electronic component of relaxation, T_{1e} [19]. This component display less temperature dependence than does the other component discussed. For systems where T_{1e} dominates, relaxation data plotted on a temperature curve should therefore display a lesser slope [20]. Similar processes also apply to T_2 relaxation.

1.4.2 Determination of T_1

The T_1 relaxation time can be found by an inversion recovery experiment, which utilises a series of the following pulse sequence, applied in a rotating coordinate system [2]:

$$(5\ T_1 - 180^{\circ}_{x'} - \tau - 90^{\circ}_{x'} - \text{FID})_n$$

where 5 T_1 is a relaxation time of five times the longest expected T_1 relaxation time in order to ensure complete relaxation between sequences, $180^{\circ}_{x'}$ and $90^{\circ}_{x'}$ are pulses capable of flipping the magnetisation vector the specified amount of degrees around the specified axis, τ is a pulse delay and FID is acquisition of the signal. The initial $180^{\circ}_{x'}$ pulse flips the M_z vector into the negative z-axis. As there is no phase coherence to be lost in the x'y'-plane, the vector decays solely through T_1 relaxation during the period τ, before a $90^{\circ}_{x'}$ pulse flips the vector onto the y'-axis followed by spectrum acquisition. The output signal thus depends on the length τ, and varying this time allows mapping of the relaxation rate. If τ is equal to or longer than T_1, then a maximum value will be found for the measured transverse magnetisation vector.

The T_1 value is found as follows [2]. First, the Bloch equation for T_1 Eq. 1.10 is integrated, yielding:

$$M_0 - M_z = Ae^{-t/T_1} \qquad \textit{Equation 1.13}$$

For t = 0 and $M_0 = -M_z$, A = 2 M_0. This gives:

$$M_0 - M_z = 2M_0\, e^{-t/T_1} \qquad \textit{Equation 1.14}$$

Taking the logarithm of both sides and substituting magnetic components for spectrum intensities yields:

$$\ln(I_0 - I_z) = ln\ 2I_0 - \frac{t}{T_1} \qquad \textit{Equation 1.15}$$

The slope of this equation as a function of time is $-T_1^{-1}$. For the special case of $I_z = 0$, the equation simplifies to:

$$\tau_{zero} = T_1 ln2 \qquad \textit{Equation 1.16}$$

1.4.3 Spin-spin relaxation (T_2)

According to the classical theory of NMR spectroscopy, the spin-spin relaxation takes place by loss of phase coherence between the individual magnetic dipoles constituting the macroscopic transverse

magnetisation component. The mechanism for this loss is field inhomogeneity: The Larmor frequency at which the dipoles precess is dependent on the magnetic field strength. As a result, local variations in the field will cause the nuclei in the sample to precess at different rates, causing the loss of phase coherence [2]. This also means that the T_2 relaxation can be expected to be even more affected by inhomogeneous systems than T_1, as no criterion for a frequency match exists for the relaxation pathway to be effective. The effects detailed in [14] therefore also apply to the T_2 relaxation mechanism, whilst the works of Ronczka and Muller-Petke [21], and McDonald et. al. [18] pertain directly to the application of T_2 determination in heterogeneous systems.

As for T_1, the T_2 relaxation rate is expected to be proportional to the correlation time of the molecule in which the relaxing nucleus resides. Also similar to the spin-lattice relaxation, a spin-spin relaxation mechanism exist that involve interaction with paramagnetic species [2]. Furthermore, an inverse correlation between T_2 and temperature has been found to correspond to relaxation through exchange processes [17], and the electronic relaxation component can influence T_2 as it does T_1.

1.4.4 Determination of T_2

The T_2 relaxation time can be found by applying a spin-echo experiment, the basic function of which can be shown by using the Carr-Purcell-Meiboom-Gill (CMPG) spin-echo experiment as an example [2]. The experiment uses a continuous train of pulse sequences after the first 90^o pulse, as follows:

$$90^o_{x'} - \tau - 180^o_{x'} - 2\tau - 180^o_{x'} - 2\tau - 180^o_{x'} \ldots$$

The $90^o_{x'}$ pulse flips M_z into the x'y'-plane. From there on, the rest of the pulse train revolves around removing the effects of field inhomogeneity from the T_2 analysis. This is done by using a $180^o_{x'}$ pulse after an initial pulse delay of τ. During the time τ, loss of phase coherence is seen due to the effects of field inhomogeneity on the precession rate of otherwise equal nuclei. A $180^o_{x'}$ pulse is then applied, flipping the spin vectors around the x'-axis. All these vectors can be decomposed into separate vector components on the y'- and x'-axes. The x'-component of these vectors will be unaffected by the $180^o_{x'}$ pulse. Therefore, all vectors in the spin system are now in the position that their direction and rate of precession as well as their x'-coordinates remain the same, but their y'-coordinates have been inverted. This means that at the end of the next time period τ, all spin vectors corresponding to the same real system will again be in phase at the (-y')-axis, regardless of differences due to field inhomogeneity. This "echo" is recorded by the spectrometer, and the same sequence is repeatedly applied. The result is a series of these coherent echoes, alternating between being observed at the positive and negative y'-axis every 2τ. During this period, real T_2 relaxation phenomena will manifest on the spin vectors, leading to deteriorating phase coherence in the spin system. This T_2 relaxation is seen in the receiver coil as $M_{y'}$ decaying between every echo, which can be used to find the T_2 relaxation time. Any T_1 relaxation concurrently happening will lead to an increase in $|M_z|$, but this component is merely flipped between the positive and negative y-axis by the $180^o_{x'}$ pulse, and never contributes to the signal from the transverse magnetisation vector.

Sampling a full FID for every echo in order to obtain spectral information takes a considerable period of time. The experiment can be performed in a much shorter timeframe if just a few points are sampled from the echo peaks. The intensities can then be averaged from these points, and used for the T_2 relaxation time calculations. This means the spectral data is lost as there is no saved FID which

to transform, but the ability of quickly acquiring T_2 results is valuable in dynamic studies such as performed in this thesis [22].

Using the technique on samples containing a lot of (H,H) couplings can pose a challenge because of the complexity of such spin systems. As both the water and cyclopentane molecules are symmetrical, however, such couplings will not arise, and the technique will likely be applicable to this system in spite of its physical-chemical complexity [2].

For a more in-depth treatment of the relaxation pathways of molecules at surfaces, the reader is referred to the work of Resing [23].

1.5 The NOESY experiment

1.5.1 Two dimensional NMR

In one dimensional NMR spectra, the spectroscopic data is plotted as intensities as a function of frequency in ppm or Hz. For two-dimensional NMR spectroscopy, however, intensities are plotted in the third dimension, with the two-dimensional axes both on a frequency scale. For the experiments in this thesis, both are defined as ^{1}H chemical shift axes, giving rise to a so-called two-dimensional correlated NMR spectrum. The entire subchapter is closely based on the simplified explanations provided in the book by Friebolin [2], who refers to the book by Ernst, Bodenhausen and Wokaun [24] for a more thorough, mathematical approach.

The main difference between one- and two-dimensional NMR experiments lie in the introduction of a phase of evolution and mixing between preparation and acquisition. The evolution time is designated as t_1 and the mixing time as Δ. The acquisition time will be referred to as t_2 throughout this subchapter. For the series of experiments necessary to obtain a 2D spectrum, Δ remains constant throughout the experiment series while t_1 is changed by a constant amount for every iteration. During the mixing time, the sample may be subjected to additional radiofrequency pulses, depending on the experiment being performed. Fourier transform with respect to t_2 and t_1 yields a spectrum with corresponding F2 and F1 axes in the frequency domain.

1.5.2 The gradient pulse

Using special gradient coils in the spectrometer probe, it is possible to use field gradient pulses to achieve a position-dependent variation of the sample magnetic field. The most common variant is a linear field gradient along the same axis as the external magnetic field, defined as the z-axis. Its overall effect is to subject all nuclei in the sample not at the same z-coordinate to a slightly different local magnetic environment, altering the precession rates of their magnetic vectors. This has the overall effect of destroying any phase coherence present in the xy-plane.

1.5.3 Nuclear Overhauser Enhancement (NOE)

The Nuclear Overhauser enhancement is due to relaxation processes taking place through double- or zero-quantum transition between spin states. As a result, these transitions cannot be induced by the radiofrequency pulses used during NMR spectroscopy, and does not manifest in the spectra. Its

effects can be most clearly explained by examining a spin system AX without a scalar coupling between A and X.

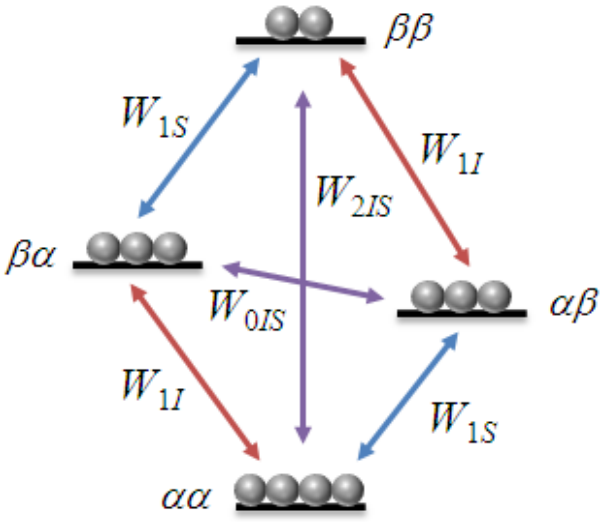

Figure 1.3: Schematic of the spin states and transitions in an AX spin system without scalar couplings. The spins of nuclei are designated as α *and* β*, respectively designating spins as parallel or antiparallel to the external magnetic field. Transitions are marked as W, with the subscript number designating the multiplicity of the spin transition. For example, W_0 corresponds to a zero-spin transition. Taken from [25].*

Irradiation from radiofrequency pulses can induce the W_{1I} transitions in Fig. 1.3, establishing a new population distribution. Given the condition of saturation, the population levels in αβ and ββ will be equal, as will the populations of αα and βα. As a result, the system will attempt to relax to equilibrium through the W_{2IS} and W_{0IS} transitions. The W_{2IS} transition will therefore increase the population of the αα energy level at the cost of ββ, which corresponds to an increase in the population differences between states αα and βα as well as αβ and ββ, and as such leads to an increase in the signal. The W_{0IS} transition will increase the population of the αβ level at the cost of βα, which generally has the inverse effect.

The two competing relaxation pathways depend on the correlation times of the molecules in question, with W_{0IS} the major one at long correlation times and W_{2IS} the dominant process at short correlation times. The reason for this is that the zero-quantum transition is induced by low-frequency fluctuations in the local magnetic field, whilst the opposite is true for the double-quantum transition. As these relaxation pathways depend on the same mechanisms as does dipole-dipole relaxation, the same spatial relationship apply:

$$NOE \propto \frac{1}{d^6} \qquad \textit{Equation 1.17}$$

where d is the internuclear distance.

1.5.4 Nuclear Overhauser Enhancement Spectroscopy (NOESY)

The pulse sequence for the homonuclear ^{1}H NOESY experiment is as follows:

$$-90^{o}_{x'} - t_1 - 90^{o}_{x'} - \Delta - 90^{o}_{x'} - t_2 \text{ (FID)}$$
$$G_1 \qquad\qquad G_2$$

where $90^{o}_{x'}$ are pulses rotating the spin vectors 90^{o} around the x' axis, t_1 is the evolution time, Δ is the mixing time, t_2 is the acquisition time and G_1 and G_2 are identical field gradient pulses, applied before the first $90^{o}_{x'}$ pulse and during the mixing time, respectively. The result of this sequence is that the M_z spin vectors are flipped into the x'y'-plane by the first 90^{o} pulse, where they disperse according to their differing precession rates during the evolution time t_1. The second 90^{o} pulse flip the y'-components of these vectors back onto the z-axis, where they undergo relaxation as well as cross-polarisation by NOE during the mixing time Δ. The final 90^{o} pulse flips these vectors back into the x'y'-axis for acquisition of the transverse magnetisation vector during t_2. The gradient pulses induce a coherence loss in any residual macroscopic magnetisation in the x'y'-plane, allowing shorter relaxation times between each experiment.

Due to the cross-polarisation according to the nuclear Overhauser enhancement during the mixing time, the Fourier transform with respect to t_2 and t_1 yields peaks not only at the coordinates of the nuclei in each spectrum, but also at the coordinates corresponding to polarisation transfer between different protons. As an example, in a sample where protons A and X are close enough for cross polarisation to occur, the two dimensional spectrum gives rise to peaks not only at the (ν_X, ν_X) and (ν_A, ν_A) coordinates but also at the coordinates (ν_X, ν_A) and (ν_A, ν_X). The two latter peaks are called correlation peaks, as they show that nuclei X and A are close enough in space for the NOE to take effect. The technique is mostly used for qualitative aid in molecular structure determination, but the technique can also be used to find internuclear distances [26].

1.6 Previous hydrate NMR research

1.6.1 Non-spinning NMR

In 1993, an article by Fleyfel et. al. [27] was published based on a combination of ^{13}C NMR spectroscopy and macroscopic methods. The work was also presented at the International Conference on Natural Gas Hydrates the following year [28]. The results are claimed to be proof that NMR techniques can be used to probe metastable hydrate systems. Hydrate formation was accomplished by cooling a system of liquid heavy water pressurised with a ^{13}C enriched methane-propane gas mixture in a visual hydrate rocking cell capable of logging pressure and temperature, which yielded the hysteresis loop of hydrate formation and dissociation. A clear water sample was withdrawn from the cell at 279 K and analysed by ^{13}C NMR spectroscopy at the same temperature. To determine that the acquired spectra was indeed due to hydrate particles, an analysis was performed on a sample taken during initial cooling, outside of the hydrate stability region, which yielded no peaks in the spectrum. Another spectrum was acquired on a sample taken at point in the pressure-temperature loop where no remnants of hydrates could be found visually. This yielded a methane hydrate peak much smaller relative to the peak of dissolved methane than in the clear water sample and a propane hydrate peak that had disappeared completely, showing that a snapshot of the microscopic dissociation had been achieved. The seemingly preferential dissociation is attributed to guest-size induced cavity strain. The nuclear spin densities of enclathrated species can be found from the equation

$$\rho_i = \chi_i \rho = \left(\frac{N}{RT}\right)(\chi_i \Delta P) \qquad \textit{Equation 1.18}$$

where

$$\chi_i = A_i / A_t \qquad \textit{Equation 1.19}$$

A_i is the area under peak i, A_t is the sum of all peak areas, ρ is spin density in nuclei/L, N is Avogadro's number, R is the gas constant, T is temperature in Kelvin and ΔP is initial minus final pressure in psia. From this, the number of nuclei can be found:

$$n_i = \rho_i V \qquad \textit{Equation 1.20}$$

where V is sample volume in litres.

In the 2004 work of Kini et. al. [29], non-spinning ^{13}C NMR was performed on a methane-propane sII hydrate system using a purpose-built spectrometer probe in order to probe formation kinetics as a function of ice-particle size. The probe used was capable of in-situ hydrate formation and pressure control at a temperature range of 153-373 K, allowing simultaneous NMR and pressure measurements during hydrate formation. The resolution was insufficient to identify methane in large sII cages, but the authors were able to find a quantification in earlier published ^{13}C MAS NMR on a hydrate system of similar composition [30].

No sI hydrate formation was observed for the explored system. Two formations schemes were found from peak intensities, the first of which was identified by an area of linear growth hypothesised to correspond to hydrate formation on an ice surface. In the second stage, hydrate growth were found to no longer progress linearly. This was attributed to the formation of a hydrate layer on the ice, and corresponding diffusion effects coming into play. Although the small 5^{12} cages in sII outnumber the large $5^{12}6^4$ cages 2:1 in terms of filling by hydrocarbon compounds, the propane-filled large cages were found to form at twice the rate of their small methane counterparts. A discrepancy between this result and that found by Fleyfel et. al. [28] is believed to be due either to the latter's use of liquid water instead of ice, or much higher methane content in the gas mixture. Furthermore, a comparison between the ratios of guest to cage diameter is invoked to explain the results, where a filled cage with ratio closer to 1 is expected to yield greater stability. From this assumption, the propane large cage would be more stable and therefore form more easily. A linear relation was also found between initial hydrate formation rates and both total surface area of ice and partial pressure of the gaseous formers, in agreement with the theory of a surface process taking place.

1.6.2 ^{13}C MAS NMR

The work of Subramanian et. al. from 2000 [31] verified earlier results that suggested that binary methane-ethane gas mixtures form sII hydrates in presence of water at certain thermodynamic conditions, using Raman spectroscopy for the main body of work and MAS NMR spectroscopy as verification. In the latter, the spectra of sI hydrates formed from either methane or ethane are compared with both methane-ethane sII hydrates and sII hydrates formed from a Green Canyon gas mixture. The methane-ethane hydrate was found to be structure II by using the peak for ethane in the $5^{12}6^4$ cage of Green Canyon gas hydrate as reference – this hydrate mixture was previously found to be sII by Davidson et. al. [32]. A sufficient difference between the chemical shifts of ethane in the

large cages of sI and sII hydrates was found to warrant its use as a marker for hydrate type. Finally, ^{1}H NMR was used to determine the composition gas mixture after hydrate formation was finished, using the formula

$$\chi_i = \frac{I_i/n_i}{\sum(I/n)} \qquad \textit{Equation 1.21}$$

where χ is mole fraction, I is peak intensity and n is the number of hydrogen atoms in the compound giving rise to a specific peak.

A 2007 study by Gupta et. al. [33] investigated the dissociation of methane hydrates using ^{13}C MAS NMR. The relation between the chemical shift of the methane carbon and pressure and temperature was established in order to allow estimation of the pressure within the sample container. The ratio of small to large cage occupancy of methane in the sI hydrate was found to remain constant throughout the decomposition process, showing the absence of a preferential melting mechanism.

In the 2009 article by Dec [34], several findings using ^{13}C solid-state MAS NMR are presented, with some corrections to the article given in [35]. First, the hydration number of aqueous ethane was determined to be 26. Furthermore, the number of methane $5^{12}6^2$ cages was found to be greater than the number of methane 5^{12} cages during the initial stage of sI hydrate formation at 274 K. Ethane-methane sII hydrates were also found under thermodynamic conditions where the corresponding sI hydrates are the sole stable hydrate phase. It was shown that methane-ethane sII hydrates at 268 K contain less methane than used during formation. At the same temperature, the existence of a quasi-liquid layer of water was found, and this layer was capable of dissolving both methane and ethane. Its contents of dissolved gas molecules were below detection limits at 253 K, however, and significantly smaller amounts of sI and sII hydrates were found at this temperature compared with those at 268 and 274 K. Finally, methane and ethane dissolved in water both liquid and quasi-liquid was found to enhance hydrate formation at 268 and 274 K, with sI formation favoured at the former and sII at the latter. The results was used to create a model which states that the structure of the initial hydrate phase is governed by the aqueous hydration number of the hydrate former most readily dissolved in water. The model validity was verified by density functional theory computations, and successfully used to explain the formation processes of other hydrates.

An article published in 2009 by Seo et. al. [36] covers formation kinetics of mixed hydrates using gas uptake measurements, and how formation conditions influence the composition of the hydrate phase. Methane, ethane, propane and isobutane were used as formers. ^{13}C MAS NMR was used to find the distributions of guests in the lattice cavities when hydrate was formed from either bulk water or water in porous silica gel. When the heavy hydrocarbon compounds in the vapour phase is depleted, sI methane hydrates was found to form in place of the mixed sII hydrates, with the two structures coexisting. This is in accordance with earlier reports of a preference for formation of mixed hydrates from heavier formers [37-39]. In the porous silica, this preference was found to be further enhanced. Guest distributions were found from the ratios of integrated peak areas along with chemical potential considerations.

The NMR studies were performed using a 400 MHz solid state spectrometer under high-power proton decoupling and a spinning rate of 2-4 kHz at a temperature of 243K, with sample contained in 4mm Bruker ZrO_2 rotors. NMR sample preparation was done at liquid nitrogen temperature, from hydrates formed in the gas uptake measurement instrument.

In a 2011 article by Alavi et. al. [40], structure H hydrates of large alkanes with methane help gas was studied by solid state ^{13}C NMR to find how conformational changes in the guest molecules and dipolar coupling between guest and host contributes to changes in the NMR spectrum. Hydrate lattice structure was determined using X-ray diffraction.

1.6.3 T_1 relaxation studies

The proton T_1 relaxation behaviour of a series of formers was studied in 1997 by Jacobs et. al. [41]. Inversion recovery T_1 experiments were performed over a temperature range from 20-263 K on hydrates in a D_2O host lattice. Two spectrometers were used: The upper temperature range from 140 – 263 K was studied using a 300 MHz instrument, whilst the lower region <140 K was studied using a 60 MHz instrument.

The data fitting was achieved by only evaluating intramolecular dipole-dipole interactions, which the authors claim to be the sole contribution at low temperatures, and Albayrak et. al. [42] is cited on the irrelevance of intermolecular dipole-dipole interactions. Therefore, interactions of geminal protons were seen as the premier cause of relaxation, with protons within 2.0-2.5 Å providing another 20 % contribution to the overall relaxation. Molecular vibrations will cause a reduction in the spectral density during T_1 measurements, and this reduction will be confounded with coupling constant reduction.

The asymmetric relaxation rate when plotted against inverse temperature is described as a Cole-Davidson distribution of reorientational correlation times [43]:

$$J_{CD}(\omega) = \frac{\sin(\beta \arctan(\omega\tau_c))}{\omega(1+\omega^2\tau^2)^{\beta/2}} \qquad \textit{Equation 1.22}$$

where J(ω) is the spectral density and β is a shape parameter which measures the relaxation rate versus inverse temperature curve asymmetry. For β=1 this yields a Poisson-distribution and a corresponding symmetric Bloembergen-Purcell-Pound spectral density. The cut-off correlation time τ_0 is assumed to follow Arrhenius behaviour.

The Arrhenius behaviour of the relaxation rate was found to differ between high (>200 K) and low temperature ranges. It is hypothesised by the authors that this might be due to clathrate instability, as incomplete crystallisation will lead to higher relaxation rates. Using X-ray diffraction, the authors did find evidence of a “pre-melting” region, which supports this theory. In addition, lattice motions that start to manifest at around 200 K could lead to differing rotational behaviour of the guests at high and low temperature. A third explanation provided is that spin-rotation interactions might come into play at higher temperatures, especially for small molecules. Due to the complex and uncertain nature of the guest-host interaction in the high-temperature range, the authors only used low-temperature relaxation rates during data evaluation.

Several conclusions were drawn from the experimental data. For instance, the results for the binary hydrates of THF and ethylene oxide was in agreement with previous results obtained for deuterated-lattice THF hydrates, with and without H_2S co-guest [42]. This provided evidence that little, if any, interaction takes place between guests in different cavities. In addition, correlation time and activation energy results showed that the rotation of THF in the hydrate cavity is nearly unhindered compared to the liquid phase and that the frequency of collisions between THF and cavity wall is

about 1000 times more infrequent than intermolecular collisions in the liquid phase. Overall, this indicates that guests do not rotate through a “small step” diffusive process, but maintain a high degree of mobility, a notion supported by dielectric relaxation studies [44].

Dioxolane was found to have higher correlation times and lower activation energies than tetrahydrofuran, giving rise to yet higher rotational mobility and further hindering guest-host collisions. For cyclopentane, the fit parameters are similar to those of dioxolane, resulting in near equal rotational speeds.

In a 2005 study, Gao et. al. [45] performed formation and dissociation studies of deuterated-lattice tetrahydrofuran hydrates using T_1 inversion recovery. A T_1 data point was achieved in 4-6 minutes. Viscosity measurements were also performed as part of the study.

The article states that the rotational activation energy of the guest can be found from the slope of $\ln(1/T_1)$ versus $1/T$, which gives clues about the water structure around the molecules. This can be shown as follows: T_1 is inversely proportional to the rotational correlation time τ_c [2]. Furthermore, the Arrhenius equation is assumed to describe the correlation time. This gives the following relationship:

$$\frac{1}{T_1} \propto \tau_c \qquad \textit{Equation 1.23}$$

and

$$\tau_c = \tau_0 e^{E_a/RT} \qquad \textit{Equation 1.24}$$

where τ_0 is a pre-exponential constant, E_a is the rotational activation energy, T is the temperature in kelvin and R is the molar gas constant. By combining the equations 1.21 and 1.22, equation 1.23 is attained:

$$\frac{d\ln\left(\frac{1}{T_1}\right)}{d\left(\frac{1}{T}\right)} = \frac{E_a}{R} \qquad \textit{Equation 1.25}$$

Dissolved oxygen was removed by repeatedly flushing the sample headspace with nitrogen gas, and periodically shaking the sample to increase oxygen diffusion rate. An increase in T_1 of approximately two seconds was observed as a result of deoxygenation. However, the study was largely performed in the liquid state.

The authors found no evidence of precursor molecules upon lowering of the temperature into the hydrate formation range, and no change was observed under nucleation during extended periods of subcooling. However, T_1 values were found to be lower after hydrate melting compared to before formation. This was linked to greater microscopic sample homogeneity after hydrate dissociation, as the effect persisted at temperatures at which memory effects should no longer manifest. A large difference in rotational activation energy was found between the tetrahydrofuran in aqueous hydration shells and the solid hydrate phase, leading to the conclusion that a large difference exists even when hydrate formation is thermodynamically favourable. Around 8.5 ^{o}C, the activation energy increased slightly as the temperature fell, a fact that remains unexplained in the article. Work to elucidate the reason is said to be underway.

In a 2015 study, Nelson et. al. [46] performed deuteron NMR-studies on hydrates of cyclic guests using both detuerated guests in water and guests in deuterium oxide. Ether-type guests capable of inducing proton defects in the hydrate lattice were also studied. These hydrates were doped with ammonia, which creates Bjerrum D defects in the lattice which can interact with the Bjerrum L defects created by the guests. Cyclopentane hydrates were crystallised from solution using a procedure found in [47], with further theoretical background provided in [48, 49].

X-ray diffraction was used to determine the hydrate crystal structure, as well as to quantify ice content. The latter shows that rapidly crystallised hydrates contain higher amounts of ice contaminant, with slowly formed cyclopentane samples containing about 50 % ice by weight. Ice and hydrate dynamics were distinguishable, however, on the basis of either differing time scales between guest and lattice, or on the difference between spin-lattice relaxation times. The lattice constants, *a*, were determined and found to have a linear correlation with guest diameter [50, 51].

The complex dielectric constant was also measured, to determine dipole moment at very low temperatures (slightly below 10 K to 30K). Partial deuteration of cyclopentane yields a permanent dipole moment, but a very small one already exists due to the non-planar molecular conformations of cyclopentane, in the range of 10-20 mD.

T_1 was measured using the saturation recovery technique with solid-echo refocusing, at very low temperature. For deuterated guests in a H_2O lattice, the maximum relaxation rate ($T_{1\ MAX}^{-1}$) is found to be inversely proportional to guest radius. The opposite is found to be true when only the host structure is deuterated. T_1 rates were described quantitatively using an expression attributed to Bloembergen, Purcell and Pound [52] and Abragam [53], yielding:

$$\tau(T) = \tau_0 \exp\left(\frac{E_A}{k_B T}\right) \qquad \textit{Equation 1.26}$$

Fitting to the Cole-Davidson spectral density equation yields τ_0, E_A and β (distribution of molecular correlation times). δ_{eff} is also listed. δ_{eff} is found to be smaller than δ_Q, providing evidence of anisotropic guest motion.

For the deuterated host samples, the main mechanism for relaxation is heteronuclear dipolar interactions between water deuterium and guest protons. The aforementioned parameters are found to be in agreement with the ones found for the deuterated lattice.

Stimulated-echo experiments were used to probe the lattice dynamics caused by Bjerrum L defects. Cyclopentane lattice dynamics were found to be ice-like from comparisons with the work of Geil et. al. [54].

Reorientation activation energies show a near-linear increase with guest size, apart for the nonpolar cyclopentane. Dipole moment does not seem to be important on the basis that a trend is followed by species of widely different polarities. Cyclopentane hydrates show a larger guest-host distance than its guest radius would dictate, and the authors argue that this is due to the cyclopentane molecule having its centre of mass better placed in the middle of the cage due to lack of polar forces pulling it towards the cage walls. It is known that many guests deviate considerably from cage centre in order to maximise favourable cage-guest interactions [7, 51, 55, 56]. These interactions are hard to probe using NMR due to the time-averaging present in the technique. The technique can, however, probe

whether hydrogen bonding between guest and host takes place, as well as how guest polarity enhances water dynamics.

1.6.4 T_2 relaxation studies

The proton T_2 relaxation of tetrahydrofuran hydrates in a deuterated lattice was explored in a 2009 article by Gao et. al [57]. A low-field spectrometer at 2 MHz was used, a common technique in rock and fluid characterisation in the petroleum industry [58]. The technique had rarely been used before in hydrate research due to its low signal-to-noise ratio.

Trace paramagnetic species can significantly alter the relaxation rate, and thus the sample was prepared under a nitrogen atmosphere in a glovebox using an earlier described process [45]. To ensure sample homogeneity, the system was allowed to form hydrates before being subjected to 35 ^{o}C for two hours to ensure melting and destruction of residual molecular structures.

Measurements were performed as the sample solution was cooled stepwise in the hydrate formation region. The nucleation event was determined from a rise in temperature, which prompted a slower cooling rate in order to slow down the rate of formation. The Carr-Purcell-Meiboom-Gill (CPMG) technique was used to acquire T_2 data, from which distribution peaks were found by WinDXP software after each acquisition. Each experiment took between 5 and 10 minutes depending on chosen parameters. Higher sample homogeneity will lead to narrower, more symmetrical T^2 distribution peaks. After studying the transition from solution to hydrate, the temperature was lowered further to investigate T_2 as a function of temperature.

T_2 relaxation studies can provide information about the molecular environment of the species observed. It was shown that the technique is able to simultaneously determine the T_2 distributions of THF in both liquid phase and hydrate cages. Evidence was also found that the presence of hydrates influence the behaviour of a coexisting liquid phase, in line with previous work by the authors [59].

As for T_1, Arrhenius behaviour is assumed for T_2. This allows the rotational activation energy to be found from the slope of $\ln(1/T_2) \approx 1/T$ [60]. A change in this slope was found during the cooling process, at a temperature 1-2 K above the formation temperature of the hydrates. This indicates a structural change in the molecular environments of THF, but no attempt was made in providing a mechanism. Between 260 K and 275 K, a rotational activation energy of 31 kJ/mol was found.

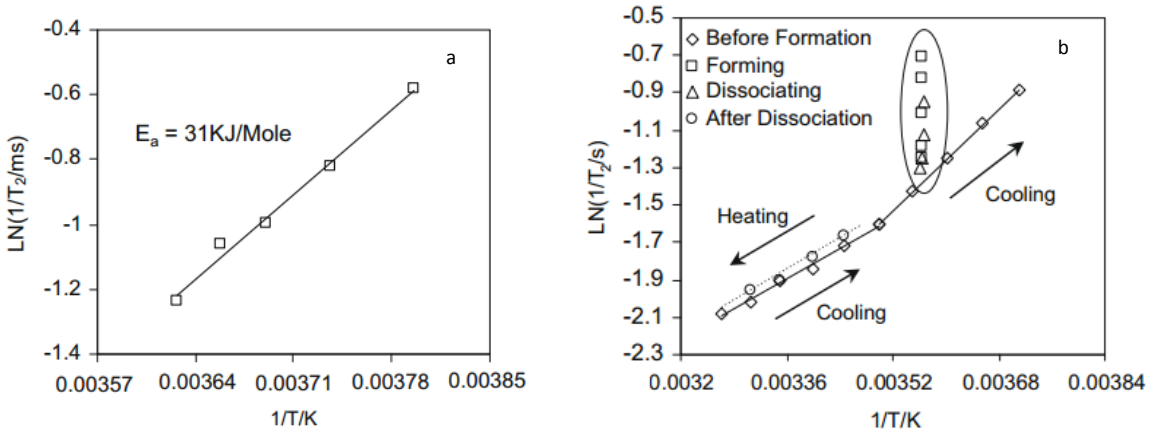

Figure 1.4: Taken from [41], this figure shows the relaxation behaviour of the system with respect to

changing temperature. Part a *shows the determination of rotational activation energy. Part* b *shows the formation-dissociation experiments, where two areas of different slopes are present. Formation and dissociation processes leads to a near vertical change in ln(1/T_2).*

1.6.5 Two-dimensional NMR experiments

The work done by Dec in 2012 [61] utilised 2D exchange ^{13}C MAS NMR spectroscopy and ^{13}C MAS NMR intensity results to probe the transition between sI and sII structures as the hydrate system reaches equilibrium. The transition is found by ^{13}C intensity data to mainly progress through the simultaneous decomposition of methane-ethane sI hydrate to gas and water and formation of sII methane-ethane from water and gas, a process that takes place at the surface of the hydrates. The results of the 2D technique are in agreement with these findings, and also show that sI and sII hydrates are not closely mixed.

The rate of ^{13}C MAS NMR intensity change was measured using continuous 32-minute experiments over a period of 45 hours. The results allow sorting the results into several different reaction stages. During the first stage, both sI and sII methane-ethane hydrates formed at surface sites. This phase transition is dependent on a layer of liquid or quasi-liquid water for the gaseous products to be dissolved at ice or hydrate surface sites [34, 35]. Throughout stage 1, sII hydrates comprise a metastable phase [1]. During the second stage, the number of methane and ethane sI $5^{12}6^2$ cages reached a stable value. The consumption of methane rapidly increased in comparison with stage 1, while the ethane consumption remained near equal. A large increase in the rate of ethane $5^{12}6^4$ and methane 5^{12} cage formation was observed during the stage, indicating that sI had replaced sII as the metastable phase. In stage 3, the number of ethane and methane $5^{12}6^2$ cages were found to decrease, meaning that sI dissociation was occurring. A preference for ethane $5^{12}6^4$ cage formation was found by formation rate comparisons, in agreement with previous work by the author claiming that formation of this cage controls the overall formation of sII methane-ethane hydrates [34, 35]. Stage 4 is regarded as the final step towards steady-state, as evidenced by a drastic reduction of all formation rates and a stabilisation of the mole fraction of methane gas.

The 2D technique used was able to resolve the 5^{12} cages of sI and sII hydrate. No cross-peaks were observed for the ethane $5^{12}6^2$ and $5^{12}6^4$ peaks, showing that the sI and sII hydrate phases are not interspersed. This is consistent with a sI $\leftrightarrow$ sII structure transition taking place through a gaseous intermediary, and inconsistent with a transition taking place in the bulk hydrate.

In an article published in 2015, Moudrakovski et. al. [62] investigates the effects of guest-host hydrogen bonding on the diffusional mobility of guest molecules between water cages. Two pairs of hydrate formers, THF-CO_2 and isobutane-CO_2, is investigated, as these are expected to respectively increase and diminish the guest-host hydrogen bonding and thus guest diffusion. The guest positions in the lattice are determined by single crystal X-ray studies, and molecular dynamics simulations were performed on unit cells corresponding to the X-ray data. Along with ^{13}C and 2D exchange spectroscopy (EXSY) NMR experiments, a model of the structure and dynamics of these binary hydrates was established. The EXSY experiment is used to measure the polarisation transfer between nuclei participating in exchange processes, and as such can yield information on which nuclei in a sample undergoes a change from the resulting cross-peaks in the 2D spectrum [2].

Hydrate samples were prepared by freezing degassed water by dropwise addition to liquid nitrogen, followed by powdering of the formed ice and introduction to a Pyrex tube with a glass joint. The tube was connected to a vacuum line and air was evacuated, before adding ^{13}C-labled CO_2. The sample container was then flame-sealed. It is claimed that any residual ice will have no effect on the overall experiment. For preparation of the binary hydrates the same procedure is used, with the exception that pure water is replaced with a solution of tetrahydrofuran in water in order to form CO_2-THF hydrates, and using a 1:1 mixture of $^{13}CO_2$ and isobutane gas for formation of CO_2-isobutane hydrate. Samples were allowed to warm to 276 K, and remained at that temperature for a minimum of four days.

Due to large line-widths, either cross polarisation or a Hahn-echo pulse utilising direct excitation [63] was used during acquisition. The Hahn-echo matching conditions was determined on an adamantine reference sample [64]. The pulse sequence used is based on the work of Jeener et. al. [65], using time-proportional incrementation [66] and high power proton decoupling. Experiments were performed in the 173-263 K range in steps of 10 K. The sample was allowed to reach thermal equilibrium using at least a 15 minute rest period on achieving the desired temperature.

Citing the works of Ratcliffe and Ripmeester [67] and Alavi et. al. [68] the authors state that at temperatures around 273 K, the line shapes of guest NMR spectra results from a time-averaged symmetry of the cages. For lower temperatures, this symmetry decreases as H_2O molecules freeze into one of many proton positions, restricting the motional freedom of the guests. This results in a broader powder pattern at lower temperatures.

The CO_2 molecules are found to move faster in the small sI cage of the binary CO_2-THF hydrate than in the large sI cage in pure CO_2 hydrate. As a result, the ratio of cavity-to-guest size is found not to be the determining factor for guest dynamics. In addition, the powder spectrum of CO_2 in the small cage collapses into a narrow line above 243 K, which indicates isotropic averaging of the shielding tensor. The change was found to be reversible, and is believed to be due to an activated process. For the shielding tensor to average to zero by molecular motion alone, a set of highly specific orientations would have to be available to the guest, which is improbable. However, the averaging can also be explained if the CO_2 molecule diffuses into different cages. This would require either a water vacancy or a Bjerrum defect between the cages in question, which is in accordance with the fact that the transition was observed only for the CO_2-THF hydrates. The EXSY results obtained in the study also supports this conclusion.

The speed of water reorientation in the lattice was found to be as follows: CO_2-THF > CO_2 > CO_2-isobutane, which provides evidence that synergistic effects exist between guests in separate cages. These effects are believed to be related to the introduction and propagation of Bjerrum defects in the water lattice [62].

1.7 Objective and approach

1.7.1 Objectives

Following the first published application of NMR to the study of hydrates by Davidson in 1969 [69], NMR techniques have become a powerful tool within the field. Many different methods have been established and refined by several separate research groups and authors, as discussed above.

However, proton-NMR on hydrate systems with both guest and host lattice devoid of detuerated components have not received much attention. Furthermore, approaches to these problems usually involve the use of MAS NMR spectroscopy due to its much-improved resolution.

Employing static NMR opens up the possibility of using gradient pulses, integral to several 2D spectroscopy techniques as well as MRi, and greater understanding of the behaviour of such static systems might aid in the application of these techniques. Furthermore, several benefits are present if the natural-isotope approach is successful, the most important being a more direct observation of the behaviour of, and interactions between, guest and host when both are simultaneously probed within the same sample. In addition, natural-isotope gas hydrates might behave somewhat differently than its isotope-exchanged counterparts, especially in relation to NMR studies. If such differences could be pinpointed, it would facilitate the application of NMR research to understanding real gas hydrate behaviour for results from studies of both sets of hydrate systems; isotope-exchanged or not. A third consideration is price and availability, with detuerated compounds being far more expensive than their proton analogues. At the moment of writing, a kilogram of 99.9 % deuterium oxide costs 8,142.99 NOK (1,006.81 USD) from Sigma-Aldrich [70], whilst a price of 499.00 USD is found for 10 mg of cyclopentane-d_{10} [71]. In comparison, 2 L of reagent grade (98%) natural-isotope cyclopentane can be acquired from Sigma-Aldrich for 346.29 USD [72], while H_2O of several different purity grades are readily available at most scientific facilities.

As the body of literature is lacking in this specific field, an important goal of this thesis is to provide a solid framework for future work by establishing procedures, probing what techniques are promising and using the experimental results for a discussion of how to refine and optimise the work in further studies. As a result, the benefits and drawbacks of all operations will be discussed, from hydrate formation and workup and sample preparation to NMR experiments, as well as sample transport and storage. The recommendations for further work section will elaborate on what steps should be optimised or improved, additional experiments that are believed to complement the results, and ideas of how to accomplish these improvements.

An important aspect of the thesis is to gauge the sample-to-sample homogeneity, in order to have an informed discussion of both the quality of the sample preparation and handling procedures as well as the inherent variance between samples. Repeat measurements are therefore preferred over continuous optimisation of experimental parameters, as the latter could well lead to confounding of the effects of experimental changes with actual differences between samples.

1.7.2 Approach

Whilst intensities and chemical shifts of hydrate constituents have been studied in the past, especially for ^{13}C-NMR, most such studies rely on magic angle spinning. The information contained within static proton spectra of hydrates, however, has never received significant study. These are suspected to change considerably during dissociation, and will give clues to the structural alterations taking place during phase transitions on the basis of changing line widths, intensities and chemical shifts. Such spectra are assumed to be difficult to analyse due to unavoidable sample inhomogeneity during phase transitions, and resulting artefacts in the spectra. Nonetheless it provides a method that, if successful, can provide quick and simple sample state monitoring and data acquisition, which in conjunction with other methods can shed light on the processes taking place within the sample.

Analysing static spectra in conjunction with MAS-spectra of the same sample would be beneficial. However, changing from static to dynamic mode on the spectrometer is challenging when operating at temperatures other than ambient with temperature-sensitive substances. The feasibility of accomplishing this without unreasonable trade-offs is briefly explored, as having this capability would be beneficial to future studies. It is not utilised for the majority of the experiments in this thesis, however.

Several previous studies have probed the relaxation times of components in the hydrate structure, but most of these have been performed at low temperatures well within the range of hydrate stability. The work of Gao et. al. [45] is a notable exception, and their work proves the feasibility of using T_1 relaxation experiments to monitor structural changes during hydrate formation and dissociation. T_1 relaxation experiments are therefore included in the thesis work, to probe whether a similar technique can also be used when lattice protons are present, and how to correctly execute and analyse the experiments. However, the results in this thesis are expected to be inferior to those attained by Gao et. al. on the basis that the hydrate reactor used in this work precludes effective sample degassing. Combining the experimental procedures found in previous literature with knowledge of available equipment, ideas of how to rectify this in future studies will be provided in accordance with the thesis goal.

T_2 relaxation experiments are also performed, using a pulse program capable of attaining results over a short time span. This technique can also be used to find structural information on the cyclopentane hydrate system, and verifying its applicability is an important part of the thesis. The ^{1}H-spectrum along with T_1 and T_2-measurements are taken in rapid succession in order to continuously probe the evolution of the hydrates with respect to temperature and time.

Lastly, application of 2D-NMR techniques to the hydrates is attempted by using NOESY to measure proton-proton distances in the hydrate structure. At this time, such an approach to hydrate research is in its infancy, with only two studies published on the basis of a 2D technique [61, 62].

Chapter 2 Methods and experimental procedures

2.1 Materials

Table 2.1: Compounds used during the experiments.

Compound	Supplier	Purity
H_2O	UiB	Deionised
D_2O	Sigma-Aldrich	99.98 %
Cyclopentane	Sigma-Aldrich	98 %

2.1.1 The cyclopentane hydrate model system

As most natural gas hydrates require high pressure, low temperature conditions for formation, specialised equipment and safety procedures are needed for their preparation and analysis. Instead,

a model system is used where cyclopentane constitute the hydrate former. This system forms solid sII hydrates at atmospheric pressures and a temperature of +7.7 ^{o}C [73, 74].

Table 2.2: Properties of cyclopentane.

Chemical formula	Molar mass (g/mol)	Density (g/cm^3)	Boiling point (^{o}C)	Solubility in water at 25^{o}C (mg/L)
C_5H_{10}	70.13	0.751	49.2	156

As the cyclopentane phase is poorly miscible with water, stirring is required during hydrate formation experiments. For the NMR spectra of the system, two major peaks are expected: One at high chemical shifts, corresponding to water, and one at lower chemical shifts that corresponds to cyclopentane. This assumption is founded in the shielding effect provided

2.1.2 NMR sample containers

The NMR samples were prepared in 4 mm ZrO_2 rotors from Bruker, fitted with Kel-F drive caps for sealing and spinning capability from the same manufacturer.

2.2 Hydrate formation and workup

2.2.1 Experimental setup

A cooling bath was utilised in hydrate formation, using a volumetrically even mixture of distilled water and diethyl glycol as a coolant liquid per a procedure found in the thesis of Abdulkader [75].

A modified version of a procedure found in the work of Corak et al. [76] was used for hydrate preparation. A round-bottomed flask containing deionised water (250 mL) and cyclopentane (50 mL) was immersed in the cooling bath and secured by a flask clamp. The upper part of the flask extruding from the bath was insulated using aluminium foil. A stirrer at a rotational speed of 150 rpm was used to ensure continuous mixing of the liquids. The sample temperature was logged by two temperature probes connected to a Testo 176T2 temperature logger. When the system reached 1.5^{o}C, hydrate nucleation was induced by addition of ice crystals. The hydrate growth phase was considered complete either when the sample temperature restabilised at 1.5^{o}C, or six hours after first observed hydrate formation. The water-wet hydrates were vacuum-filtered and centrifuged. The samples were stored under lid at -30^{o}C. Due to the paramagnetic properties of iron ions, care was taken to avoid contact with metal equipment throughout the preparation.

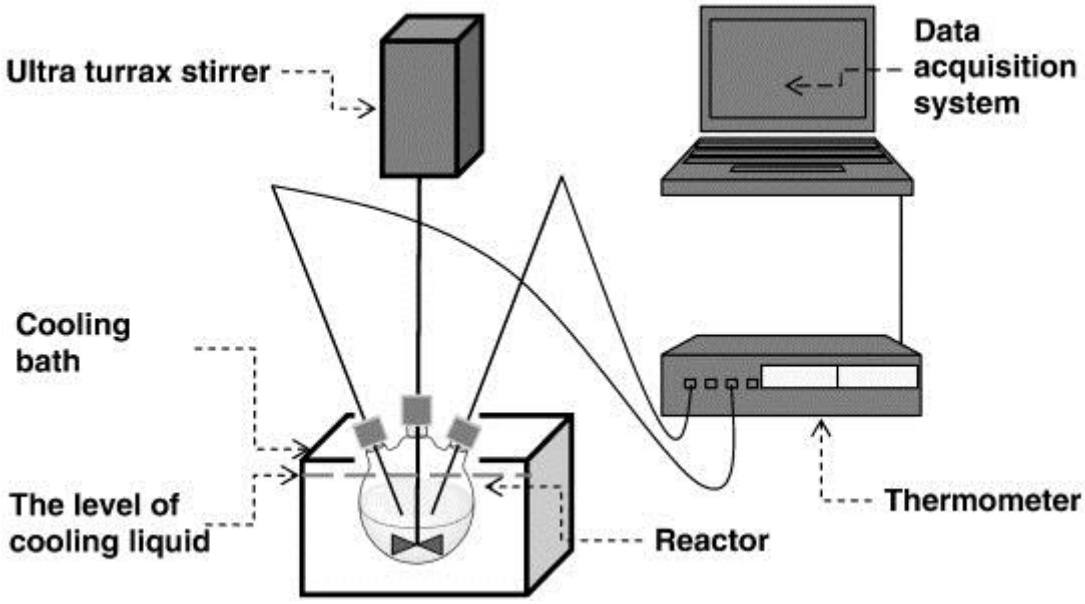

Figure 2.1: Schematic of the hydrate reactor, taken from [76].

2.2.2 Centrifugation procedure

The centrifugation procedure differed for the different hydrate batches, although all used procedures were based on that of Corak et. al. [76]. A cooling centrifuge was pre-cooled to a temperature of -5 ^{o}C. A spinning rate of 4000 rpm was used, the maximum attainable by the centrifuge. A cotton plug was placed in the bottom of each of the four centrifugation tubes used, in order to absorb the water phase, and the hydrates were distributed equally between these tubes.

The batch 1 hydrates were not centrifuged, while the batch 2 hydrates were centrifuged for a period of 5 minutes. The batch 3 hydrates were first centrifuged for 5 minutes, followed by transfer to new centrifugation tubes containing fresh cotton plugs. The samples were then centrifuged for 10 additional minutes, with all other variables remaining equal. The contents of the four tubes were transferred to four separate containers, marked as bulk samples a, b, c and d, and placed in storage.

2.3 Rotor packing procedure

Before NMR-experiments, a small amount of stored hydrate sample was transferred to a ZrO_2 rotor, usually done one to three days before using the rotor. The following subchapter describes the experimental procedures used to produce the NMR samples. As body heat was sufficient to rapidly melt the small volumes of hydrate, all sample manipulation was done using tweezers as far as possible, and using paper towels as insulation when hand precision was required. As before, the risk of paramagnetic contaminants were minimised by the exclusion of metal equipment whenever contact with the hydrate sample was possible.

Figure 2.2: Rotor packing rod and funnel (left) and sealed rotor (right). Not to scale.

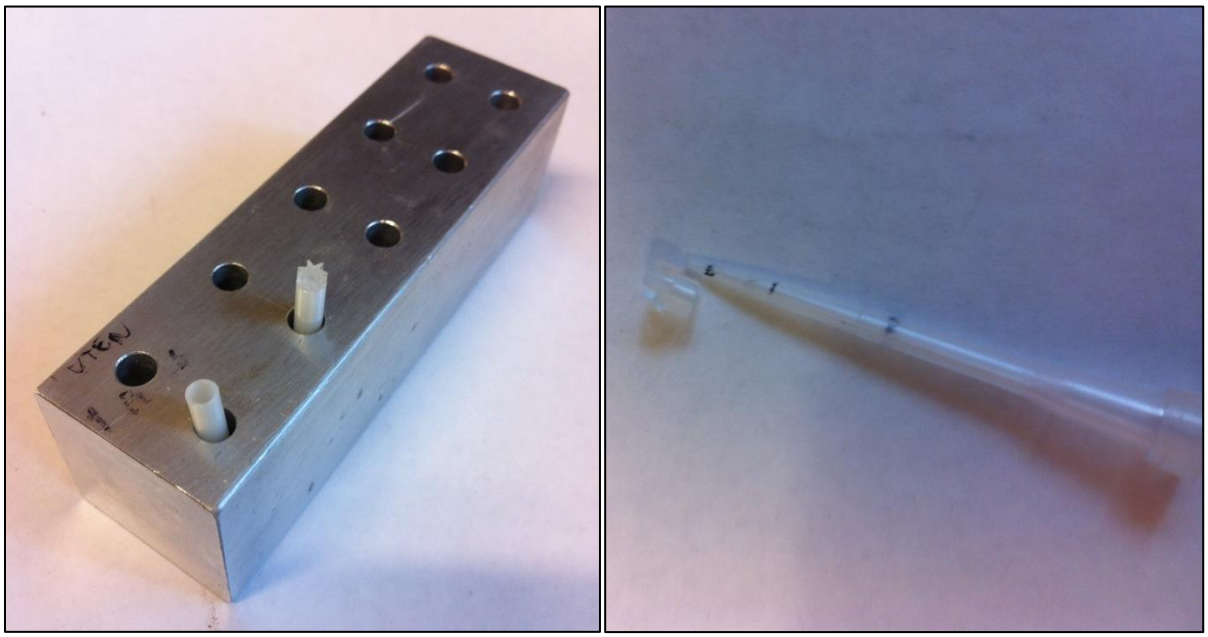

Figure 2.3: Sample holder with sealed and unsealed rotor (left) and sample depth gauge with lid (right).

2.3.1 Rotor naming

Filled rotors are named by the batch number and storage method of the bulk sample it originates from, as well as progressively numbering rotors prepared from one given bulk sample. For batch number three, the naming nomenclature also differentiates between the different bulk storage containers, called *a, b, c* and *d*. As rotors were routinely emptied and reused, the nomenclature identifies the contents of the specified rotor, not the rotor itself.

Overall, this gives the designation **B*X*Si*Y***, where **B*X*** is hydrate batch number ***X***, **S** is storage method (**F** for freezer at -30^{o}C and **C** for cooler at 3-4^{o}C), **i** denotes which of the bulk sample containers *a, b, c* or *d* the hydrates were taken from (only used for batch 3), and ***Y*** is the rotors number in line in relation to the specific identifiers given earlier. As an example, the third rotor filled with batch 3 hydrate sample from container *a,* stored in a freezer, would be named B3Fa3. For the first sample in a series, the ***Y*** identifier is dropped. Thus, a name of B3Fa is given to the first sample in the series from the corresponding bulk sample, not B3Fa1

The rotors themselves were unmarked, but were stored in their respective zip lock bags to which the sample identifiers were added. In addition to this local identifier, each rotor bag was also separately marked with a global sample number for contingency.

2.3.2 Cooling cabinet procedure

The initial procedure was established for work within a cooling cabinet capable of temperature adjustments of ± 0.1^{o}C, spanning a range from -50 to 50^{o}C. The cabinet is fitted with a door of acrylic glass, with closable holes to allow work within the cabinet while maintaining a cold atmosphere. The temperature is adjusted and monitored on a side-mounted temperature controller, and an auxiliary thermometer is placed within the cabinet for temperature verification. Several hours are usually required for the cabinet to reach the designated temperature when starting from room temperature.

Initially, the weight of the empty rotor with lid was measured. The rotor was then placed inside a funnel designed for rotor filling using a dedicated packing rod. The funnel, rod, rotor, tweezers, an aluminium sample holder, sample depth meter and a glass spatula was placed in the cooling cabinet at 1.5^{o}C for pre-cooling. After approximately one hour, the hydrate sample was placed in the cooling cabinet and crushed to a powder. Hydrate crystals were introduced to the funnel, a small spatula tip at a time, with rigorous packing between additions. Any liquid observed during the packing was wiped off the rod and funnel. In order to measure the filling level, the rotor was transferred from the funnel to the aluminium sample holder using tweezers. The level of filling of the rotor was gauged using a plastic pipette tip with the intrusive length of the lid marked. The rotor was deemed full when two conditions were met: Touching the hydrate surface with the pipette tip placed the lid marking in line with the rotor edge, and no depression could be felt when applying a small amount of force to the sample with the packing rod.

When full, the rotor was placed in the aluminium sample holder using tweezers, and a shallow bath of liquid nitrogen was prepared in a Styrofoam lid on the workbench outside of the cooling cabinet. The rotor lid was immersed in liquid nitrogen for a few seconds before being placed, wings down, on a stable surface. The sample holder, with rotor, was placed beside the liquid nitrogen bath. Using tweezers, the rotor was partially immersed in liquid nitrogen for a few seconds, and then pinched by fingers using a folded paper towel for insulation. The rotor opening was aligned with the lid, which was then secured by pressing the rotor down against the lid in two main steps: First a light push to achieve partial insertion at the correct angle, followed by a firmer push to fully insert the lid after confirming alignment. Care was taken to always keep the application of force perpendicular to the surface of the workbench. If a slight misalignment between lid and rotor was observed, or no insertion was achieved in approximately 15 seconds, both rotor and lid was re-immersed in liquid nitrogen before repeating the procedure. Sufficient sealing was confirmed by the absence of gaps

between rotor and lid, and lack of lid rotation upon application of moderate torque to the lid by hand. The sealed rotor was then weighed and placed in freezer storage. The entire procedure, excluding pre-cooling, was found to take approximately 40 minutes.

For some static experiments, the rotor wings were removed using a scalpel after securing the lid. During wing removal, the rotor was held using insulating paper towels and was immersed in liquid nitrogen for a few seconds at intervals of approximately 15 seconds. After wing removal, the rotor was weighed and stored. This entire step was found to be unnecessary.

2.3.3 Modified packing procedures

Due to a compressor failure, the packing procedure had to be reworked in order to function without the cooling cabinet. This meant working in environments at an ambient temperature above the melting point of the cyclopentane hydrates, relying on liquid nitrogen coolant to maintain sample integrity.

The first attempt utilised liquid nitrogen as the sole cooling agent. A glovebox with the rubber gloves removed was fitted with a thermometer. Two Styrofoam lids were placed in the glove box, along with a Styrofoam container filled with liquid nitrogen. Liquid nitrogen was poured into the two lids from the container, creating two shallow reservoirs. These were refilled as needed. The rod and funnel, tweezers, rotor, lid, aluminium sample holder, depth meter and glass spatula was placed inside the box for pre-cooling. The hydrate sample was crushed to a powder within its container and placed in an ice bath inside the box. Care was taken to ensure that the ice could not contaminate the hydrate sample. The empty rotor was removed from the sample holder using tweezers, partially immersed in liquid nitrogen, and placed within the funnel. Packing of the rotor then proceeded as per the original procedure, but with partial immersion of the rotor in liquid nitrogen after every two or three sample additions. The cooling mist provided by the evaporating nitrogen proved too effective, as the ceramic packing rod shattered from minute application of force due to cold shock after successfully packing one sample.

The final procedure was performed inside a cold storage room, along with use of liquid nitrogen for additional cooling. The packing rod and funnel, tweezers, rotor, lid, aluminium sample holder, depth meter, glass spatula and a Styrofoam lid was placed on a workbench in a cold storage room and left to pre-cool for one hour at approximately 9^{o}C. The hydrate sample container was placed in an ice bath on the workbench, and its contents was pulverised. The Styrofoam lid was filled with liquid nitrogen. The empty rotor was removed from the sample holder using tweezers, partially immersed in liquid nitrogen, and placed within the funnel. Packing of the rotor then proceeded as per the original procedure, but with partial immersion of the rotor in liquid nitrogen after every one to three sample additions. Due to the semi-stable temperature conditions achieved by this procedure, rapid sample preparation was mandatory, and a rotor was usually packed full within 20 minutes. As a result this procedure is expected to yield samples of lower density, and thus quality, than the others.

As the neither of the packing procedures functioned without a proper packing rod, improvisation was necessary when the original one broke. A makeshift rod was made by gently hammering the tip of the broken rod into the end of a plastic gypsum plug, securing it from the other side with an empty ink cartridge from a pen. The cartridge was further secured by application of duct tape to the top of the rod. The improvised packing rod is sketched below.

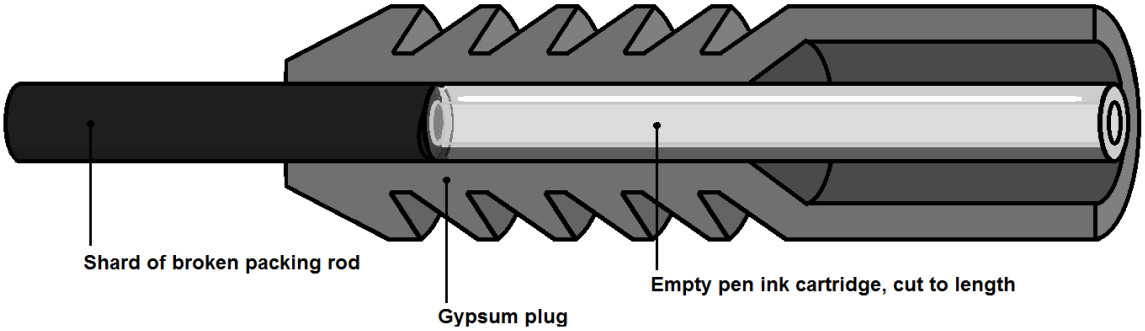

Figure 2.4: A sketch showing the improvised packing rod. The main structural element is the gypsum plug, shown as a cross-section that reveals how the tip of the broken packer was secured.

The structural integrity of the improvised packer was more than satisfactory. However, its shortcoming compared to the original was the shorter tip: Length was lost both due to the splintering failure mode of the original rod and the need for envelopment of part of the shard by the plug. This meant that the packing rod could not reach the bottom of the rotors, instead relying on packing the sample by compacting the bulk hydrate phase once within reach. This is expected to have adversely affected sample quality. Except for B3Fa, all batch 3 samples were packed using this rod.

2.3.4 Cooling chain continuity

All samples were immersed for a few seconds in liquid nitrogen before and after weighing, which was done immediately following preparation and prior to spectrometer insertion. Except for operations in the immediate vicinity of the spectrometer, all sample handling was done by tweezers or insulating paper towels. All batch 3 hydrates were transported in an ice bath.

2.3.5 Emptying the rotor

The rotor lid was removed by immersing the lid in liquid nitrogen, and the necessary immersion time varied somewhat between samples. Maintaining immersion led to pressure-driven auto-ejection, which would frequently result in disappearance of the lid. To counteract this, a procedure was established where the lid was immersed in liquid nitrogen for eight seconds, before attempting to manually remove the lid. If removal was unsuccessful, the lid was re-immersed for three seconds before retrying manual removal. This last step was repeated until lid removal was successful.

The rotor was emptied using hot water. A small drop of ethanol was added to the water-filled rotor before being further washed with hot water. The liquid was then ejected by shaking. Residual liquid was removed under a stream of nitrogen gas.

2.4 NMR techniques

2.4.1 Spectrometers

Except for the NOESY experiments and their supporting ^{1}H spectra, all experiments in the thesis were performed on a Bruker Advance 500 Ultrashield spectrometer fitted with a MAS probe head, called

AV500 for short. The resonance frequency for protons for the spectrometer was 500 MHz, and the accuracy of its temperature controller is regarded as accurate within ±0.5 K from experience of previous operators [77].

The NOESY experiments with supporting ^{1}H spectra were acquired on a Bruker Advance 600 Ultrashield spectrometer, operating at a frequency of 600 MHz for protons. It was fitted with a BBO cryo-probe head, and its temperature accuracy for the successful experiments has been estimated to ±0.7 K due to a rapidly oscillating temperature curve.

2.4.2 Pulse programs

For the majority of the experiments performed on the AV500 spectrometer, the following pulse sequences were used:
Static ^{1}H spectra utilising a 90^{o} pulse
Determination of T_1 using an inverse recovery experiment
Determination of T_2 using a modified CMPG experiment, provided courtesy of John Georg Seland of the University of Bergen.

In addition, MAS ^{1}H experiments were performed on the AV500 spectrometer and NOESY experiments were performed on the AV600 spectrometer, with supporting ^{1}H experiments.

The theoretical background of all experiments can be found in Chapter 1, and the specific parameters for every experiment are provided in Appendix B.

2.4.3 Data analysis

The analysis of all ^{1}H spectra was performed using the Bruker TopSpin v3.2 software, licenced through the Department of Chemistry at the University of Bergen. The Topspin T1/T2 module of the same software was used to analyse the inversion recovery experiments. The NOESY spectra were also processed and analysed in TopSpin, per the comprehensive guide published on the University of Columbia website [78]. The CMPG experiments were analysed using a set of MATLAB scripts, provided courtesy of John Georg Seland of the University of Bergen and modified by the author. These can be found in Appendix A.

2.4.4 Temperature control

The TopSpin software includes a function for altering and monitoring the sample temperature. The control suite includes a temperature logging function that by default is off. This logging function should be switched on whenever the spectrometer is used, the reason for which is threefold. First and most importantly, it provides verification that the spectrometer temperature remained at the set point during the entire experiment, which it too frequently did not throughout this thesis. When a history of the sample temperature is saved, conclusions from the sample data can be drawn with much greater certainty. Secondly, the presence of a temperature log greatly mitigates the problems tied to loss of temperature control: A set of experiments inadvertently performed outside the region of hydrate stability can still be useful. If the thermodynamic state of the system is unknown, however, analyses of such results are conjecture. The third reason to maintain a running temperature log is the fact that experiments can be cross referenced with the log based on time of

acquisition, a capability which Excel and MATLAB functions have been written to exploit. This comes in especially handy when running the temperature ramping function, where the temperature is otherwise unknown for a range of experiments.

For the AV500 spectrometer, the temperature control issues were found by chief engineer Olav-Audun Bjørkelund to be due to two factors: The first was a cut-off of coolant flow, seemingly occurring at random. No issues were found with the pressure of the system, and the issue was further isolated to the MAS hardware. The problem was largely fixed by re-routing the coolant chain. The second problem was due to the connection between probe and cooling gas supply line. This was improved by using a different clamp to secure the connection, although the issue persisted to some degree. Readjustments of the input-line would sometimes correct the issue when an unsolicited temperature increase was observed, but this was not always successful, nor always in time.

Chapter 3 Results

3.1 On result presentation

In order to facilitate reading of this chapter, the data will as far as possible be presented in a recognisable pattern. The presentation methodology is briefly covered for each of the different sets of repeated measurements in the following subchapters.

3.1.1 ^{1}H-spectra

Most experiment series contain a large number of ^{1}H spectra, which are acquired to monitor sample changes. In order to facilitate comparison, nearly all presentations will utilise multiple spectra display. Where applicable, two main variants of such displays are presented. The first uses a stacked plot, where all spectra lie on the same shift and intensity axes. This approach facilitates identification of changes in shifts, areas and intensities, but can in many instances make it hard to identify which spectra correspond to which experiment. This is mitigated by also presenting the same data by the second variant, which inserts a vertical and horizontal offset between each spectrum. During this approach, the first spectrum in the series is the one front and bottom unless stated otherwise. The rest of the spectra then follow in a consecutive order, meaning that a perceived time-axis is created in the third dimension. This approach is well suited for pinpointing specific areas of change in an otherwise cluttered series of spectra but makes it hard to identify changes in chemical shift, and to a lesser degree areas and intensities.

To more easily show changes in peak area or chemical shift in cluttered plots, the spectra can instead be plotted using only horizontal or vertical offset, respectively.

As the samples contain two peaks of very different sizes, the axes are sometimes adjusted in order to only show one of the peaks. This will be specified in the figure text. For the same reason, however, the majority of presentations do not show the spectra in their entirety, instead zooming in on the most relevant area.

3.1.2 T_1 relaxation

In the T_1 experiments, each peak in the spectrum give rise to a different set of T_1 values, the number of which depends on the number of components selected for the analysis. For instance, analysis of a spectrum containing two peaks using a three-component approach will give six different T_1 values. In this thesis, all spectra will contain at least two peaks, corresponding to water and cyclopentane. For some spectra, additional peaks may arise due to water or cyclopentane in different chemical environments. As these side peaks are often transient and hard to properly integrate, the main focus of the presentation will be on the two largest peaks. Side peaks will therefore often be excluded from the presentation as to not clutter graphs with different data points. When presented, transient peaks will be added to the graphs of their parent peaks using a distinct marking. Some side peaks of cyclopentane showed to be persistent however, and these will be presented in its own graph where applicable. The overall presentation is handled as follows: Where both two- and three- component approaches have been made, all two-component results are plotted first unless stated otherwise. For every experiment the water peak results are plotted before the ones for the cyclopentane peak, using diamonds as identifiers. All cyclopentane results are then plotted as triangles. Different components from the same peak is plotted consecutively, with component 1 presented in blue, component 2 in red and component 3 in green. For each component, the data is first plotted as T_1 versus experiment number with temperature in Kelvin presented on the secondary vertical axis, and then as $\ln(1/T_1)$ versus 1/T. A shorthand formulation is often used, where c1 is component 1, c2 is component 2, and c3 is component 3. These conventions constitute a guideline, as results are often fragmented between the main body and appendices of the thesis, and the focus in the main body of the text will be on the more reliable water peak component 1.

3.1.3 T_2 relaxation

The results of the CMPG oneshot experiments are first presented in graphs of T_2 versus experiment number, with temperature in Kelvin presented on the secondary vertical axis. The same results are then plotted as the natural logarithm of inverse T_2 as a function of inverse temperature in Kelvin. Only the two-component results are presented in the thesis, with the results of the one- and three-component approaches presented in the relevant appendix. Where several different components is evaluated, the results for the first component is presented first, followed consecutively by the second. The graphic results of different components are color-coded to facilitate identification, with component 1 results presented in blue, component 2 presented in red and component 3 presented in green. When different components are presented in the same graph, further distinction is provided by using diamonds for Component 1, squares for Component 2 and triangles for Component 3. The same component abbreviations as for the T_1 results apply to these data as well, with component 1, 2 and 3 being abbreviated c1, c2 and c3, respectively. In the main body text, only the two-component approach is presented.

3.2 Initial results

3.2.1 Spectrum appearance

The first step towards being able to do a meaningful static NMR analysis of the hydrate system was to determine whether the approach was at all viable. This was done by verifying the ability to acquire peaks of sufficient intensity and resolution.

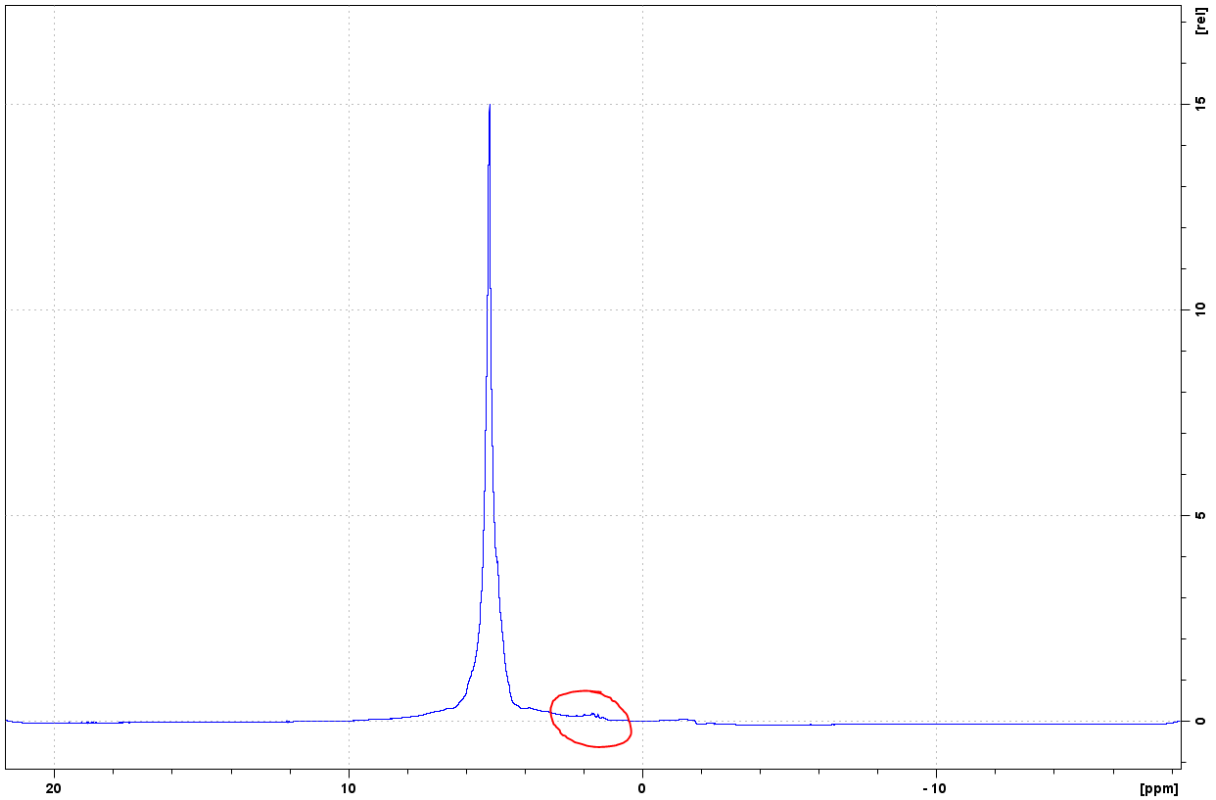

Figure 3.1: The entire static ^{1}H spectrum acquired on a batch 1 sample, using only one scan. The cyclopentane peak is marked.

The batch 1 hydrates were found to melt too quickly, making sample preparation and NMR experiments hard to properly perform, and this was attributed to high water content. A second batch was therefore prepared that greatly alleviated these problems, as evidenced by far greater facility of preparing the first sample of the batch, B2F.

Having access to a hydrate batch of satisfactory quality, the next step was to determine the appearance of the peaks of the hydrate spectra, both within and outside of hydrate stability, as well as sample tolerance for the latter of these conditions. To accomplish this, sample B2F was introduced to the spectrometer at 274 K before raising the temperature to the edge of the stability range in two steps. After observing a change at 280 K, the sample temperature was lowered in order to see if the change was readily reversed. The experiment series ended with loss of temperature control, which still allowed acquisitions above the stability region to be made.

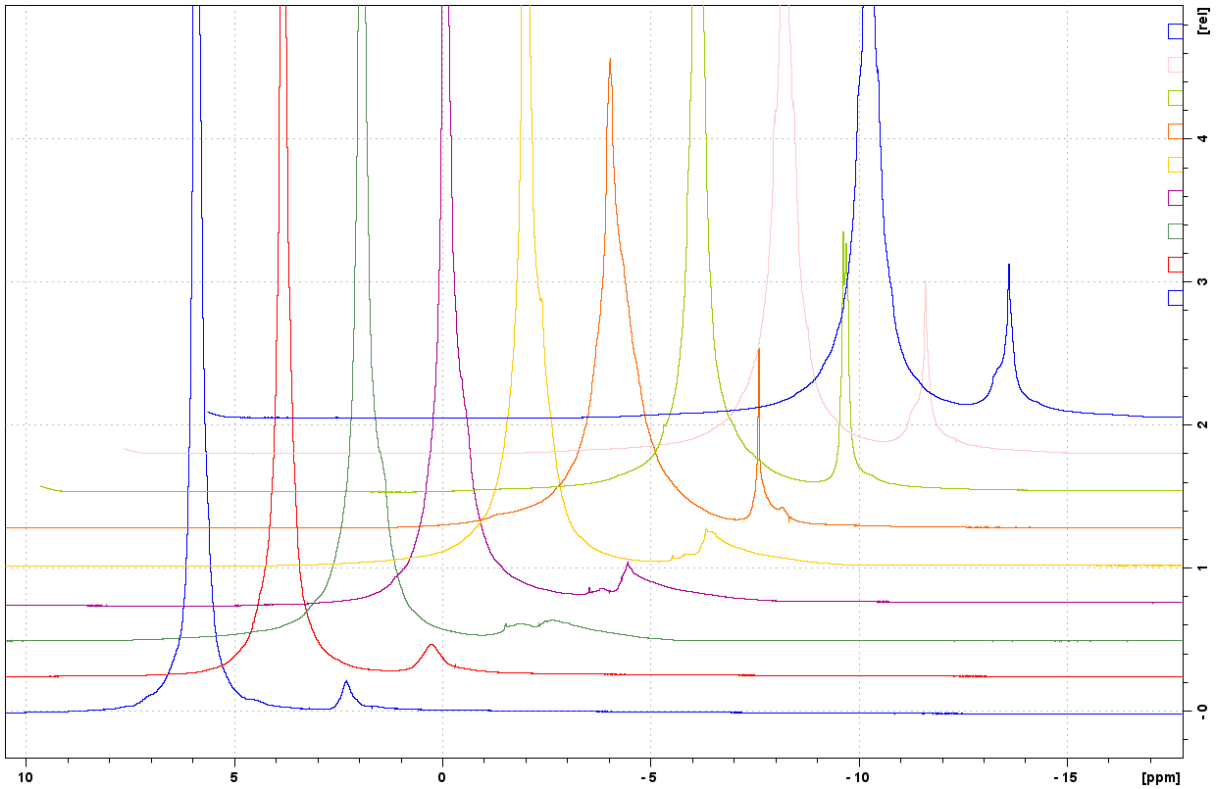

Figure 3.2: All spectra acquired on sample B2F. The display area is chosen as to have the cyclopentane peaks sufficiently scaled to allow discussion without completely removing the water peaks from view. From front to back, the first four spectra were acquired at 274, 278, 280 and 280 K, respectively. The temperature was then lowered to 274 K, and spectra five and six acquired. The temperature was increased to 278 K for spectrum seven, before the two last spectra was acquired as the temperature underwent an uncontrolled increase.

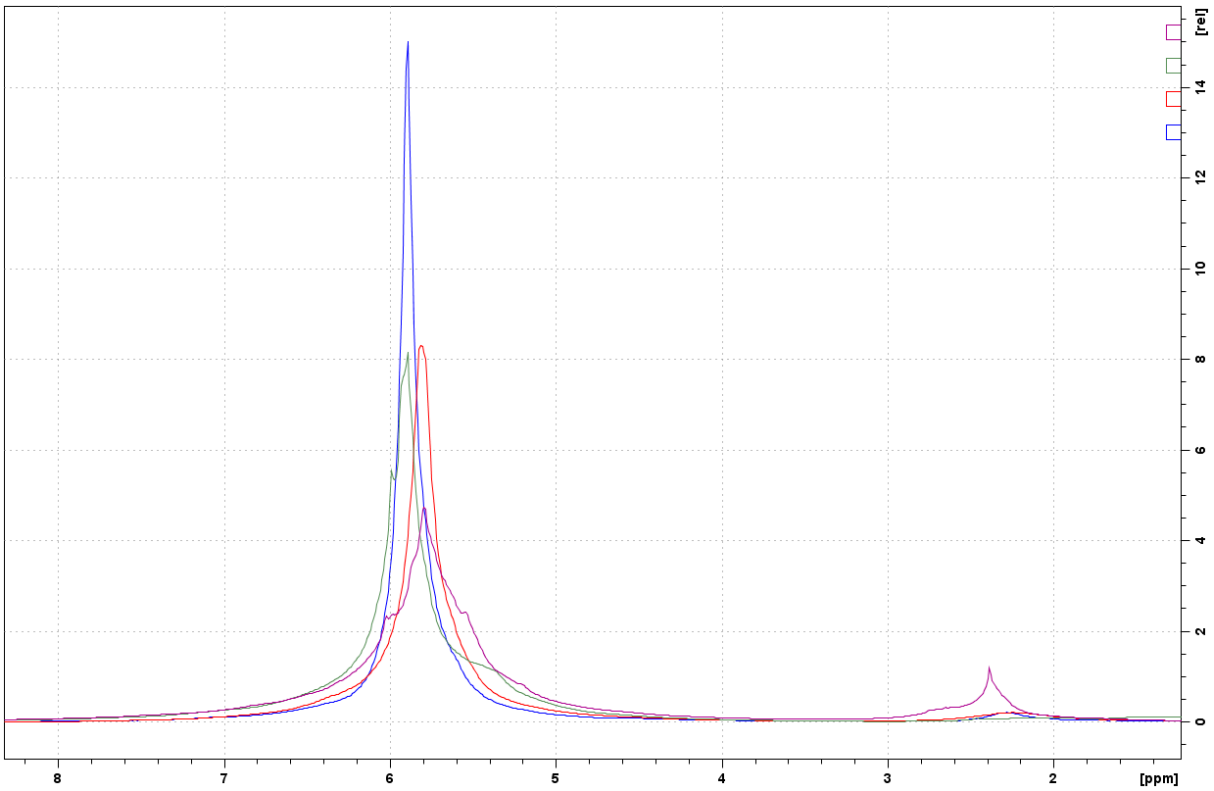

Figure 3.3: A stacked plot of the main peak areas of the four first B2F experiments. Blue: 274 K. Red: 278 K. Green: 280 K. Violet: Last spectrum taken after loss of temperature control.

The results were verified by the experiments on sample B2F2, presented below.

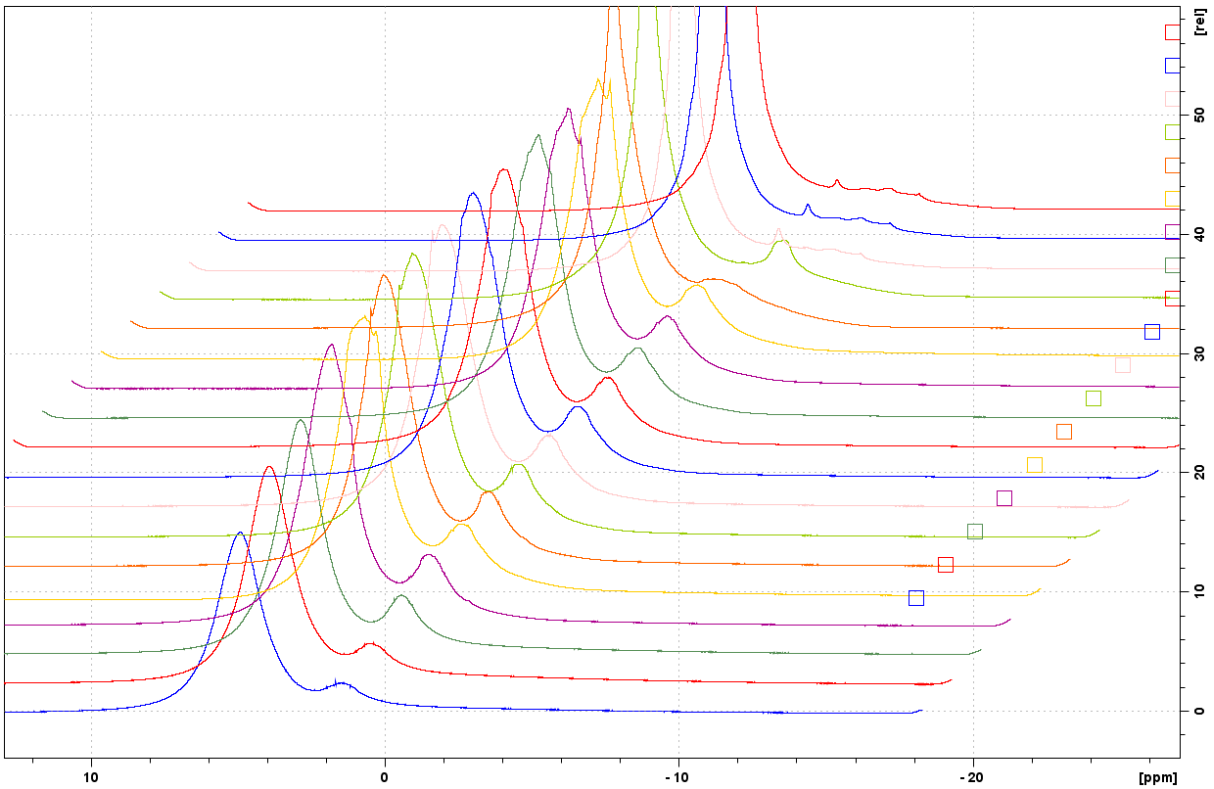

Figure 3.4: All ^{1}H experiments performed on sample B2F2. The display area is chosen as to have the cyclopentane peaks sufficiently scaled to allow discussion without completely removing the water

peaks from view. The temperature was increased from 274 to 280 K over the course of the first four experiments, in steps of 2 K with 20 minutes of thermal equilibration allowed between each change. Temperature was kept constant at 280 K for the next nine experiments before temperature control was lost, prompting a rise in temperature. This corresponds to the change in the five last spectra. The sample was subjected to freezer storage before the experiment.

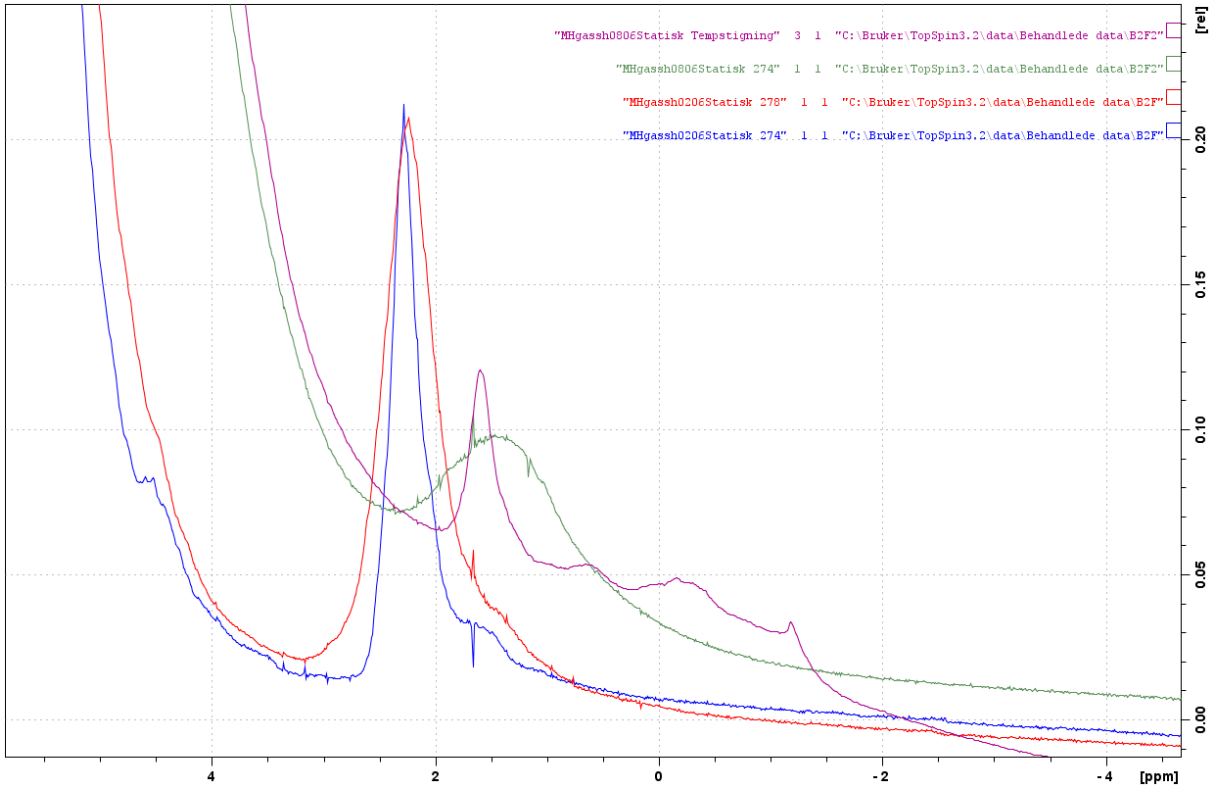

Figure 3.5: Comparison of the cyclopentane peaks of B2F and B2F2. Blue: B2F peak at 274 K. Red: B2F peak at 276 K. Green: B2F2 peak at 274 K. Violet: B2F2 peak after loss of temperature control, outside of hydrate stability range.

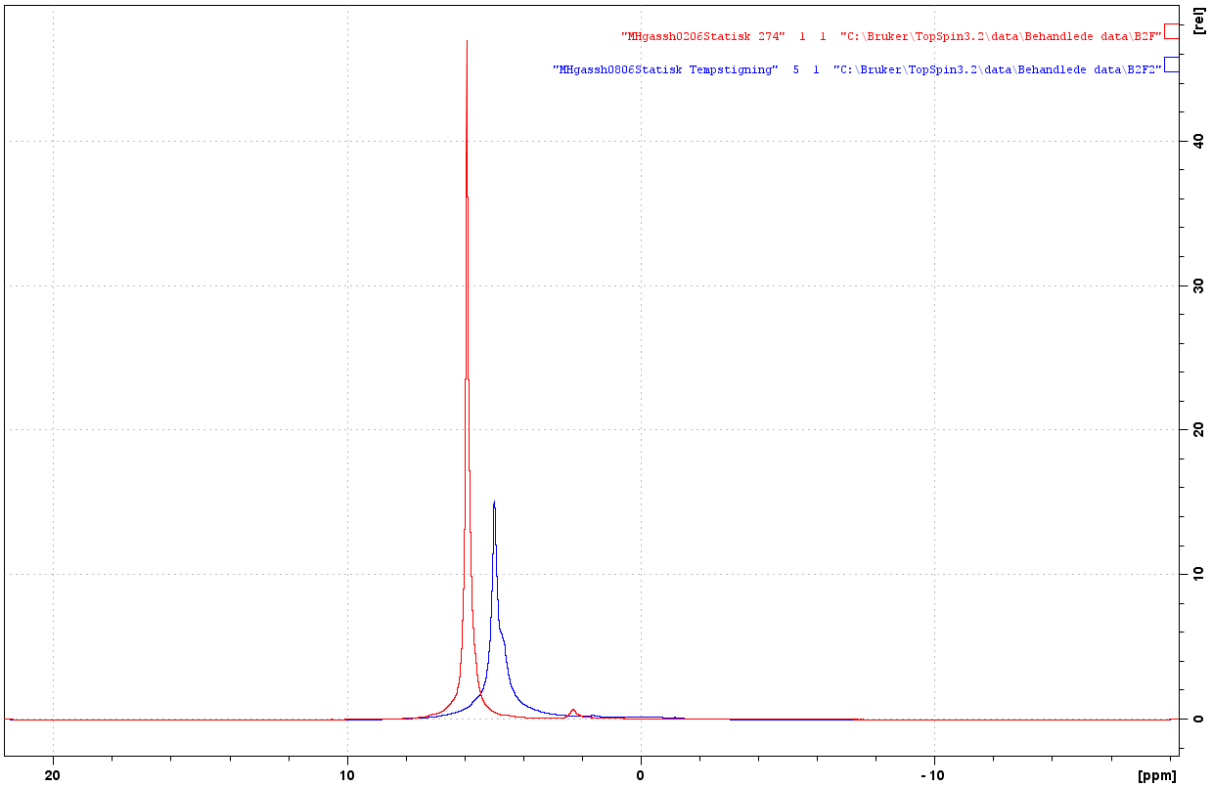

Figure 3.6: Comparison of the last spectrum outside temperature control for sample B2F2 (blue) with the initial spectrum at 274 K for sample B2F (red).

3.2.2 Sample preparation and handling

The different workup procedures for the hydrates samples yielded very different results, which is exemplified by providing integrated spectra of samples from the three different batches.

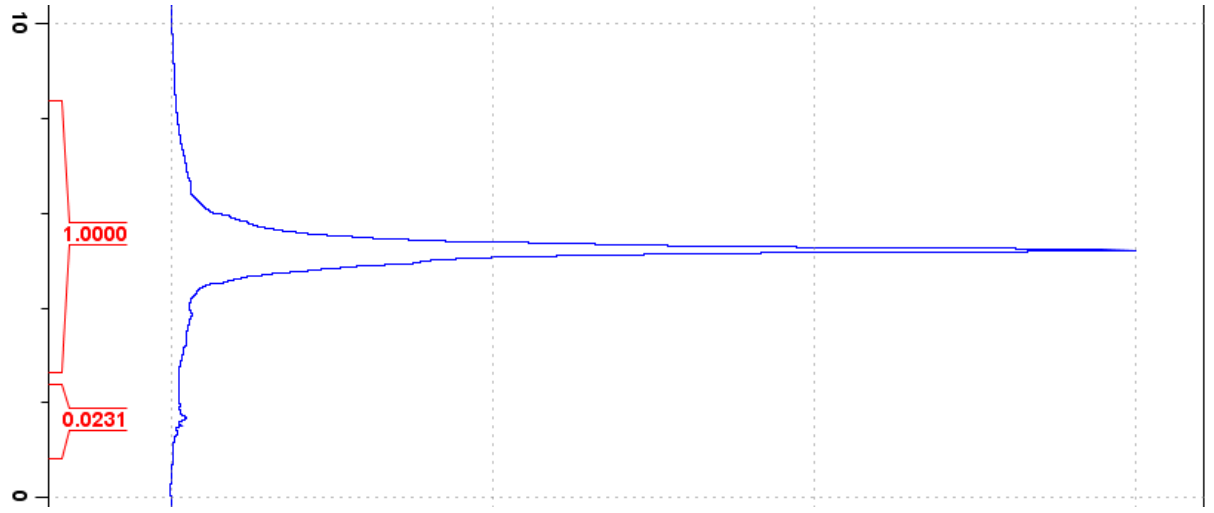

Figure 3.7: The integrated water (top) and cyclopentane (bottom) peaks for a batch 1 hydrate sample, showing only the region of most interest. The sample was packed using the cooling cabinet method. The full spectrum and acquisition parameters can be found in Appendix D.

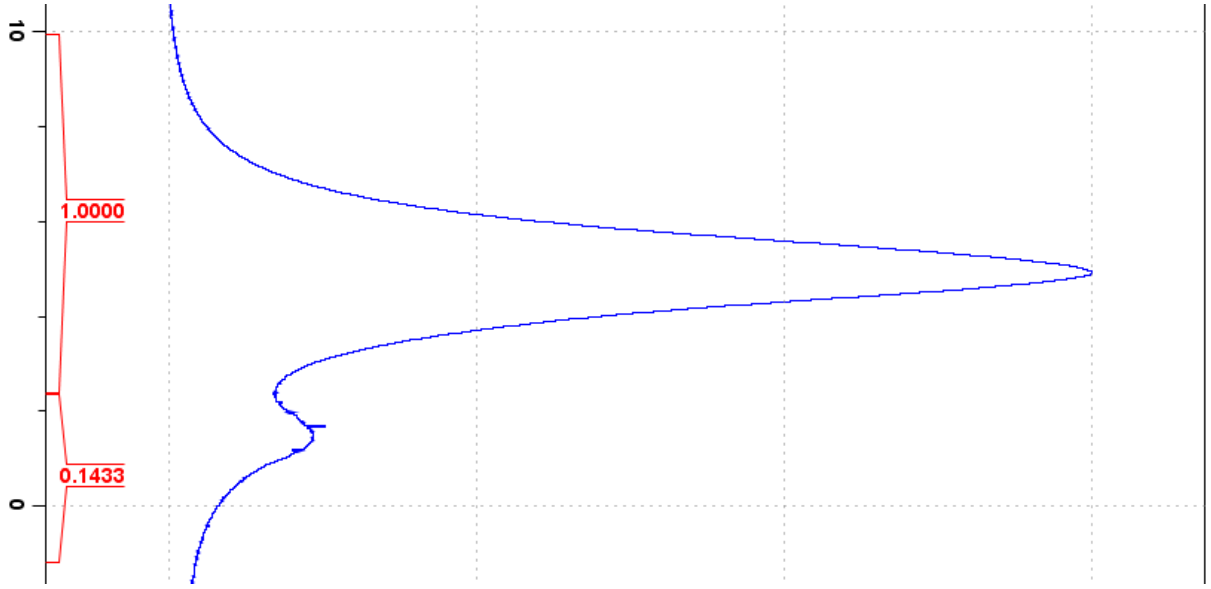

Figure 3.8: The integrated water (top) and cyclopentane (bottom) peaks for the batch 2 hydrate sample B2F2, showing only the region of most interest. The sample was packed using the cooling cabinet method. As the peaks were not resolved and the entire baseline region was found to slope, integration regions were chosen as to end or start at the minimum between the peaks, and cover the areas of perceived change in slope. The full spectrum and acquisition parameters can be found in Appendix D.

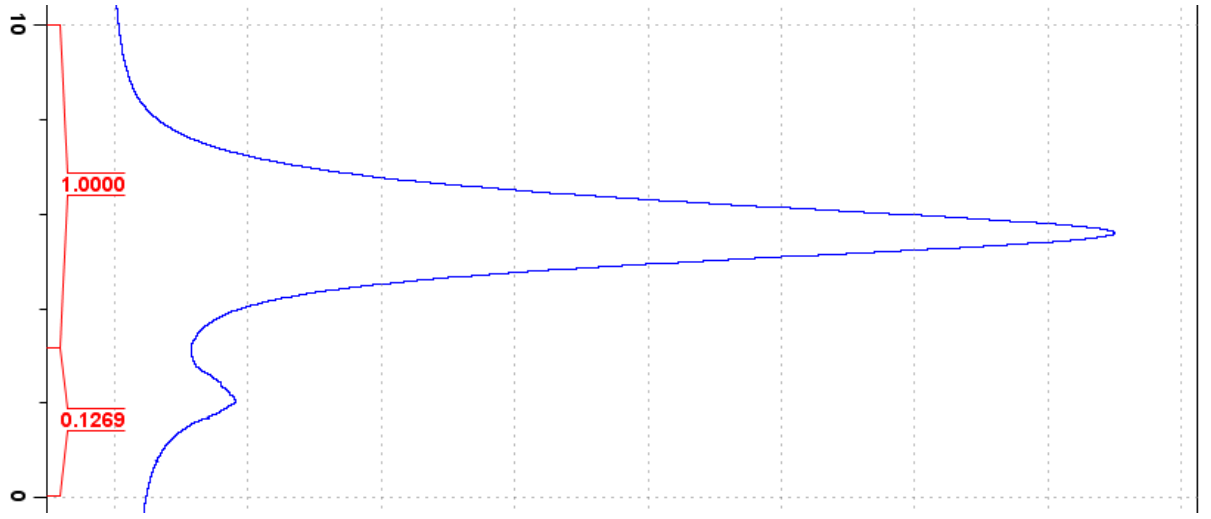

Figure 3.9: The integrated water (top) and cyclopentane (bottom) peaks for the batch 3 hydrate sample B3Fb, showing only the region of most interest. The sample was packed using the cold storage method. As the peaks were not resolved and the entire baseline region was found to slope, integration regions were chosen as to end or start at the minimum between the peaks, and cover the areas of perceived change in slope. The full spectrum and acquisition parameters can be found in Appendix D.

Table 3.1: The weighing found for a number of samples during analysis operations. Preparation is after sample packing, Insertion is before introduction to the spectrometer, Removal is after removal from the spectrometer and Weighing ambient is weighing after letting the sample sit at room temperature. Number of days after preparation is given under every value.

	Hydrate mass (g)					
	Preparation	Insertion	Removal	Insertion 2	Removal 2	Weighing ambient
B3Fa	0,0766	0,0768	0,0764	0,0774		
Time (Days)	0	2	3	6		
B3Fb	0,0971	0,0978	0,0969	0,097	0,0974	
Time (Days)	0	2	3	5	6	
B3Fc	0,0705	0,0714	0,0709			0,0704
Time (Days)	0	6	7			17
B3Fa2	0,0705	0,0689	0,0715			
Time (Days)	0	1	3			
B3Fa3	0,0747	0,0757	0,0745			
Time (Days)	0	3	4			
B3Fa4	0,0747	0,0766	0,075	0,0755	0,0747	
Time (Days)	0	1	8	21	22	
B3Fb2	0,0776	0,078	0,0776			
Time (Days)	0	6	7			
B3Fa5	0,0666	0,0668	0,0667			
Time (Days)	0	6	14			
B3Fa6	0,0727	0,0733	0,0729			
Time (Days)	0	13	14			
B3Fa7	0,0863	0,0863	0,0863			0,0852
Time (Days)	0	1	2			3
B3Fa8	0,0759	0,0759	0,0757			
Time (Days)	0	2	3			

3.2.3 Initial 2D experiments

The 2D spectra of the second series of NOESY spectra acquired on sample B3Fa4 are shown in Appendix D. Both peaks were found to drift upfield as the series progressed, and this was attributed to instrument drift. Because this meant that the spectra were averaged from shifting FIDs, the experiments must be considered near useless in terms of providing information on the hydrate system. Also, the external ^{1}H reference spectrum acquired before the start of the series would not be applicable to the results displaying this shift. The overall effect can be seen from the comparison of two ^{1}H spectra, the first acquired before the series of NOESY experiments, the second after it.

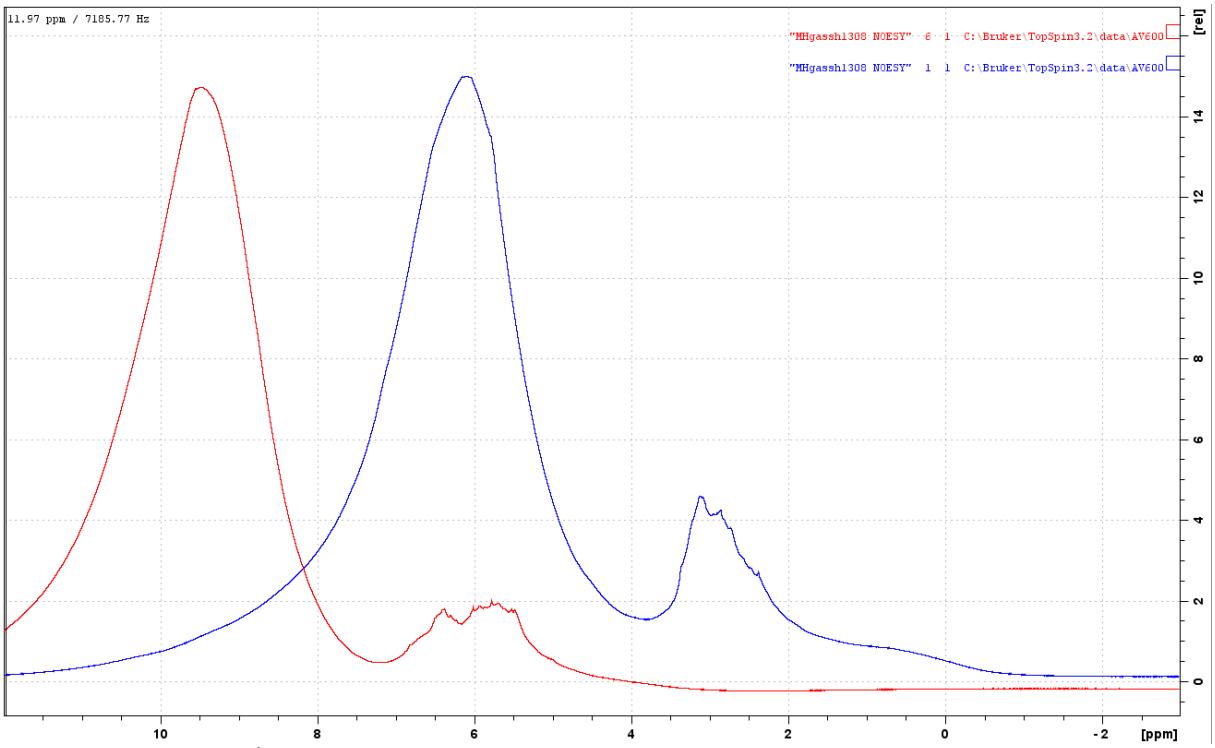

Figure 3.10: The two ^{1}H spectra acquired before (blue) and after (red) the sequence of NOESY spectra.

For the two final NOESY series, two changes to the procedure were made in order to correct this problem. The first was immersion of the ZrO_2 rotor in D_2O within the NMR tube, in order to allow deuterium locking during the experiment. This ensured that the deuterium resonance was continuously monitored, from which any drift in the signal was automatically corrected. Note that this introduces a lower sample temperature limit at the D_2O freezing point, 4 ^{o}C, which must never be crossed. An added benefit was that shimming could be done directly on the sample.

The second change was the acquisition of a ^{1}H spectrum between each NOESY experiment. This not only ensured the presence of the best possible external reference, but also allows better monitoring of sample state throughout the experiments.

There were also major issues with the temperature controller, which arbitrarily switched off during overnight runs. This was initially believed to be a one-off issue with the Topspin control software, but the error was reproduced after taking basic steps such as restarting the software and checking cable connections. In order to verify the thermal state throughout the experiments, the three final experiment series were run with the temperature logging function enabled. For all series before this, the temperatures at acquisition must be considered unknown.

Chief engineer Olav-Audun Bjørkelund hypothesised that the spectrometer might have built in fail-safes that can alter the temperature settings in order to protect the when pre-defined conditions are met. As no hardware or software issues were found, a guess was made that either the proximity of the set temperature to the freezing point of D_2O or other unknown criteria fulfilled during the experiments might have triggered such a fail-safe. Although this hypothesis has not been verified, setting the experiment temperature to the upper region of hydrate stability did result in maintained temperature control throughout the last experiment series.

3.3 B2F6

3.3.1 Sample information

The sample was packed right before insertion to the spectrometer, by the cooling cabinet method.

The goal of the experiment was to pinpoint changes to the sample as temperature was increased. This was accomplished by using a temperature ramping program to slowly increase temperature, whilst acquiring a ^{1}H spectrum approximately every minute.

3.3.2 ^{1}H results

The sample was introduced to the spectrometer, followed by a series of experiments to probe whether the fresh sample was undergoing change.

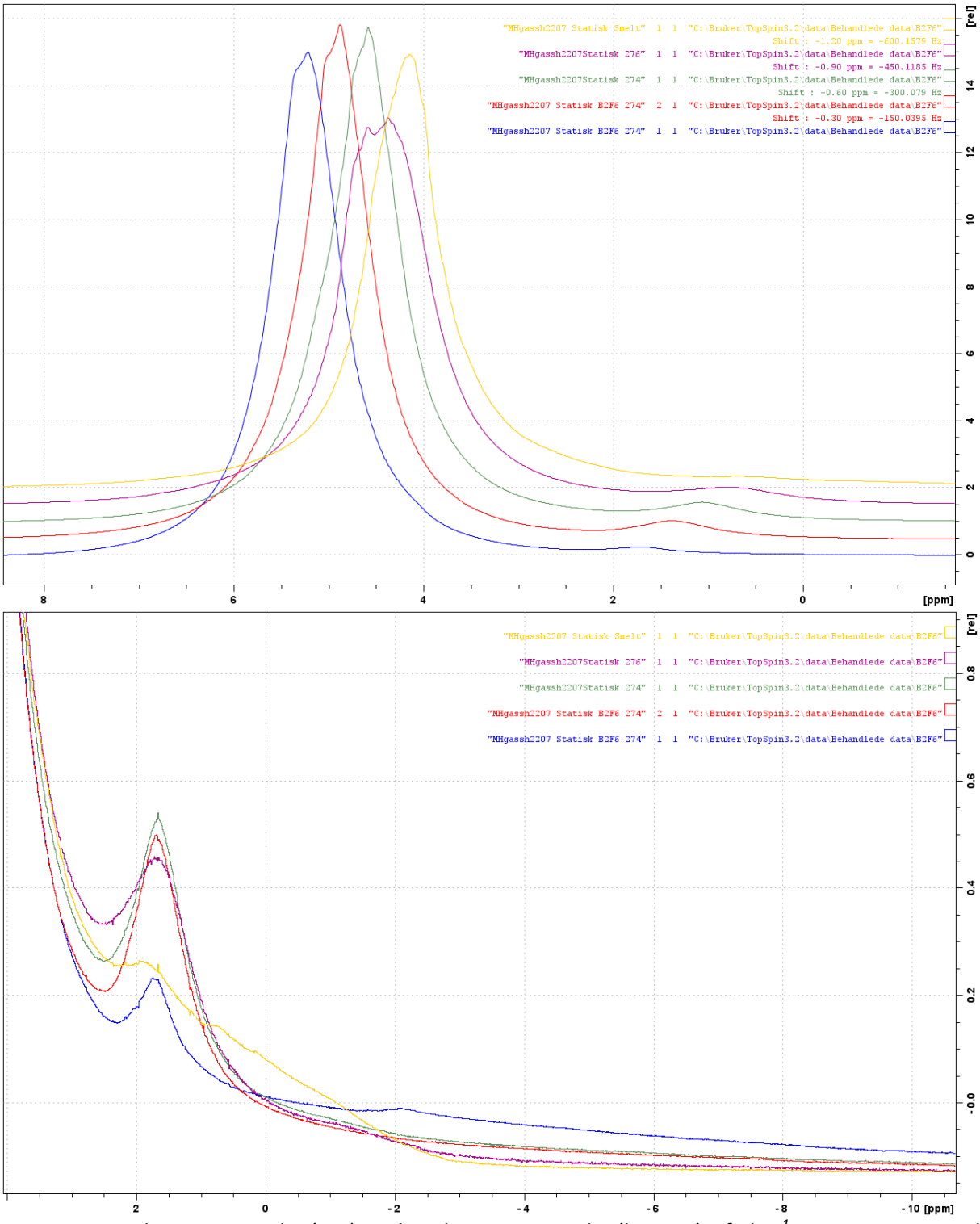

Figure 3.11: The water peaks (top) and cyclopentane peaks (bottom) of the ^{1}H spectra acquired before the ramping program of sample B2F6. The two first spectra were acquired at 274 K, 5 minutes apart shortly after insertion. The third spectrum was acquired 20 minutes later at 274 K, followed by another spectrum at 276 K after another 20 minutes. The last spectrum is the first experiment of the ramp program, acquired at a temperature of 275 K 45 minutes after the fourth.

A temperature ramping program was then run, along with a continuous acquisition of a ^{1}H spectrum every minute. A collection of all spectra from this series can be found in Appendix E.

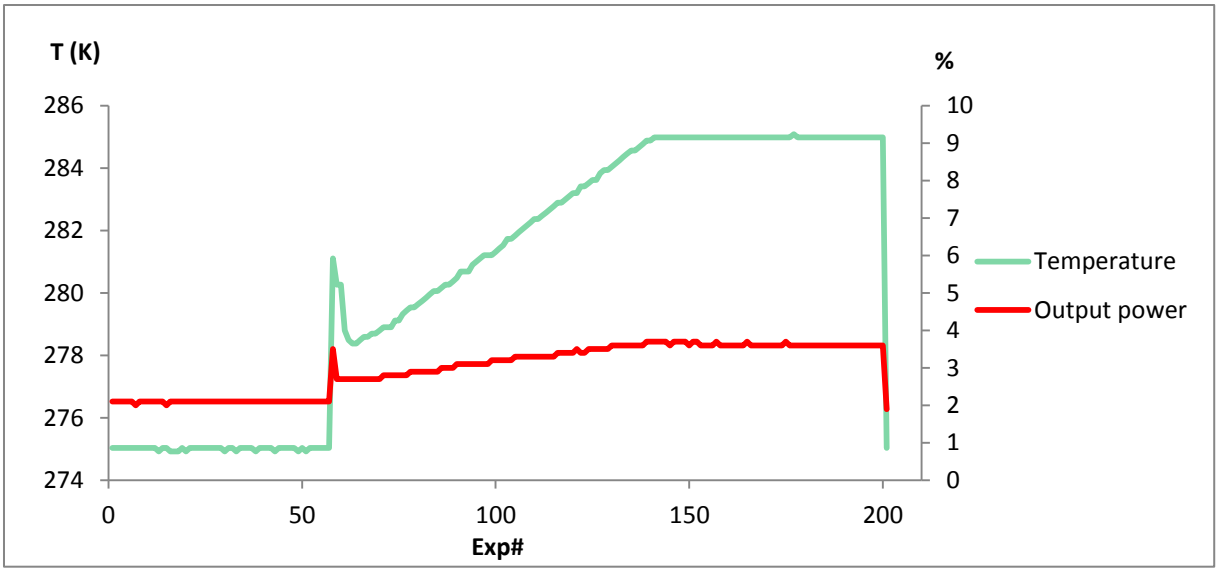

Figure 3.12: The temperature in Kelvin plotted as a function of experiment number for the B2F6 ramp program. The output power of the probe heater is plotted on the secondary axis. Notice that the temperature does not start increasing immediately, nor is there any attempt to make it do so. Instead the instrument seems to try to catch up around experiment 60, and the cause of the spike is therefore attributed to instrument error.

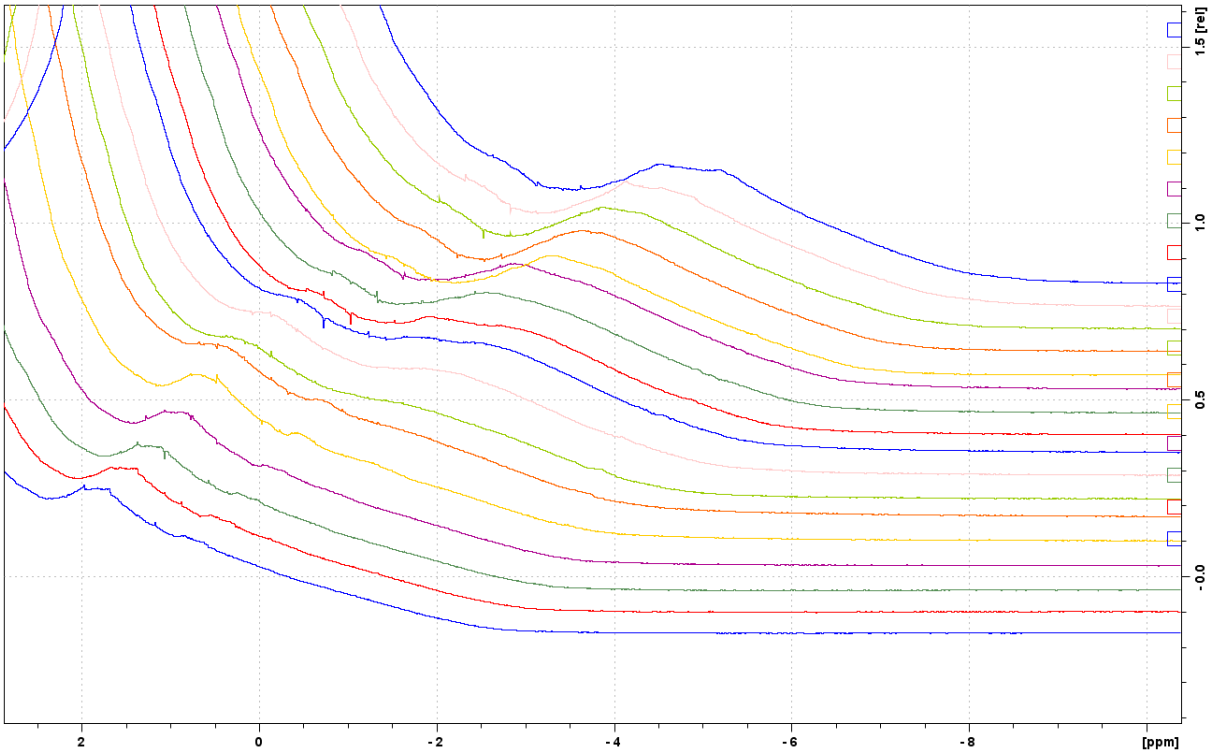

Figure 3.13: Focus on the change in the cyclopentane peak during and following the temperature spike at 281 K during the ramp program of sample B2F6, presented using horizontal and vertical offset. The change takes place over approximately 14 minutes. A stacked plot of the same spectra can be found in Appendix E.

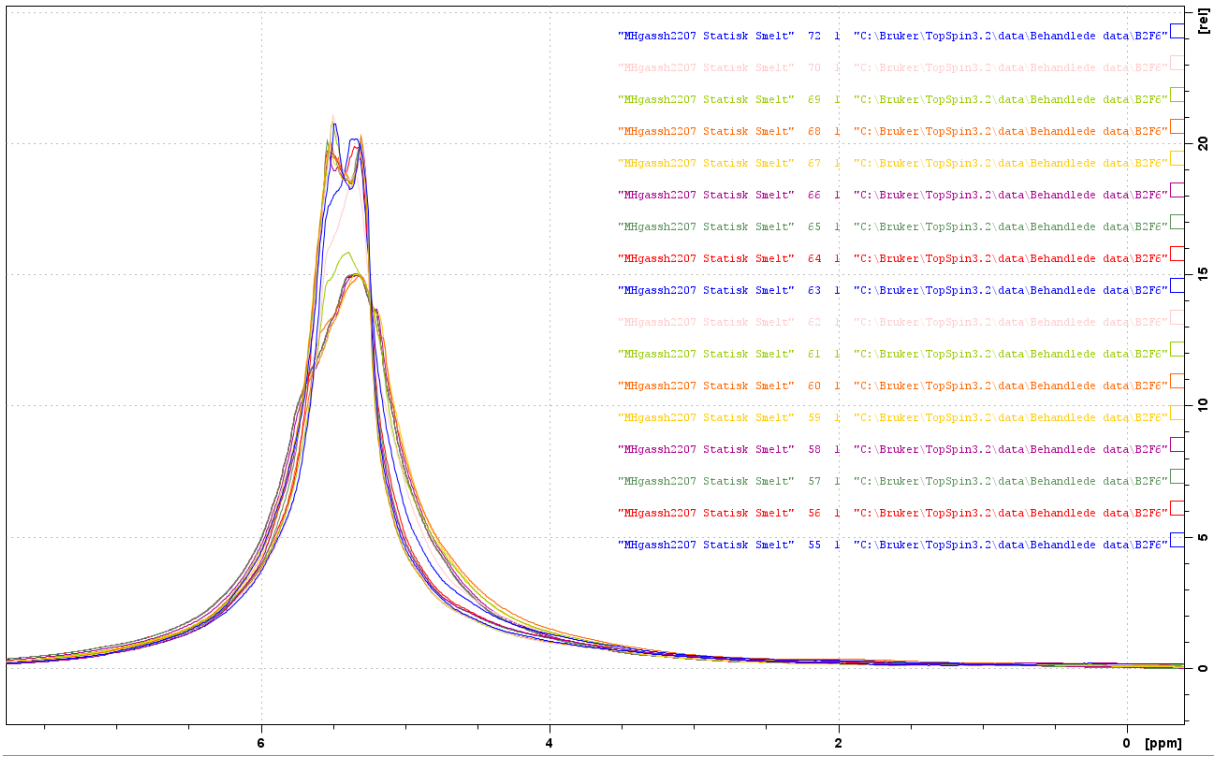

Figure 3.14: The changes in the water peak following the temperature spike at 281 K during the ramp program of sample B2F6. The spectra plotted are the same as for the preceding figure.

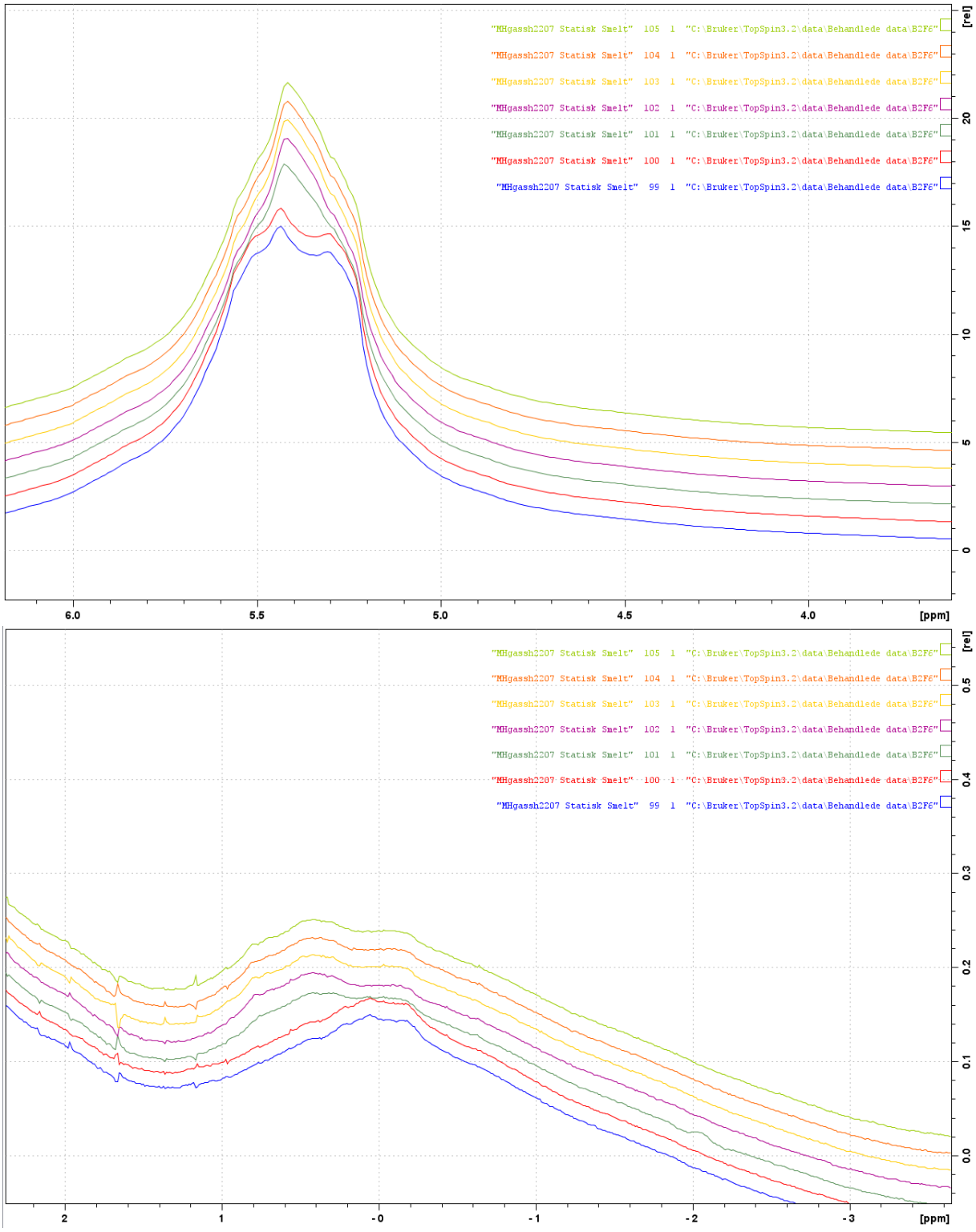

Figure 3.15: Focus on the second change in the water peak (top) and cyclopentane peak (bottom) at 281 K during the ramp program of sample B2F6, plotted with vertical offset between spectra. The change takes place over approximately one minute.

Finally, the sample temperature was lowered to 274 K for half an hour plus equilibration time and a set of ^{1}H spectra acquired, which can be found in Appendix E. No change was observed.

Two CMPG oneshot experiments were performed, along with two inverse recovery experiments. The results of these are found in Appendix E.

3.4 B2F7

3.4.1 Sample information

The sample was prepared using the cold storage packing method.

The goal of this experiment series was to see how the sample changed after spectrometer introduction. This was done by performing a continuous he sample temperature was then raised to dissociation temperature to verify the results.

3.4.2 ^{1}H results

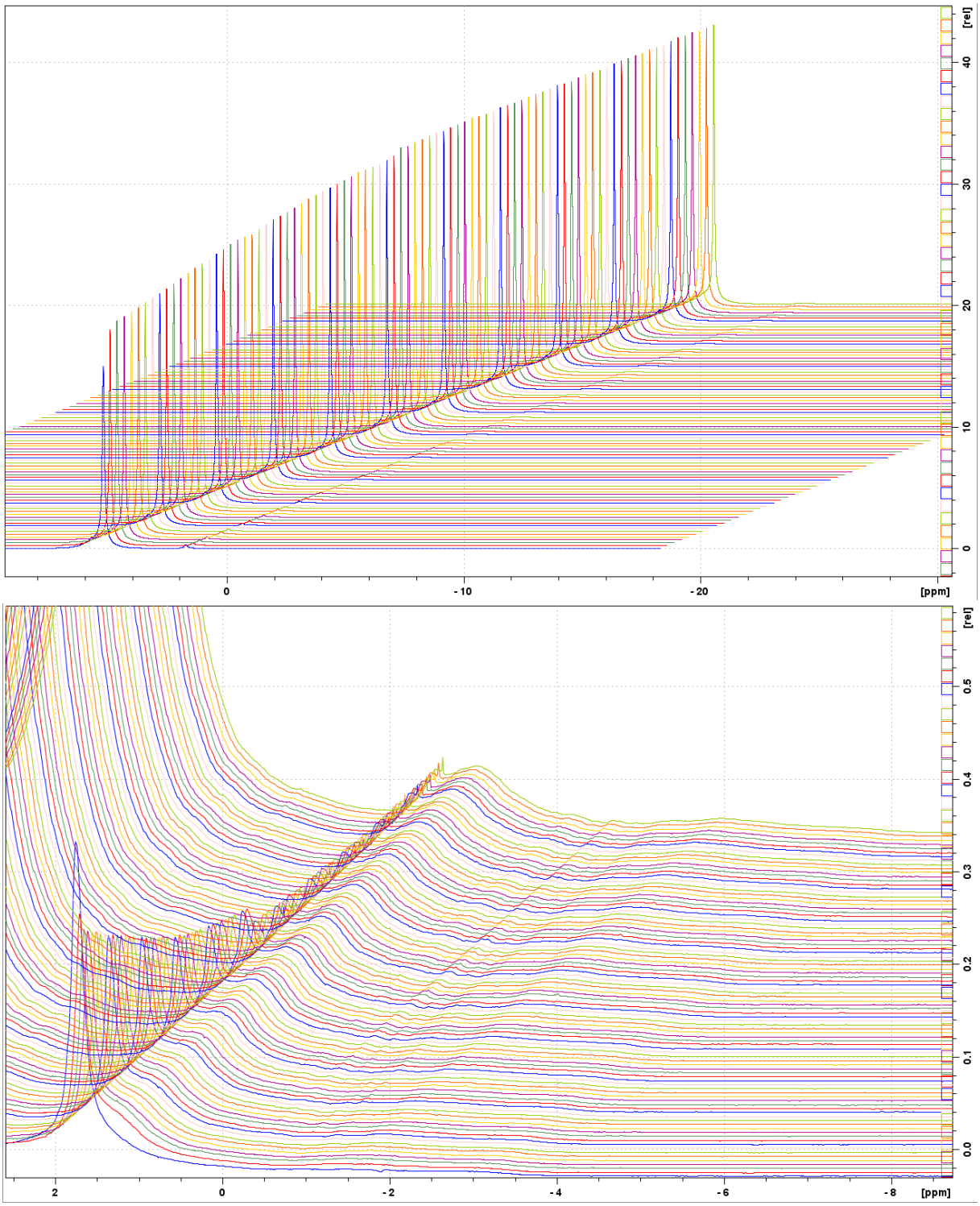

Figure 3.16: The initial ^{1}H acquisition series of 87 spectra, acquired at 274 K approximately one minute apart. The aquisitions were initiated right after sample B2F7 was introduced to the spectrometer. Top: View of the entire spectrum. Bottom: Focus on the cyclopentane area. A sharp water peak can be seen, and the same initially applies to the cyclopentane peak. This peak, however, is quickly found to stabilise into a more rounded peak. Several broad peaks seem to be present downfield.

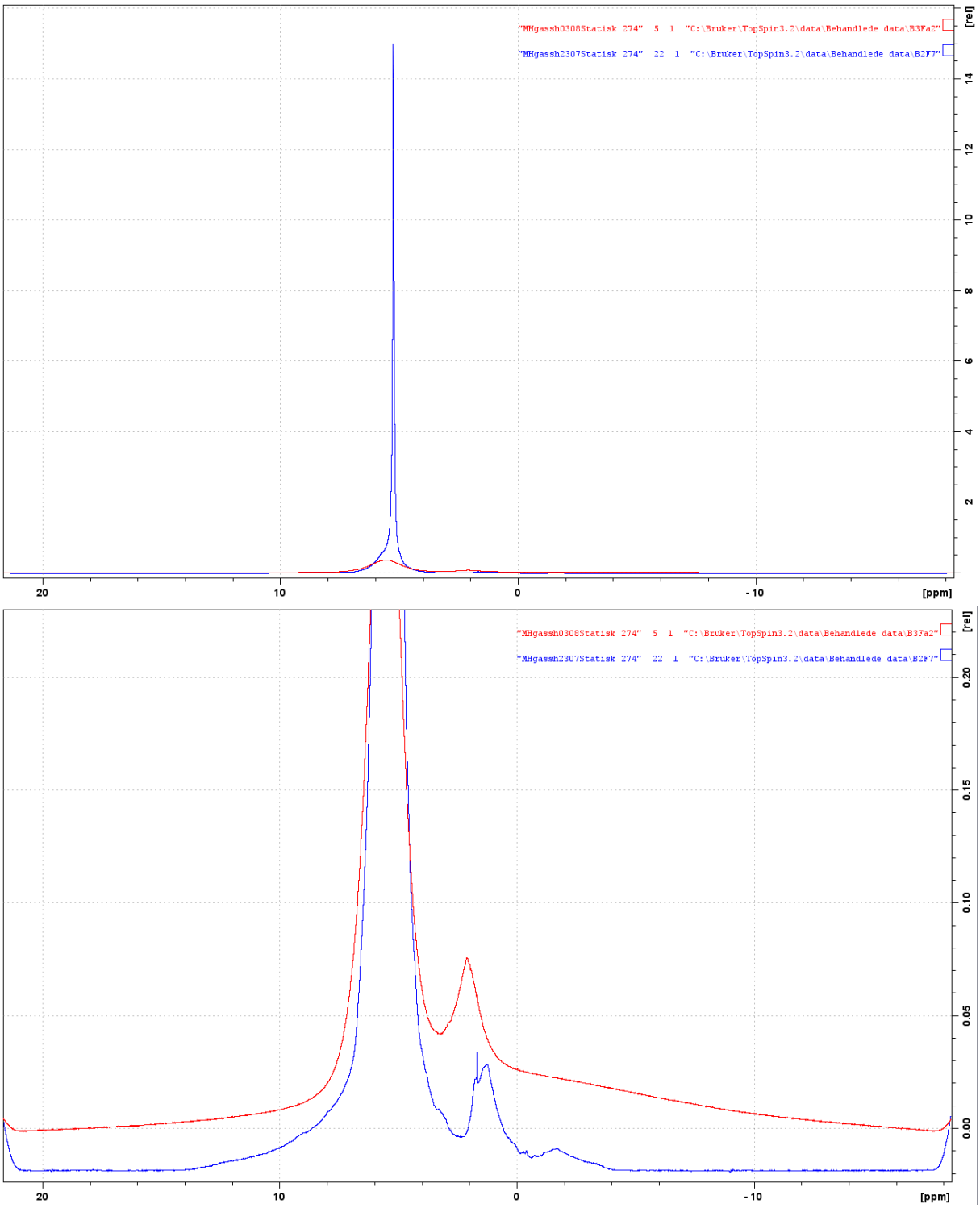

Figure 3.17: Comparison of the last spectrum at 274 K for sample B2F7 (blue) with the corresponding one for sample B3Fa2 (red). Top: full spectrum. Bottom: Full spectrum with appropriate zoom. The main differentiating properties can be found for the water peak and baseline.

3.4.3 T_2 relaxation results

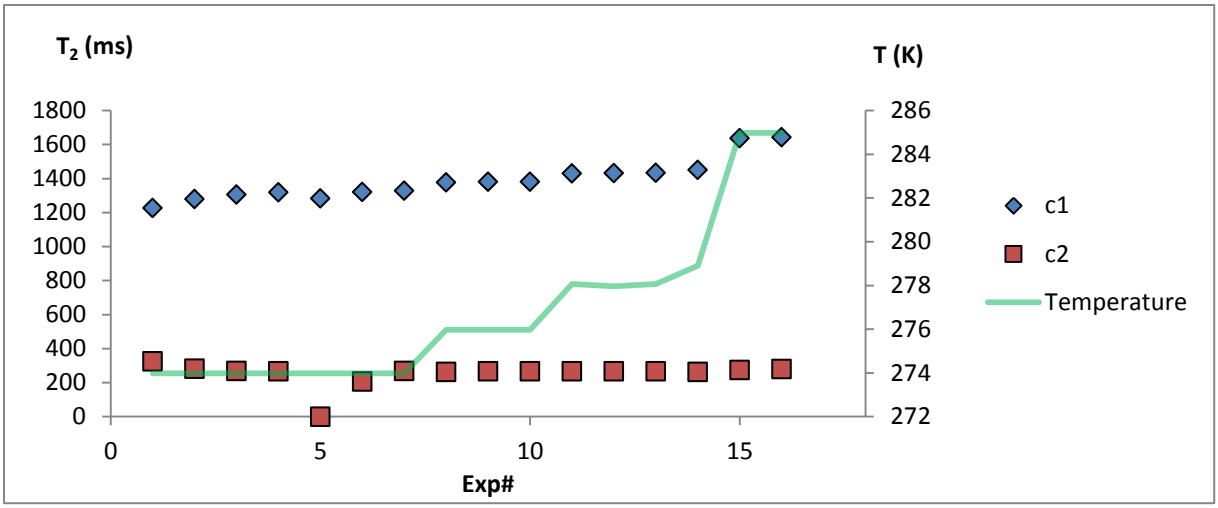

Figure 3.18: T_2 results for sample B2F7.

3.5 B3Fa

3.5.1 Sample information

The sample was prepared using the glove box packing method. It was not cooled in liquid nitrogen during the weighing and insertion procedure.

The goal of this experiment was to investigate how a sample responded to an extended period at 285 K, followed by lowering of the temperature into hydrate formation range. After the first experiment series, the sample was returned to freezer storage at -30 ^{o}C for approximately 3 days, followed by another experiment series performed within the hydrate stability range.

3.5.2 ^{1}H spectra

The sample was weighed and introduced to the spectrometer, which was pre-cooled to 274 K. Tuning and matching was performed on the sample, after which a series of six ^{1}H experiments was run, interspaced by CMPG and inversion recovery experiments, resulting in a time of 20 minutes between each spectrum.

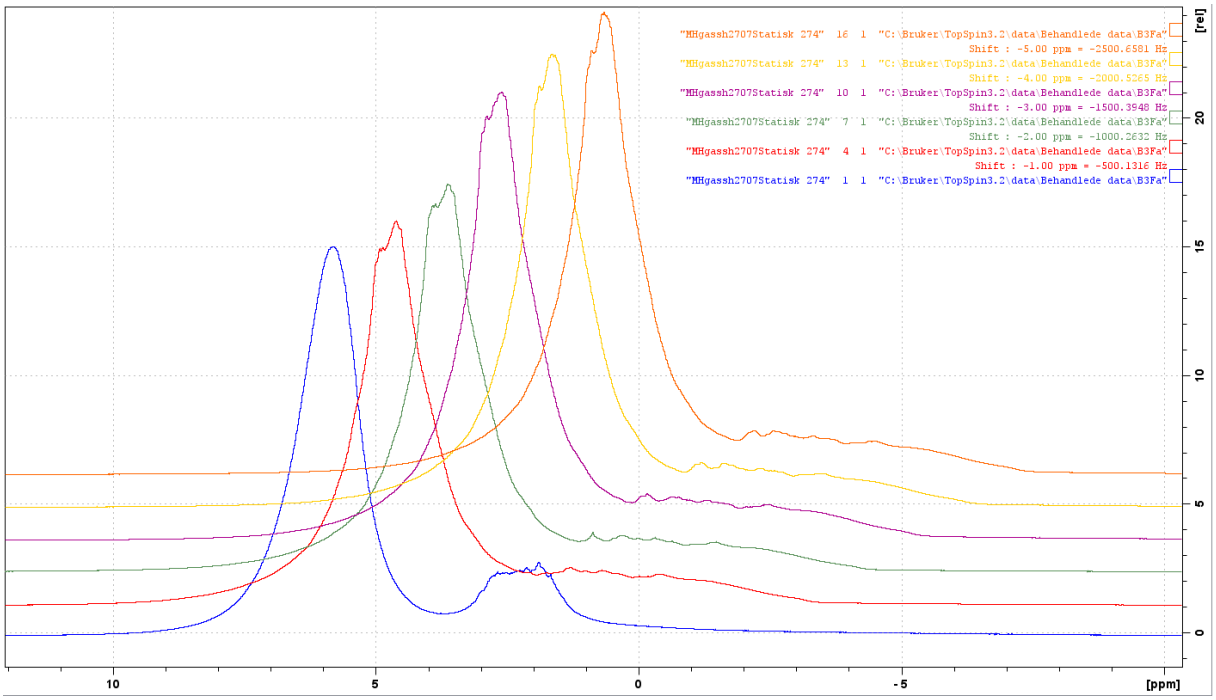

Figure 3.19: The ^{1}H spectra of sample B3Fa acquired at 274 K, presented using vertical and horizontal offset. The blue spectrum is the first spectra after insertion, with each spectrum separated by 20 minutes on the implied time axis in the third dimension.

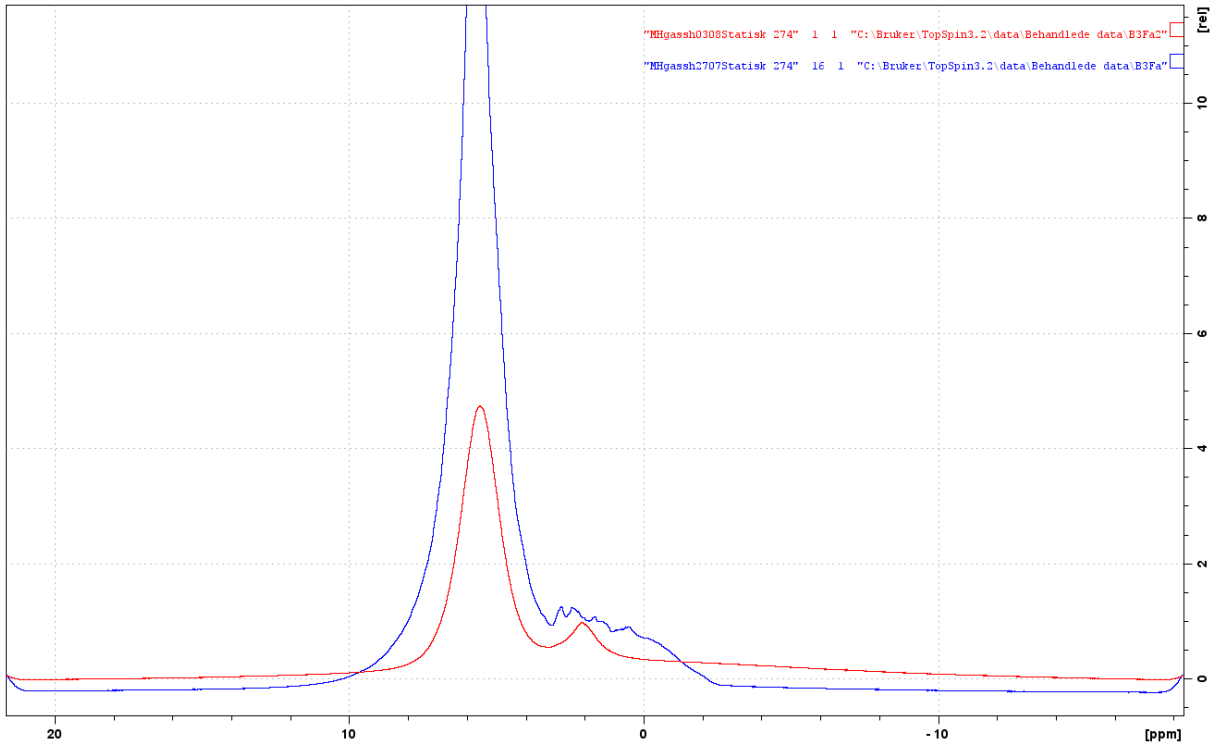

Figure 3.20: The last ^{1}H spectra of sample B3Fa acquired at 274 K (blue) compared with that for sample B3Fa2 at the same temperature (red). Note that these spectra was acquired using the same acquisition parameters and receiver gain. The sample hydrate contents are 0.0766 and 0.0705 g, respectively.

The temperature was then increased to 278 K. Following a 20 minute stabilisation time after reaching the set temperature, tuning and matching was performed. Another repeating sequence of ^{1}H –

CMPG – Inverse recovery totalling 10 experiments was initiated, starting and ending with ^{1}H experiments. The results of this series can be found in Appendix E.

A temperature ramping program was then started, increasing the temperature to 285 K using a ramping rate of 0.05 K/min. At the same time, a continuous acquisition series totalling 240 ^{1}H spectra was started. 40 dummy scans was used between to increase the spacing of spectra to approximately 4 minutes. The results of this analysis were subjected to first order phase correction in order to remove the slopes at the edges of the spectra. A plot of all the ^{1}H spectra is provided in Appendix E.

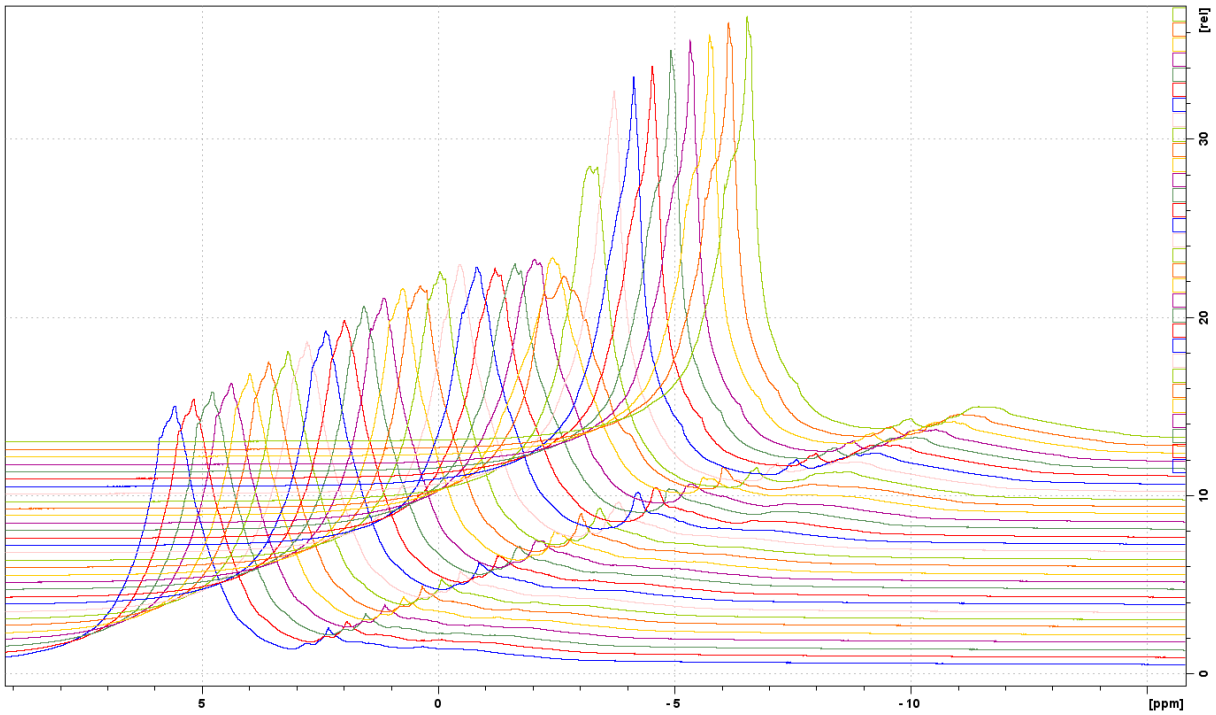

Figure 3.21: The first 31 spectra of the 278-285 K ramp program of sample B3Fa. This area comprises the entire temperature ramp: the spectrometer temperature is stable at 285 K beyond this range. The sample is expected to reach thermal equilibrium within 20 minutes of this point, corresponding to approximately 5 spectra.

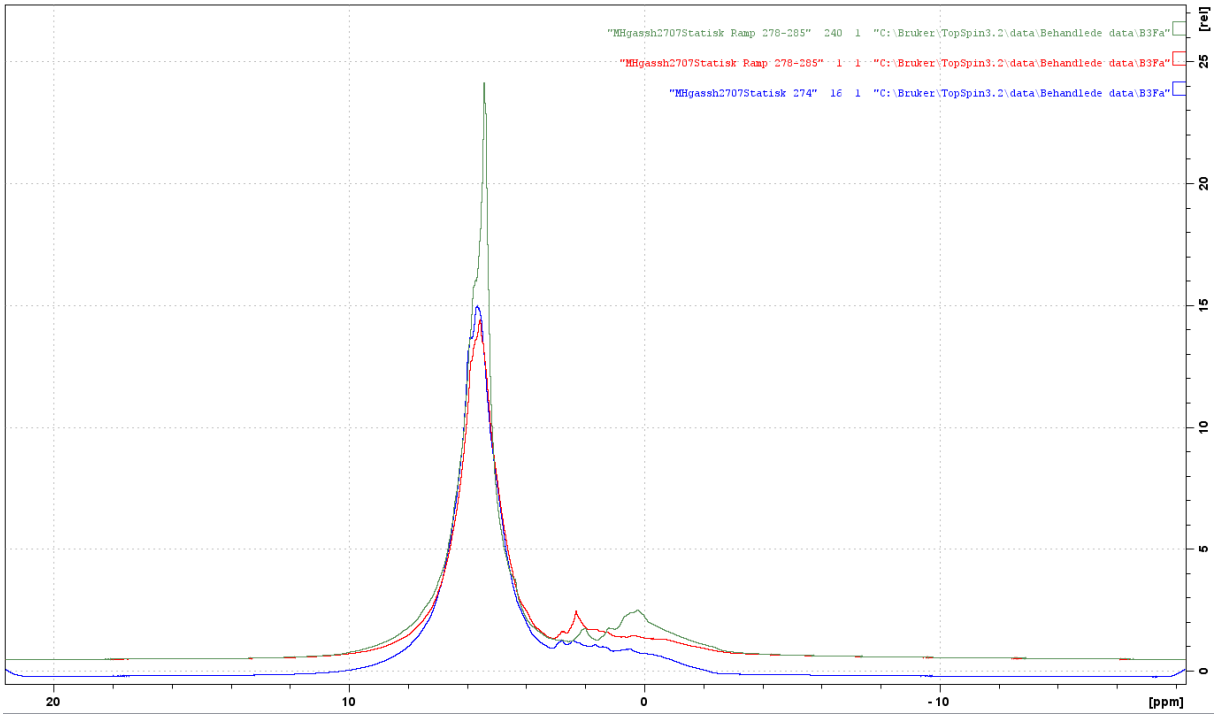

Figure 3.22: Sample B3Fa. The last spectrum taken at 274 K (blue) compared with the first (red) and last (green) spectra of the 278-285 K ramp program. The perceived difference in the baseline might be influenced by the fact that first order phase corrections have been performed on the latter spectra.

Three additional ^{1}H spectra were acquired at 285 K after finalisation of the ramp, the first of which half an hour later, the last an hour later. Tuning and matching was performed after the first of these acquisitions, the results of which can be found in Appendix E.

The temperature was then stepwise lowered back into the range of hydrate stability. Three ^{1}H spectra were taken at each of the temperatures 280 K, 278 K and 276 K, before an extended experiment series was acquired at 274 K. The sample was then removed and placed in a freezer for three days, before testing the sample at 274 K, 276 K and 278 K. All these results can be found in Appendix E.

3.5.3 T_1 relaxation results

The sample was kept at 285 K for 19 hours between experiments 9 and 10, but no inversion recovery experiments were performed during this interval. The three last experiments were performed after the sample was removed from the spectrometer and stored at -30 ^{o}C for three days in an attempt to reform hydrates.

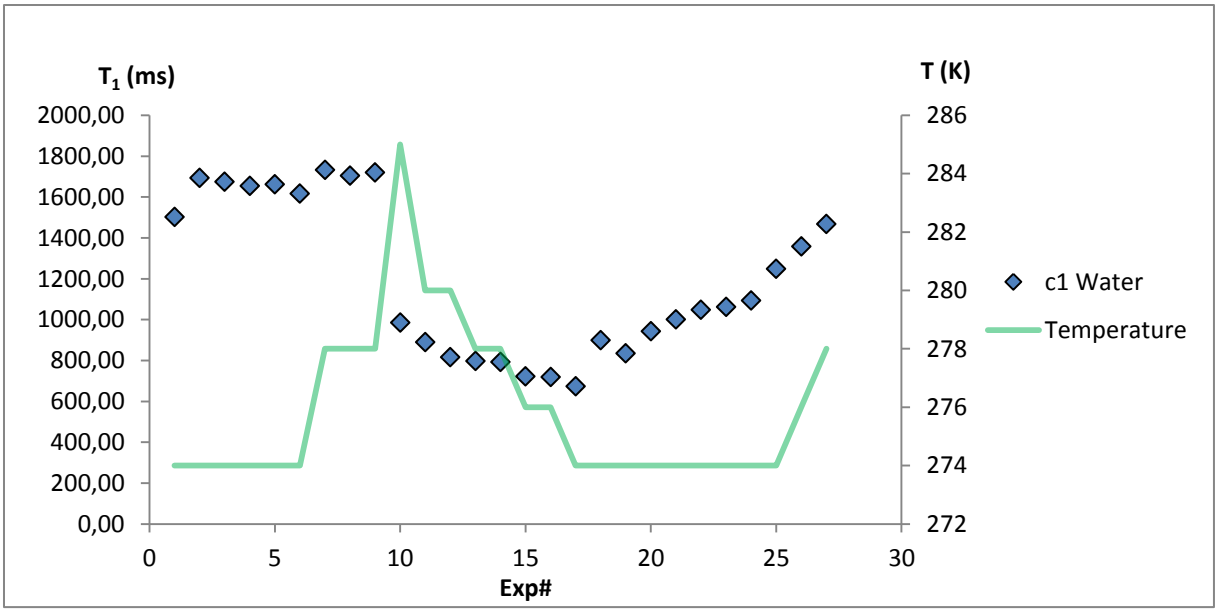

Figure 3.23: The water peak c1 T_1 values found from the two-component analysis of all inversion recovery experiments performed for sample B3Fa, plotted as a function of experiment number. The three last experiments were performed after the sample was removed from the spectrometer and stored at -30 ^{o}C for three days in an attempt to reform hydrates. The sample was kept at 285 K for almost a day between experiments 9 and 10. The spectrometer temperature in Kelvin is plotted on the secondary axis.

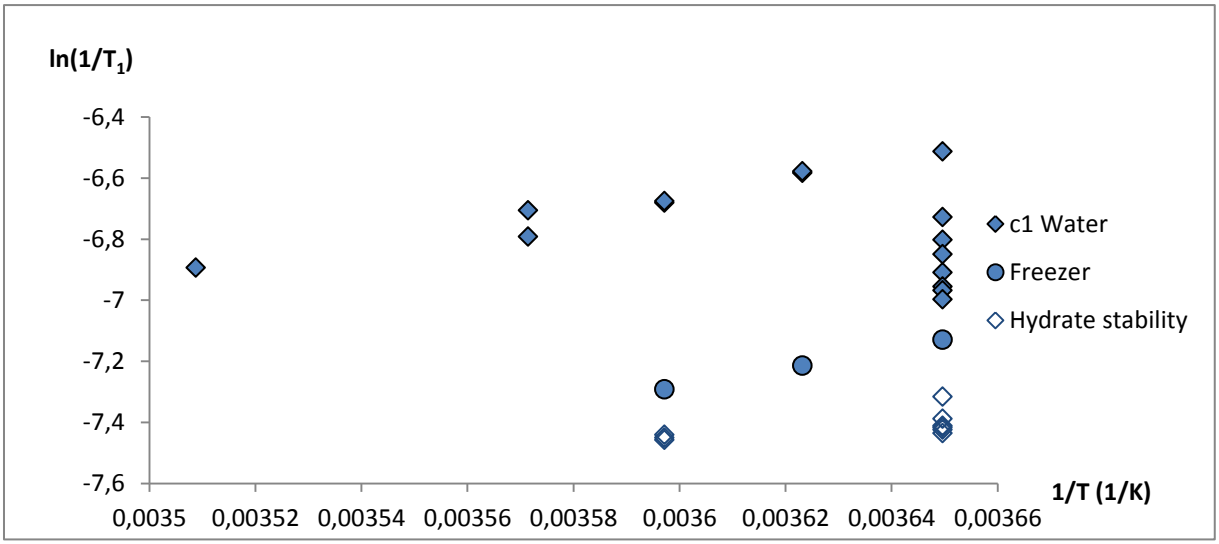

Figure 3.24: The water peak c1 values found from the two-component analysis of all inversion recovery experiments performed for sample B3Fa, plotted as the natural logarithm of inverse T_1 versus inverse temperature in Kelvin. The experiments performed before reaching the hydrate dissociation temperature are marked with open diamonds, while the experiments following freezer storage are marked with circles.

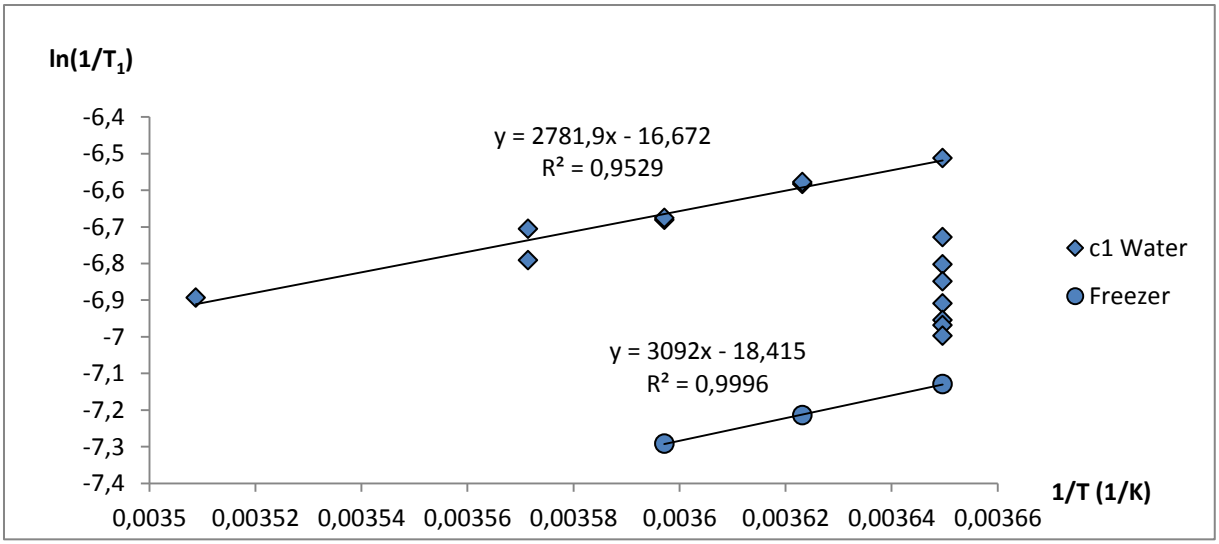

Figure 3.25: The water peak c1 values found from the two-component analysis of all inversion recovery experiments performed after sample B3Fa had been subjected to hydrate dissociation temperature. The experiments following freezer storage are marked with circles. The freezer storage values represented a linear range, as did parts of the first experiment series. Both of these were fitted to regression lines, the functions and R^2 values of which is displayed above their respective lines. A clear downwards trend was observed for the 274 K transition as a function of time, meaning that the series might constitute part of a hysteresis loop.

The T_2 analysis of the water peak second component and the cyclopentane peak components can be found in Appendix E.

3.5.4 T_2 relaxation results

The sample was kept at 285 K for 19 hours between experiments 9 and 10, but no CMPG experiments were performed during this interval. The three last experiments were performed after the sample was removed from the spectrometer and stored at -30 ^{o}C for three days in an attempt to reform hydrates.

The one- and three-component approaches can be found in Appendix E, along with the guess values used in the analyses.

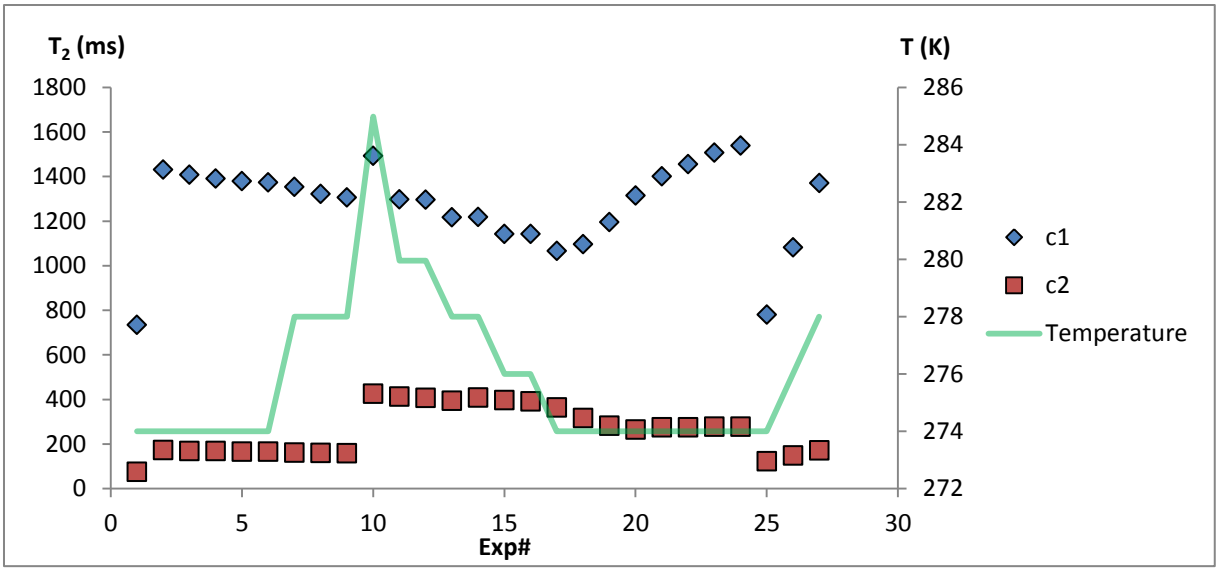

Figure 3.26: The results of two-component analysis of all CPMG oneshot experiments on B3Fa, plotted as T_2 in ms as a function of experiment number. The green curve is the temperature in Kelvin, plotted on the secondary vertical axis. Note that the T_2 values are high for all but the first experiment.

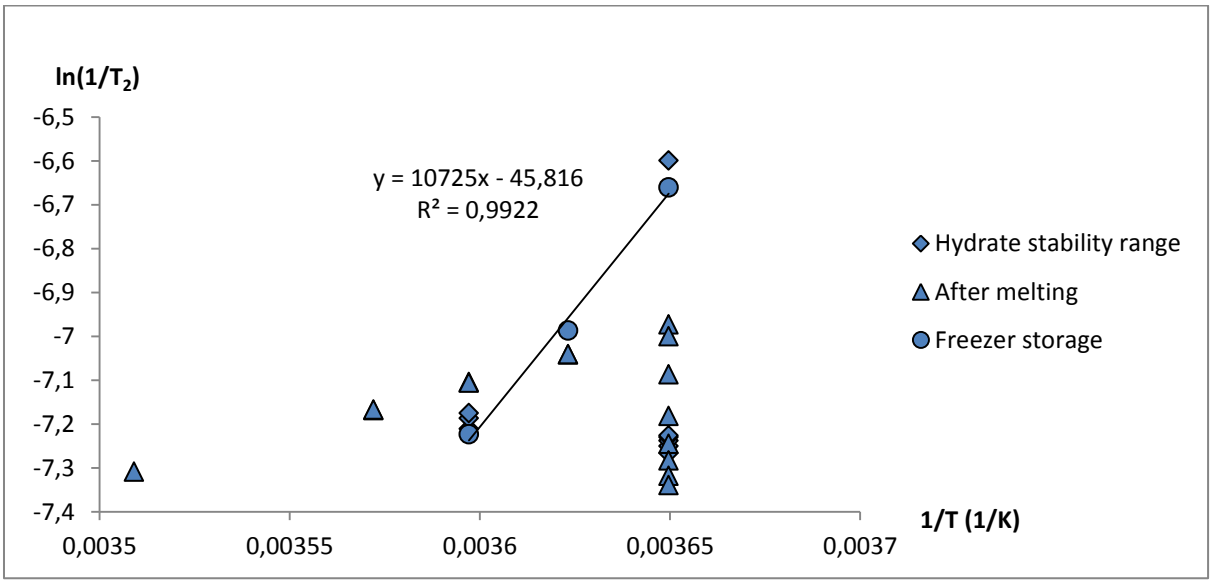

Figure 3.27: The c1 results of two-component analysis of all CPMG oneshot experiments on B3Fa, plotted as plotted as $ln((T_2)^{-1})$ as a function of T^{-1}. Experiments performed after the sample had been subjected to temperatures beyond the hydrate stability region are shown as "After melting". Measurements performed after the freezer reformation attempt is shown as circles. These are seen to form a linear range that is fitted to a regression line, the function and R^2 value of which is provided above the line.

The "after melting" points seem to follow a linear trend before entering a transition range at 274 K. This area is therefore re-plotted and the applicable results fitted to a regression line.

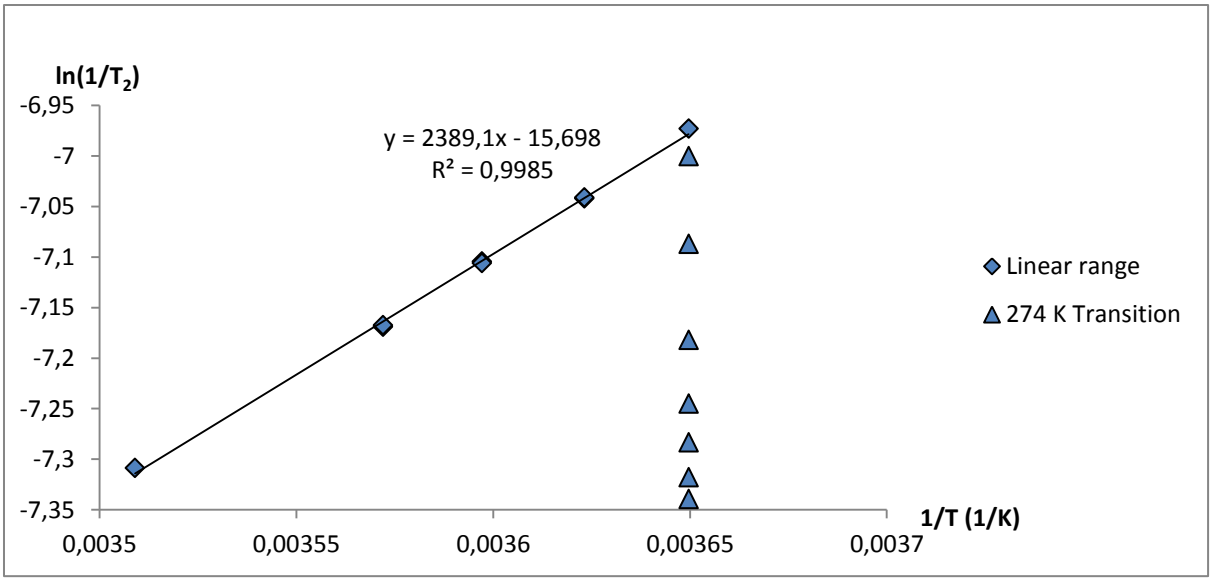

Figure 3.28: The c1 results of a two-component approach for the eight first experiments performed outside the range of hydrate stability for B3Fa are plotted as diamonds and fitted to a regression line, the formula and R^2 value of which is shown. The following experiments are plotted as triangles, and proceeds from top to bottom as a function of time.

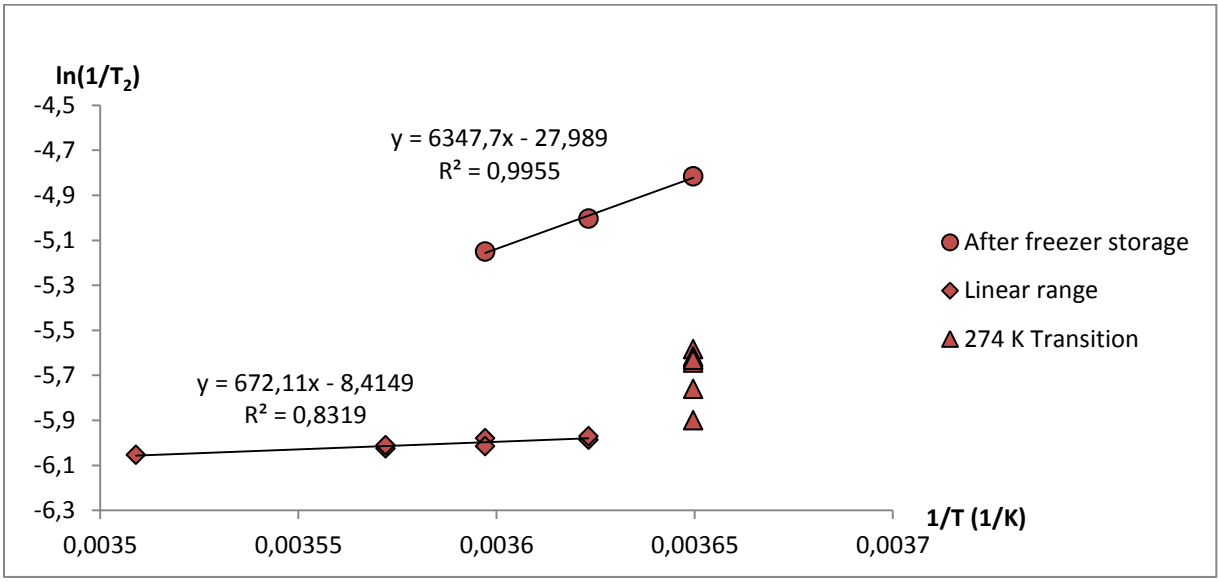

Figure 3.29: The c2 results of a two-component approach for the seven first experiments performed outside the range of hydrate stability for B3Fa are plotted as diamonds and fitted to a regression line, the formula and R^2 value of which is shown. The experiments during the 274 K transition are plotted as triangles, initially increasing as function of time before forming a distribution around a possible final value. Measurements performed after the freezer reformation attempt is shown as circles. These are seen to form a linear range that is fitted to a regression line, the function and R^2 value of which is provided above the line.

3.5.5 Summary

Table 3.2: Activation energies found from the slope of $ln(1/T_1) / (1/T)$ with corresponding R^2 values for the B3Fa hydrate former system using different methods for reforming.

		Spectrometer reformation		Freezer reformation	
Peak	**Component**	**E_a (J/mol)**	**R^2**	**E_a (J/mol)**	**R^2**
Water	1	2781,9	0,9529	3092	0,9996
CP main	1	1405,7	0,2093	244,07	0,1639
	2	1405,7	0,2093	-	-
CP side	1	-	-	760,54	0,2164
	2	-	-	244,07	0,1639

Table 3.3: Activation energies found from the slope of $ln(1/T_2) / (1/T)$ with corresponding R^2 values for the B3Fa hydrate former system using different methods for reforming.

		Spectrometer reformation		Freezer reformation	
Approach	**Component**	**E_a (J/mol)**	**R^2**	**E_a (J/mol)**	**R^2**
1-Comp	1	2032,2	0,9991	10039	0,9872
2-comp	1	2389,1	0,9985	10725	0,9922
	2	672,11	0,8319	6347,7	0,9955
3-Comp	1	2430,3	0,9287	10048	0,9746
	2	3555,1	0,0031	-2512	0,156
	3	-1508,4	0,0018	-37347	0,7229

3.6 B3Fb

3.6.1 Sample information

The sample was prepared using the cold storage packing method.

The two experiment series had different goals. During the first series, the final spectrometer temperature was set as to have the boundary of hydrate stability located within its accuracy of ±0.5 K, in order to perform continuous experiments on a slowly changing sample, which was the main goal of the series. The acquisitions at lower temperature leading up to these experiments provided both time for the sample to equilibrate near the target temperature, as well as a reference with which to compare the final results.

For the second series, the sample was analysed after being stored at room temperature for three days. Analyses were done at near ambient conditions as well as on the edge of- and within the hydrate stability region. The reason for this approach is that it provided a set of results: First, a reliable weight could be obtained for the sample, followed instantly by measurements of the sample in order to put eventual changes into context. Furthermore, the melted sample was expected to have reached ambient physical-chemical equilibrium, and thus provides a reference for other experiments. Third, it provided an opportunity to probe how a room-tempered water-cyclopentane system reacts to re-introduction to the hydrate stability range.

3.6.2 ^{1}H results

The sample was introduced to the spectrometer, pre cooled to 274 K. A series of experiments was performed at 274 K, 276 K and 278 K. This was followed by ramping the temperature from 278-280.5 K using a ramp rate of 0.1 K/min. At the same time, a continuous acquisition of alternating ^{1}H and

CMPG experiments was run, totalling 240 experiments. The results of all these experiments are presented in Appendix E.

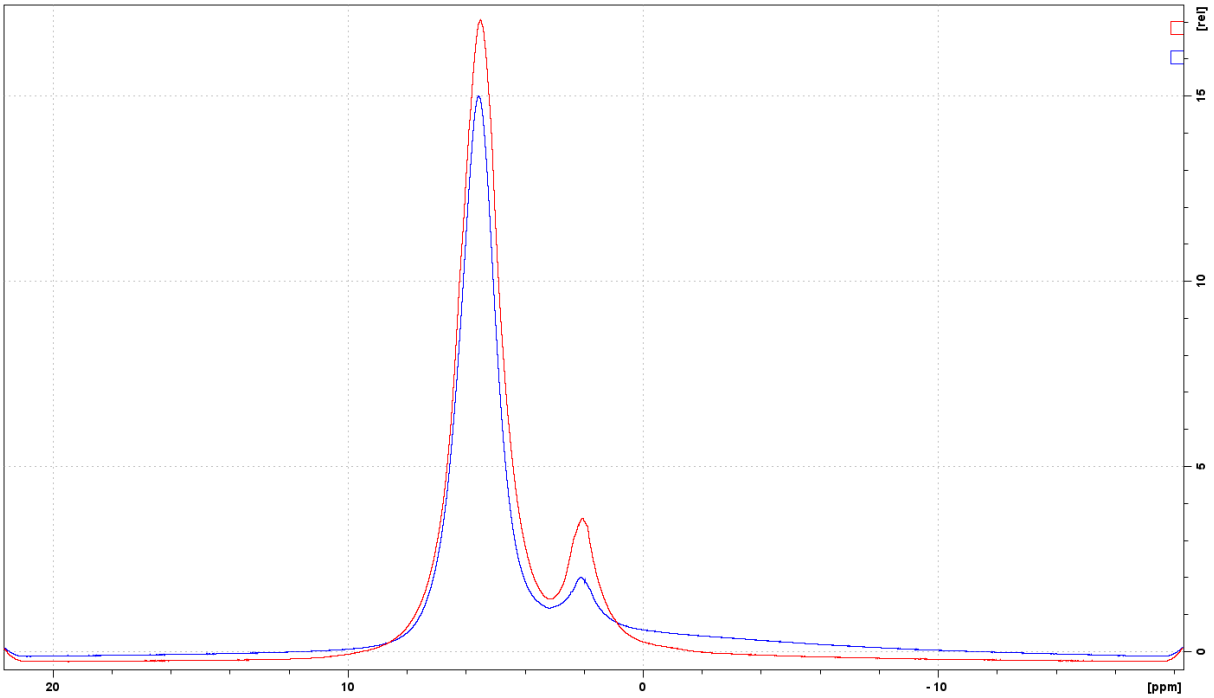

Figure 3.30: Comparison between the first (blue) and last (red) spectra of the 278-280.5 K ramping program of sample B3Fb, acquired approximately 11 hours apart. Considerable growth is observed for both the cyclopentane and water peaks, corresponding to a decrease in the area beneath the sloping baseline. Both peaks retain their smooth curvature throughout the experiment series.

Following the ramping program, the sample was removed from the spectrometer and stored at room temperature for three days. It was then reintroduced to the spectrometer, which was set at a temperature of 295 K. A series of experiments were performed at this temperature, before acquiring similar series at 281 K, 280 K, 278 K, 276 K and 274 K. The results of these experiments can be found in Appendix E.

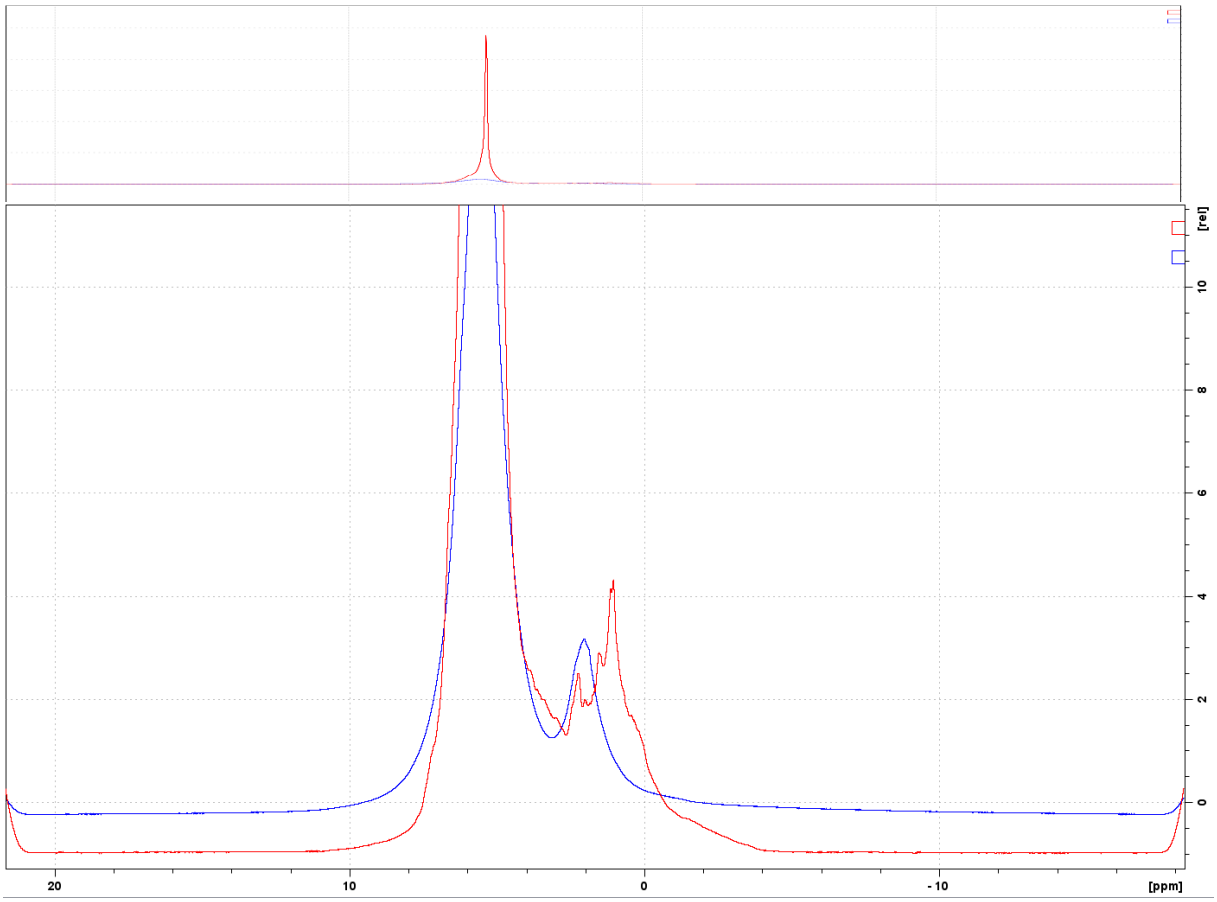

Figure 3.31: The last spectrum of the 278-280.5 K ramping program (blue) of sample B3Fb, compared with the last spectrum acquired at 295 K after the sample had been subjected to room temperature for three days (red). Top: full spectra. Bottom: Zoomed intensity axis. It seems the melting process did not finalise during the ramping program.

3.6.3 T_2 relaxation results

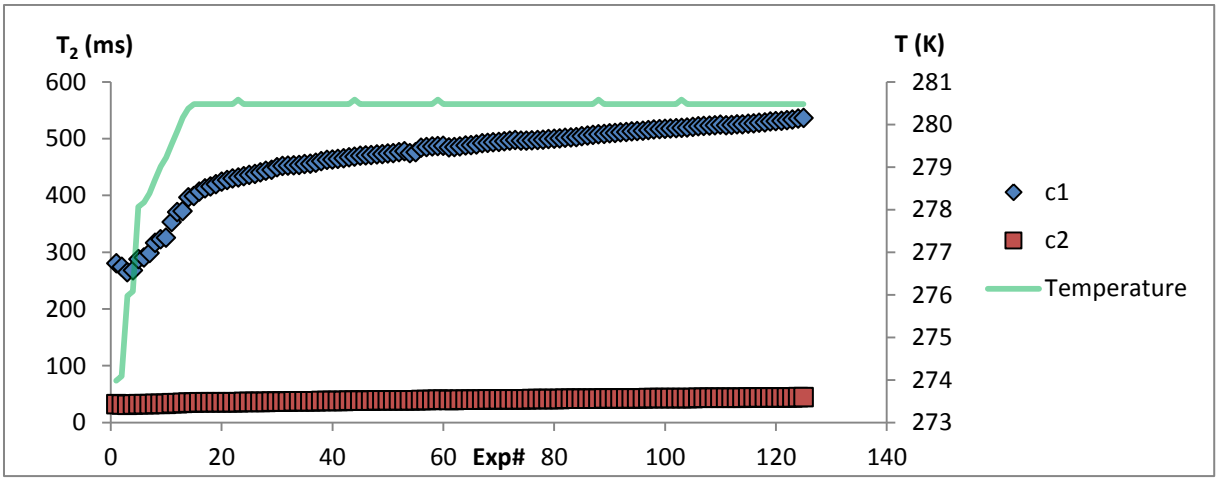

Figure 3.32: The T_2 results for all experiments in the first B3Fb analysis series using the two-component approach, plotted as a function of experiment number. The T_2 values can be seen to lie considerably lower than those observed for other series.

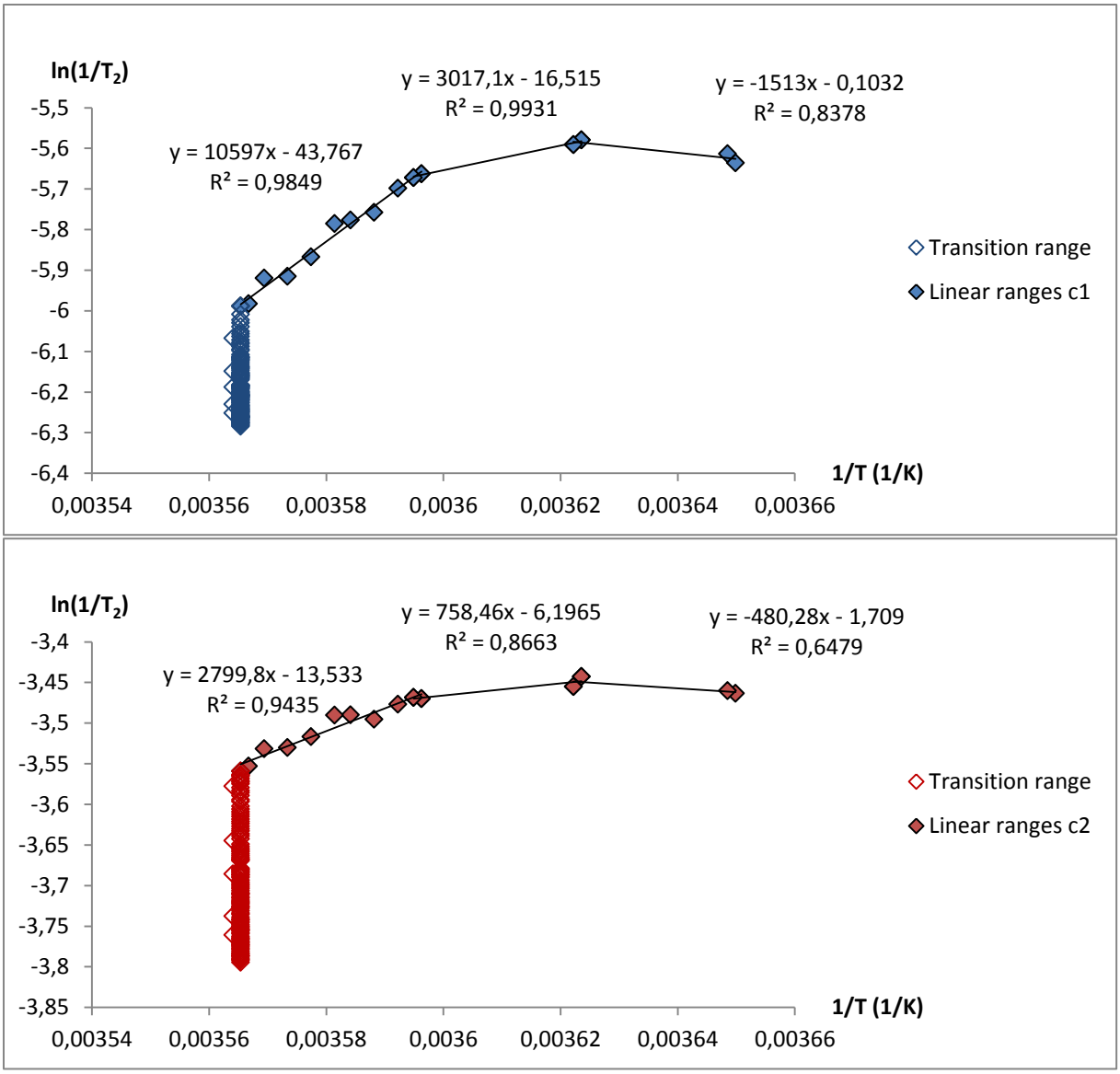

Figure 3.33: The T_2 results for all experiments in the first B3Fb analysis series using the two-component approach, plotted as $ln(1/T_2)/(1/T)$. The c1 results are shown on top, while the c2 results are shown at the bottom. All regions of different slope are fitted to regression lines.

The remaining results for the T_2 experiments of this series can be found in Appendix E.

3.6.4 Summary

Table 3.4: Activation energies found at different temperature ranges from the slope of $ln(1/T_2) / (1/T)$, with corresponding R^2 values. The results were found for the B3Fb hydrate former system during the initial experiment series. Different components of the one- and three-component approaches showed changes in slope at different points, all in close proximity to 279.5 K, which is reported as the temperature of change where applicable.

Temperature range (K):		278-279.5		279.5-280.5	
Approach	Component	**E_a (J/mol)**	**R^2**	**E_a (J/mol)**	**R^2**
1-Comp	1	5406,1	0,943	30182	0,9961

2-Comp	1	10597	0,9849	10597	0,9849
	2	2799,8	0,9435	2799,8	0,9435
3-Comp	1	2982	0,9712	-3106,6	0,7325
	2	565,15	0,8875	3282,2	0,8487
	3	1339,3	0,8213	956,86	0,9593

3.7 B3Fc

3.7.1 Sample information

The sample was packed using the cold storage process.

As the results of the B3Fb experiment series showed that changes to the sample was seemingly still occurring after 11 hours at the upper edge of the hydrate stability region, another experiment series reproducing this ramp-program was selected. In addition, this series would be followed by directly lowering the sample temperature back into the hydrate stability region to see whether the changes were reversible.

3.7.2 ^{1}H results

All ^{1}H results of the experiment are provided in Appendix E.

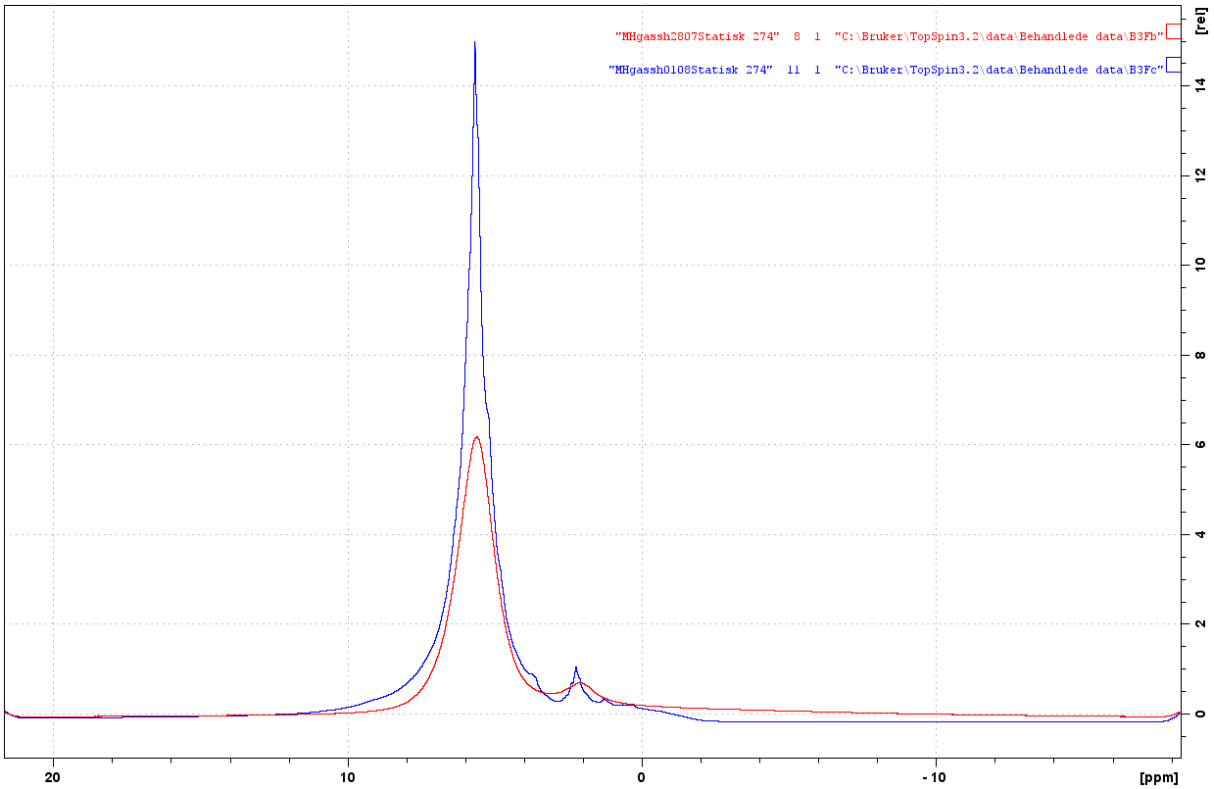

Figure 3.34: The last ^{1}H spectrum of sample B3Fc acquired at 274 K (blue) compared with the last spectum at the same temperature acquired for sample B3Fb (red). A large difference is observed, and B3Fc was assumed to have undergone a for practical purposes irreversible melting process.

3.7.3 T_2 relaxation results

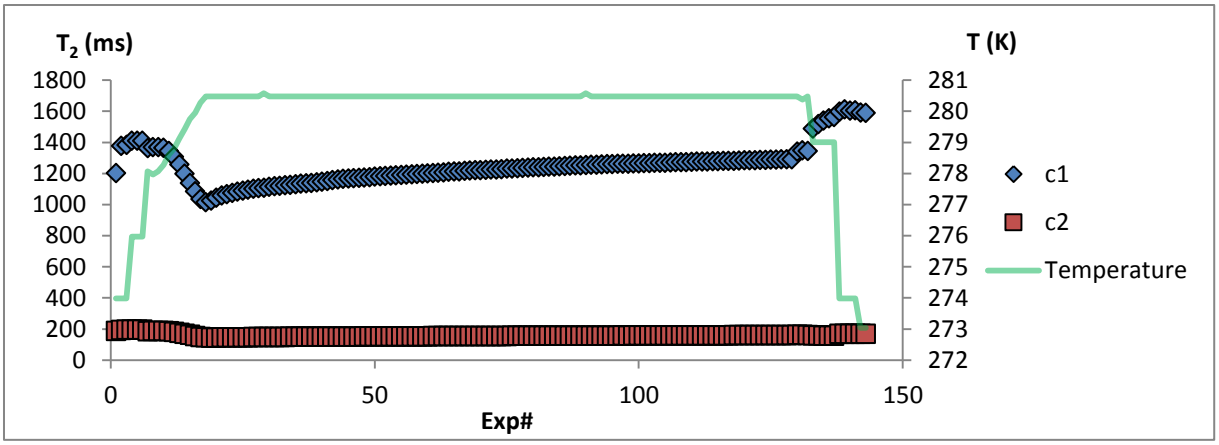

Figure 3.35: The results of two-component T_2 analysis of all CMPG experiments performed on sample B3Fc as a function of experiment number. The T_2 values are seen to be trending downwards during the initial temperature ramp, a trend that is arrested upon reaching 280.5 K.

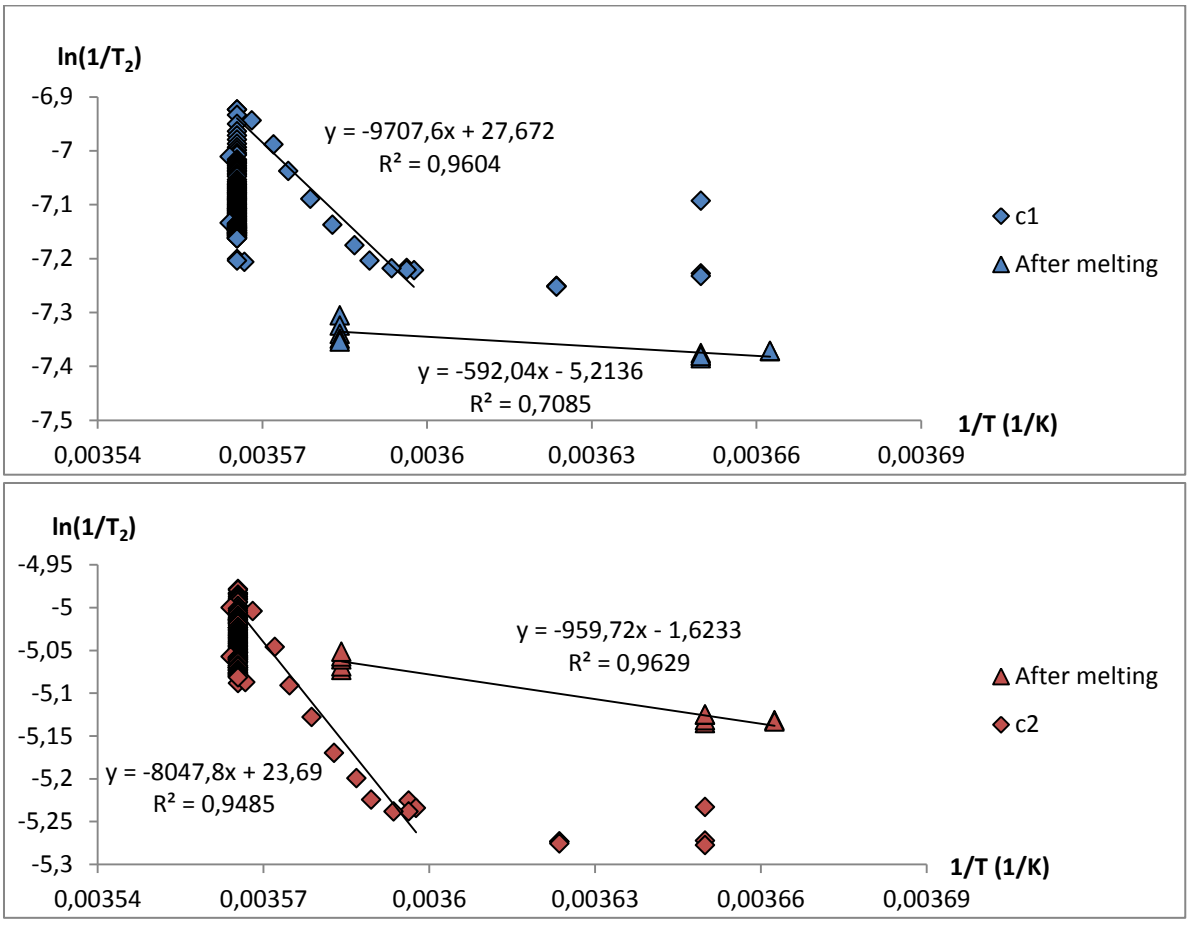

Figure 3.36: The T_2 results for all experiments of sample B3Fc using the two-component approach, plotted as $\ln(1/T_2)/(1/T)$. Points acquired after the temperature was lowered from 280.5 K are marked as 'After melting'. The linear regions are fitted to regression lines, with functions and R^2 values provided above their respective lines. c1 is plotted in the topmost graph, c2 in the bottom one.

Further T_2 data is provided in Appendix E, along with the guesses used during the data analysis.

3.8 B3Fa2

3.8.1 Sample information

The sample was prepared using the cold storage packing method.

A larger than usual NMR timeslot was delegated to this experiment, allowing an investigation of the sample behaviour after insertion at a sub-zero temperature, as well as a long series of experiments at both 274 and 280.5 K. The latter of these was selected as the effects seen for sample B3Fb still was not verified, and prompted further study. A short experiment series was then ran at 282 K, before the sample temperature was lowered to 274 K. Another short series of experiments was also run at this temperature to see if any changes could be observed during a small timeframe.

3.8.2 ^{1}H spectra

The sample was weighed and introduced to the spectrometer, which was pre-cooled to a temperature of 272 K, and a ^{1}H spectrum was immediately acquired. Tuning and matching on the sample was performed, followed by the acquisition of a new ^{1}H-spectrum every five minutes for 15 minutes. Following this 5-minute interval acquisition, further ^{1}H spectra acquired was interspaced with CMPG and inversion recovery experiments. This three-pronged acquisition was continued until the spectrum stabilised.

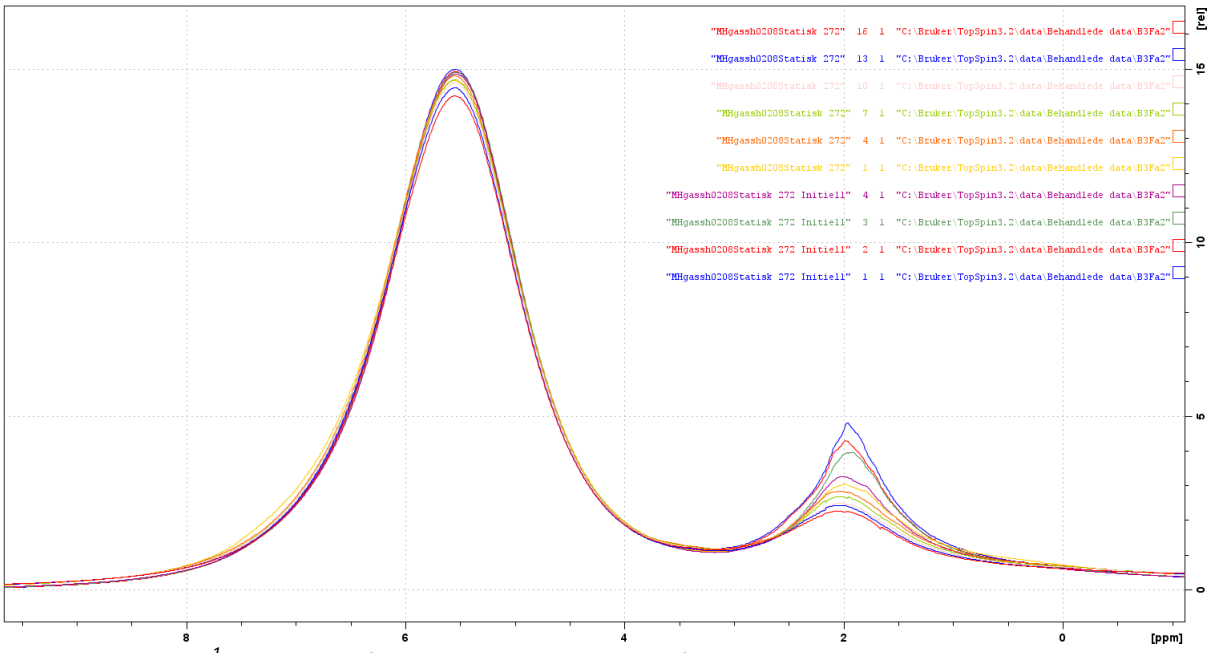

Figure 3.37: The ^{1}H spectra of sample B3Fa2 at 272 K following insertion to the spectrometer. The initial spectrum is shown as the topmost blue line. The first four spectra are taken approximately 5 minutes apart. The remaining 6 have a spacing of 21 minutes, and time span between the first and last spectrum is 2 ½ hours.

When the sample peaks were found to have stabilised after insertion, a temperature ramping program was used to increase the temperature to 274 K using a ramp rate of 0.05 K/min. During and after the temperature ramp was complete, a continuous acquisition of alternating ^{1}H and CMPG experiments was run, totalling 120 ^{1}H experiments with a spacing of approximately 5 minutes between each in addition to 120 T_2 measurements. The results of all ^{1}H experiments can be found in Appendix E.

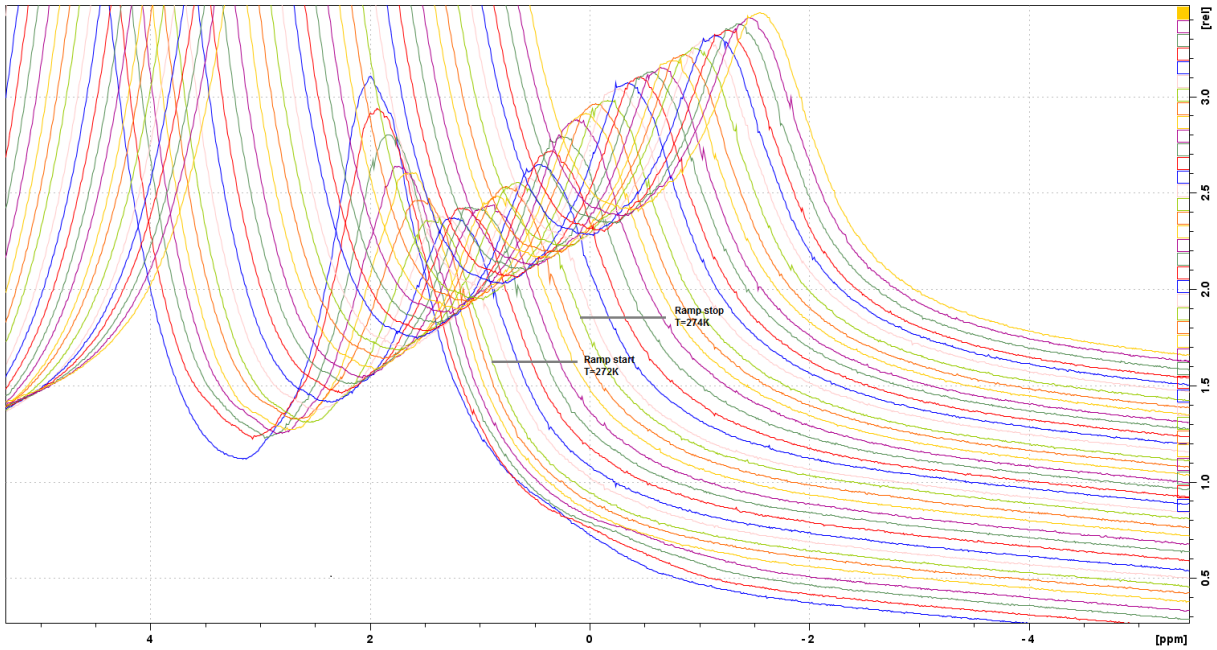

Figure 3.38: From left to right, the fifth through tenth ^{1}H spectra of sample B3Fa2 at 272 K is presented along with the 31 first spectra in the ramping program, using vertical and horizontal offset. Note that this means the time between each spectrum is longer for the first six spectra. The spectra taken closest to the temperature ramp start- and endpoint are marked.

Following the finalisation of the serial acquisitions, an initial ^{1}H spectrum was acquired before tuning and matching the sample at 274 K. Following this, the three-experiment approach was again adopted. The three resulting spectra can be seen in Appendix E.

As the sample was believed not to be undergoing any further change at this point, the temperature was increased to 276 K. When the sample had been allowed to reach thermal equilibrium during a 15 minute period, a single sequence of $^{1}H - T_2 - T_1 - {}^{1}H$ experiments was run. For one last spectrum at this temperature, the sweep width was increased, along with an increase of number of scans. No significant change was observed over the course of the experiments, and the temperature was further increased as per procedure, first to 278 K, and then to 279 K. The spectra at these temperatures are presented in Appendix E.

At this point, another temperature ramping program was started, going from 279-280.5 K at a rate of 0.05 K/min. The same experiments as previously were run, with the exception of substituting every 40th experiment with a T_1 inversion recovery experiment with an expected time of approximately 20 minutes.

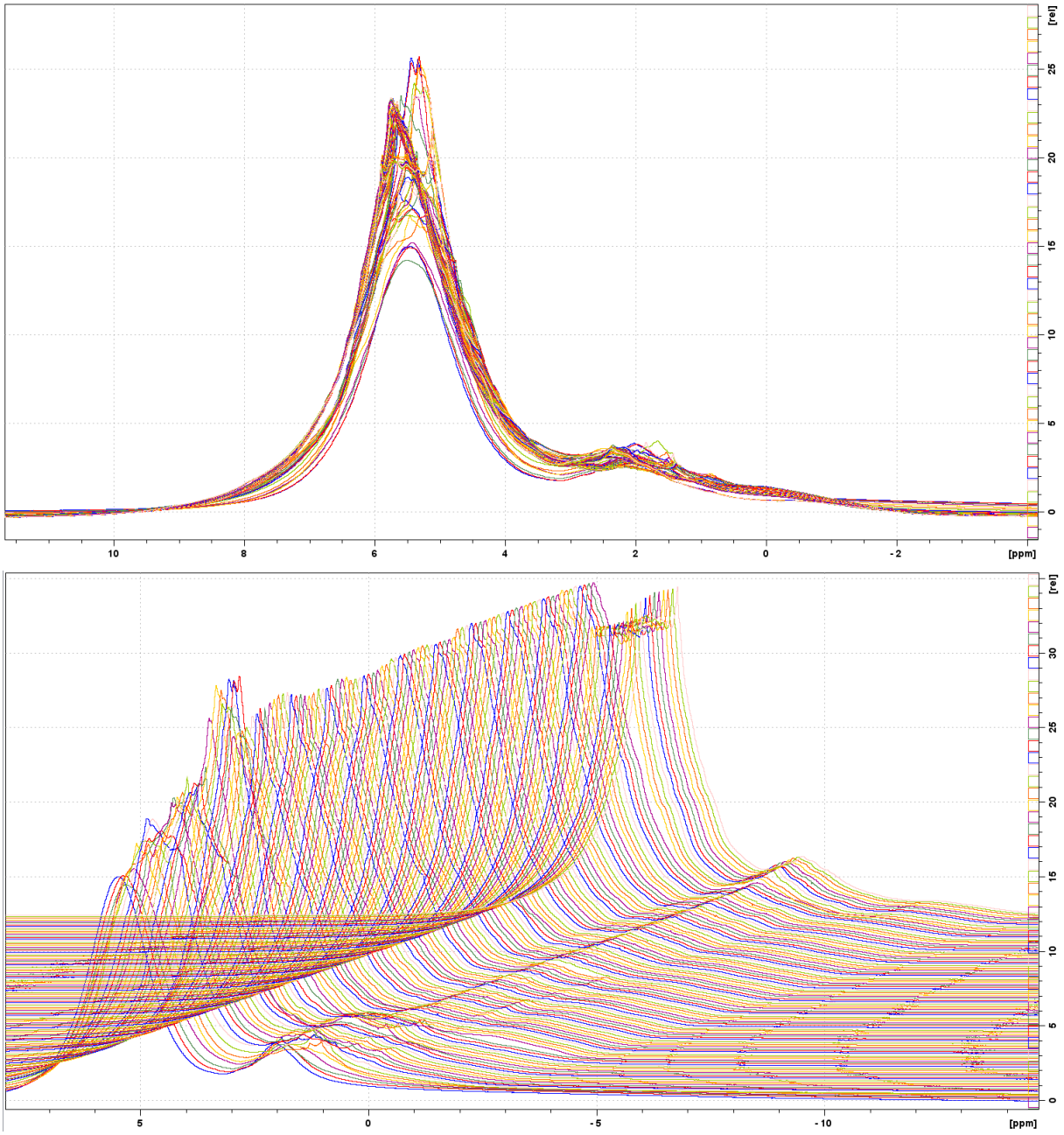

Figure 3.39: The 120 ^{1}H experiments acquired during and after the temperature ramp using a) a stacked plot and b) horizontal and vertical offset. From sample B3Fa2.

A sudden change in the water peak of the spectra was observed towards the final stages of the experiment sequence.

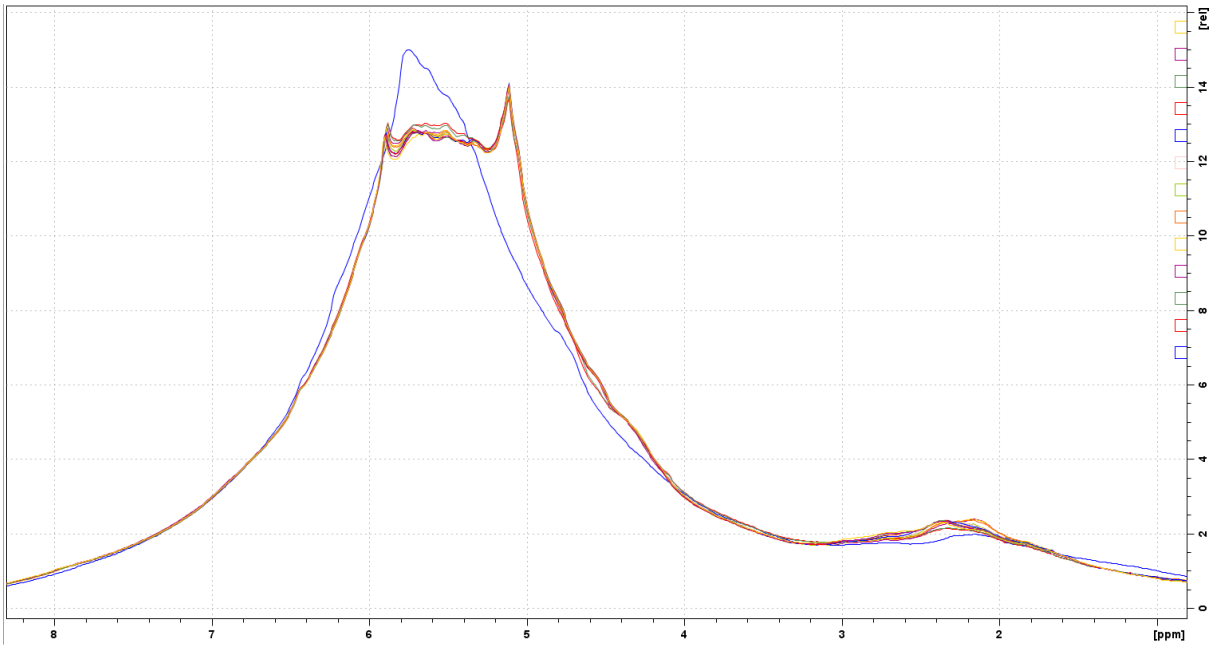

Figure 3.40: The 12 final spectra of the ramp sequence of sample B3Fa2, compared with the one immediately preceding them (blue). The change takes place within a five minute interval.

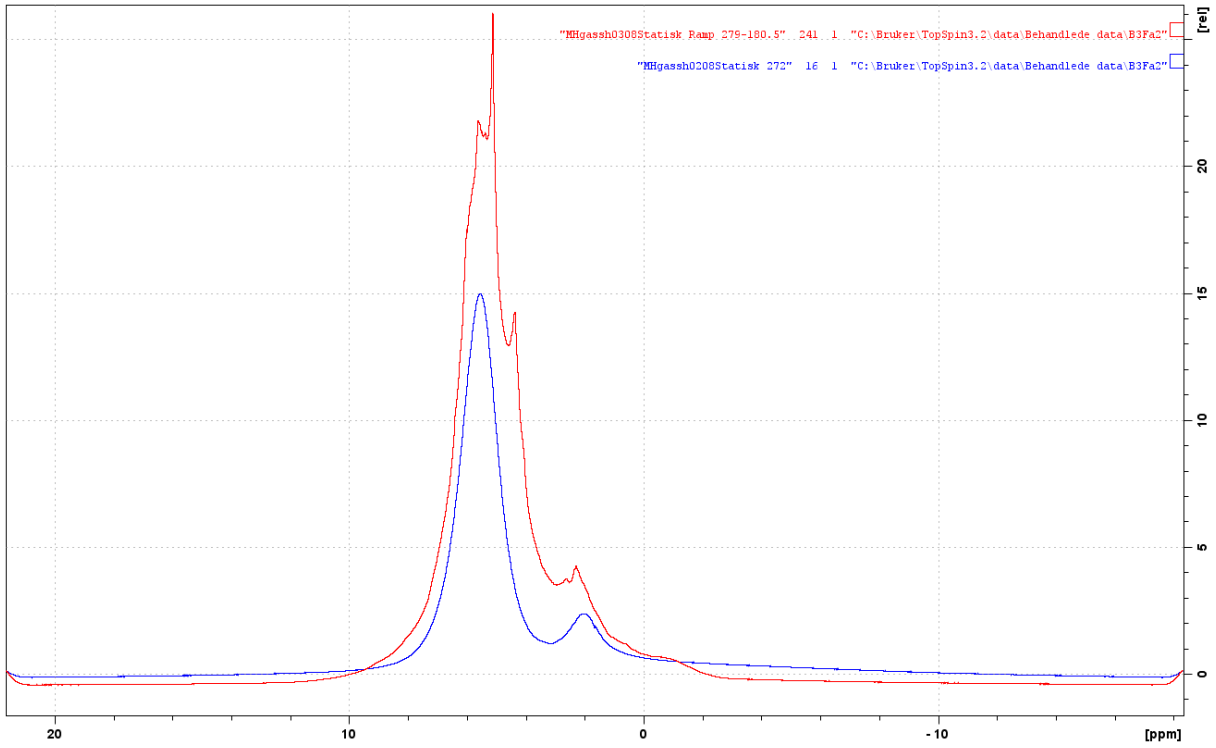

Figure 3.41: The last spectrum of B3Fa2 at 272 K (blue), compared with the last spectrum taken at 280.5 K (red). Note the sloping baseline in the former, possibly due to a very wide peak of low intensity. This eventual peak does not seem to be present in the latter.

3.8.3 T_1 relaxation results

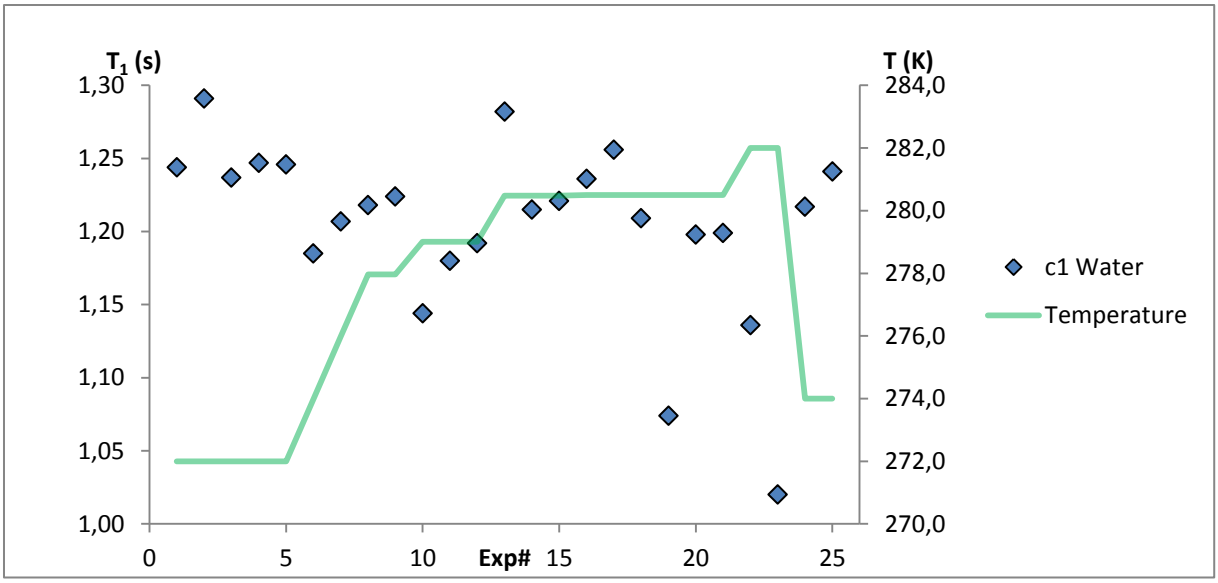

Figure 3.42: The component 1 results of two-component analysis of the water peak in all B3Fa2 T_1 measurements plotted as a function of experiment number. The temperature in Kelvin is plotted on the secondary axis.

The remaining two-component results are presented along with all three-component results in Appendix E.

3.8.4 T_2 relaxation results

The guessranges used for the analyses of the following results are provided in Appendix E along with the one- and three-component results.

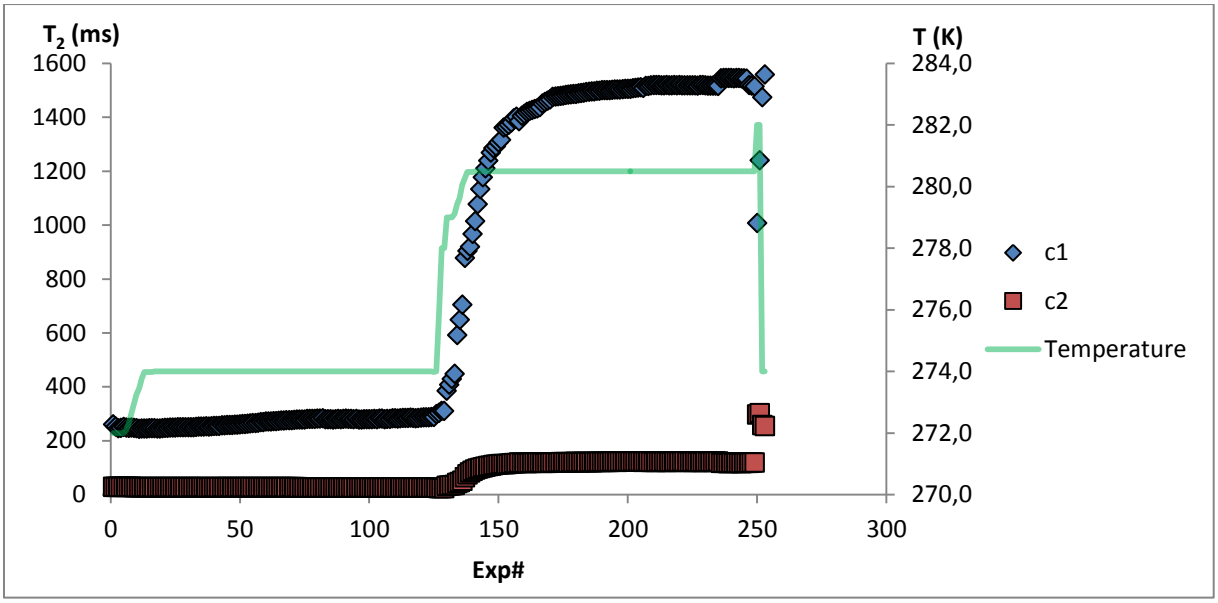

Figure 3.43: The results of two-component analysis of all CPMG oneshot experiments on B3Fa2, plotted as T_2 in ms as a function of experiment number. c1 is the results for component 1, while c2 is the result for component 2. The green curve is the temperature in Kelvin, plotted on the secondary vertical axis.

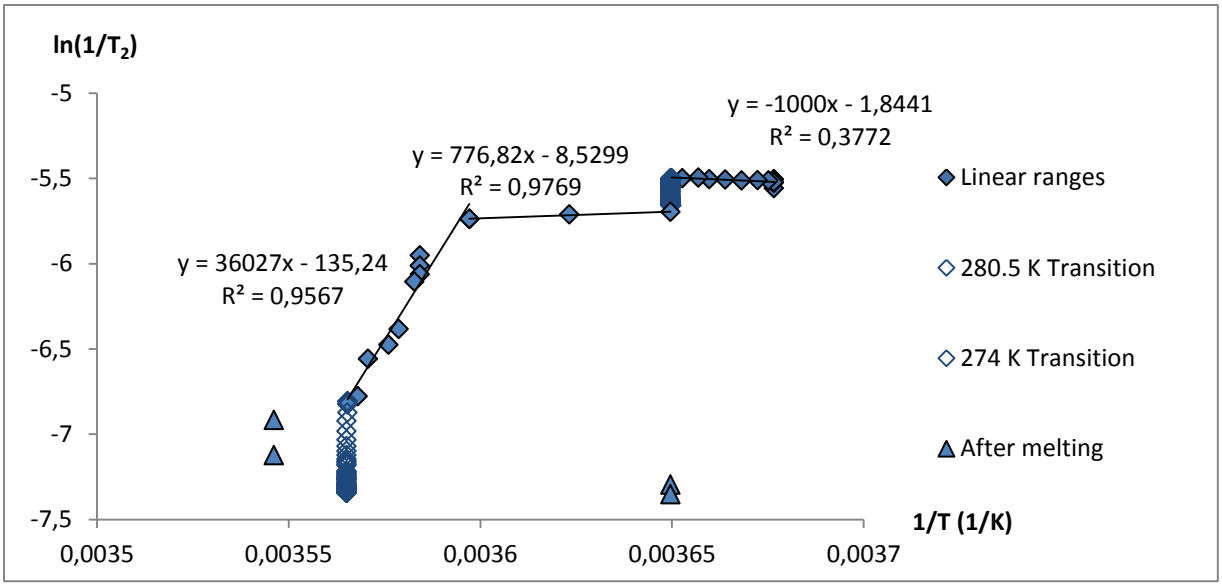

Figure 3.44: The results of component 1 from two-component analysis of all CPMG oneshot experiments on B3Fa2, plotted as $\ln((T_2)^{-1})$ as a function of T^{-1}. Three linear ranges are identified and separately fitted to regression lines, the functions and R^2 values of whose are provided above their respective lines. The two ranges of rapid change are designated as transitions, marked with open diamonds. These results are not factored into regression. Experiments performed after the last transition is shown as "After melting", but is not included in the regression. A close-up of the low-temperature range can be found in Appendix E.

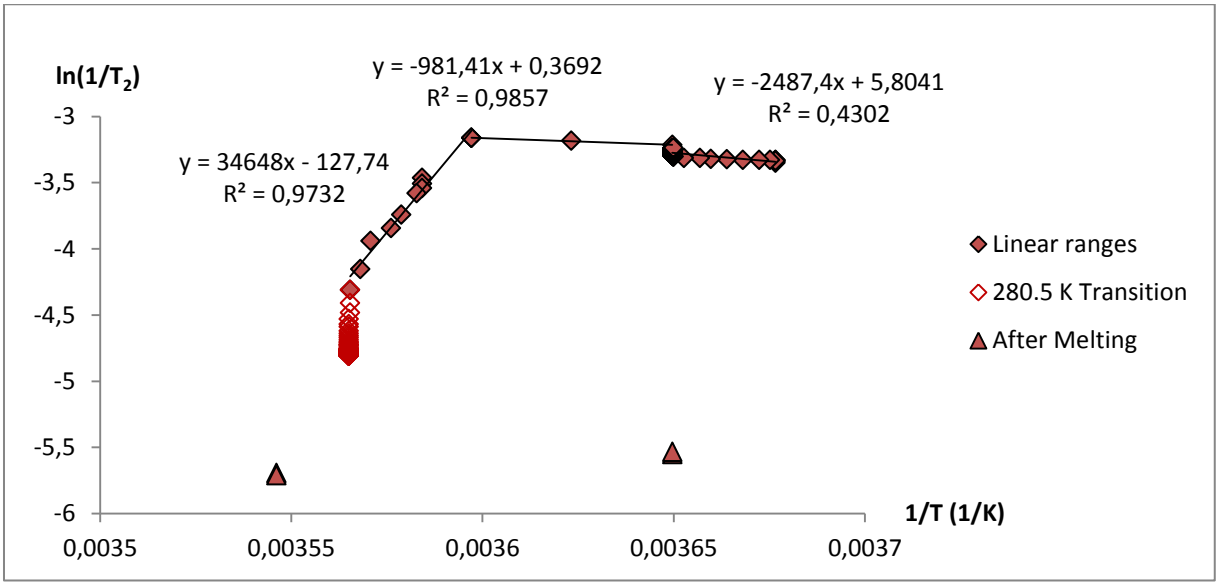

Figure 3.45: The results of component 2 from two-component analysis of all CPMG oneshot experiments on B3Fa2, plotted as $\ln((T_2)^{-1})$ as a function of T^{-1}. Three linear ranges are identified and separately fitted to regression lines, the functions and R^2 values of whose are provided above their respective lines. The range of rapid change is designated as a transition, and these results are not factored into regression. Experiments performed after the last transition is shown as "After melting", but is not included in the regression.

The results of the one- and three-component approaches as well as well as remaining two-component plots are provided in Appendix E.

3.8.5 Summary

Table 3.5: Activation energies found at different temperature ranges from the slope of ln(1/T_1) / (1/T) with corresponding R^2 values for the B3Fa2 hydrate former system.

Temperature range (K):		272-276		276-280.5	
Peak	**Component**	**E_a (J/mol)**	**R^2**	**E_a (J/mol)**	**R^2**
Water	2	-4482,1	0,7227	4335,2	0,6681
Cyclopentane	1	13612	0,7362	-31558	0,9048
	2	-10025	0,8527	4725,7	0,9918

Table 3.6: Activation energies found at different temperature ranges from the slope of ln(1/T_2) / (1/T) with corresponding R^2 values for the B3Fa2 hydrate former system.

Temperature range (K):		272-274		274-278		278-280.5	
Approach	**Component**	**E_a (J/mol)**	**R^2**	**E_a (J/mol)**	**R^2**	**E_a (J/mol)**	**R^2**
1-Comp	1	-2092,4	0,8498	-1007,6	0,6016	78651	0,9905
2-Comp	1	-1000	0,3772	776,82	0,9769	36027	0,9567
	2	-2487,4	0,4302	-981,41	0,9857	34648	0,9732
3-Comp	1	2964	0,4907	128,53	0,0531	16525	0,7098
	2	843,54	0,0014	843,54	0,0014	25153	0,9406
	3	553,35	0,0008	553,35	0,0008	15922	0,9669

3.9 B3Fb2

3.9.1 Sample information

The sample was prepared using the cold storage packing method.

The initial ^{1}H spectra revealed anomalous behaviour of the sample, and it was hypothesised that it had partially melted during the spectrometer introduction procedure. To verify, the sample was subjected to a temperature of 285 K for a prolonged time.

3.9.2 ^{1}H NMR

A temperature ramping program was used to increase the spectrometer temperature to 285 K. Meanwhile, a continuous acquisition of 240 experiments was started; alternating between ^{1}H and CMPG experiments with inversion recovery experiments replacing a CMPG experiment every 40 experiments. 40 dummy scans were used for every ^{1}H experiment to achieve proper spacing. In addition, another experiment was performed another nine hours later, amounting to a total of 21 hours after the first experiment. A selection of the spectra are shown below, with the rest presented in Appendix E.

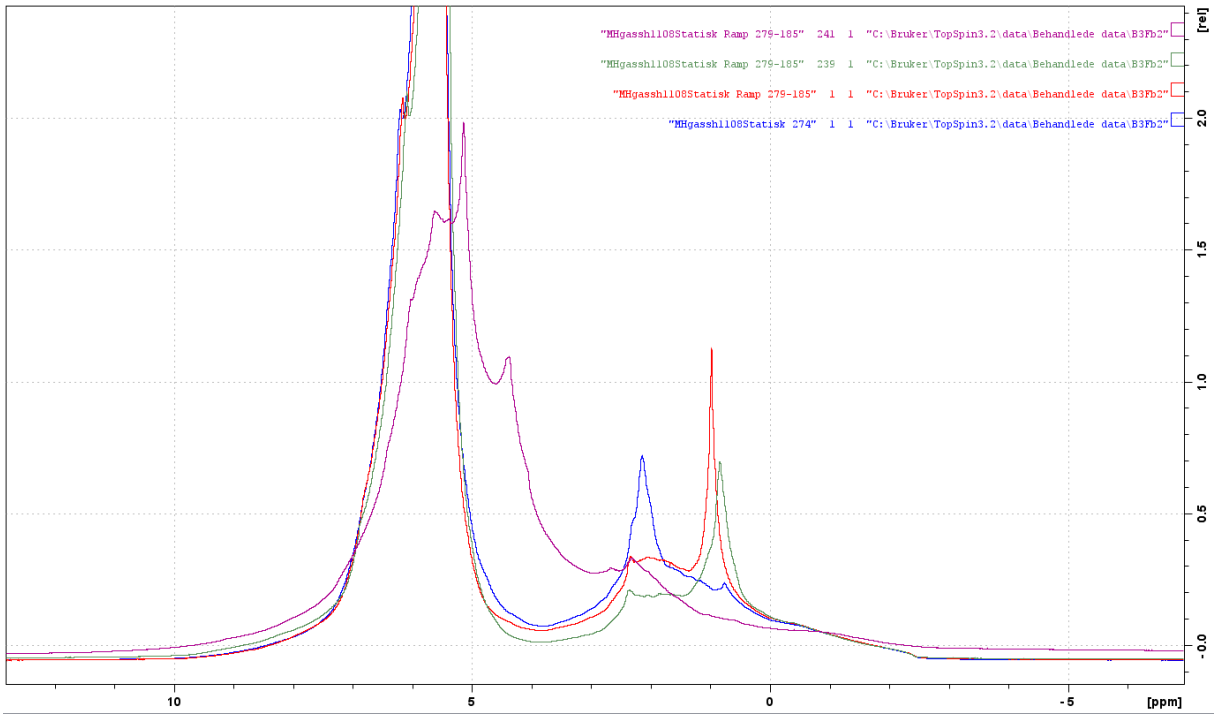

Figure 3.46: The initial spectrum of sample B3Fb2 (blue) compared with the first (red) and last (green) spectra of the ramping program, and the spectrum acquired after 21 hours (indigo).

3.9.3 T_1 relaxation results

Throughout the analysis, the three-component analysis gave widely varying results on small changes to guesses, while the two-component approach was found to be much more robust. The first experiment was impossible to attain a good fit for. Experiments 5 and 6 were also hard to analyse for both approaches, and a bias was introduced as guesses were selected as to attain results that resembled previous ones. For the last experiment, the two-component approach yielded a good fit without much guess iteration whilst the three-component approach failed. The two-component results are presented in Appendix E.

3.9.4 T_2 relaxation

The T_2 results are provided in Appendix E, along with the guesses used for the analysis.

3.10 B3Fa6 MAS experiments

3.10.1 Sample information

The B3Fa6 sample was used for the following experiments, and was packed using the cold storage method.

The goal of the experiment series was to use MAS NMR to find evidence for the presence of a wide, underlying peak being misrepresented as a sloping baseline. This was done by acquiring a series of spectra at the same temperature under different spin rates, in order to determine which peaks remain at the same position: Such static peaks correspond to real peaks in the spectrum. A secondary objective was to probe the viability of changing between static and spinning modes on the

spectrometer whilst a sample was present. As this changeover involves a short cut-off of cooling gas flow, the spectrometer was pre-cooled to a temperature of 270 K before sample insertion in order to have some leeway for temperature increases.

The experiment series was plagued by a series of issues however, starting at sample insertion. The spectrometer repeatedly failed to insert the sample, and the sample was placed in cold storage or cooled in liquid nitrogen between attempts in order to maintain hydrate integrity.

Furthermore, the sample was so easy to spin that it often maintained a spin of a few Hz, even when run in static mode without a drive pressure. This necessitated constant tweaking of gas flow parameters in order to acquire static reference spectra.

The spin detector of the instrument was also malfunctioning meaning the sample spin had to be set manually by altering drive and bearing pressure, and the resulting spin rate had to be estimated from spinning sidebands in the spectra. This was little more than an inconvenience, however, as the exact spin rates need not be known for the approach to be successful.

The last problem was that of temperature control: The gas flow provides sample cooling, and adjusting the flow parameters therefore had an influence on the cooling capability of the spectrometer. This resulted in a lot of work being done in order to find a combination of temperature and gas flow parameters that allowed the acquisition of non-spinning spectra without spinning sidebands, whilst still allowing a range of spin rates to be investigated without loss of temperature control. Eventually, the cooling capability deteriorated to a point at which the hydrate stability temperature could no longer be maintained, most likely attributed to a faulty connection between spectrometer and cooling air supply. Attempts to rectify were unsuccessful.

In order to probe the extent of sample deterioration, the experiment series was finalised by running a continuous acquisition of non-spinning ^{1}H, CMPG and inversion recovery experiments, as described previously, at 285 K. The results of this experiment series was compared with a series of non-spinning experiments performed at 270 K shortly after insertion. As the results are not viable for application towards understanding of the hydrate system, they are presented in Appendix E.

3.10.2 Summary

In conclusion, a range of problematic instrumental aspects led to the sample cooling chain being far from optimal leading up to the experiment series. Replacement of the sample with a new one not subjected to these conditions was considered because any eventual pre melting of the sample was expected leave the main experiment goal unobtainable. However, this was opted against due to risk management considerations: If the same problems re-emerged on introduction of a new sample, the secondary objective would also be in jeopardy due to time limitations.

3.11 B3Fb3 NOESY experiments

3.11.1 Sample information

The sample was prepared using the cold storage packing process, and was analysed directly after preparation. After weighing, the sample was introduced to a NMR tube containing a small amount of D_2O in order to ensure a deuterium lock, which both allows shimming the sample and prevents drift.

The rotor, contained within the tube, was then introduced to the AV 600 instrument, pre-cooled to a temperature of 279 K, a set temperature that was kept throughout the experiment series. The spectrometer temperature was found to oscillate within a range of 279.0 ± 0.5 K.

The main goal of the experiment series is to attain viable 2D NMR data through acquisition of NOESY spectra. A series of NOESY sequences was run with different mixing times, in an attempt to determine the optimum value of this parameter.

Application of water suppression was also attempted for one of the NOESY experiments. In addition, following the progress of the ^{1}H spectra taken between each NOESY experiment to verify sample integrity can also give valuable clues as to whether the freshly made sample behave differently to samples that have been in storage.

3.11.2 ^{1}H spectra

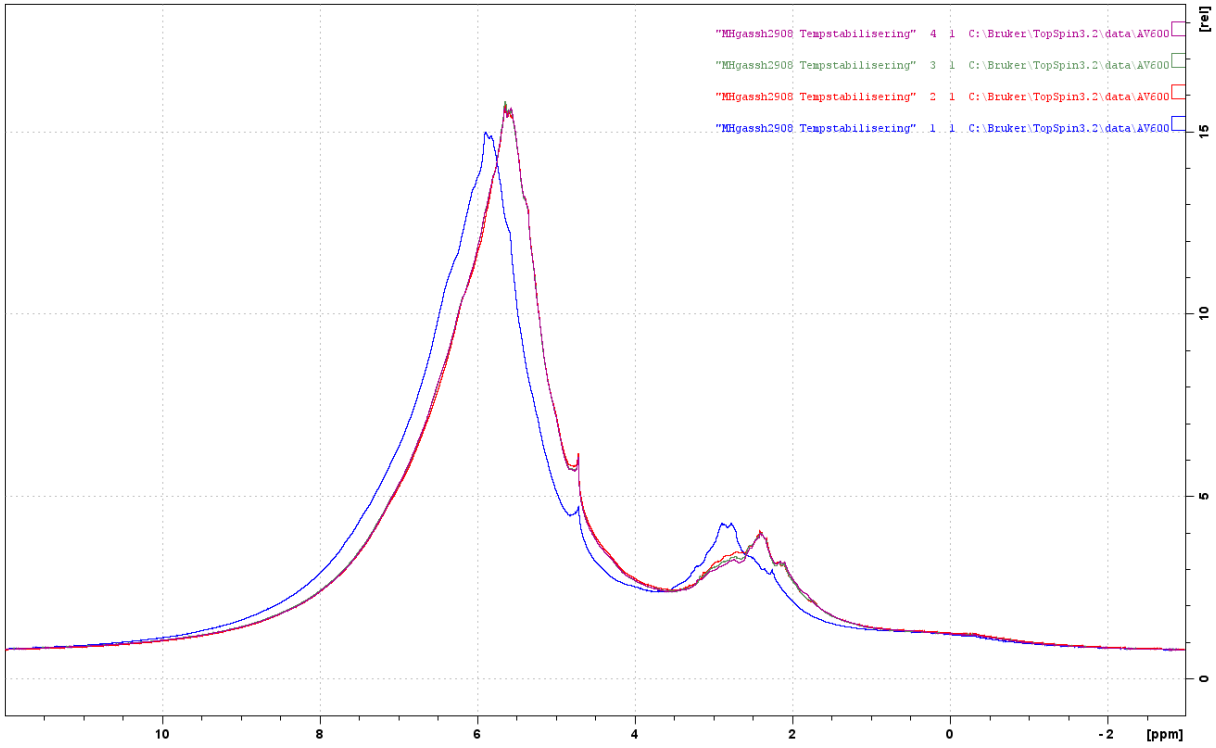

Figure 3.47: Before initiation of the B3Fb3 NOESY programs, sample stabilisation was verified by ^{1}H spectra. The first spectrum (blue) was not shimmed, instead the spectrum was immediately acquired in order to have an initial reference as close to insertion as possible. The four spectra spanned a time of approximately 35 minutes.

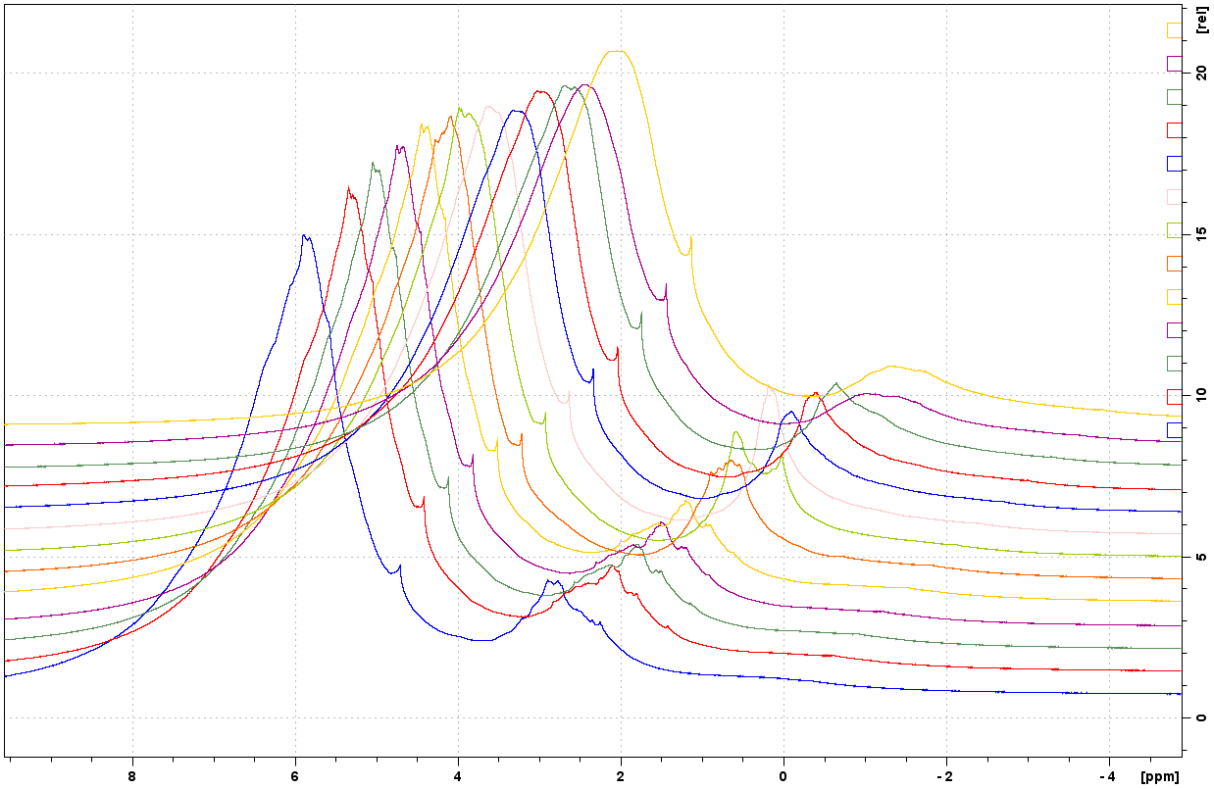

Figure 3.48: All ^{1}H spectra acquired between the 2D experiments on sample B3Fb3. As the runtime of the NOESY sequences is dependent on the variable parameter of interest, the spectra are not constantly spaced with respect to time. The entire timespan between the first (foremost) and last (rearmost) spectra is approximately 40 hours. The two last spectra cover a time of approximately three hours.

3.11.3 NOESY experiments

Several considerations were made regarding the order of the experiments. First, running the experiments in an arbitrary order minimises the risk of results being confounded with other processes that might take place in the sample. This risk is further reduced by running a duplicate experiment as number 3 and 6. However, the last of these had to be aborted early due to the end of the reserved NMR timeslot. Another factor is time management: As the value of the mixing time will have a major impact on the overall experiment time for a given sequence, experiments with different mixing times can be tailored to fit specific timeslots.

The 2D spectra and projections of individual experiments can found in Appendix E.

Table 3.7: The mixing times (d8) used during analysis of sample B3Fb3, and the order in which the corresponding experiments were run. Experiment 6 was halted due to end of the spectrometer timeslot. Resulting cross peak integrals from projections are also reported, relative to the water peak.

Experiment number	3	2	1	5	4	6
Mixing time (s)	0.1	0.3	0.5	1.0	1.5	0.1
Integral of cross peaks	0.0135	0.0112	0.0079	0.0061	0.0092	-

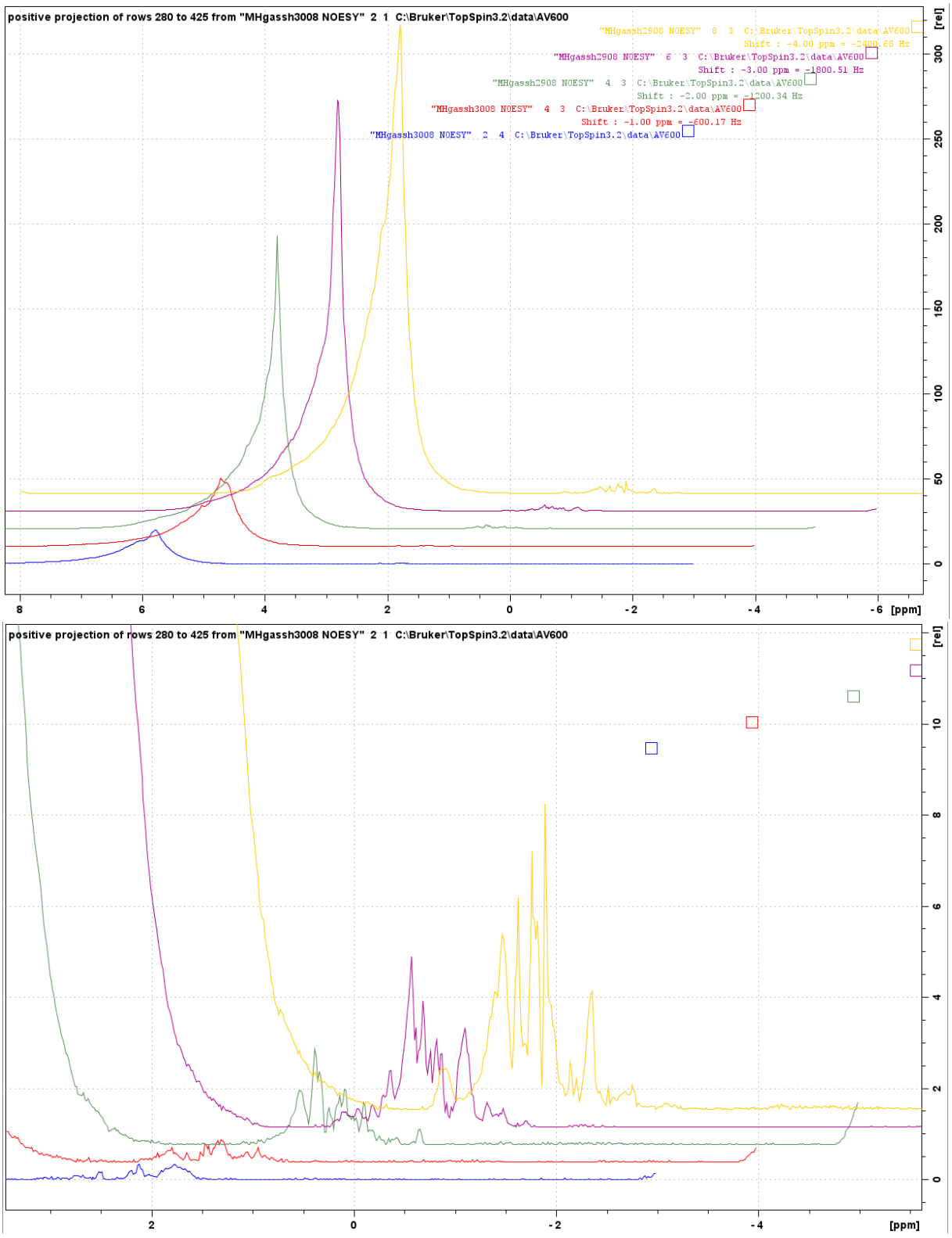

Figure 3.49: Projections of the cross peak areas for the NOESY experiments of sample B3Fb3. Top: both peak areas displayed. Bottom: Cross-peak areas displayed. The projections are sorted by decreasing mixing time from front to back.

Chapter 4 Discussion

4.1 Initial Results

4.1.1 Peak appearances

From the experiments performed on samples B2F and B2F2, shown in Figs. 3.2 and 3.3, a stable hydrate phase is seen to give rise to a broad, regular curve, in keeping with solid state NMR theory. Furthermore, the peaks are seen to rapidly transition in response to conditions outside the range of hydrate stability, although the results are neither conclusive nor equal between the two samples.

Upon closer inspection, the spectra also differed considerably between these samples. For instance, the water peak in B2F is much higher and sharper than that of B2F2, possibly corresponding to the presence of a significant amount of liquid water in the sample. The coexistence of hydrate particles and liquid water had been observed for cooler-stored bulk hydrate, and the growth of a water phase could also sometimes be observed while packing batch 2 hydrate samples. Also worth noting is the fact that the water peak is about half the height and far rounder in the next experiment in the series, acquired at 278 K. This seems to indicate that the hydrate phase was in transition even after 40 minutes within the hydrate stability region. The most reasonable explanation is that a melting process had started as a result of sub-optimal cooling conditions before introduction to the spectrometer, but not progressing so far as to be a major hindrance to reforming processes. Another fact suggesting at least partial melting can be seen in Fig. 3.6, showing that the water peak of B2F at 274 K is far higher than that of B2F2 outside of the hydrate stability range.

A more thorough analysis of the cyclopentane peaks of the two samples, the most important ones displayed in Fig. 3.5, also revealed similar differences. At 274 K, the cyclopentane peak of sample B2F seemed to consist of two separate components: One broad and partially obscured by the second, which was sharp considering the assumed solid state of the hydrates. As observed for the water peak, the sharp peak had undergone a change and was more rounded in the spectrum acquired at 278 K, now engulfing the entire broad peak seen earlier. Compared to the spectra of B2F2, the peaks of B2F show greater similarity to the peak acquired outside the region of hydrate stability than the round cyclopentane peak that dominated the entire hydrate stability temperature range during B2F2 experiments. In addition, the peaks of B2F changed instantly on introduction to 280 K, whilst the spectra of B2F2 remained near constant over a period of several hours at the same temperature, showing only a small, gradual change in the water peak before the temperature regulation failed. This lead to a rapid increase in water peak height and sharpness, whilst the cyclopentane peak decomposed into irregularity. The different response of the samples might also be due to real differences in temperature due to instrument accuracy and precision.

In spectra following the seeming transition from solid hydrates to liquid, the peaks were found to be not only sharp, but also irregular. This can be attributed to field inhomogeneity, created by the interaction of the applied field with local magnetic fields created for instance at phase boundaries. Such interphases is expected to be absent in the spectra of samples constituted only by solid hydrates, but would necessarily appear as the sample underwent melting. As the sample volume is small, interfaces in the sample would constitute a reasonably high fraction of this volume, possibly giving rise to peaks comparable in size to the main peak. This assumption is underpinned by the assumption that there will be considerable overlaps between the broad distributions of resonance

frequencies of molecules in remaining but diminishing solid hydrate peaks, and those established by magnetic fields created in the sample. This also means that the decomposition of the stable bulk hydrate peak cannot directly be equated to complete hydrate dissociation, again referring to the bulk hydrate sample seen to partially dissociate in refrigerator storage where visual observation showed the suspension of hydrate particles in liquid water. Such a system would also display inhomogeneity effects and reasonably sharp peaks, meaning that the spectra could well be showing such a system. If this is indeed the case, further distinctions exist as to whether the system is stable or dissociating, which depends on the thermodynamic state of the sample. Unfortunately, acquisitions to verify these assumptions were not made as the temperature rose, as effort was instead focussed on isolating and correcting

Although the results were interesting, these spectra served first and foremost as a reference for following experiments, and a discussion on the exact nature of a mixed water-hydrate system requires consideration of factors outside the scope of these preliminary experiments. Therefore, the conclusive arguments are as follows: Evidence of averaging molecular motions typical of liquids was found within the hydrate stability region for both the water and cyclopentane peaks of sample B2F, likely resulting from a melting process that was at least partially recoverable. Although both samples were subjected to what is believed to be equal handling, no similar evidence was found for sample B2F2 before the boundary of hydrate stability was crossed. Spectrum inhomogeneity effects were seen to manifest as the bulk hydrate phase underwent a transition, along with an expected increase of liquid character in the peaks.

4.1.2 Sample preparation and handling

The integrated spectra of selected samples from batch 1, 2 and 3, shown in Figs. 3.7, 3.8 and 3.9 give an estimate of the quality of samples from the different batches. Batch 1 samples had no utility besides use in preliminary experiments, as evidenced by the comparisons. Furthermore, the results show that samples of seemingly equal quality can be prepared using both batch 2 and 3 hydrates. What they fail to convey, however, is the difference in sample quality found by handling samples from the different batches. For instance, the batch 3 samples were prepared with little difficulty by the makeshift cold storage packing method, using a repaired packing rod of inferior quality. Packing the batch 2 samples provided a challenge, however, and was found to melt easily even though the use of the cooling cabinet method ensured that samples were packed well within the temperature range of hydrate stability. Some of this comes down to experience with the packing procedure, but the fact remains that successfully preparing batch 2 samples using the modified procedures would have been near impossible.

For the batch 2 hydrates, the packing procedure took a considerable amount of time. This issue was exacerbated by the fact that critical failures were a frequent phenomenon, prompting procedure restart. Furthermore, preparation of the easier-to-handle batch 3 hydrates coincided with failure of the cooling cabinet, meaning a new procedure had to be established and validated. As a result, samples had to be made at least a day before the NMR experiment as to not risk wasting NMR time attempting to produce samples. This mandated sample storage, and as such very little work have been done in order to probe sample properties following preparation. The ability to quickly pack samples under sub-optimal conditions have been proven for the given procedures, however, meaning samples can be prepared right before insertion to the spectrometer. However, the

consistency of results is still found to be lacking, attributable to the sub-optimal equipment available for temperature control and sample packing. Also, the work-up process for the hydrates has not been verified as optimal, and further improvements to the utilised methods might also yield improved results.

Preliminary results indicate that an extended period of time at low temperature is required in order for the sample to stabilise after preparation, an observation that should be verified. Furthermore, some evidence has been found that transitions take place upon introduction of freezer-stored hydrates to temperatures above the freezing point of water, possibly related to the ice-formation from melt-water after placement in freezer storage. The presence of ice does seem to be near unavoidable, however, as seen in the results found by Nelson et. al. These show that slowly crystallised cyclopentane hydrates contain nearly 50 % ice by mass, while rapid cooling leads to even higher contents of ice. As a result, the liquid nitrogen cooling made ubiquitous by the failure of the cooling cabinet must be considered to result in high quantities of ice formed from any eventual melt-water, and cooling should therefore be done so frequently as to never allow formation of a liquid phase as the transition might not be readily recoverable. The possible transition between ice and hydrate structures should also be subjected to further analysis.

The results in Table 3.1 show that a considerable decrease in mass was found for only one sample, which was after storage at room temperature. Another observation is that the weights at insertion were consistently higher than other measurements, and this is linked to the condensation of water vapour on cold samples coming directly from the freezer. As the primary objective during this phase is to keep the sample cold, this problem is hard to avoid, but a solution was attempted where the samples were shortly rolled on a paper towel using tweezers before weighing. This approach was used for samples B3Fa5, 6, 7 and 8 as well as B3Fb2, and was found to return hydrate masses much closer to those taken under other measurement conditions. However, only one of these samples ever displayed a spectrum corresponding to a stable solid hydrate phase, and the operation must be considered excessive. Two solutions to the problem are therefore proposed: The first is to not weigh samples before spectrometer insertion, as the information gained is not worth compromising the cooling chain integrity. The second is to weigh all samples at an ambient temperature within the hydrate stability range, allowing time to equilibrate before measurement.

4.1.3 Number of components in T_1 analysis

The results of the optimisation of T_1 can be found in Appendix C. The fitting curves of the T_1 inversion recovery data analyses were often found to be lacking, and in most cases were slightly worse for the 2-component approach. However, the three component analyses showed a greater propensity for overfitting: Often a reasonable fit would change little as the guesses were altered, whilst returning widely varying results. The first component results for both methods correlate reasonably well, even though the two component approach seems to fail towards the end of the experiment series. The second component of the three-component approach, however, seems to largely model noise, which might be connected to the seen overfitting. During the first half of the experiment series, the 3-component c3 and 2-component c2 seem to model the same information, and both seem to turn increasingly noisy as the experiment progresses. A conclusion is hard to draw, but good modelling practice dictates that the approach with the smallest number of components should be favoured. The two-component approach was therefore adopted.

Furthermore, only the first component of water seemed to return values of high enough consistency. Therefore, this is the only T_1 component discussed in this chapter. This might be connected to the sloping baseline in the spectra, leading to the analysis software attempting to fit inapplicable data to the fitting function.

4.1.4 Streamlining of T_2 analysis

The quick analysis using the *T2_tilpasning_serialProcessingRapid.m* script returned values near equal to the ones previously found, except for the three-component approach. These values were easily corrected using a new set of guesses. A near equal situation was encountered for the analysis of a new sample with no previous reference analysis: A single guessrange was sufficient for successful analysis of the one- and two-component data, whilst the three-component approach visibly failed. Again, this was easily corrected. Further analyses showed the method to be resistant to both overfitting and faulty guesses, even as the hydrate system underwent changes. The three-component approach frequently failed when the others did not, and the two-component method was therefore adopted for all experiments.

When it comes to script selection, the benefits and drawbacks of both are outlined in Appendix C, and the selection is largely situational. For large experiment series where continuous lines are formed by the data, the accelerated process of the *Rapid* version of the script is invaluable. It does, however, rely heavily on the ability to verify results by comparison with other values of the same series. The regular version has no drawbacks to the original version, and can thus safely be applied to any analysis where the original would have been used. It should preferentially be used when the data series is small.

4.2 Sample stabilisation

4.2.1 B2F6 – Changes in a freshly made sample

The B2F6 hydrate sample was prepared right before introduction to the spectrometer, and the initial acquisitions on the sample can therefore provide clues as to the changes within the sample shortly after packing. This was unfortunately done only as a last resort, because the samples originally made for the analysis proved to be of too low quality to warrant investigation, and the planned experiment series was not sufficiently modified to incorporate a proper analysis of this phenomenon. As a result, the information is confounded with the effects of changing temperature, at least initially. The timeframe of the experiment is neither long enough to report conclusive findings. The main goal of the experiment series might also have been affected if an underlying process was also on-going, although the results show that if that was the case, it progressed very slowly. The results obtained are nonetheless discussed.

The initial spectra are presented in Fig. 3.11, which shows that during the initial five minute period after insertion, the cyclopentane peak displayed considerable growth, while a low but seemingly very wide downfield peak disappeared. After increasing the temperature to 276 K and allowing the sample to reach thermal equilibrium, this peak was seen to decrease somewhat, although the intensity of the minimum between the cyclopentane and water peaks continued an upwards trend present for all four initial spectra. A decrease was also observed for the water peak, which also showed tentative evidence that a new water peak was forming up-field of the first. A large change

was observed for the final spectrum in the display, at a temperature of 275 K. The cyclopentane peak had broadened significantly, and was seemingly asymmetrical although obfuscation by the water peak precludes conclusion. This corresponded to an intensity loss, resulting in the cyclopentane peak being near invisible when the water peak was in view. At the same time, the water peak adopted a rounded shape downfield of the initial peaks, possibly completing the process seen happening in the previous spectrum. During this acquisition, the temperature was supposed to increase due to a temperature ramping program, but for unknown reasons no significant change was observed in the temperature before almost 60 minutes had passed, during which time the spectrum appearances remained near constant.

A definitive analysis of these results is difficult; the temperature range experienced by the sample should not result in sample changes. However, one or two processes might explain the behaviour, namely sample stabilisation following exposure to room temperature, and melting of eventual sample ice content. Evidence of the first process is seen in the initial spectra, and explains the dataset well if the spectra at 275 K represent the steady-state of the hydrate system. If this is the case, then the disappearance of the slight sharpness of the water peaks corresponds to re-integration of a small liquid water phase into the hydrate lattice. However, this should not give rise to the homogeneity effects observed for the sample. Cyclopentane hydrate formation has, however, been shown to progress slowly even with agitation, and the sample might be at a point where the diffusion-limited reforming process progresses extremely slowly, whilst small pockets of liquid in the sample gives rise to field inhomogeneity without being otherwise detectable. Another possible explanation is the presence of or boundaries within the hydrates themselves.

The same conclusion in many ways applies to the hypothesis pertaining presence of melted ice. The rounded peak shape suggests the sample integrity remained, and no major evidence of liquid character was found. As such, this hypothesis also requires that the melt water occupy pockets within an overall hydrate phase, establishing local magnetic field gradients without being identified as a liquid phase. A third possibility is that pockets of air exist in the sample, or a presence of paramagnetic contaminants.

Two T_2 experiments were performed early in the sample B2F6 experiment series, and can be found Appendix E. Comparison of these results show that at the moment of acquisition, the T_2 values of B2F6 correspond to what was found to be a transition area for other samples, on a slightly upwards trend. The dataset is too small for definitive conclusions to be drawn, especially pertaining to process direction. However, this information supports a notion that a stable hydrate phase was not present.

4.2.2 B3Fb3 – The stabilisation time of fresh samples

Like sample B2F6, B3Fb3 was analysed immediately after preparation, and the ^1H results of the experiment series can be applied to understanding the changes occurring in the sample following preparation. An overview of all these spectra is found in Fig. 3.48. Notice that there are some important differences between this and the B2F6 sample: First of all, the two samples were prepared from different batches, using different packing procedures. The samples were also analysed using different instruments, B2F6 using the AV500 MAS probe and B3Fb3 using an AV600 spectrometer fitted with a BBO probe. As part of the NOESY procedure, the sample B3Fb3 rotor was immersed in D_2O, meaning that if the rotor seal was not near perfect, liquid might have been introduced to the

sample. The sample temperature of was also kept at 279 K throughout the entire experiment, meaning the comparison of different spectra is not confounded by temperature effects. Finally, the B3Fb3 experiment spanned approximately 40 hours, compared to the approximate two and a half hours spent within the hydrate stability region for sample B2F6. This means that the time between each of the ^{1}H acquisitions before and after individual NOESY spectra for the B3Fb3 sample was longer than the entire relevant experiment time for sample B2F6. Because of its long timeframe, conclusions for this sample can be drawn with much greater certainty. Due to it being mainly a NOESY-experiment, it unfortunately lacks supporting T_1 and T_2 experiments.

The occurrence of some process throughout the spectra is evident. Initially, both the water and cyclopentane peaks are seen to display considerable liquid behaviour, while the peaks still remain wide and comparatively low. The water peak is steadily increasing, maintaining a few kinks that seem to indicate sample inhomogeneity. The cyclopentane peak area seems to be influence by the appearance of three to five main peaks. The first can be seen downfield of the main peak area, as merely a lump in the baseline with a small tip protruding from it. This peak is seen to initially shrink slightly, before widening considerably for the last experiment whilst returning to near initial intensity. A similar peak was seen for sample B2F6 as well, but this shrunk quickly following insertion and never recovered within the experiment timeframe. An underlying broad solid hydrate peak also seems to be present, but the irregularity of the peak area makes this hard to ascertain. A more intense, reasonably sharp peak seems to lie at the same shift as the broader variant, attributed to the presence of cyclopentane in a liquid phase. This peak is possibly flanked by two smaller but similar peaks both up- and downfield.

Notice, however, that this assignment of peaks is merely an attempt to simplify and systemise the analysis. Under the assumption of partial sample melting, the signal-containing parts of the spectrum is expected to contain a near-continuum of small peaks arising due to interaction of protons with local magnetic fields resulting from sample inhomogeneity. However, these peaks might also form distributions, giving rise to inhomogeneity regions of increased intensity. Explaining the occurrence of one such peak would then provide information on all other peaks resulting from various degrees of exposure to the effecting cause.

For the sixth experiment, the cyclopentane peak grows considerably, creating a plateau seemingly made up of four peaks at slightly differing chemical shifts, before splitting into two sharp peaks up- and downfield. For experiment eight, the downfield peak seems to have shifted upfield, merging with the other peak observed in the previous experiment and creating one large peak. This peak corresponds to the maximum intensity observed in this area for the entire experiment series. From there on in, the underlying solid hydrate peak seems to grow at the expense of the sharp liquid peak, yielding a smooth and broad solid hydrate peak for the two last experiments. These spectra seem to be a lot less affected by sample inhomogeneity and at this point, it is reasonable to assume that the hydrate system had achieved a stable steady state with any residual liquid in the sample below the limit required for affecting the spectra to any significant degree.

Notice that throughout the entire experiment, the water peak fine structure seems to approximate that of the cyclopentane peak, meaning both peaks may be influenced by the same inhomogeneity phenomenon. The sharp peak downfield of the water-peak might even correspond to the far downfield peak of cyclopentane, but this is tentative.

From the obtained results, an attempt is made to explain the shifting locations of the peaks. The five first spectra remained largely equal, with up- and downfield components centred round the liquid peak. This might for instance be attributed to cyclopentane molecules being distributed over a concentration gradient across a liquid-liquid water-cyclopentane interphase, or residing in pockets of liquid with varying concentrations. If an interface is present, hydrate particles is also expected to reside at this interface giving rise to complex boundaries that might explain the fact that side peaks are observed both up- and downfield. The sixth peak is a special case. Here, four peaks of near equal intensity are observed with severe overlap. The three side peaks all seem to be located downfield of the main peak, and an intensity decrease is seen in the entire upfield region, ending at the water peak. At the same time, a small new peak is observed in the upfield water region of the spectrum. This might indicate that a physical equilibrium is establishing, for instance placing the two components either side of an interface. The results of spectrum seven seem to support this conclusion, as the upfield water peak component grows while the downfield cyclopentane components coalesce into one comparatively large peak even further downfield of the main peak. At this point, it is hypothesised that the cyclopentane molecules resided in a quasi-liquid water layer at the surface of the hydrates, and that the plateau in experiment six results from an interaction of cyclopentane with this layer. Such a quasi-liquid layer was found by Dec to be capable of dissolving ethane and methane as well as accelerating the hydrate formation from these, and can explain the results of the following spectra. In the next experiment, the water and cyclopentane side peaks both collapse into their main peaks, and the following experiments show the cyclopentane becomes broader and less intense for every experiment, losing its liquid character and eventually stabilising as the stable state is achieved.

If the proposed dissolution of cyclopentane into such a quasi-liquid layer is indeed true, this might well be the limiting step for growth of cyclopentane hydrate. However, this is mainly conjecture on the part of the author, and should be verified. A simpler explanation is that the formation of hydrates progress continuously, but is obscured by unrelated physical-chemical changes in the sample.

The definitive results are significant in several respects. From a technical point of view, the absence of field inhomogeneity effects in the final B3Fb3 spectra proves that liquid D_2O either did not contaminate the sample, or that it was incorporated in the solid phase. It therefore shows that rotor immersion in deuterium oxide is a viable method for preventing instrument drift. A timeframe of over 37 hours for the stabilisation of freshly packed samples is also established at 279 K, which is too long to warrant their application for anything but experiments to further probe this stabilisation process. This might be alleviated, however, if the process is faster at lower temperatures. Furthermore, it shows that an unstable hydrate phase can be recoverable, yielding results that indicate that the sample in its final state was of no lesser quality than ones stored at freezer temperatures. However, it also carries the implication that freezer storage might be best avoided, especially during the first days following sample preparation. The reasoning for this is simple: Liquid components were found to be present in the sample following insertion, and at sub-zero temperatures liquid water might also form ice. The ability of regenerating the hydrate phase completely has been demonstrated at 279 K, and temperatures in the 274-279 K range should therefore be utilised instead. The results of other samples prove that freezer storage is not preclusive to attaining samples of sufficient quality, but it might nonetheless explain the failure of some samples.

4.3 B2F6 – False flags for solid hydrates

The evolution of sample B2F6 before the melting point of the hydrates was passed was discussed in the previous subchapter. As the boundary of thermodynamic stability was crossed, the sample was found to exhibit properties indicating it was arrested in a physical-chemical state intermediate between a solid hydrate system and a melted sample. The hydrate melting point was initially crossed when the instrument temperature spiked to 281 K before rapidly falling to 278.5 K, from where it initiated the temperature ramp programmed to start an hour earlier, as can be seen in Fig. 3.12. This issue was attributed to instrument error. The temperature spike corresponded to a change in both the water and cyclopentane peaks, shown in Figs. 3.13 and 3.14. The main cyclopentane peak grew to a maximum before falling to a lower than initial intensity, seemingly due to the growth of a broad downfield peak. This indicates a removal of cyclopentane from the vicinity of water, but the peak broadness also suggests that the majority of cyclopentane molecules resided in a solid phase. The peak is however not consistent with the expected chemical shift for a hydrate phase, and bears a strong resemblance to the final spectrum acquired after an hour at 285 K, outside the hydrate stability range. Concurrent with the change in the cyclopentane peak, the water peak suddenly rose in intensity, seemingly forming two sharper peaks that were barely resolved near maximum height. The two sharp water peaks might then represent the liquid water phase, one in bulk and the other influenced by local magnetic fields at a water-hydrate interface. These peaks collapse into one around experiment 100, possibly corresponding to the disappearance of the remnant hydrate phase.

One potential explanation for the broad distribution of cyclopentane signals is the size of the cyclopentane bulk phase. It might be small enough as to place the entire bulk sample within the reach of the interface field inhomogeneity effect. Interface curvature by capillary forces could also contribute, as the angle of the interface to the external magnetic field would then continuously change over the coordinates perpendicular to the magnetic field. As the water content of the sample is much higher than that of cyclopentane, this assumption is reasonable. It is therefore concluded that the cyclopentane peak shape alone is a poor marker of hydrate stability. Instead, a rounded cyclopentane peak should be attributed to a solid phase in conjunction with its size relative to the water peak as well as the identification of solid state patterning in the water peak. Helpful for the latter is the identification of the very wide water ice peak seemingly present in stable hydrate spectra as a sloping baseline. However, the main objective of the experiment series was to attain information on the appearance and temperature of changes to the hydrate phase. The information attained is unfortunately marred by too much uncertainty, and the main goal was not attained due to both low sample quality and erratic temperature control.

4.4 B2F7 – Appearance of a melted sample

B2F7 was found to have melted before introduction to the spectrometer as seen from the results in Fig. 3.17, and no change in the hydrate region could be seen during attempts to reform. However, the results in Fig 3.16 provide verification of the hypothesis stated for sample B2F6: A small, liquid cyclopentane phase seems to give rise to a broad distribution approximating that of solids when analysed at the magic angle. This is probably linked to angular interactions between interfaces in the sample and the external magnetic field, and the gradual decrease in the sharp cyclopentane peak might be due to a physical-chemical equilibrium re-establishing after being subjected to freezer

temperatures, room temperature and 274 K in rapid succession, in addition to the mechanical agitation that comes with transport. The results therefore provide a good reference to the approach to hydrate verification outlined earlier, as none are fulfilled in this case. The T_2 results are also included in Fig 3.18, and with the exception of two outliers these stay high throughout the experiment. Also note that the T_2 value lie close to the values expected for water at these temperatures. The T_2 values were found to be much lower in samples where the presence a solid hydrate phase is confirmed, reaching the values seen for this sample through a transition area when subjected to higher temperatures. As a result, T_2 measurements can serve as a rapid verification of sample state.

4.5 B3Fa – Evidence of a partially dicossiated hydrate

Whether or not the B3Fa sample had already melted before spectrometer insertion is hard to ascertain, as seen in the results in Fig. 3.19. The initial spectrum shows that a comparatively large cyclopentane peak is seen at a chemical shift corresponding to solid hydrates, although it does not display the expected round peak. Furthermore, the water peak shows no liquid character. However, the spectra rapidly deteriorated for the following acquisitions; the water peaks is seen to grow in experiment 4, and all water peaks following the first display field inhomogeneity effects. However, the peak is still not so intense as to completely dwarf the cyclopentane area. Such effects are also seen for the cyclopentane peak in all spectra of the sample, and the broad downfield peak of liquid cyclopentane can be seen to appear. Furthermore, the baseline slope seems to decrease, indicating that the wide ice peak has disappeared or shrunk considerably. However, there still seems to be an appreciable intensity at the solid hydrate peak area and, along with the moderately round water peak, it is hypothesised that this series correspond to a partially dissociated hydrate system with high liquid water content.

The spectra appeared to undergo a considerable change approximately halfway into the temperature increase, shown in Fig. 3.21. First, the cyclopentane main peak was found to grow, along with the broad downfield peak observed for earlier experiments. Shortly after, the water peak was found to broaden, exhibiting major signs of sample inhomogeneity. At this point, the system might well have been dominated by a wealth of differing magnetic environments, although several different causes may be proposed to explain this. For instance, the sample might be made up by an aqueous dispersion of rapidly dissociating hydrate particles, and the catastrophic failure of a solid hydrate phase could explain the rapid change seen for one of the water peaks in the series. Another explanation is that the hydrates have all dissociated at this point, and that the inhomogeneity is due to a dispersion of cyclopentane droplets coalescing into a bulk phase, which might explain the visible increase in the downfield cyclopentane peak towards the end of the series. Also, a combination of these effects might be taking place.

To verify the results, attention is turned to T_1 and T_2 measurements. For the water T_2, shown in Fig. 3.26, the first value is found to be much lower than the rest. This indicates that the experiment was performed during a period of rapid sample change. The second component, expected to correlate to cyclopentane, also rapidly increases during this time. Leading up to the 278 – 285 K ramping program, however, the water values are seen to slowly decrease, independent of temperature. This might indicate that hydrates were reforming in the system or that phase equilibrium was establishing, due to the implication of exchange processes from the negative slope. However, the

change seems somewhat independent of temperature, and might be due to the growth of interfaces leading to progressively faster relaxation processes. The first and second T_1 measurements, acquired over the 20 minutes following the T_2 measurements and displayed in Fig. 3.23, show a similar transition. These values also seem to slightly decrease over time, but increase with temperature.

After the sample had been subjected to 285 K for an extended time, the T_1 values were found to be considerably lower than before. For the T_2 results, the water component result rose for the one experiment at 285 K, before it returned to a level comparable to that which was seen earlier. The cyclopentane T_2 value curve also went through a discontinuity, lying higher than before the temperature change. Note that this discontinuity is caused by the absence of regular T_1 and T_2 measurements at 285 K, the one measurement of each taken right before again lowering temperature. The T_2 values across this period are consistent with the expected results, with temperature effects explaining the seemingly outlying value at 285 K, as well as the following decrease. The increase in cyclopentane T_2 values most likely correspond to a change in the chemical environment of cyclopentane, either through melting of residual hydrates or diffusion into an non-polar phase, possibly both.

After reaching 274 K, the water components of both T_1 and T_2 started rising, whilst the cyclopentane T_2 values fell. This might be explained by the exothermic behaviour of hydrate formation: The heat of formation would then lead to an increase in the relaxation times of excess water due to a sample temperature increase, an increase offset for cyclopentane by the inclusion in mobility-restricting cavities. It would also explain the levelling out of the increase over time, as hydrates growing on a water-cyclopentane interface would eventually slow down the transition rate, reducing the temperature increase. Such a temperature transition would not necessarily result in a changing temperature reading in the spectrometer, as cooling of the probe space where the sample resides is much more effective than the cooling of the sample itself. A dynamic thermal equilibrium between the coolant flow and heat of formation is therefore not unthinkable, but this should be reflected in compensation in heater output power on the part of the spectrometer. This variable was unfortunately not logged for this part of the experiment, precluding a conclusion. More likely is the physical-chemical equilibration of the system leading to less interaction with interfaces: Spectra of other samples show that changes in the peaks still occur after several of hours at temperatures above the range of hydrate stability, precluding nearly all causes except such equilibration.

As data is lacking for one of the transition ranges in this experiment, no attempt to further analyse the relaxation results is made. The ^{1}H results for the ramp program and 274 K reformation experiments can be found in Appendix E, and show that formation of a broad downfield cyclopentane peak, as seen in previous experiments, takes place at high temperature. These changes are then somewhat reversed during the period at 274 K, along with the growth of a small cyclopentane peak at approximately 2 ppm, corresponding to cyclopentane in close proximity to water. It may, however, be too sharp to correspond to solid cyclopentane hydrates. Another peak grows out of the downfield one. The water peak loses intensity at the lower temperature as well, and eventual temperature dependent shifts in position cannot be seen due to overall peak change. However, as the cyclopentane peak is too sharp to be readily attributed to hydrate growth, no conclusions are drawn from the experiment series.

For the freezer storage experiments, found in Appendix E, the only discernable change takes place in the water peak, presumably due to melting of some solid ice/hydrate mixture remaining after spectrometer insertion. The cyclopentane peak area bears some resemblance to the initial spectra of the sample during the first experiment series, leading to an assumption that the sample might have melted beyond a readily recoverable state even before initial storage. The relaxation times following initial insertion are also similar, but the sudden increase seen for the first series is not observed here. This might mean that the reformed sample rotor cooling chain was better maintained, although no specific difference in procedure was utilised. Instead, an upwards trend is observed, consistent with the temperature increase and observed melting.

From the results in Table 3.2 and 3.3, the activation energies are seen to be positive for all transition ranges at differing temperatures for all components from one- and two-component analyses, corresponding to domination of the rotational correlation time on both T_1 and T_2 relaxation. However, the two techniques do not seem to be in agreement for the freezer reformation experiment. As the temperature was not sufficiently changed for some of the other transitions discussed above, their temperature dependence is not discussed.

4.6 B3Fb – The region of bulk hydrate stability

As the results in Appendix E show, little change occurs for the sample throughout the period it was held at 280.5 K and below, which is right at the edge of the hydrate stability range. Fig. 3.30 shows that although the line shapes are nearly equal throughout the hydrate stability range, the intensities are not. These intensities seem to show some temperature dependence, and cannot directly be equated to sample changes. However, the observed increase in both the water and cyclopentane peak seems to correspond to a decrease in the underlying ice-like peak. This might indicate that the peak corresponds to water ice, and that the water trapped in this ice is incorporated into the hydrate structure at temperatures above the freezing point of water, but below the melting point of hydrates. If this is indeed true, then freezer storage might be inadvisable for cyclopentane hydrates. However, the change in the water also peak seems to be localised to a certain point in the ramp program, and the underlying broad peak initially seemed to grow. This indicates that the observed change is neither due to sample temperature or a slowly progressing establishment of a new thermal equilibrium, but a sudden transition upon reaching a specific temperature. The spectra also show that the studied sample is solid, meaning that any eventual change in the hydrate phase under freezer storage will only pertain to unfilled hydrate cages, or that liquid created remain undetectable.

Even if the observed change is in fact due to a transition between ice and hydrates, it doesn't necessarily mean that freezer storage causes conversion of gas hydrate into ice. Instead, the observed effect might be kinetic in nature, the reasoning for which is as follows: During sample preparation and transport the hydrate phase is expected to dissociate to a small degree, especially considering the sub-optimal conditions under which batch 3 hydrates were packed. This means that when the sample is placed at freezer temperatures, ice and hydrate will likely form concurrently from the excess liquid. The stability of both solid phases means little transition between them is likely to occur, albeit this requires further study in order to ascertain.

The T_2 data obtained in this range, shown in Figs. 3.32 and 3.33, is interesting. Initially, both the two-component c1 and c2 T_2 values show a decrease with increasing temperature, consistent with the

domination of the relaxation time by transfer processes. This can be explained by hydrates reforming from a small liquid phase created during exposure of the sample to room temperature during sample weighing and introduction to the spectrometer. The slope for this region is highly uncertain due to the small number of data points, but the process seems to be finalised within an hour. The T_2 values then increase linearly with temperature until the maximum temperature is reached. The T_2 values then slowly increase as a function of time, indicating that the sample is undergoing a change resulting in greater mobility for both c1 and c2. This might constitute a slow dissociation of the hydrate phase, as the boundary of hydrate stability lies within the accuracy range of the instrument. If that is the case, it progresses very slowly. In the same timeframe, no liquid character can be inferred from the ^{1}H spectra. Also interesting is the deterioration of the broad peak characteristic of ice during this period, which might correspond to an ice-hydrate transition or a selective pre-melting mechanism that influences both water and cyclopentane relaxation times in the hydrate lattice.

The results of the second series of experiments on the sample can be found in Appendix E. The ^{1}H spectra showed no change except temperature dependent changes in shift for the water peak. The cyclopentane peak area seemed to be chaotic, indicating interfacial systems in the sample. The T_2 values increased linearly with temperature, as expected for a system at equilibrium. However, the T_2 values were lower than expected, which is attributed to the presence of interfaces in the sample. The conclusions drawn from the second set of experiments are as follows: No semblance to the spectra from the first series was found, providing validation for the first series. Also, no evidence of hydrate formation was observed within the four hours spent by the sample in the temperature region of hydrate stability.

4.7 B3Fc – T_2 as a marker for hydrate formation

A spectrum of B3Fc shortly after insertion is compared with a corresponding sample for a sample with the confirmed presence of hydrates in Fig. 3.34, showing clearly that the sample was not made up by a single, stable bulk hydrate phase. Otherwise, the ^{1}H spectra leading up to the temperature ramping program were hard to interpret, owing most likely to macroscopic sample inhomogeneity. The ^{1}H results are provided in Appendix E. The T_2 measurements, however, yielded interesting results, displayed in Figs. 3.35 and 3.36. Between the first and second measurements, the T_2 relaxation time is seen to increase rapidly for component 1, probably corresponding to the finalisation of a melting process initialised following removal from the freezer. For the following experiments however, the T_2 values show a relatively rapid, near linear decrease with increasing temperature, indicating that the relaxation processes were dominated by exchange phenomenon. As the sample temperature reached 280.5 K, this decrease was arrested, indicating that the observed decrease was due to hydrate reformation. Instead, it was replaced with a slow increase with time, closely mirroring that seen for sample B3Fb at the same temperature. Over the course of the 280.5 K temperature experiments, spanning nearly 21 hours, the T_2 values never again reached their maximum values. This indicates that complete hydrate dissociation never occurred. Furthermore, the following decrease in temperature resulted in a rapid increase in T_2 being observed, which leads to the assumption that exchange processes again became the major relaxation mechanism. Due to the causal link with the hydrate formation temperature, it is reasonable to conclude that the areas of inverse proportionality between T_2 and temperature correspond to areas of hydrate formation.

Further verification can be found in the ^{1}H spectra acquired during and after the period at 280.5 K, also provided in Appendix E. For the experiments at 280.5 K, a clear trend is present where the relative intensities of the up- and downfield cyclopentane peaks shift in favour of the latter, and the inverse is true for the experiments performed as the temperature was decreased well into the range of hydrate stability. In accordance with the criteria laid out earlier for hydrate-containing versus hydrate non-containing samples, this also provides evidence of an on-going hydrate formation process in the sample. Due to the persistent complex nature of the ^{1}H spectra and sharpness of the water peak, any reformation process is expected to have taken place by the growth of hydrate particles dispersed in an aqueous phase. Apart from inferences from the changes observed within the experiment timeframe, no real conclusions can be drawn as to the timescale required for full recovery of the hydrate bulk phase, or whether full recovery is indeed possible without further sample agitation.

If the conclusions drawn from the results are correct, the experiment series establishes T_2 measurements by the CMPG one-shot technique as a quick and powerful tool for identifying on-going formation or dissociation of cyclopentane hydrates in heterogeneous systems without the use of isotope-exchanged compounds.

4.8 B3Fa2 – Transitions of the hydrate system

4.8.1 Observations at 272-279 K

The initial spectra after sample insertion can be seen in Fig. 3.37. The reformation and stabilisation of a stable hydrate bulk phase is evident. During the following temperature ramping program, shown in Fig. 3.38, a near-linear increase in cyclopentane peak intensity with temperature is seen over the area of temperature increase when factoring in thermal equilibration time. Such increases are also seen for the other temperature transitions investigated, presented in Appendix E, albeit no other changes seem to be occurring.

The T_1 relaxation times found for the first component of water, presented in Fig. 3.42, at first glance seems to model noise. On closer inspection, however, there seems to be two trends present leading up to the 279-280.5 K temperature transition, namely that the results increase with time and decrease with temperature. This might indicate that exchange processes leading to greater mobility of the water in the sample is on-going. Alternately, an on-going exchange process might be causing the inverse correlation with temperature, with the results obscured by poor experimental precision. This might be correlated with the increasing peak intensities in the spectra, but the results are inconclusive.

The T_1 results are not supported by the T_2 measurements in Fig. 3.43, which show only a small increase at far lower relaxation times, most likely due to the increase in temperature to over the freezing point of water. This also indicate that the introduction to above-zero temperatures leads to a slight change in the mobility of water from structural changes, as the increase in T_2 extends far beyond the time believed necessary for the sample to reach thermal equilibrium before stabilising. Because of the near non-existent spread in results, the T_2 values are deemed a much more reliable source of information on the sample than the T_1 technique, and no further attempt will be made to explain the results of the latter.

The T_2 results also show that starting at the temperature increase to 276 K, and further accelerating upon following increases, the relaxation times of both components go through a comparatively rapid transition to higher relaxation times. Due to the long time spent by this sample at 272 K and 274 K, and the observed stability of the T_2 values at the latter temperature, this series of experiments should provide a much better estimate of the temperature dependence of the spin-spin relaxation time than that observed for other samples. The apparent absence of major sample inhomogeneity inferred by the stability of the hydrate phase also contribute to the perceived quality of these results, although a greater number of measurements should probably have been performed at these temperatures as the spread in results is hard to gauge for this range. For more accurate determination, the T_2 values should be allowed to stabilise at every probed temperature as to ensure the results are not confounded by sample changes.

Also note that the apparent temperature dependence of T_2 differs greatly between the 272-274 K and 274-279 K ranges. This might be due to the hydrate lattice being much less susceptible to temperature-induced molecular movement at these lower temperatures, but can also be caused by the presence of exchange-processes that display the opposite temperature dependence. The latter seems to be supported by the linear regression lines in Figs. 3.44 and 3.45, where an inverse temperature dependence seems to be present leading up to 274 K, followed by a transition to higher values due to a change in molecular mobility as the temperature stabilises. If these mechanisms operate on the same timescales, the results of both will be confounded with the other, and the value obtained from regression analysis should not be considered accurate.

4.8.2 Observations at 279 K and above

The spectra taken during and after the 279-280.5K temperature ramping program are shown in Fig. 3.39, which displays the bulk hydrates rapidly deteriorating into an inhomogeneous system shortly after initiation. This seems to support the earlier assumption that setting the spectrometer temperature to 280.5 K might place the actual temperature either side of the boundary of hydrate stability due to instrument accuracy. As the spectra immediately following the transition must represent a rapidly changing and complex system of interfaces and concentration gradients, no attempt is made to provide a closer explanation. However, both peaks do seem to stabilise somewhat over the course of the program.

These spectra should be considered to represent a metastable state of the system, however, given the rapid change that occurs towards the end of the experiment series. This change is sudden and most visible for the water peak, displayed more clearly in Fig. 3.40. The change occurs between two spectra, meaning it takes place within a five-minute period. The effect seems to be the downfield shift of the major water component in the sample, with a broad distribution of similar-height peaks upfield of it. However, these spectra do not seem to correspond to the final state of the system either, as evidenced by the last spectrum acquired at 280.5 K shown in Fig. 3.41. This spectrum was acquired nine hours after the appearance of the peaks mentioned above, and shows the water peak split into three major components of unequal size, broadened to the extent where the resolution between the cyclopentane and water peaks is nearly non-existent. The remaining ^{1}H experiments of the series can be found in Appendix E. Further analysis at 280.5 K seemed to yield no change, but raising the temperature to 282 K led to the disappearance of the downfield water peak. Furthermore, the broad downfield cyclopentane peak was seen to grow at the cost of further intensity loss for the

upfield component. No change was observed upon lowering the temperature to 274 K. However, this seems to indicate that even after more than half a day outside the range of hydrate stability, no chemical-physical equilibrium was achieved.

The size and location of the peaks in these spectra might give clues as to the final numbers and distributions of interfaces in the sample, as well as possibly concentration-based inhomogeneity for the metastable peaks. However, the exact nature of these arises due to complex interactions between the spectrometer field, sample inhomogeneity and magnetic susceptibilities of the different phases, further complicated by the angled sample in relation to the field. It is therefore sufficient to state that final chemical-physical equilibrium seems to be very slow to establish, and that it in its seemingly final state has two major distinct water environments and two main cyclopentane environments, although this might also change given even longer time to equilibrate.

The T_1 values obtained after the temperature was raised beyond 279 K is also shown in Fig. 3.42. However, these results were already deemed inaccurate for the low-temperature region, and the analysis quality only deteriorates in the face of a more complex sample. As a result, it is concluded that these results have little applicability to the system, and that the technique needs improvement in order to be useful for the analysis of cyclopentane hydrates.

The T_2 results presented in Figs.3.43 and3.44, however, does not seem to contain any major deviations during these experiments. Furthermore, the linear regression analysis provided in Table 3.6 yields rotational activation energies similar to those found for tetrahydrofuran hydrates by Gao et. al. This is reasonable, given the similar size of these guest molecules. These correspond poorly with the similar results from T_1 measurements, provided in Table 3.5. Furthermore, the values found after melting of the hydrates lie consistently higher than that observed for stable hydrates, although the sample size is small. In conclusion, the results of this experiment provide further evidence of the ability of the CMPG technique to quickly provide reliable information on these hydrate systems even under conditions of rapid change.

4.9 B3Fb2 – Validation of observed melting behaviour

A selection of ^{1}H results for sample B3Fb2 are shown in Fig. 3.46, and show an initial spectrum indicating that the hydrates had already melted due to the sharp water and cyclopentane peaks. The figure also shows a final spectrum, taken up 21 hours after insertion. Comparing this spectrum with the final one acquired for sample B3Fa2 in Fig. 3.41 show that they share the same shape, providing evidence that this line shape seemingly corresponds to a relatively stable configuration of the system and not a random distribution of interfaces. The remaining spectra of the experiment series show a system either dissociating or attaining phase equilibrium from an unknown starting point, and are not discussed further.

4.10 B3Fb3 - NOESY

As the ^{1}H spectra of sample B3Fb3 was detailed in a previous subchapter, they will not be discussed here. It is sufficient to note that the ^{1}H spectra were continuously changing through the NOESY-experiments, resulting in only the last full NOESY experiment of the series being performed on stable

hydrates, as seen in Fig. 3.48. Because of these sample changes no quantitative explanations of the results are attempted, but this was never the main goal of the experiment series.

Fig. 3.49 show the results of the last and successful series of NOESY experiments, whilst the entire spectra can be seen in Appendix E. A response is clearly seen in the cross peak area, but this is not clear-cut as the peaks sign seems to oscillate in the full spectra. Furthermore, the integrated values, found in Tab. 3.7 is hard to interpret. The maximum value is found at a mixing time of 0.1 s, but the 1.5 s mixing time experiment constitutes an outlier in an otherwise linear decrease with increasing mixing time. This might be attributed to the fact that the sample was undergoing change, as the water peaks in the projections are widely dissimilar. Also, NOESY experiments are very sensitive to paramagnetic contamination and sample oxygen should therefore be removed by a freeze-pump-thaw cycle for future experiments, although the technical implementation of this is not unproblematic. The conclusion is that the method needs not necessarily be discarded, but has neither been validated.

Chapter 5 Conclusions

Procedures for rapidly packing hydrate samples even while lacking dedicated equipment have been established and validated. However, the ability to maintain a sufficient cooling chain leading up to spectrometer insertion is still lacking. This is pinpointed to two causes: The ambient conditions lying outside the thermodynamic stability range for the hydrates under sample preparation, and unnecessary exposure to room temperature during weighing before spectrometer insertion. Another possible cause is that freezer storage converts a melt-water phase to ice instead of hydrates, yielding a hydrate sample with less analyte and greater susceptibility to melting, an argument that also applies to the usage of liquid nitrogen as a coolant.

Identification of samples as stable is done using a set of criteria from the initial spectra: A broad, rounded water peak is present, along with a similar cyclopentane peak at a shift of around 2 ppm that is readily visible even when the entire water peak is in view. Furthermore, a very broad ice-like peak should be present, manifesting as a sloping baseline. T_2 relaxation times should be low, with component 1 at approximately 200 ms and component 2 at approximately 30 ms. Whether a partially melted sample is recoverable within a viable timeframe should in most cases be evident from the progression of its initial spectra, but more research should be done into the time required for this transition, as well as identifying the point where a sample should be abandoned.

Evidence has been found that newly packed hydrate samples require nearly 40 hours to stabilise into a pure bulk phase at 279 K, and that most freezer-stored samples also require several hours at temperatures within the temperature region of hydrate stability in order to reform after transport, weighing and insertion to the spectrometer.

Increasing the centrifugation time during hydrate workup yielded hydrates of much higher quality, but the effects of even further centrifugation has not been examined.

The melting of samples seems to be followed by a very long period of interface equilibration, where several intermediary stages also seem to be present.

The CMPG oneshot technique used to find T_2 values seems to be a quick, accurate, sensitive and robust tool for probing sample state, with evidence indicating its utility in identifying structural transitions as well as exchange processes not immediately evident from ^1H spectra. Although the experiments in this thesis must be considered qualitative, this technique should also be applicable to a quantitative study of exchange processes, molecular mobility and pore size determination. Work has also been done to expedite the analysis of these results.

The inversion recovery T_1 experiments performed were found lacking, as the results were marred by high spread and poor fit to experimental data, with applicable results attained only sporadically for the first component of water.

An attempt has been made to perform two-dimensional NOESY experiments on the sample, but results remain inconclusive. Issues pertaining to instrument drift have been solved, however, and the experiment could possibly be made to work using a stable sample that has been subjected to removal of paramagnetic contaminants.

Chapter 6 Recommendations for further work

A proper cooling chain, from sample preparation until spectrometer insertion, must be established. This is probably only possible by moving the packing procedure back to ambient temperatures within cyclopentane thermodynamic stability. Given the appropriate equipment, this can be accomplished by using the original packing procedure. If such a set-up is unavailable, packing should be performed in a cooling room at sufficiently low temperatures. The weighing operation before spectrometer insertion should be performed at low temperatures, or discarded altogether, and the same applies to a lesser degree to weighing after sample preparation. Furthermore, the hydrates should be stored at temperatures right above 0^oC, and improved centrifugation of the hydrates might also yield improved resistance to melting.

The removal of O_2 seems not to be critical for the T_2 experiments, but might explain why the NOESY results were inconclusive. As the preparation of cyclopentane mandates thorough mixing, the only solution for achieving better O_2 removal using a variant of the current procedure is to place the hydrate reactor under an inert atmosphere, and using water and cyclopentane separately subjected to freeze-pump-thaw cycles as reagents. This would most likely require moving the entire reactor system into a glove-box. Another possibility might be to mix the purified reagents in a sealed container, letting the transition reach equilibrium through a prolonged period of time at sufficiently low temperatures as seen for different hydrate formers in other studies, although the feasibility of this has not been explored in any depth.

The MAS NMR experiments failed for the attempt in this thesis, although this is linked mainly to compounded instrument failures. The fact remains that the technique would be a valuable asset in determining relative peak intensities due to the improved resolution inherent to the technique, as well as possibly aiding the identification of other, smaller peaks obscured by the broader ones.

The two-dimensional approach remains largely unexplored, but could possibly be utilised to determine for instance the internuclear distances in the hydrates. 2D techniques other than NOESY might also hold greater promise, but has not been covered in the thesis work. ^{13}C NMR has neither

been explored, further than verifying that spectrum acquisition is possible within viable timeframes. Applying the CMPG oneshot technique to quantitative analysis of the hydrate system seems especially promising, whilst the inverse recovery experiment needs considerable improvement in order to be viable.

Appendix A: Data analysis software

Excel

Microsoft Excel was used to plot the T_1 and T_2 results. The spectrometer temperature was continuously measured and logged at one-minute intervals, and this allowed the results acquired during changing temperature conditions to be plotted against actual temperature measurements, as well as a way of verifying temperature stability without continuous observation. However, for the majority of the experiments the spectrometer temperature remained stable enough that the use of target temperature was sufficient to plot the data without loss of accuracy.

For experiments performed under changing temperatures, the time of acquisition was cross-referenced with the times of temperature measurements in the temperature log from the spectrometer. In order to facilitate this work, an INDEX-MATCH Excel function was written, which searches for and returns the temperature measurement closest in time to the time of acquisition.

The INDEX function returns the value at an intersection between a given row and column, using the following arguments:

*Value = INDEX(**Value array**; **Row number**)* *A1*

The MATCH function uses a lookup value to find the closest or exact same value in an ordered array, and returns the numeric position of that item in the array, in this case the row number. The input arguments are written as follows:

*Row number = MATCH(**Lookup value**; **Lookup array**; **Match type**)* *A2*

The **Match type** argument specifies the search method, using a value of 1, 0, or -1. An argument of 1 returns the largest value smaller than or equal to **Lookup value**, 0 returns the first exact match, and -1 returns the smallest value larger than or equal to **Lookup value**. Using 1 and -1 requires that the **Lookup array** is in an increasing or decreasing order, respectively. If no value is entered, the function will default to 1. Due to the structure of the data, a value of 1 should be used; therefore **Match type** needs not be specified. In order to use -1, the entire dataset must be tabularised and sorted inversely according to time, whilst exact matches from using 0 will only occur sparsely due to chance unless times are rounded.

Replacing **Row number** in Eq. A1with the MATCH function gives the INDEX-MATCH function:

*Value = INDEX(**Value array**; MATCH(**Lookup value**; **Lookup array**))* *A3*

Substituting generic identifiers with application specific ones yields:

$T_{aq} = INDEX(\mathbf{T_{log}}; MATCH(t_{aq}; \mathbf{t_{log}}))$ *A4*

where T_{aq} is the temperature at the time of acquisition, $\mathbf{T_{log}}$ is the column vector of measured temperatures, t_{aq} is the time of acquisition, and $\mathbf{t_{log}}$ is the column vector of temperature measurement times. In order for the function to work, the measured temperature at each point

must be found in the same row as its time of measurement, and the times of measurement must be ordered as per instructions for the MATCH function.

The temperature measurements are saved by date in separate files spanning 24 hours of data, and thus many experiment sequences will cross over between different logfiles during overnight runs. By including acquisition date in the data matrix, the function can be altered to automatically cross-reference dates and run the INDEX-MATCH function on the correct set of logged values, per the following modifications.

An IF function can be used to determine whether or not to run another function, using the argument:

$$Output = IF(\textbf{Logical test}; \textbf{Output if TRUE}; \textbf{Output if FALSE}) \quad A5$$

The output arguments are optional, but one of them must be present. The **Logical test** in this case can be formulated as:

$$d_{aq} = d_{log} \quad A6$$

where d_{aq} is acquisition date and d_{log} is the temperature log date. Whether or not these are equal will then determine the output. Substituting the MATCH-INDEX function for **Output if TRUE** yields a function that will only return a temperature if the correct dataset is referenced:

$$T_{aq} = IF(d_{aq} = d_{log}; INDEX(\mathbf{T_{log}}; MATCH(t_{aq}; \mathbf{t_{log}}))) \quad A7$$

Note that this function still has an undefined **Output if FALSE** argument. Using another IF statement as the **Output if FALSE** creates so-called nested IF statements, where the second IF function is only evaluated if the success-condition of the first is not met. Defining two sets of Eq. 4.7 by referencing separate temperature logs gives the following functions:

$$a) \quad T_{aq} = IF(d_{aq} = d_{log1}; INDEX(\mathbf{T_{log1}}; MATCH(t_{aq}; \mathbf{t_{log1}})); \textbf{Output if FALSE}) \quad A7a$$

$$b) \quad T_{aq} = IF(d_{aq} = d_{log2}; INDEX(\mathbf{T_{log2}}; MATCH(t_{aq}; \mathbf{t_{log2}})); \textbf{Output if FALSE}) \quad A7b$$

The two different temperature data sets are differentiated using the names log1 and log2 in the subscripts. By substituting Eq. A7b for **Output if FALSE** in Eq. A7a, a function capable of using measurement dates to select the correct time and temperature from two sets of data is attained:

$$T_{aq}=IF(d_{aq}=d_{log1};INDEX(\mathbf{T_{log1}};MATCH(t_{aq};\mathbf{t_{log1}})); \ldots \quad A8$$
$$IF(d_{aq}=d_{log2};INDEX(\mathbf{T_{log2}};MATCH(t_{aq};\mathbf{t_{log2}})))$$

where T_{aq} is the temperature at the time of acquisition, d_{aq} is acquisition date, d_{log} is the temperature log date, $\mathbf{T_{log}}$ is the column vector of measured temperatures, t_{aq} is the time of acquisition, and $\mathbf{t_{log}}$ is the column vector of temperature measurement times. The two different temperature data sets are differentiated using the names log1 and log2 in the subscripts.

A value for **Output if FALSE** can still be entered for the second IF function. This can be used to display a specific error message upon both IF statements meeting failure conditions, for instance, alerting the user that the function is no longer applicable and must be altered to incorporate a new temperature log. Regardless, as long as all spreadsheets are properly managed this function will not return a numerical value unless the right dataset is referenced, minimising the risk of error. However, vigilance is required when analysing data with an incomplete temperature log: If the dates match,

the function *will* assign the temperature measured closest to the acquisition time even if the times vary greatly.

While the argument structure could theoretically be expanded further, a maximum of two different temperature logs can be cross-referenced simultaneously by a single function due to a limitation on the number of input arguments in Excel. If a scenario arises where more than two datasets must be simultaneously referenced, several nested IF INDEX-MATCH functions should be able to work in tandem in separate columns before using another function to consolidate the results.

In addition, an Excel spreadsheet of a specific format was created to serve as a basis for a series of MATLAB scripts for T_2 analysis. The formatting requires a COUNTA function, which returns the number of non-empty cells in a specified range. This case, the number of active cells in column A was to be determined, and thus the function was used as follows:

Number of cells in Column A = COUNTA(A:A) *A9*

The requirements of the file as a basis for the MATLAB scripts are as follows:

1) The sheet containing the following is named Sheet1.
2) A function that returns the number of non-empty cells in column A is present in cell B1.
3) Each cell in column A is filled with the folder location directory corresponding to the experiment in the same row, starting from A3. Nothing else should be entered to the column. Note that the input must be the folder containing the specific experiment folder, not the folder containing the experiment files, and it must be terminated with a backslash.
4) Each cell in column B is labelled per the experiment number found in TopSpin for the experiment in the same row, starting from B3.
5) Eleven columns of data will be returned by the scripts, filling columns E through O starting from row 3. These columns should not contain other data, as it will be overwritten.
6) In order to identify the resulting data, the contents of TableA1 should be present in the range E1:O2.

Table A1: Identifiers for automatically entered T_2 results.

1-Comp	2-Comp		3-Comp			2-Comp	3-Comp			
T1 c1 (ms)	T1 c1 (ms)	T1 c2 (ms)	T1 c1 (ms)	T1 c2 (ms)	T1 c3 (ms)	I2	I31	I33	Date	Time

Most requirements above can be easily altered by altering the code of the MATLAB scripts, provided in the following subchapter.

MATLAB

The results of the CMPG oneshot T_2 experiment were analysed by a MATLAB script provided by Totland and written by Seland, and its components are provided later in the appendix. A modification to the script was done in order to provide the capability of exporting T_2 values directly to a given Excel file, with the user able to specify target row and column on query by the script, using the following code:

```
%export results

C = {T_to, T_en1, T_en2, T2_en1, T2_en2, T2_en3};

out5=input('What column and row in excel to export values to?', 's');

filename = 'DISK:\EXAMPLE DIRECTORY\EXAMPLE SUBDIRECTORY\FILENAME.xlsx';
xlswrite(filename, C, 'Sheet1', out5)

disp('Done')
```

The target file defined as *filename* must be specified by altering the script itself before running. In cases where the same parameters could be reused, guess values and other parameters were written directly into the script in order to remove the query-sections and speed up the analysis. This basic function was later replaced with superior code.

Handling export of results and constantly changing the 'current folder' in MATLAB to load new datasets still took up a considerable part of the analysis time for T_2 data. To counteract this, the script was again rewritten to facilitate the analysis, although no changes were made that would alter the results of the analysis functions. The final workflow made use of three different scripts as well as the target Excel sheet discussed in the previous chapter, the formatting of which is important for the process to work.

The initial code presented contains the core functionality for all the rewritten scripts, as it provides the necessary variables for constructing indices of all relevant file locations. It has the following form:

```
%Find number of rows to read:
excelFile = 'DISK:\DIRECTORY\SUBDIR\filename.xlsx';
readSheet = 'Sheet1';
constantReadRange = 'A3:B';

numberOfRows = xlsread(excelFile,'B1:B1');

charOfRows = num2str(numberOfRows);
readRange = strcat(constantReadRange,charOfRows);

%Read Excel experiment numbers and convert fo full fileformat:
[targetDirectory,masterDirectory] = xlsread(excelFile,readSheet,readRange);
targetDirectoryChar = num2str(targetDirectory);
targetDirectoryString = cellstr(targetDirectoryChar);
targetDirectoryTrim = strtrim(targetDirectoryString);

fullDirectory = strcat(masterDirectory,targetDirectoryTrim);
matrixSize = size(fullDirectory,1);
loopSize = matrixSize
```

The filename of the excel file must be manually entered within the script, and updated if a different file is to be loaded. A COUNTA-function in cell B1 in the target Excel sheet returns the number of non-empty cells in column A. This is used to determine the number of rows the *xlsread* function will read from the Excel sheet, and is the basis for matrix size and loop iteration calculations throughout the scripts. As a result, column A must be empty but for the necessary data and identifiers in rows 1

and 2, and its contents should never deviate from this standardised formatting when using these scripts. The relevant contents of column A and B are then imported to MATLAB, and the rest of the operations are done in order to convert the directory names to a usable format. Provided by this code is an index of all experiment directories for the set of experiments specified in the Excel file, which allows writing further functions to read, create and write to any file in these directories. All following code relies on this core.

```
%Create an index of all audita.txt files:
repAudita= repmat({'\audita.txt'},matrixSize,1);
auditaLocation = strcat(fullDirectory,repAudita);

%Extract a time data matrix from all audita.txt files:
timeStampT = cell(1,loopSize);
for a=1:loopSize
    fileInfo = dir(auditaLocation{a});
    timeStampT{a} = fileInfo.date;
end
timeStamp = timeStampT';

dateTime = regexp(timeStamp,' ','split');
timeLog = cat(1,dateTime{:});

%Export experiment times to Excel:
excelSheet = 'Sheet1';
excelRange = 'N3';
xlswrite(excelFile,timeLog,excelSheet,excelRange);
```

The directory index capability is exploited in the code above, which reads the acquisition date and time of every experiment included in the series from the creation parameters of its identifying audita.txt file. It then writes the results to the correct location in the source spreadsheet, which combined with the INDEX-MATCH function discussed previously allows automated filling of the temperature column. The audita.txt file should never be altered if the script is to be used, as this will cause the script to return erroneous values. However, any errors should quickly be identified, as they will break the pattern in the Excel sheet.

```
%Create an index of all T2_data.txt files:
repT2_data= repmat({'\T2_data.txt'},matrixSize,1);
T2_dataLocationC = strcat(fullDirectory,repT2_data);
T2_dataLocation = cellstr(T2_dataLocationC)

%Create an index of all fid files:
repFid= repmat({'\fid'},matrixSize,1);
fidLocation = strcat(fullDirectory,repFid);

matrixSize = size(T2_dataLocation,1);

for a=1:loopSize
    varKeep =
{'oneComp','twoComp1','twoComp2','threeComp1','threeComp2','threeComp3',...

'a','constantReadRange','dateTime','excelFile','excelRange','excelSheet','loop
Size',...

'fidLocation','matrixSize','numberOfRows','OneComp','readRange','readSheet','T
2_dataLocation',...

'T2_values_all','timeStamp','timeLog','twoComp1','twoComp2','threeComp1','thre
eComp2','threeComp3'};
    clearvars('-except',varKeep{:})
    fclose('all')

    fid=fopen(fidLocation{a},'r','b');
    data=fread(fid,'int32');

(.....)

    save(T2_dataLocation{a},'It','-ascii','-tabs')
    %save  -ascii -tabs T2_data It
end
```

The original method contained a separate script for creating the required T2_data.txt files from the experiment FIDs during each T_2 analysis. By creating indices of where to find the FIDs and where to save the results of this analysis, the function was rewritten per the changes above to loop over all experiment FIDs and save the results in the right location in one run. Except for updating file references with the appropriate matrices and selection criteria, the operations to generate T_2 results remained unchanged. The unaltered part of the code is omitted for brevity.

```
%Create an index of all T2_data.txt files:
repT2_data= repmat({'\T2_data.txt'},matrixSize,1);
T2_dataLocationC = strcat(fullDirectory,repT2_data);
T2_dataLocation = cellstr(T2_dataLocationC);

%Create an index of all final excel file locations:
repT2_results= repmat({'\results.xlsx'},matrixSize,1);
resultsLocation = strcat(fullDirectory,repT2_results);

%Analouge of T2_tilpasning3.m
experimentNumber = input('What is the global experiment number (among all CMPG
experiments)?');

load(T2_dataLocation{experimentNumber});

(...)

%Results:
T2_values = {T2;T1_1;T1_2;T2_1;T2_2;T2_3;I1;I21;I22};
T2_valuesLabel = {'T2_1comp(ms)';'T2_2comp_1(ms)';'T2_2comp_2(ms)';...

'T2_3comp_1(ms)';'T2_3comp_2(ms)';'T2_3comp_3(ms)';'I_2comp';'I_3comp_1';'I_3-
comp_2'};

%Choose whether to export data. All answers but 'n' is followed by export.
exportChoice = input('Do you want to save the results? y/n','s');
if isequal(exportChoice,'n')
    disp('Data not exported')
else
    xlswrite(resultsLocation{experimentNumber}, T2_valuesLabel, 'Sheet1',
'A1:A9');
    xlswrite(resultsLocation{experimentNumber}, T2_values, 'Sheet1', 'B1:B9');
    disp('Data exported to');
    disp(resultsLocation{experimentNumber});
end

%Continue prompt:
rerunChoice = input('Do you want to analyse another experiment? Enter *n* for
no','s');
if isequal(rerunChoice,'n')
    disp('Done')
else
    disp('The last experiment analysed was')
    experimentNumber
    T2_tilpasning3_serialProcess;
end
```

The code above is used in conjunction with the code in the original *T2_tilpasning3.m* script. Except for updating file references with the appropriate matrices and selection criteria, the operations to generate T_2 results was not altered and are omitted from the presentation. Before running the script, the appropriate T2_data.txt files must be created by running the *T2_createT2_data.m* script discussed above. A failed effort was made to create a for-loop for the process, but this should be possible to accomplish with a slight proficiency at programming. The code incorporates major workflow improvements, the most important of which is the capability to create an Excel file in the correct experiment directory and save the T_2 results to it. It also allows the user to analyse any experiment specified in the source Excel file from entering its global experiment number, and ends with a prompt to run again and analyse another experiment. The export function is used in conjunction with the last piece of code written:

```
%Create an index of all excel result-file locations:
repT2_results= repmat({'\results.xlsx'},matrixSize,1);
resultsLocation = strcat(fullDirectory,repT2_results);

%Import the experiment results to MATLAB:
T2results = {matrixSize};
for ii=1:loopSize
    T2results{ii} = xlsread(resultsLocation{ii},'Sheet1','B1:B9');
end
T2resultsMat = cell2mat(T2results);
T2resultsExport = T2resultsMat';

%T2export =
%Write the results to the original Excel file
xlswrite(excelFile, T2resultsExport, 'Sheet1', 'E3');
disp('Data collection complete');
```

This code loops over all Excel result-files created by the *T2_tilpasning3_serialProcessing.m* script, generating a matrix of experiment results with the same index as the time- and experiment data from previous steps. The matrix is then exported to the appropriate position in the Excel file from the core code. The script requires that *T2_createT2_data.m* have been run, followed by any variant of *T2_tilpasning3_serialProcessing.m* for all experiments, as a missing *results.xlsx* file in any experiment location will break the loop. However, the assumed location of a missing file is returned as part of the resulting error message, meaning missing experiments can quickly be identified by cross-reference with the source Excel sheet.

When reasonable guesses have been found for all experiment ranges, these can be written directly into the script, further accelerating the analysis. The overall result of this, along with the Excel and MATLAB functions detailed, is that a spreadsheet can quickly be filled with date, time, temperature and T_2 data from only experiment numbers and the location of the NMR data. In addition, premade graphs and calculations can be included in the template, further reducing the time spent analysing data. Note that this approach cannot be guaranteed to work if the NMR data structure deviates from that used in this thesis, where for instance process numbers have not been defined for any of the T_2 experiments.

Use of the code is not necessarily limited to T_2 experiments: It was only written around scripts that is. It has for instance been applied to find the acquisition times and dates of a series of ^{1}H experiments performed during temperature ramping programs, in order to quickly find the corresponding spectrometer temperatures.

MATLAB scripts

In the following section, all scripts are presented in their entirety. The data analysis part of all these were provided courtesy of John Georg Seland of UiB, and some were rewritten by the author according to the section above. T2_resultScoop.m and NMR_TimeFinder.m was written from scratch.

T2_tilpasning3.m

```
%Program to calculate T2 values from a CPMG experiment.
%one- and two-components fits
close all
clear all
T2_500
load T2_data.txt
n=input('How many point do you want to include? ');
temp=T2_data(2:n,1);
I=T2_data(2:n,2);
Y=log(I);

figure;
plot(temp,Y,'*')

disp('For the one-component fit:')
T_2=input('what is the expected (monoexp) T2 value (in ms)? ');
T_2=T_2*1e-3;
tilpasst2;
T2=t2_1komp*1e3
T_to=num2str(T2);
I_mod_1komp=I_mod;
out1=['One-component fit, T2 =' T_to 'ms'];

disp('For the 2-component fit:')
T_21=input('What is the expected T2 value for 1st component (ms)? ');
T_22=input('What is the expected T2 value for 2nd component (ms)? ');
T_21=T_21*1e-3;
T_22=T_22*1e-3;
tilpasst2_2komp;
T1_1=t1_1komp*1e3
T1_2=t1_2komp*1e3
I1=I_1komp./(I_1komp+I_2komp)

T_en1=num2str(T1_1);
T_en2=num2str(T1_2);
I_en=num2str(I1);

I_mod_2komp=I_mod;
out2=['                                Two-component fit, T2-1 =' T_en1 'ms,
T2-2= ' T_en2 'ms, p1 = ' I_en];

disp('For the 3-component fit:')
T2_21=input('What is the expected T2 value for 1st component (ms)? ');
T2_22=input('What is the expected T2 value for 2nd component (ms)? ');
T2_23=input('What is the expected T2 value for 3rd component (ms)? ');
T2_21=T2_21*1e-3;
T2_22=T2_22*1e-3;
T2_23=T2_23*1e-3;

tilpasst2_3komp;

T2_1=t1_1komp*1e3
T2_2=t1_2komp*1e3
T2_3=t1_3komp*1e3
I21=I_1komp./(I_1komp+I_2komp+I_3komp)
I22=I_2komp./(I_1komp+I_2komp+I_3komp)

T2_en1=num2str(T2_1);
T2_en2=num2str(T2_2);
T2_en3=num2str(T2_3);
```

```
I2_en=num2str(I21);
I2_to=num2str(I22);

I_mod_3komp=I_mod;
out3=[' Three-component fit, T2-1 =' T2_en1 'ms, T2-2= ' T2_en2 'ms,  T2-3=
' T2_en3, 'ms, p1 ='  I2_en, 'p2 ='  I2_to];

%plot the results in a figure

out4=input('Title of the figure? ','s');

figure;
subplot(3,2,1)
plot(temp,I_mod_1komp,'b-')
hold on
plot(temp,I,'ro')
grid on
xlabel('time (s)')
ylabel('Intensity')
hold off

subplot(3,2,2)
plot(temp,(I_mod_1komp-I)./I_mod_1komp,'bx-')
xlabel('time (s)')
ylabel('residuals')
grid on

subplot(3,2,3)
plot(temp,I_mod_2komp,'b-')
hold on
plot(temp,I,'ro')
xlabel('time (s)')
ylabel('Intensity')
grid on
hold off

subplot(3,2,4)
plot(temp,(I_mod_2komp-I)./I_mod_2komp,'bx-')
xlabel('time (s)')
ylabel('residuals')
grid on

subplot(3,2,5)
plot(temp,I_mod_3komp,'b-')
hold on
plot(temp,I,'ro')
xlabel('time (s)')
ylabel('Intensity')
grid on
hold off

subplot(3,2,6)
plot(temp,(I_mod_3komp-I)./I_mod_3komp,'bx-')
xlabel('time (s)')
ylabel('residuals')
grid on

subplot(3,2,1)
title(out4)
```

```
subplot(3,2,2)
title(out1)

subplot(3,2,3)
title(out2)

subplot(3,2,5)
title(out3)
```

T2_500.m

```
%Program (or function) for procssing data obtained using the cpmg_oneshot
%or intg_cpmg_oneshot pulse sequence on the %500 MHz instrument at UiB.
%Final result is a T2-decay (magnitude)

%function [] = G0_T2_500
close all
clear all
fid=fopen('fid','r','b');
data=fread(fid,'int32');

td2=size(data);
td2=td2(1)-2;
data=data(1:td2);
ser_r=data(2:2:td2);
ser_i=data(1:2:td2);
ser_t=complex(ser_r,ser_i);

td3=td2/2;

t = [1:1:td3];
tau=input('What is echo time (ms) in the CPMG train (d20)? ');
t=t.*2*tau*1e-3; %Sampler bare annenhvert ekko
t=t';

%Magnitude of the complex signal
ser_tt=abs(ser_t);

figure(1)
plot(ser_r,'b*')
hold on
plot(ser_i,'ro')
hold off


%Phasing of the signal
%ser_tt(:,i)=ser_t.*exp(-i*phi);

figure(2)
plot(ser_tt,'*')

It=[t,ser_tt];

save -ascii -tabs T2_data.txt It
```

tilpasst2.m

```
% Program for å tilpasse T2 data, 2 komponenter
% Program for å tilpasse T2 data, 2 komponenter
%
global  I temp T_2

% Her må startverdier settest inn

I1 = I(1);
t1 = T_2;


x0 = [I1 t1]'

x  = fminsearch('funkt2',x0);

I_1komp = x(1)
t2_1komp = x(2)

I_mod=I_1komp*exp(-temp/t2_1komp);
```

tilpasst2_2komp.m

```
% Program for å tilpasse T2 data, 2 komponenter
%
global  I temp T_21 T_22

% Her må startverdier settest inn
I1 = 0.5*I(1);
t1 = T_21;
I11 = 0.5*I(1);
t11 = T_22;

x0 = [I1 t1 I11 t11]'

x  = fminsearch('funkt2_2komp',x0);

I_1komp = x(1)
t1_1komp = x(2)
I_2komp = x(3)
t1_2komp = x(4)

I_mod=I_1komp*exp(-temp/t1_1komp)+I_2komp*exp(-temp/t1_2komp);
```

tilpasst2_3komp.m

```
% Program for ? tilpasse T2 data, 3 komponenter
%
global  I temp T2_21 T2_22 T2_23

% Her m? startverdier settest inn
I1 = 0.3*I(1);
t1 = T2_21;
I11 = 0.3*I(1);
t11 = T2_22;
```

```
I111 = 0.3*I(1);
t111 = T2_23;

x0 = [I1 t1 I11 t11 I111 t111]'

x  = fminsearch('funkt2_3komp',x0);

I_1komp = x(1)
t1_1komp = x(2)
I_2komp = x(3)
t1_2komp = x(4)
I_3komp = x(5)
t1_3komp = x(6)

I_mod=I_1komp*exp(-temp/t1_1komp)+I_2komp*exp(-temp/t1_2komp)+I_3komp*exp(-
temp/t1_3komp);
```

createT2_data.m

```
%Program to extract T2 data from the fids of all CMPG experiments
%specified in a specific Excel file. The data can then quickly be analysed
%by a T2_tilpasning_serialProcess script. Designed for a pulse train of
%1 ms, if other values is desired, this must be altered by the user.

fclose all
clear all

%Find number of rows to read:
excelFile = 'H:\DIRECTORY\SUBDIRECTORY\filename.xlsx';
readSheet = 'Sheet1';
constantReadRange = 'A3:B';

numberOfRows = xlsread(excelFile,'B1:B1');

charOfRows = num2str(numberOfRows);
readRange = strcat(constantReadRange,charOfRows);

%Read Excel experiment numbers and convert fo full fileformat:
[targetDirectory,masterDirectory] = xlsread(excelFile,readSheet,readRange);
targetDirectoryChar = num2str(targetDirectory);
targetDirectoryString = cellstr(targetDirectoryChar);
targetDirectoryTrim = strtrim(targetDirectoryString);

fullDirectory = strcat(masterDirectory,targetDirectoryTrim);
matrixSize = size(fullDirectory,1);
loopSize = matrixSize

%Create an index of all audita.txt files:
repAudita= repmat({'\audita.txt'},matrixSize,1);
auditaLocation = strcat(fullDirectory,repAudita);

%Extract a time data matrix from all audita.txt files:
timeStampT = cell(1,loopSize);
for a=1:loopSize
    fileInfo = dir(auditaLocation{a});
    timeStampT{a} = fileInfo.date;
end
timeStamp = timeStampT';
```

```
dateTime = regexp(timeStamp,' ','split');
timeLog = cat(1,dateTime{:});

%Export experiment times to Excel:
excelSheet = 'Sheet1';
excelRange = 'N3';
xlswrite(excelFile,timeLog,excelSheet,excelRange);

%Create an index of all T2_data.txt files:
repT2_data= repmat({'\T2_data.txt'},matrixSize,1);
T2_dataLocationC = strcat(fullDirectory,repT2_data);
T2_dataLocation = cellstr(T2_dataLocationC)

%Create an index of all fid files:
repFid= repmat({'\fid'},matrixSize,1);
fidLocation = strcat(fullDirectory,repFid);

matrixSize = size(T2_dataLocation,1);

%T2_500
for a=1:loopSize
    varKeep =
{'a','constantReadRange','dateTime','excelFile','excelRange','excelSheet','
loopSize','fidLocation',...
'matrixSize','numberOfRows','readRange','readSheet','T2_dataLocation','time
Stamp','timeLog'};
    clearvars('-except',varKeep{:})
    fclose('all')

    fid=fopen(fidLocation{a},'r','b');
    data=fread(fid,'int32');

    td2=size(data);
    td2=td2(1)-2;
    data=data(1:td2);
    ser_r=data(2:2:td2);
    ser_i=data(1:2:td2);
    ser_t=complex(ser_r,ser_i);

    td3=td2/2;

    t = [1:1:td3];
    %tau=input('What is echo time (ms) in the CPMG train (d20)? ');
    tau=1;           %Tast inn verdi her
    t=t.*2*tau*1e-3; %Sampler bare annenhvert ekko
    t=t';

    %Magnitude of the complex signal
    ser_tt=abs(ser_t);

    %figure(1)
    %plot(ser_r,'b*')
    %hold on
    %plot(ser_i,'ro')
    %hold off


    %Phasing of the signal
```

```
    %ser_tt(:,i)=ser_t.*exp(-i*phi);

    %figure(2)
    %plot(ser_tt,'*')

    It=[t,ser_tt]

    save(T2_dataLocation{a},'It','-ascii','-tabs')
    %save  -ascii -tabs T2_data It
end

disp('done')
```

T2_tilpasing3_serialProcess.m

```
%Program to quickly analyse a 3-component set of T2 CPMG experiments in
%different folders and export results to Excel. Requires FIDs to already
%have been processed by createT2_data.m, and a strictly formatted
%Excel base sheet.

close all
clear all

%Find number of rows to read:
excelFile = 'H:\DIRECTORY\SUBDIRECTORY\filename.xlsx';
readSheet = 'Sheet1';
constantReadRange = 'A3:B';

numberOfRows = xlsread(excelFile,'B1:B1');

charOfRows = num2str(numberOfRows);
readRange = strcat(constantReadRange,charOfRows);

%Read Excel experiment numbers and convert fo full fileformat:
[targetDirectory,masterDirectory] = xlsread(excelFile,readSheet,readRange);
targetDirectoryChar = num2str(targetDirectory);
targetDirectoryString = cellstr(targetDirectoryChar);
targetDirectoryTrim = strtrim(targetDirectoryString);

fullDirectory = strcat(masterDirectory,targetDirectoryTrim);
matrixSize = size(fullDirectory,1);
loopSize = matrixSize

%Create an index of all T2_data.txt files:
repT2_data= repmat({'\T2_data.txt'},matrixSize,1);
T2_dataLocationC = strcat(fullDirectory,repT2_data);
T2_dataLocation = cellstr(T2_dataLocationC)

%Create an index of all final excel file locations:
repT2_results= repmat({'\results.xlsx'},matrixSize,1);
resultsLocation = strcat(fullDirectory,repT2_results);

%Analouge of T2_tilpasning3.m
experimentNumber = input('What is the global experiment number (among all
CMPG experiments)?');

load(T2_dataLocation{experimentNumber});
n=input('How many point do you want to include? ');
```

```
temp=T2_data(2:n,1);
I=T2_data(2:n,2);
Y=log(I);

figure;
plot(temp,Y,'*')

disp('For the one-component fit:')
T_2=input('what is the expected (monoexp) T2 value (in ms)? ');

T_2=T_2*1e-3;

tilpasst2;

T2=t2_1komp*1e3
T_to=num2str(T2);
I_mod_1komp=I_mod;
out1=['One-component fit, T2 =' T_to 'ms'];

disp('For the 2-component fit:')
T_21=input('What is the expected T2 value for 1st component (ms)? ');
T_22=input('What is the expected T2 value for 2nd component (ms)? ');

T_21=T_21*1e-3;
T_22=T_22*1e-3;
tilpasst2_2komp;

T1_1=t1_1komp*1e3
T1_2=t1_2komp*1e3
I1=I_1komp./(I_1komp+I_2komp)

T_en1=num2str(T1_1);
T_en2=num2str(T1_2);
I_en=num2str(I1);

I_mod_2komp=I_mod;
out2=['                                Two-component fit, T2-1 =' T_en1 'ms,
T2-2= ' T_en2 'ms, p1 = ' I_en];

disp('For the 3-component fit:')
T2_21=input('What is the expected T2 value for 1st component (ms)? ');
T2_22=input('What is the expected T2 value for 2nd component (ms)? ');
T2_23=input('What is the expected T2 value for 3rd component (ms)? ');

T2_21=T2_21*1e-3;
T2_22=T2_22*1e-3;
T2_23=T2_23*1e-3;
tilpasst2_3komp;

T2_1=t1_1komp*1e3
T2_2=t1_2komp*1e3
T2_3=t1_3komp*1e3
I21=I_1komp./(I_1komp+I_2komp+I_3komp)
I22=I_2komp./(I_1komp+I_2komp+I_3komp)

T2_en1=num2str(T2_1);
T2_en2=num2str(T2_2);
```

```
T2_en3=num2str(T2_3);
I2_en=num2str(I21);
I2_to=num2str(I22);

I_mod_3komp=I_mod;

out3=[' Three-component fit, T2-1 =' T2_en1 'ms, T2-2= ' T2_en2 'ms,  T2-3=
' T2_en3, 'ms, p1 ='  I2_en, 'p2 ='  I2_to];

%plot the results in a figure

out4=input('Title of the figure? ','s');

figure;
subplot(3,2,1)
plot(temp,I_mod_1komp,'b-')
hold on
plot(temp,I,'ro')
grid on
xlabel('time (s)')
ylabel('Intensity')
hold off

subplot(3,2,2)
plot(temp,(I_mod_1komp-I)./I_mod_1komp,'bx-')
xlabel('time (s)')
ylabel('residuals')
grid on

subplot(3,2,3)
plot(temp,I_mod_2komp,'b-')
hold on
plot(temp,I,'ro')
xlabel('time (s)')
ylabel('Intensity')
grid on
hold off

subplot(3,2,4)
plot(temp,(I_mod_2komp-I)./I_mod_2komp,'bx-')
xlabel('time (s)')
ylabel('residuals')
grid on

subplot(3,2,5)
plot(temp,I_mod_3komp,'b-')
hold on
plot(temp,I,'ro')
xlabel('time (s)')
ylabel('Intensity')
grid on
hold off

subplot(3,2,6)
plot(temp,(I_mod_3komp-I)./I_mod_3komp,'bx-')
xlabel('time (s)')
ylabel('residuals')
grid on
```

```
subplot(3,2,1)
title(out4)

subplot(3,2,2)
title(out1)

subplot(3,2,3)
title(out2)

subplot(3,2,5)
title(out3)

%Results:
T2_values = {T2;T1_1;T1_2;T2_1;T2_2;T2_3;I1;I21;I22};
T2_valuesLabel = {'T2_1comp(ms)';'T2_2comp_1(ms)';'T2_2comp_2(ms)';...

'T2_3comp_1(ms)';'T2_3comp_2(ms)';'T2_3comp_3(ms)';'I_2comp';'I_3comp_1';'I
_3-comp_2'};

%Choose whether to export data. All answers but 'n' is followed by export.
exportChoice = input('Do you want to save the results? y/n','s');
if isequal(exportChoice,'n')
    disp('Data not exported')
else
    xlswrite(resultsLocation{experimentNumber}, T2_valuesLabel, 'Sheet1',
'A1:A9');
    xlswrite(resultsLocation{experimentNumber}, T2_values, 'Sheet1',
'B1:B9');
    disp('Data exported');
end

%Continue prompt:
rerunChoice = input('Do you want to analyse another experiment? Enter *n*
for no','s');
if isequal(rerunChoice,'n')
    disp('Done')
else
    disp('The last experiment analysed was')
    experimentNumber
    T2_tilpasning3_serialProcess;
end
```

T2_tilpasing3_serialProcessRapid.m

```
%Program to quickly analyse a 3-component set of T2 CPMG experiments in
%different folders and export results to Excel. Requires FIDs to already
%have been processed by createT2_data.m, and a strictly formatted
%Excel base sheet.

close all
clear all

%Find number of rows to read:
excelFile = 'H:\DIRECTORY\SUBDIRECTORY\filename.xlsx';
readSheet = 'Sheet1';
constantReadRange = 'A3:B';

numberOfRows = xlsread(excelFile,'B1:B1');
```

```
charOfRows = num2str(numberOfRows);
readRange = strcat(constantReadRange,charOfRows);

%Read Excel experiment numbers and convert fo full fileformat:
[targetDirectory,masterDirectory] = xlsread(excelFile,readSheet,readRange);
targetDirectoryChar = num2str(targetDirectory);
targetDirectoryString = cellstr(targetDirectoryChar);
targetDirectoryTrim = strtrim(targetDirectoryString);

fullDirectory = strcat(masterDirectory,targetDirectoryTrim);
matrixSize = size(fullDirectory,1);
loopSize = matrixSize

%Create an index of all T2_data.txt files:
repT2_data= repmat({'\T2_data.txt'},matrixSize,1);
T2_dataLocationC = strcat(fullDirectory,repT2_data);
T2_dataLocation = cellstr(T2_dataLocationC)

%Create an index of all final excel file locations:
repT2_results= repmat({'\results.xlsx'},matrixSize,1);
resultsLocation = strcat(fullDirectory,repT2_results);

%Analouge of T2_tilpasning3.m
experimentNumber = input('What is the global experiment number (among all
CMPG experiments)?');

load(T2_dataLocation{experimentNumber});
n=input('How many point do you want to include? ');

temp=T2_data(2:n,1);
I=T2_data(2:n,2);
Y=log(I);

figure;
plot(temp,Y,'*')

disp('For the one-component fit:')
T_2=input('what is the expected (monoexp) T2 value (in ms)? ');

T_2=T_2*1e-3;

tilpasst2;

T2=t2_1komp*1e3
T_to=num2str(T2);
I_mod_1komp=I_mod;
out1=['One-component fit, T2 =' T_to 'ms'];

disp('For the 2-component fit:')
T_21=input('What is the expected T2 value for 1st component (ms)? ');
T_22=input('What is the expected T2 value for 2nd component (ms)? ');

T_21=T_21*1e-3;
T_22=T_22*1e-3;
tilpasst2_2komp;

T1_1=t1_1komp*1e3
```

```
T1_2=t1_2komp*1e3
I1=I_1komp./(I_1komp+I_2komp)

T_en1=num2str(T1_1);
T_en2=num2str(T1_2);
I_en=num2str(I1);

I_mod_2komp=I_mod;
out2=['                                Two-component fit, T2-1 =' T_en1 'ms,
T2-2= ' T_en2 'ms, p1 = ' I_en];

disp('For the 3-component fit:')
T2_21=input('What is the expected T2 value for 1st component (ms)? ');
T2_22=input('What is the expected T2 value for 2nd component (ms)? ');
T2_23=input('What is the expected T2 value for 3rd component (ms)? ');

T2_21=T2_21*1e-3;
T2_22=T2_22*1e-3;
T2_23=T2_23*1e-3;
tilpasst2_3komp;

T2_1=t1_1komp*1e3
T2_2=t1_2komp*1e3
T2_3=t1_3komp*1e3
I21=I_1komp./(I_1komp+I_2komp+I_3komp)
I22=I_2komp./(I_1komp+I_2komp+I_3komp)

T2_en1=num2str(T2_1);
T2_en2=num2str(T2_2);
T2_en3=num2str(T2_3);
I2_en=num2str(I21);
I2_to=num2str(I22);

I_mod_3komp=I_mod;

out3=[' Three-component fit, T2-1 =' T2_en1 'ms, T2-2= ' T2_en2 'ms,  T2-3=
' T2_en3, 'ms, p1 ='  I2_en, 'p2 ='  I2_to];

%plot the results in a figure

out4=input('Title of the figure? ','s');

figure;
subplot(3,2,1)
plot(temp,I_mod_1komp,'b-')
hold on
plot(temp,I,'ro')
grid on
xlabel('time (s)')
ylabel('Intensity')
hold off

subplot(3,2,2)
plot(temp,(I_mod_1komp-I)./I_mod_1komp,'bx-')
xlabel('time (s)')
ylabel('residuals')
grid on

subplot(3,2,3)
```

```
plot(temp,I_mod_2komp,'b-')
hold on
plot(temp,I,'ro')
xlabel('time (s)')
ylabel('Intensity')
grid on
hold off

subplot(3,2,4)
plot(temp,(I_mod_2komp-I)./I_mod_2komp,'bx-')
xlabel('time (s)')
ylabel('residuals')
grid on

subplot(3,2,5)
plot(temp,I_mod_3komp,'b-')
hold on
plot(temp,I,'ro')
xlabel('time (s)')
ylabel('Intensity')
grid on
hold off

subplot(3,2,6)
plot(temp,(I_mod_3komp-I)./I_mod_3komp,'bx-')
xlabel('time (s)')
ylabel('residuals')
grid on

subplot(3,2,1)
title(out4)

subplot(3,2,2)
title(out1)

subplot(3,2,3)
title(out2)

subplot(3,2,5)
title(out3)

%Results:
T2_values = {T2;T1_1;T1_2;T2_1;T2_2;T2_3;I1;I21;I22};
T2_valuesLabel = {'T2_1comp(ms)';'T2_2comp_1(ms)';'T2_2comp_2(ms)';...

'T2_3comp_1(ms)';'T2_3comp_2(ms)';'T2_3comp_3(ms)';'I_2comp';'I_3comp_1';'I
_3-comp_2'};

%Choose whether to export data. All answers but 'n' is followed by export.
exportChoice = input('Do you want to save the results? y/n','s');
if isequal(exportChoice,'n')
    disp('Data not exported')
else
    xlswrite(resultsLocation{experimentNumber}, T2_valuesLabel, 'Sheet1',
'A1:A9');
    xlswrite(resultsLocation{experimentNumber}, T2_values, 'Sheet1',
'B1:B9');
    disp('Data exported');
end
```

```
%Continue prompt:
rerunChoice = input('Do you want to analyse another experiment? Enter *n*
for no','s');
if isequal(rerunChoice,'n')
    disp('Done')
else
    disp('The last experiment analysed was')
    experimentNumber
    T2_tilpasning3_serialProcess;
end
```

T2_resultScoop.m

```
%This script collects all T2 results created by the combination of
%createT2_data and T2_tilpasning3_serialProcess to the source Excel sheet.
%It requires the presence of a highly specifically formatted Excel sheet
%in order to determine the folders over which to make a pass.

%Find number of rows to read:
excelFile = 'H:\DIRECTORY\SUBDIRECTORY\filename.xlsx';
readSheet = 'Sheet1';
constantReadRange = 'A3:B';

numberOfRows = xlsread(excelFile,'B1:B1');

charOfRows = num2str(numberOfRows);
readRange = strcat(constantReadRange,charOfRows);

%Read Excel experiment numbers and convert fo full fileformat:
[targetDirectory,masterDirectory] = xlsread(excelFile,readSheet,readRange);
targetDirectoryChar = num2str(targetDirectory);
targetDirectoryString = cellstr(targetDirectoryChar);
targetDirectoryTrim = strtrim(targetDirectoryString);

fullDirectory = strcat(masterDirectory,targetDirectoryTrim);
matrixSize = size(fullDirectory,1);
loopSize = matrixSize;

%Create an index of all excel result-file locations:
repT2_results= repmat({'\results.xlsx'},matrixSize,1);
resultsLocation = strcat(fullDirectory,repT2_results);

%Import the experiment results to MATLAB:
T2results = {matrixSize};
for ii=1:loopSize
    T2results{ii} = xlsread(resultsLocation{ii},'Sheet1','B1:B9');
end
T2resultsMat = cell2mat(T2results);
T2resultsExport = T2resultsMat';

%T2export =
%Write the results to the original Excel file
xlswrite(excelFile, T2resultsExport, 'Sheet1', 'E3');
disp('Data collection complete');
```

NMR_TimeFinder.m

```
%Program to find the acquisition time and date of a series of
%NMR experiments from the parameters included in its identifying
%audita.txt file and export the results to Excel.
%Requires a strictly formatted Excel base sheet.

fclose all
clear all

%Find number of rows to read:
excelFile = 'H:\DIRECTORY\SUBDIRECTORY\filename.xlsx';
readSheet = 'Sheet1';
constantReadRange = 'A3:B';

numberOfRows = xlsread(excelFile,'B1:B1');

charOfRows = num2str(numberOfRows);
readRange = strcat(constantReadRange,charOfRows);

%Read Excel experiment numbers and convert fo full fileformat:
[targetDirectory,masterDirectory] = xlsread(excelFile,readSheet,readRange);
targetDirectoryChar = num2str(targetDirectory);
targetDirectoryString = cellstr(targetDirectoryChar);
targetDirectoryTrim = strtrim(targetDirectoryString);

fullDirectory = strcat(masterDirectory,targetDirectoryTrim);
matrixSize = size(fullDirectory,1);
loopSize = matrixSize

%Create an index of all audita.txt files:
repAudita= repmat({'\audita.txt'},matrixSize,1);
auditaLocation = strcat(fullDirectory,repAudita);

%Extract a time data matrix from all audita.txt files:
timeStampT = cell(1,loopSize);
for a=1:loopSize
    fileInfo = dir(auditaLocation{a});
    timeStampT{a} = fileInfo.date;
end
timeStamp = timeStampT';

dateTime = regexp(timeStamp,' ','split');
timeLog = cat(1,dateTime{:});

%Export experiment times to Excel:
excelSheet = 'Sheet1';
excelRange = 'N3';
xlswrite(excelFile,timeLog,excelSheet,excelRange);

disp('done')
```

Appendix B: Pulse programs

^{1}H

PULPROG	= zg	Pulse program
AQ_mod	= qsim	Acquisition mode

TD	= 8192	FID size
NS	= 8	Number of scans
SW [ppm]	= 39.9894	Spectral width
AQ [s]	= 0.2048000	Acquisition time
FIDRES [Hz]	= 4.882813	FID resolution
FW [Hz]	= 125000.000	Filter width
RG	= determined by rga*	Reciever gain
DW [µs]	= 25.000	Dwell time
DE [µs]	= 6.00	Pre scan delay
O1 [Hz]	= 2449.66	Transmitter frequency offset
P1 [µs]	= 11	Pulse length
D1 [s]	= 5	Delay
LB [Hz]	= 4	Line broadening

*Automatic determination of reciever gain

```
;zg

;avance-version (12/01/11)

;1D sequence

;

;$CLASS=HighRes

;$DIM=1D

;$TYPE=

;$SUBTYPE=

;$COMMENT=


#include <Avance.incl>


"acqt0=-p1*2/3.1416"


1 ze

2 30m

  d1

  p1 ph1
```

go=2 ph31

30m mc #0 to 2 F0(zd)

exit

ph1=0 2 2 0 1 3 3 1

ph31=0 2 2 0 1 3 3 1

;pl1 : f1 channel - power level for pulse (default)

;p1 : f1 channel - high power pulse

;d1 : relaxation delay; 1-5 * T1

;ns: 1 * n, total number of scans: NS * TD0

;$Id: zg,v 1.10.8.1 2012/01/31 17:56:41 ber Exp $

CPMG oneshot

PULPROG	= cpmg_oneshot_all_echo	Pulse program
AQ_mod	= qsim	Acquisition mode
TD	= 2048	FID size
NS	= 8	Number of scans
SW [ppm]	= 10.0023	Spectral width
AQ [s]	= 0.2046976	Acquisition time
FIDRES [Hz]	= 4.885255	FID resolution
FW [Hz]	= 125000.000	Filter width
RG	= determined by rga*	Reciever gain
DW [µs]	= 99.950	Dwell time
DE [µs]	= 142.79	Pre scan delay
O1 [Hz]	= 4481.16	Transmitter frequency offset
P1 [µs]	= 7	Pulse length
D1 [s]	= 5	Delay
LB [Hz]	= 1	Line broadening

*Automatic determination of reciever gain

Inverse Recovery

	F2	F1

PULPROG	= t1ir		Pulse program
AQ_mod	= DQD		Acquisition mode
TD	= 2048	= 18	FID size
DS	= 4		Dummy scans
NS	= 8		Number of scans
IN_F [µs]		= 150.00	Increment for delay
SW [ppm]	= 9.9973	= 13.3298	Spectral width
AQ [s]	= 0.2048000	= 0.0013500	Acquisition time
FIDRES [Hz]	= 4.882813	= 740.742432	FID resolution
FW [Hz]	= 125000.000		Filter width
RG	= determined by rga*		Reciever gain
DW [µs]	= 100.000		Dwell time
DE [µs]	= 6.00		Pre scan delay
O1 [Hz]	= 3500.91	= 3500.91	Transmitter frequency offset
P1 [µs]	= 7		Pulse length
D1 [s]	= 3		Delay
LB [Hz]	= 3	= 0.3	Line broadening

*Automatic determination of reciever gain

```
;t1ir

;avance-version (12/01/11)

;T1 measurement using inversion recovery

;

;$CLASS=HighRes

;$DIM=2D

;$TYPE=

;$SUBTYPE=

;$COMMENT=


#include <Avance.incl>


"p2=p1*2"

"d11=30m"


"acqt0=-p1*2/3.1416"
```

```
1 ze
2 d1
  p2 ph1
  vd
  p1 ph2
  go=2 ph31
  d11 wr #0 if #0 ivd
  lo to 1 times td1
exit

ph1=0 2
ph2=0 0 2 2 1 1 3 3
ph31=0 0 2 2 1 1 3 3

;pl1 : f1 channel - power level for pulse (default)
;p1 : f1 channel -  90 degree high power pulse
;p2 : f1 channel - 180 degree high power pulse
;d1 : relaxation delay; 1-5 * T1
;d11: delay for disk I/O                  [30 msec]
;vd : variable delay, taken from vd-list
;ns: 8 * n
;ds: 4
;td1: number of experiments = number of delays in vd-list
;FnMODE: undefined

;define VDLIST
```

;this pulse program produces a ser-file (PARMOD = 2D)

;$Id: t1ir,v 1.12.8.1 2012/01/31 17:56:37 ber Exp $

NOESY

	F2	F1	
PULPROG	= noesyetgp		Pulse program
AQ_mod	= DQD		Acquisition mode
FnMODE		=Echo-Antiecho	Aquisition mode for 2D
TD	= 4096	= 1024	FID size
DS	= 16		Dummy scans
NS	= 8		Number of scans
SW [ppm]	= 14.9837	= 15.0000	Spectral width
IN_F [µs]		= 111.08	Increment for delay
AQ [s]	= 0.2277376	= 0.0568725	Acquisition time
FIDRES [Hz]	= 4.391018	= 17.583185	FID resolution
FW [Hz]	= 125000.000		Filter width
RG	= determined by rga*		Reciever gain
DW [µs]	= 55.600		Dwell time
DE [µs]	= 18.00		Pre scan delay
O1 [Hz]	= 2700.76	= 2700.76	Transmitter frequency offset
P1 [µs]	= 8		Pulse length
D1 [s]	= 2		Delay
LB [Hz]	= 1	= 0.3	Line broadening

;noesyetgp

;avance-version (12/01/11)

;2D homonuclear correlation via dipolar coupling

;dipolar coupling may be due to noe or chemical exchange.

;phase sensitive using Echo/Antiecho-TPPI gradient selection

;

;$CLASS=HighRes

;$DIM=2D

;$TYPE=

;$SUBTYPE=

```
;$COMMENT=


#include <Avance.incl>
#include <Grad.incl>
#include <Delay.incl>


"p2=p1*2"
"d11=30m"


"in0=inf1"


"d0=3u"


"DELTA=p16+d16+d0"
"DELTA1=p16+d16+8u"
"TAU=d8-p16-d16"


1 ze
2 d11
3 d1
  50u UNBLKGRAD
  p1 ph1
  DELTA
  p2 ph2
  d0
  p16:gp1*EA
  d16
```

```
 p1 ph3
 TAU
 p16:gp2
 d16
 p1 ph4
 DELTA1
 p2 ph5
 4u
 p16:gp3
 d16
 4u BLKGRAD
 go=2 ph31
 d11 mc #0 to 2 F1EA(calgrad(EA), caldel(d0, +in0) & calph(ph1, +180) & calph(ph31, +180))
exit

ph1=0 2
ph2=0
ph3=0 0 0 0 0 0 0 0 2 2 2 2 2 2 2 2
ph4=0 0 2 2 3 3 1 1
ph5=0
ph31=0 2 2 0 1 3 3 1 2 0 0 2 3 1 1 3

;pl1 : f1 channel - power level for pulse (default)
;p1 : f1 channel -  90 degree high power pulse
;p2 : f1 channel - 180 degree high power pulse
;p16: homospoil/gradient pulse
;d0 : incremented delay (2D)                    [3 usec]
```

```
;d1 : relaxation delay; 1-5 * T1

;d8 : mixing time

;d11: delay for disk I/O                  [30 msec]

;d16: delay for homospoil/gradient recovery

;inf1: 1/SW = 2 * DW

;in0: 1/(1 * SW) = 2 * DW

;nd0: 1

;ns: 8 * n

;ds: 16

;td1: number of experiments

;FnMODE: echo-antiecho


;use gradient ratio:      gp 1 : gp 2 : gp 3

;                         30 :   50 :   30


;for z-only gradients:

;gpz1: 30%

;gpz2: 50%

;gpz3: 30%


;use gradient files:

;gpnam1: SMSQ10.100

;gpnam2: SMSQ10.100

;gpnam3: SMSQ10.100


;$Id: noesyetgp,v 1.10.8.1 2012/01/31 17:56:34 ber Exp $
```

Appendix C: T_1 and T_2 procedure development

Number of components in T_1 analysis

Unlike the T_2 analysis, probing the results by both two- and three-component methods amounted to a considerable increase in time requires for analysis of T_1 data. In order to determine which approach should be used, both methods were used to analyse some samples so that comparisons could be drawn. In addition, this technique gives results on a per-peak basis, and the proper way to handle multiple peaks must thus be determined.

The fit of the experimental data to the fitting curve is displayed for select experiments, in the form of screenshots from the analysis in TopSpin. Only the fitting curves of the cyclopentane peak and eventual side peaks are shown, as the fitting curve for the water peak was near perfect for all experiments, and did not noticeably change over the course of the experiments.

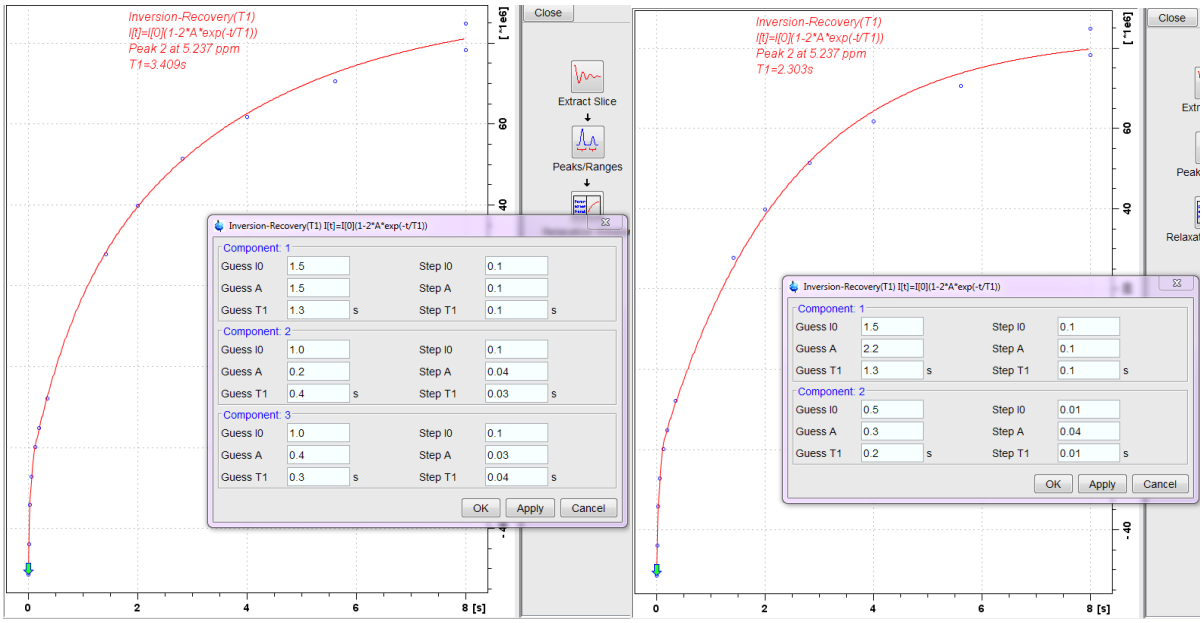

Figure C1: Comparison of the three-component (left) and two-component (right) fitting functions of the cyclopentane peak in B3Fa2 T_1 inverse recovery experiment 1.

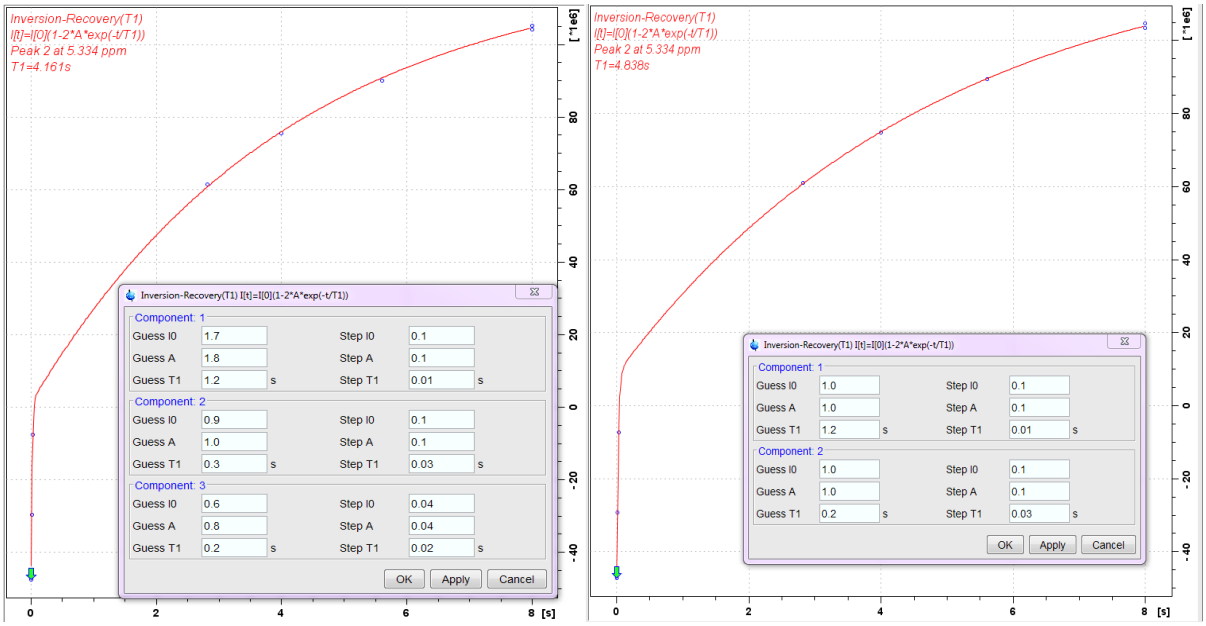

Figure C2: Comparison of the three-component (left) and two-component (right) fitting functions of the cyclopentane peak in B3Fa2 T_1 inverse recovery experiment 6. A very specific set of guesses was needed to achieve a good fit for the three-component analysis.

The same trend was observed for nearly all experiments: The three component approach resulted in a slightly better fit than its two component counterpart.

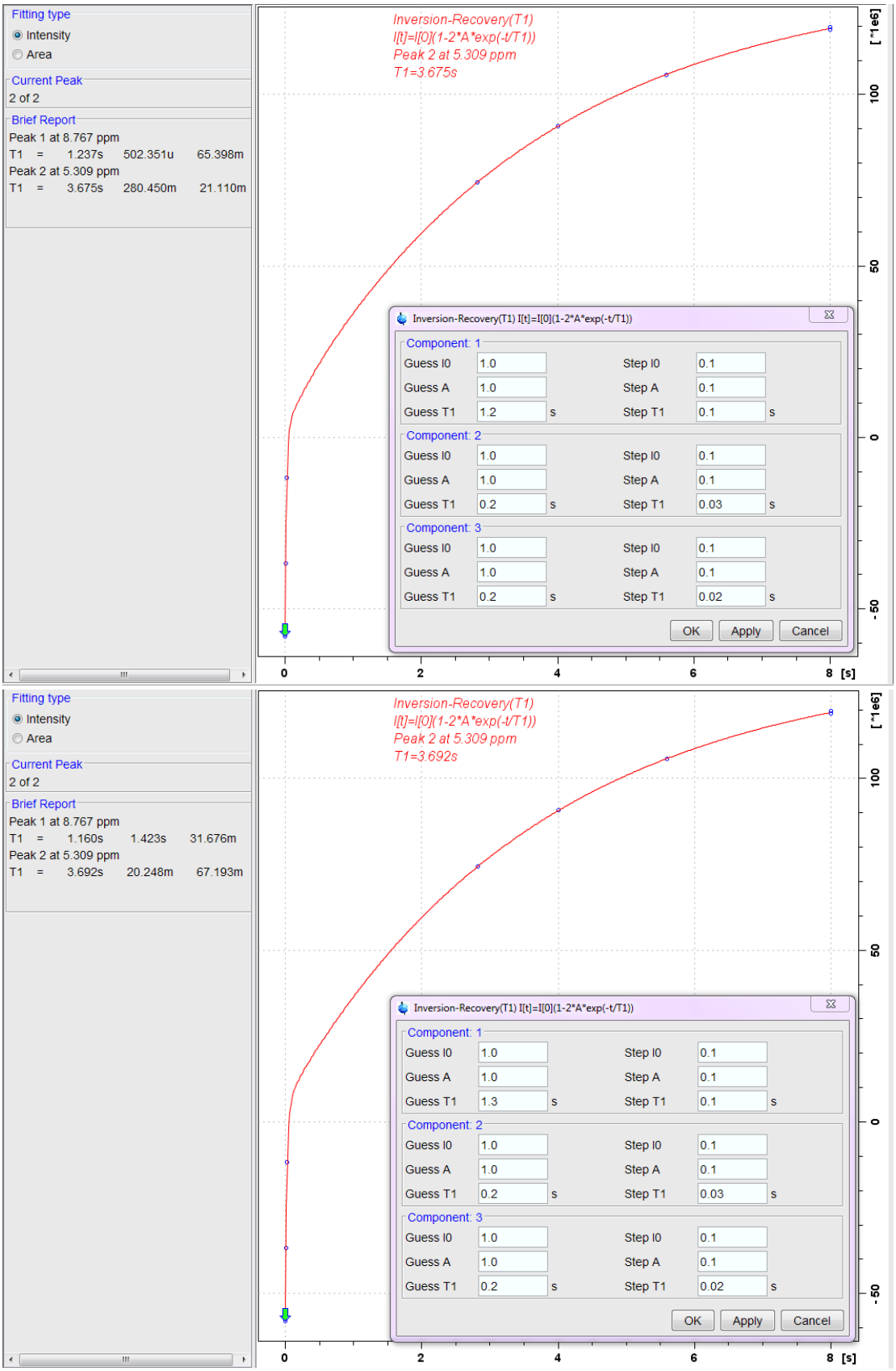

Figure C3: Two sets of three-component guesses and results for B3Fa2 T_1 inverse recovery experiment 9, along with the fitting function of the cyclopentane peak. Results are shown under Brief Report. A change in the guess for Component 1 T1 from 1.2 to 1.3 leads to a large difference in results without change in the fitting function.

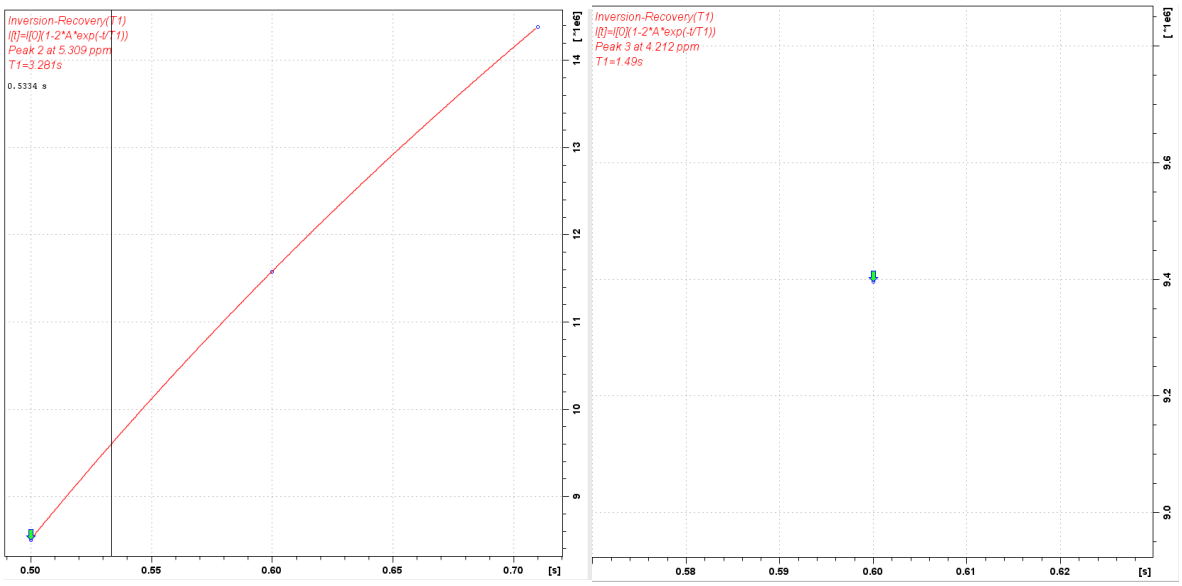

Figure C4: Appearance of cyclopentane peak fitting curves at 280.5 K, here represented by peak 2 and 3 in B3Fa2 T_1 inverse recovery experiment 14. Peak 2 corresponds to the main cyclopentane peak. Peak 3 corresponds to a side peak that appeared for experiments 13, 14, 15 and 22 through 25. It was impossible to acquire a fit for, yet necessary for achieving a proper fit for peak 2. The water peak fitting curve kept the same appearance and good fit as earlier for both the two- and three-component approaches, and is therefore not presented.

In the second part of this analysis, the T_1 results found by both approaches are compared graphically.

The results for the respective components of two- and three-component analysis were then compared in order to determine apparent spread, and whether the components seem to model the same information.

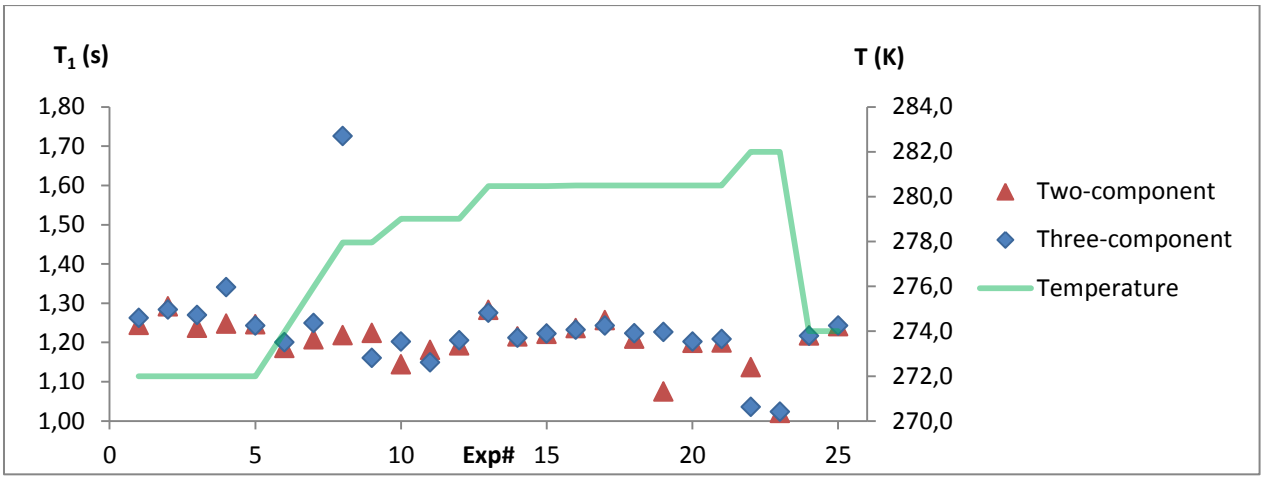

Figure C5: The results for the water peak component 1 from two- and three-component analysis of all B3Fa2 T_1 measurements as a function of experiment number.

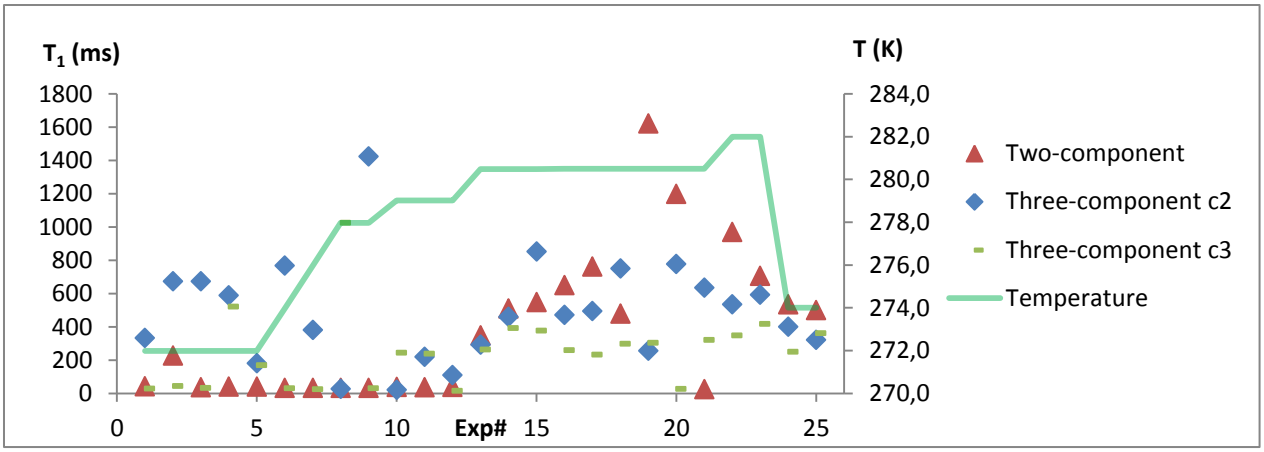

Figure C6: The results for the water peak component 2 from two- and three-component analysis of all B3Fa2 T_1 measurements as a function of experiment number. Component 3 from the three-component analysis is also included, as it has no other two-component analogue with which to compare.

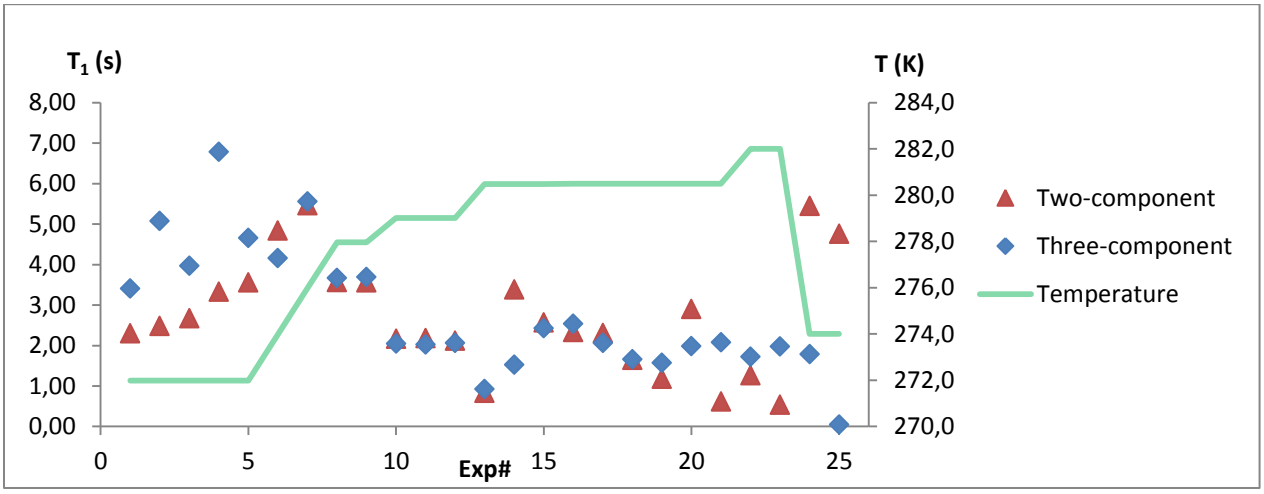

Figure C7: The results for the cyclopentane peak component 1 from two- and three-component analysis of all B3Fa2 T_1 measurements as a function of experiment number.

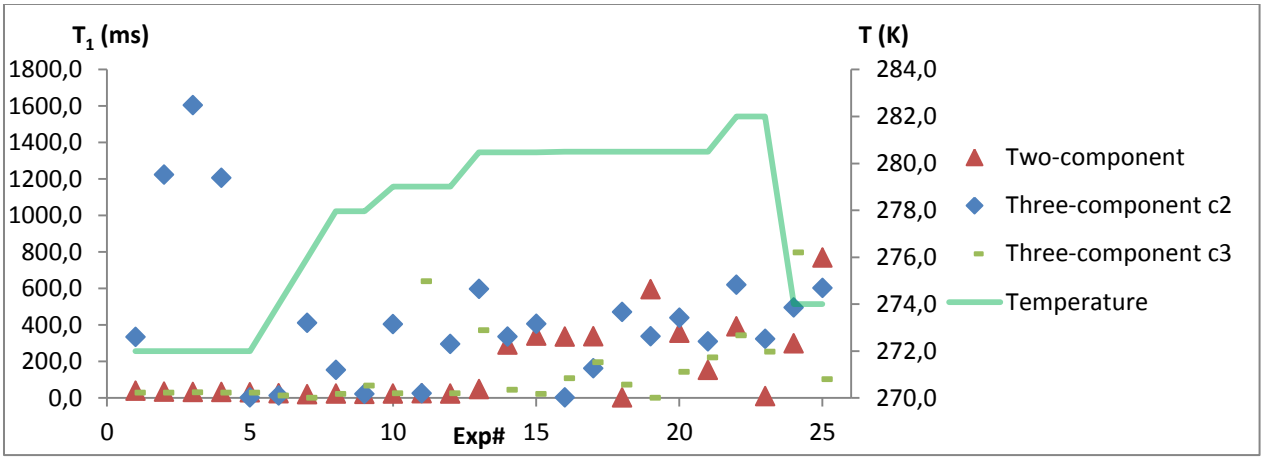

Figure C8: The results for the cyclopentane peak component 2 from two- and three-component analysis of all B3Fa2 T_1 measurements as a function of experiment number. Component 3 from the three-component analysis is also included, as it has no other two-component analogue with which to compare.

Initial determination of T_2 guess range

The first range of T_2 guesses was determined by application of the scripts provided by Totland to the B3Fa2 sample, which was chosen due to the continuous experiments performed at several different temperatures for this sample. The *T2_tilpasning3.m* script was run on the first experiment, changing the guesses until a good fit was achieved. The same script was then consecutively run on all experiments, changing the initial guesses in an iterative fashion whenever the fitting function deviated from earlier quality, assisted by graphical feedback from the script.

Table C1: The guesses found to give a good fit during the T_2 analysis of B3Fa2 using the T2_tilpasning3.m script. Guesses are the expected T_2 value in milliseconds. The Exp.range specifies which experiments were subjected to which guesses.

	One-comp	**Two-comp**		**Three-comp**		
Exp. range	**c1**	**c1**	**c2**	**c1**	**c2**	**c2**
1-126	100	250	50	400	100	50
127-137	100	300	50	600	100	50
138-143	1000	1000	100	1000	200	50
143-253	1200	1200	100	1200	300	50

Streamlining T_2 analysis

The MATLAB scripts provided for the analysis of T_2 experiments were found to be lacking the interface capabilities necessary to efficiently analyse the number of experiments performed in this thesis. The most problematic aspect was the cumbersome conversion of results to tabular data, as the original procedure relied on reading results off a figure and manually entering the results to a spreadsheet, one experiment at a time. The scripts were therefore rewritten with additional functions to automate the results collection as well as other workflow improvements, as discussed in the previous chapter. To maximise the utility of these new scripts, a robust analysis procedure had to be established in order to not sacrifice quality of results for quicker analysis.

In order to find an estimate of how sensitive the results are to changing the guesses, two new analyses of the results from sample B3Fa2 were performed. All CMPG experiments of the B3Fa2 sample had already been analysed using the old scripts, and thus provides a reference point for result quality.

Two variants of the new T_2 analysis script was written, and a decision had to be made as to which script should be used. The first script, *T2_tilpasning3_serialProcessing.m*, uses a procedure that closely mimics the one in the original *T2_tilpasning3.m* script. The only difference between them is the added utility of the new code, as it still provides graphical feedback and allows efficiently changing the guesses between every experiment. As such, the method was already validated by the analysis of B3Fa2 using the old script. It is the slowest of the proposed methods, but must also be considered the most robust, especially for small experiment series.

A second option was to use the *T2_tilpasning3_serialProcessingRapid.m* script, which performs the exact same core function as its relative. However, this script does not query the guesses for every experiment and provides no feedback. It instead relies on pre-entered guesses and verification through comparison of all results, allowing rapid processing of even series of several hundred experiments. Although the experiment-to-experiment approach is lost, the number of performed experiments in this thesis ensures that any areas of high deviation should easily be identified from

the resulting graphs, the creation of whose have also been automated. By identifying such regions, the analysis can be rerun for these specific regions using a new set of guesses. As a result, the success criterion of this approach relies on the robustness of the underlying fitting function: If a propensity for overfitting is present, then this approach will most likely introduce a bias to the T_2 results, trending towards values determined earlier for other samples. If areas of poor fit are found to return a high spread in T_2 values, however, this approach will be superior to the former due to its much shorter analysis time and facility of operation. These qualities will also help offset any quality difference, as quicker analysis facilitates performing additional analyses to improve or validate results.

It is reasonable to assume that the second option is a near equivalent of the first in terms of analysis quality given large datasets, as the two methods do apply the same iterative process of changing guesses, although by different approaches. As the second method had not previously been validated, the analysis was performed using the *T2_tilpasning_serialProcessingRapid.m* script.

During the analysis, guess values were chosen as to lie near the midpoint between the values used for different ranges of experiments, as found previously.

Table C2: The guesses used during the T_2 analysis of B3Fa2 with the T2_tilpasning3.m script (Old) and the T2_tilpasning3_serialProcessingRapid.m script (New). Guesses are the expected T_2 value in milliseconds. The Exp.range specifies which experiments were subjected to which guesses.

		One-comp	Two-comp		Three-comp		
Process	Exp. range	c1	c1	c2	c1	c2	c2
Old	1-126	100	250	50	400	100	50
	127-137	100	300	50	600	100	50
	138-143	1000	1000	100	1000	200	50
	143-253	1200	1200	100	1200	300	50
Process	Exp. range	c1	c1	c2	c1	c2	c2
New	All	500	500	100	700	200	50

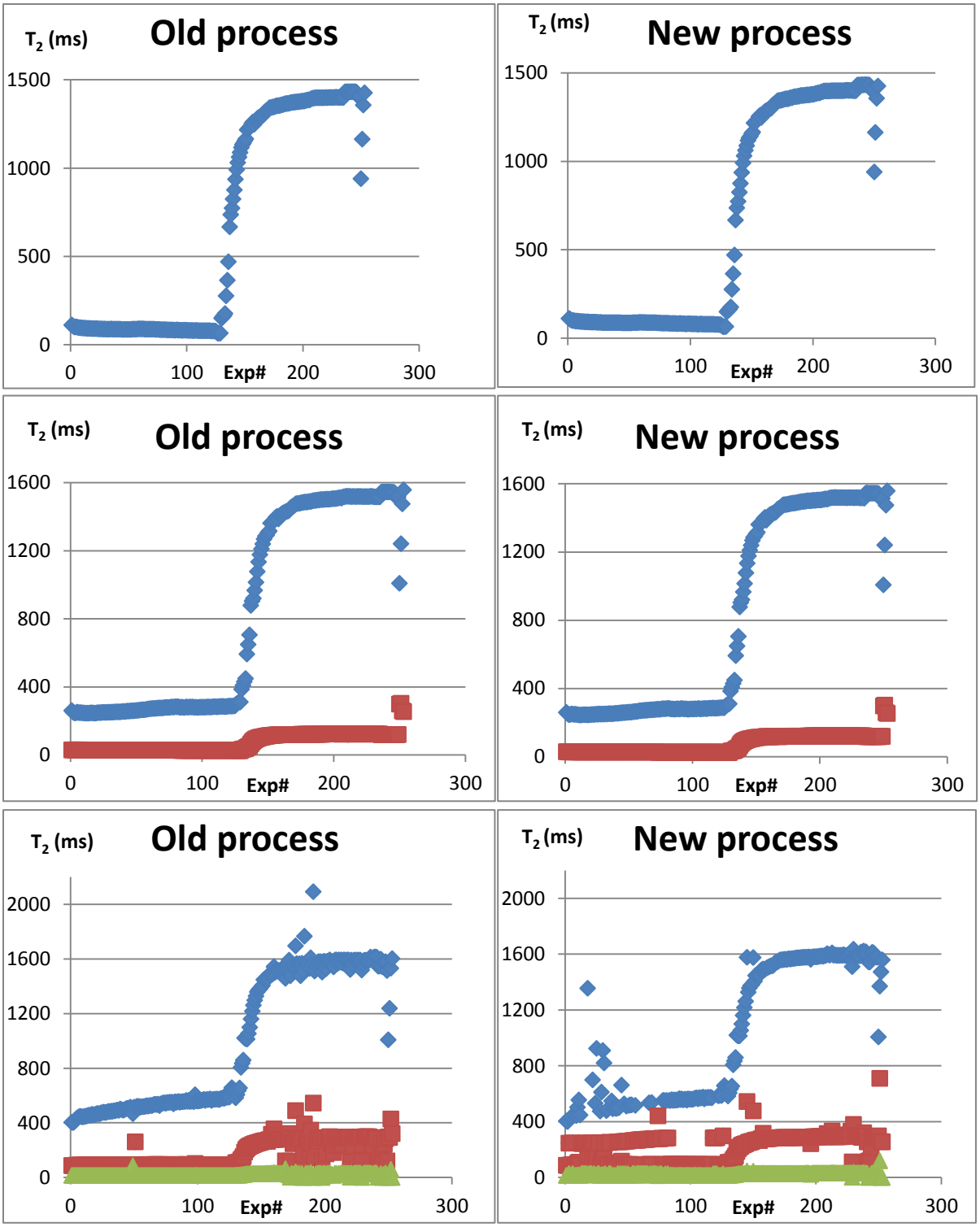

Figure C9: From top to bottom: The one-, two- and three-component results for the old and new T_2 data processing methods using one set of guesses for the new analysis.. The new process is seen to yield near equal results as the old one. Deviations are seen for the three-component results, but these are easily identified as such.

The process was then repeated using two sets of guesses for the three component analysis.

Table C3: The guesses used during the second T_2 analysis of B3Fa2 with the T2_tilpasning3_serialProcessingRapid.m script (New). Only the three-component guesses were

altered. Guesses are the expected T_2 value in milliseconds. The Exp.range specified which experiments were subjected to which guesses.

		One-comp	Two-comp		Three-comp		
Process	**Exp. range**	**c1**	**c1**	**c2**	**c1**	**c2**	**c2**
New	1-142	500	500	100	400	100	30
	143-253	500	500	100	1200	300	50

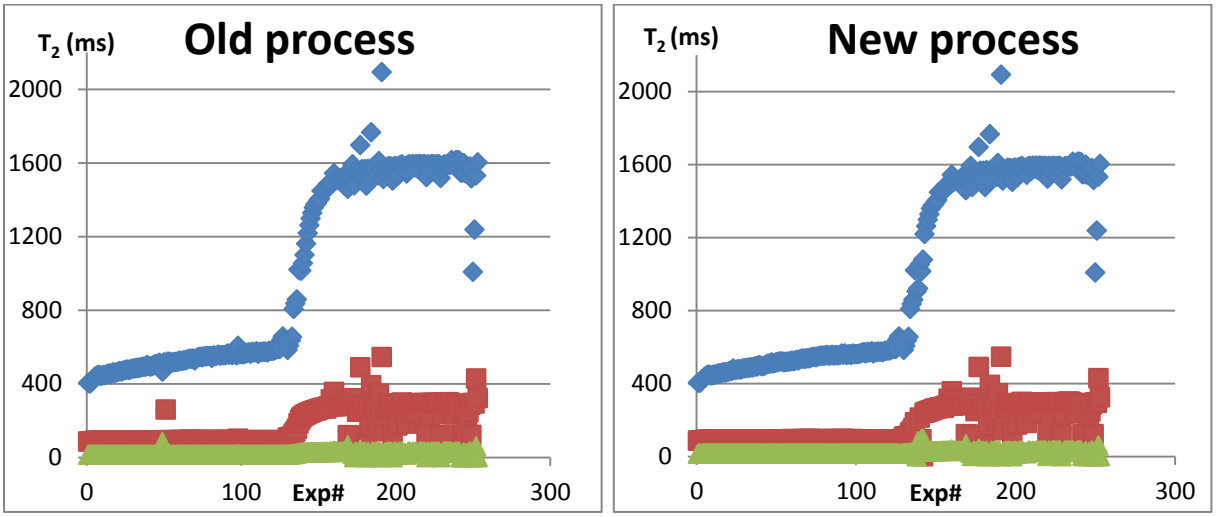

Figure C10: The three-component results for the old and new T_2 data processing methods using two sets of guesses for the New process analysis. Process parameters for the New process are listed in Table C3, while the parameters for the Old process remained the same and can be found in Table C2. The results are seen to be near equal, with the new process perhaps providing better results.

Table C4:Guesses for low-guess B3Fa3 T_2 analysis. Guesses are the expected T_2 value in milliseconds. The Exp.range specifies which experiments were subjected to which guesses.

Exp.range	1comp	2comp1	2comp2	3comp1	3comp2	3comp3
1-6	5	5	1	6	3	1
7-	5	5	1	12	6	1

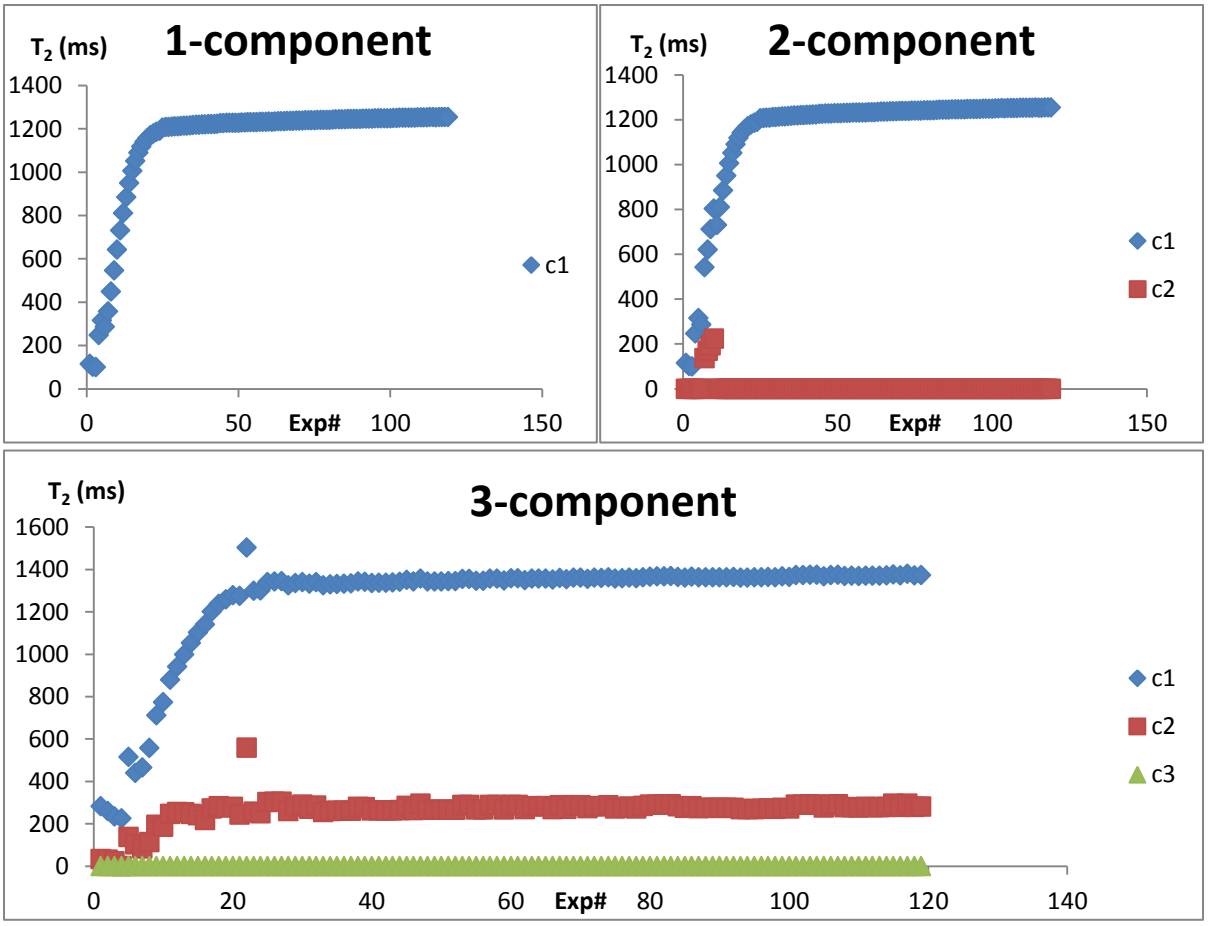

Figure C11: The one-, two- and three-component results from the second T_2 analysis of B3Fa3 using the low guesses in Table C4 and the T2_tilpasning3_serialProcessingRapid.m script. Note that c3 trends at a value of approximately 0.5 ms.

Further verification of the applicability of the method was found during analyses of samples without a previous reference. The steps in the process towards finding final T_2 results are shown below, using the analysis B3Fa3 as an example. The guessranges was chosen on the basis of earlier results, as all samples should display the same T_2 behaviour at the same temperatures, and the experiment ranges was determined from regions of temperature change expected to lead to an increase in T_2.

Table C5: Guesses for the initial T_2 analysis of B3Fa3. Guesses are the expected T_2 value in milliseconds. The Exp.range specifies which experiments were subjected to which guesses.

Exp.range	1comp	2comp1	2comp2	3comp1	3comp2	3comp3
1-119	500	500	100	600	300	30

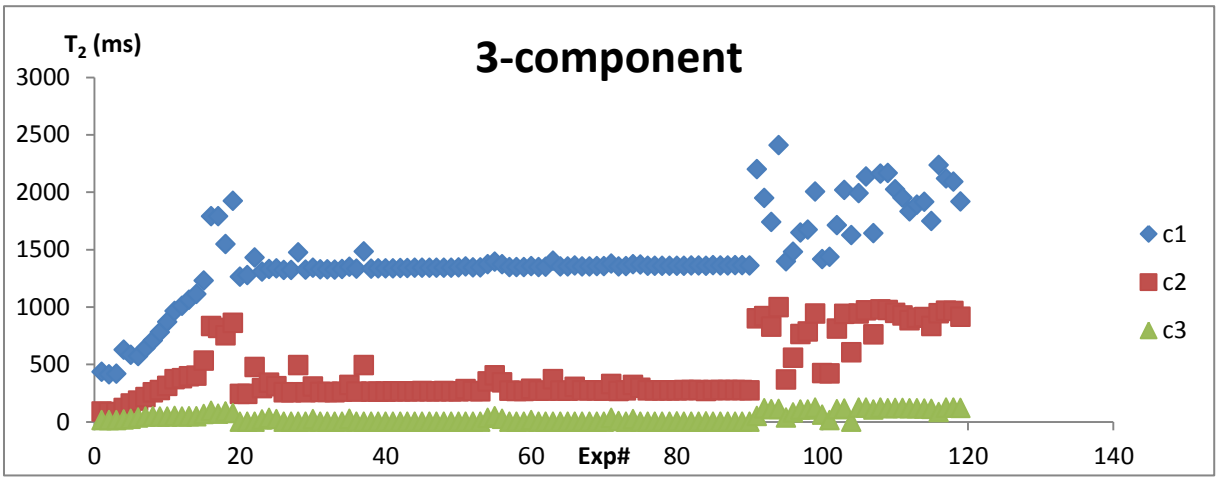

Figure C12: The three-component results from the initial T_2 analysis of B3Fa3 using the guesses in Table C5 and the T2_tilpasning3_serialProcessingRapid.m script. Results for the one- and two-component approaches are seen to correlate well with results for previous samples. Deviations in the three component approach are clearly visible.

Table C6: Guesses for the second iteration of B3Fa3 T_2 analysis. Guesses are the expected T_2 value in milliseconds. The Exp.range specifies which experiments were subjected to which guesses.

Exp.range	1comp	2comp1	2comp2	3comp1	3comp2	3comp3
1-6	300	300	100	500	100	30
7-119	500	500	100	1200	200	30

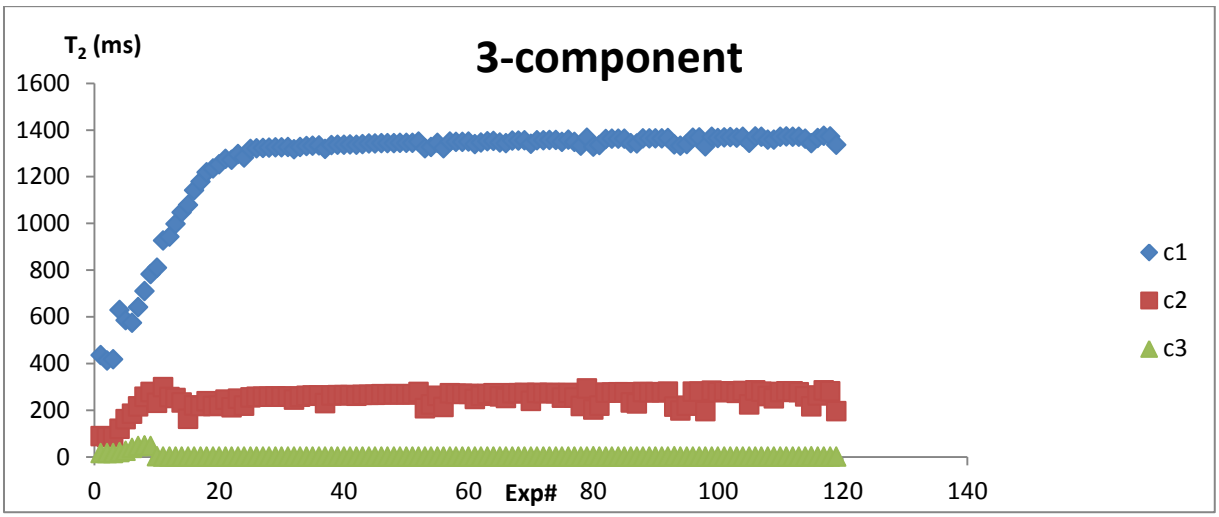

Figure C13: The three-component results from the third iteration of B3Fa3 T_2 analysis, using the guesses in Table C6 and the T2_tilpasning3_serialProcessingRapid.m script. Note that c3 trends at a value of approximately 0.7 ms. The one- and two-component approaches yielded equal results as earlier.

To verify that the T_2 results were not a result of overfitting to a local solution, a new analysis was run on sample B3Fa3 using a much lower guessrange. The results also provide a measurement of the robustness of the analysis towards faulty guesses. The results were found to be near equal to those found earlier, except for c2 of the two-component approach. Here, a few points fell near the

previously determined line during the initial period of growth, but the majority of results were found to lie close to zero.

A new iteration was performed where c3 was assigned a guess of 1 ms, consistent with earlier results. The remaining guesses were also selected close to the observed T_2 values for the respective components.

Table C7: Guesses for low-guess c3 B3Fa3 three component T_2 analysis. Guesses are the expected T_2 value in milliseconds. The Exp.range specifies which experiments were subjected to which guesses.

Exp.range	3comp1	3comp2	3comp3
1-6	500	100	30
7-11	1200	250	50
12-119	1200	250	1

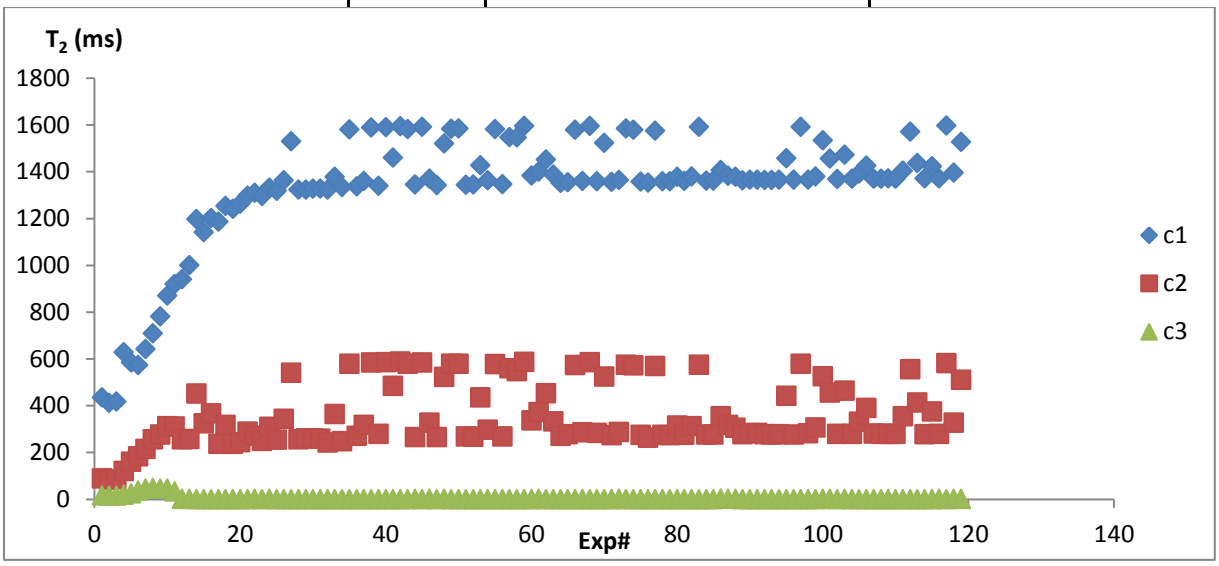

Figure C14: The three-component results from the fourth iteration of B3Fa3 T_2 analysis, using the guesses in Table C7 and the T2_tilpasning3_serialProcessingRapid.m script.

As the results seemed to indicate the presence of other T_2 solutions at 1600 and 600 ms, a new set of analyses was performed to attempt to verify these values. The analysis returned graphs of high spread, trending towards earlier values, showing that the second set of values most likely originated from overfitting to a local solution.

Table C8: Guesses for the attempt to find different T_2 ranges through B3Fa3 T_2 analysis. Guesses are the expected T_2 value in milliseconds. The Exp.range specifies which experiments were subjected to which guesses.

Exprange	1comp	2comp1	2comp2	3comp1	3comp2	3comp3
1-6	200	200	100	500	100	30
7-11	500	500	100	1200	250	50
12-119	1600	1600	600	1600	600	30

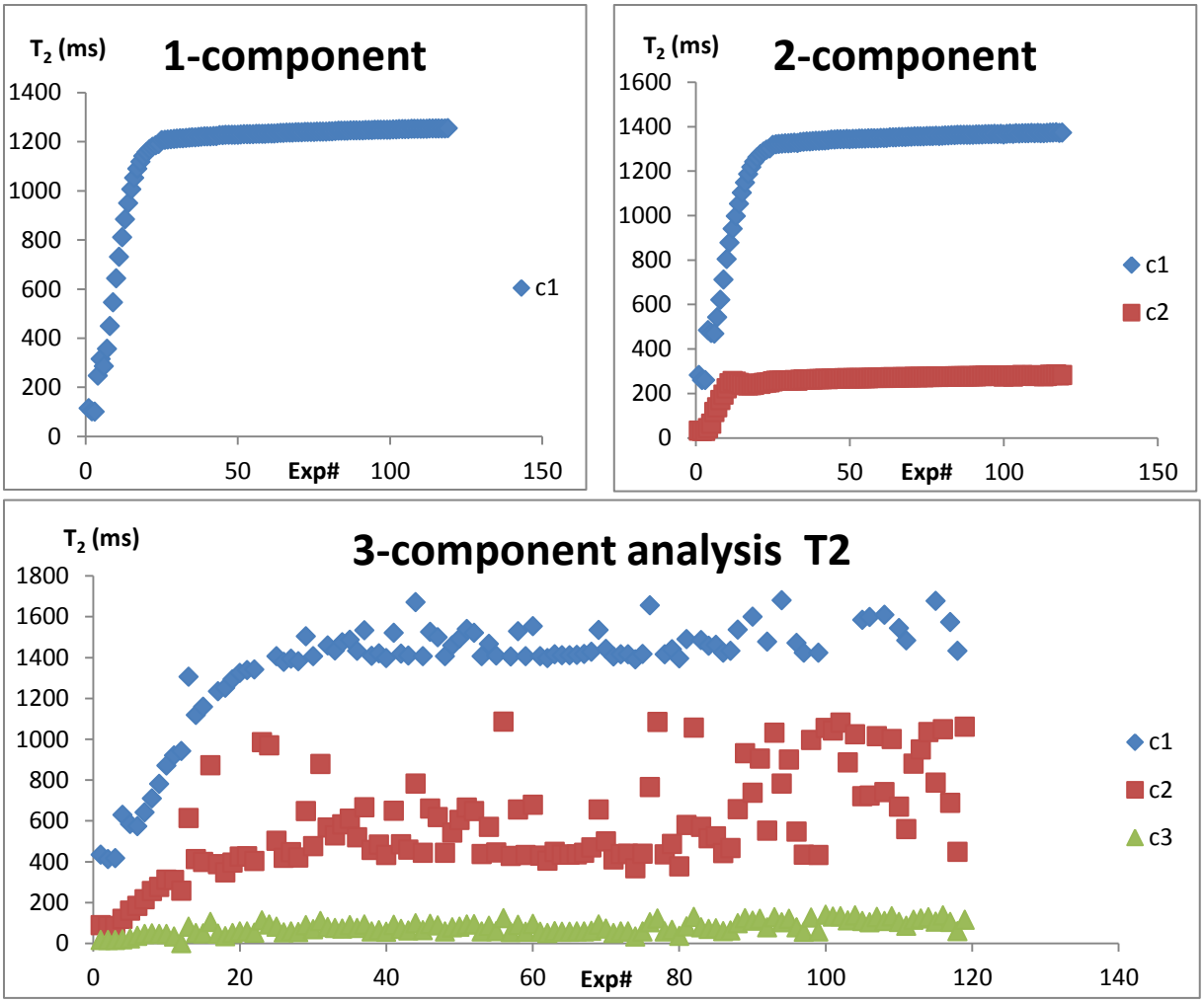

Figure C15: The one-, two- and three-component results from the attempt to verify a second set of T_2 values for B3Fa3 using the guesses in Table C9 and the T2_tilpasning3_serialProcessingRapid.m script.

Appendix D: Preliminary experiments

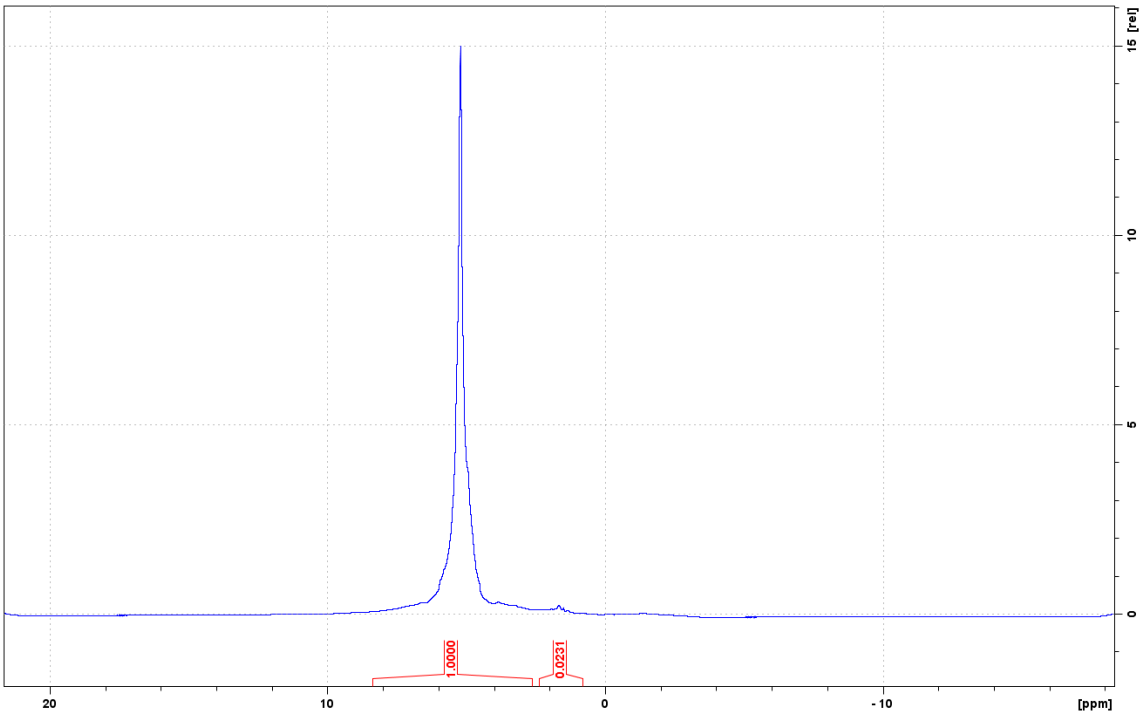

Figure D1: The integrated water (left) and cyclopentane (right) peaks for a batch 1 hydrate sample. The spectrum was acquired at 274 K using 8 scans, a sweep width of 40 ppm, a pulse length of 11 µs, a d1 relaxation time of 20 s and a receiver gain of 4.

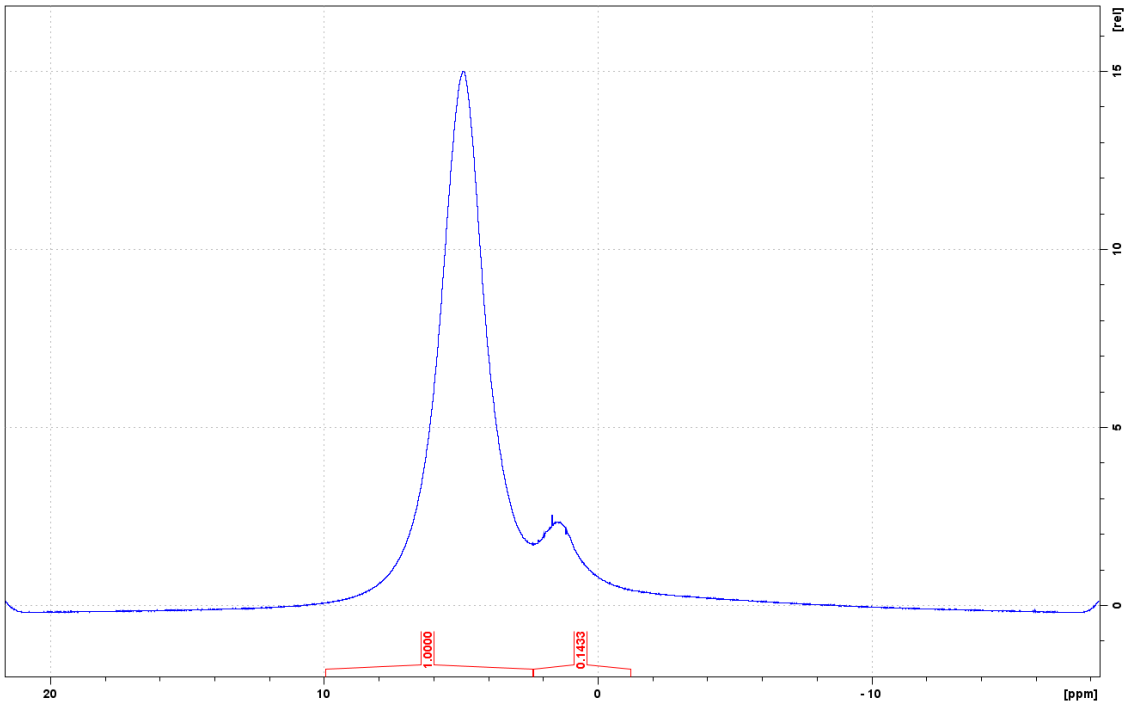

Figure D2: The integrated water (left) and cyclopentane (right) peaks for the batch 2 hydrate sample B2F2. The spectrum was acquired at 274 K using 8 scans, a sweep width of 40 ppm, a pulse length of 11 µs, a d1 relaxation time of 5 s and a receiver gain of 4.

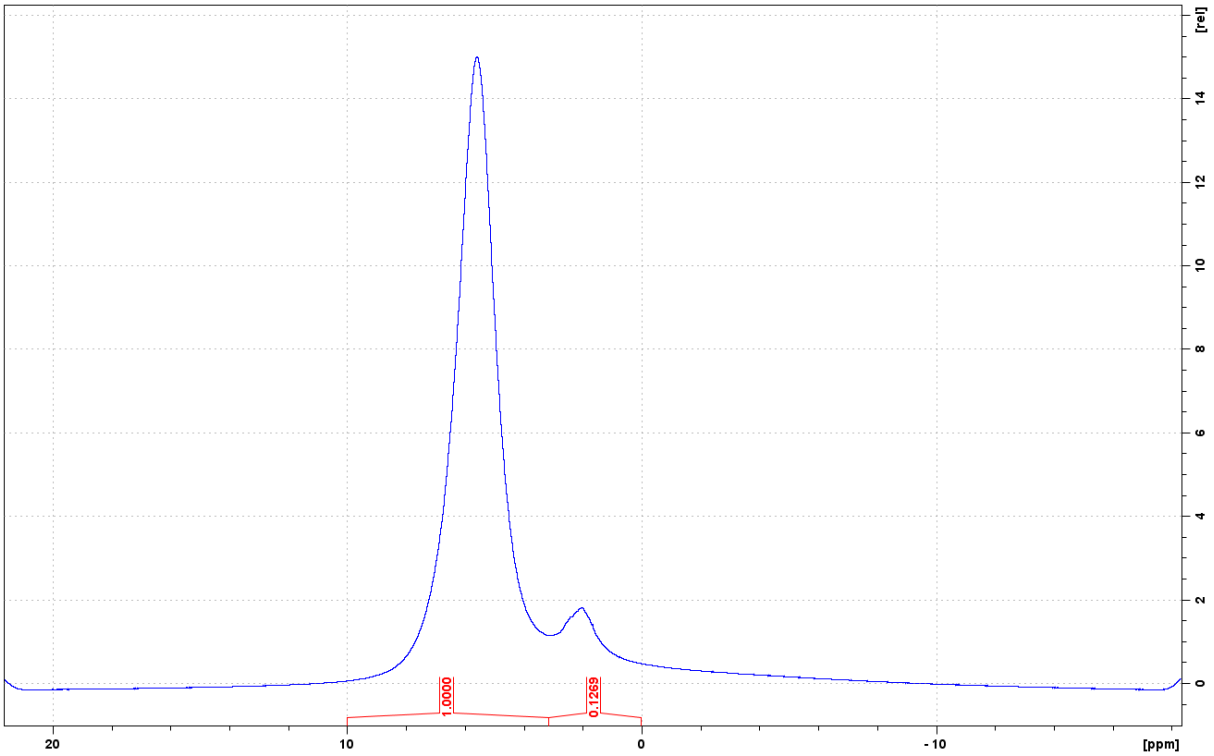

Figure D3: The integrated water (left) and cyclopentane (right) peaks for the batch 3 hydrate sample B3Fb. The spectrum was acquired at 274 K using 8 scans, a sweep width of 40 ppm, a pulse length of 11 µs, a d1 relaxation time of 5 s and a receiver gain of 8.

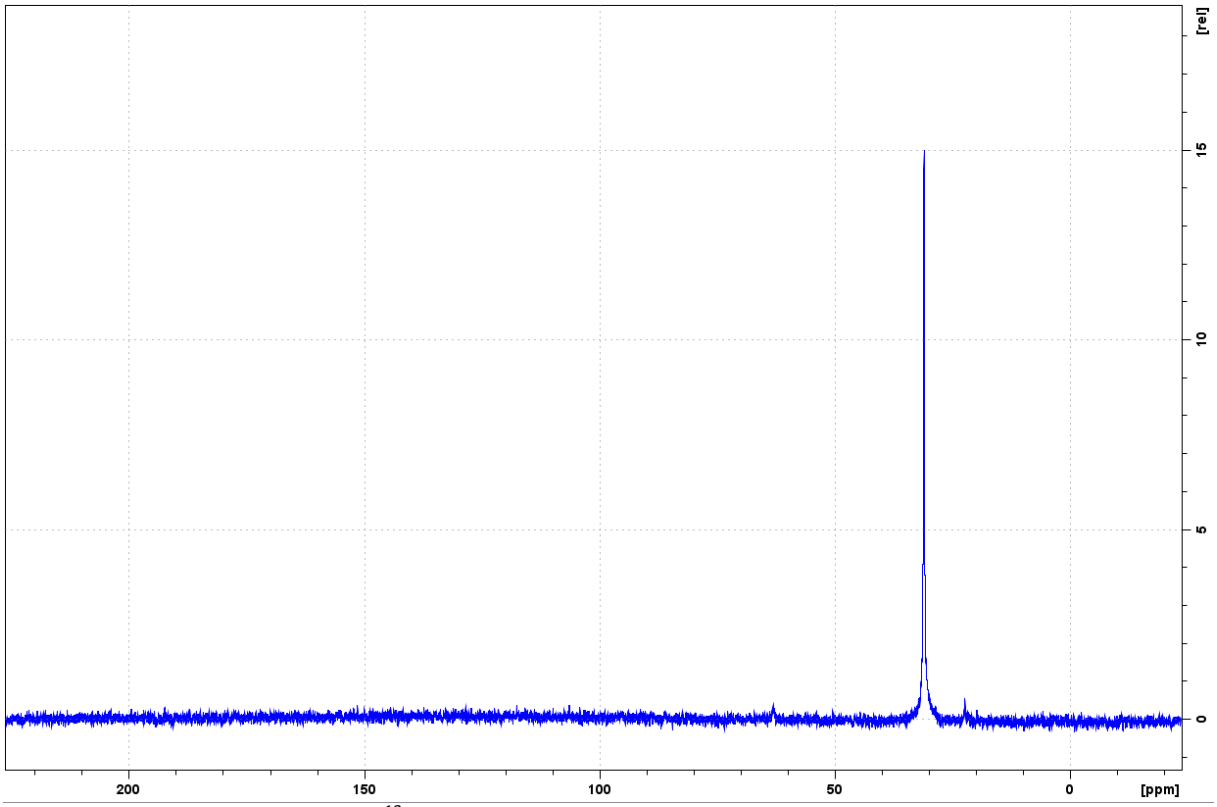

Figure D4: The viability of using ^{13}C MAS NMR on a batch 1 sample was verified. A discernable peak could be seen after only a few scans, even for these wet hydrates. However, the experiment was cut short after 1479 out of 14000 scans due to loss of temperature control. The frequent occurrence of

these temperature increases meant that the ^{13}C approach were abandoned early in the thesis work, as experiments averaging results over several hours are not robust towards changing conditions.

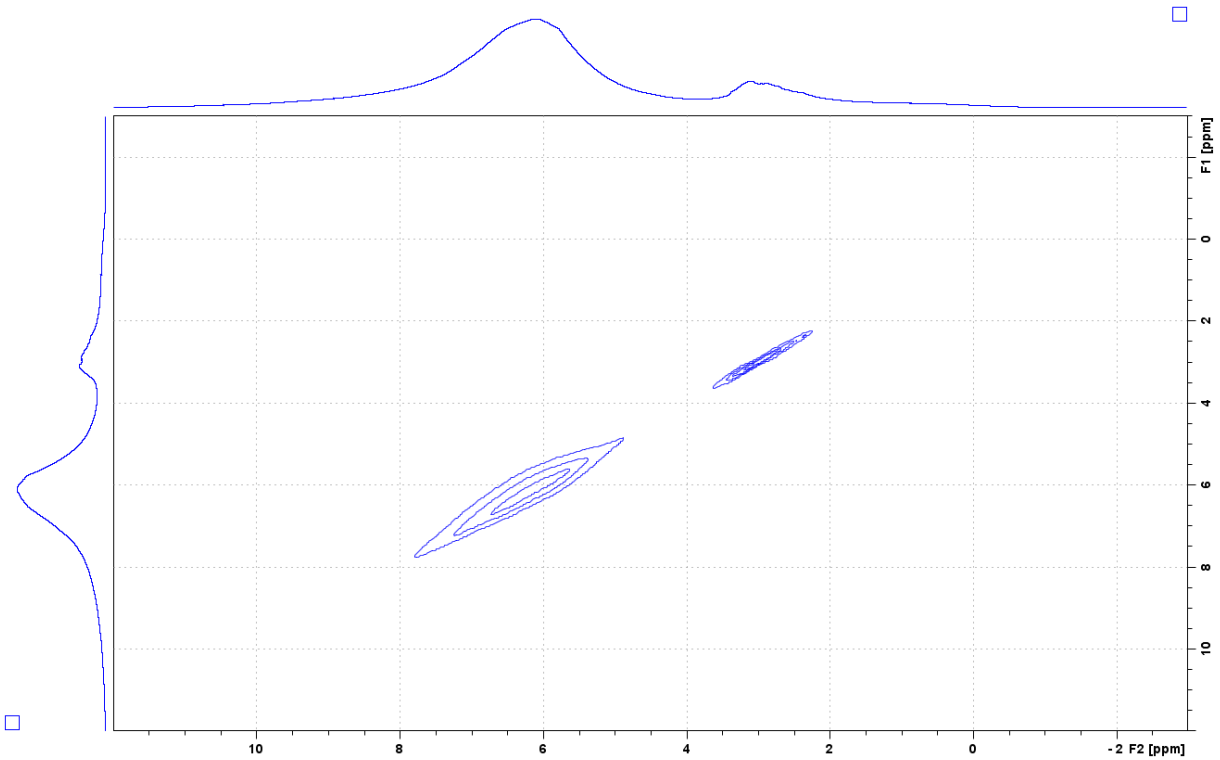

Figure D5: The first NOESY 2D spectrum of the second NOESY series with an external reference ^{1}H spectrum taken at the start of the series on both axes.

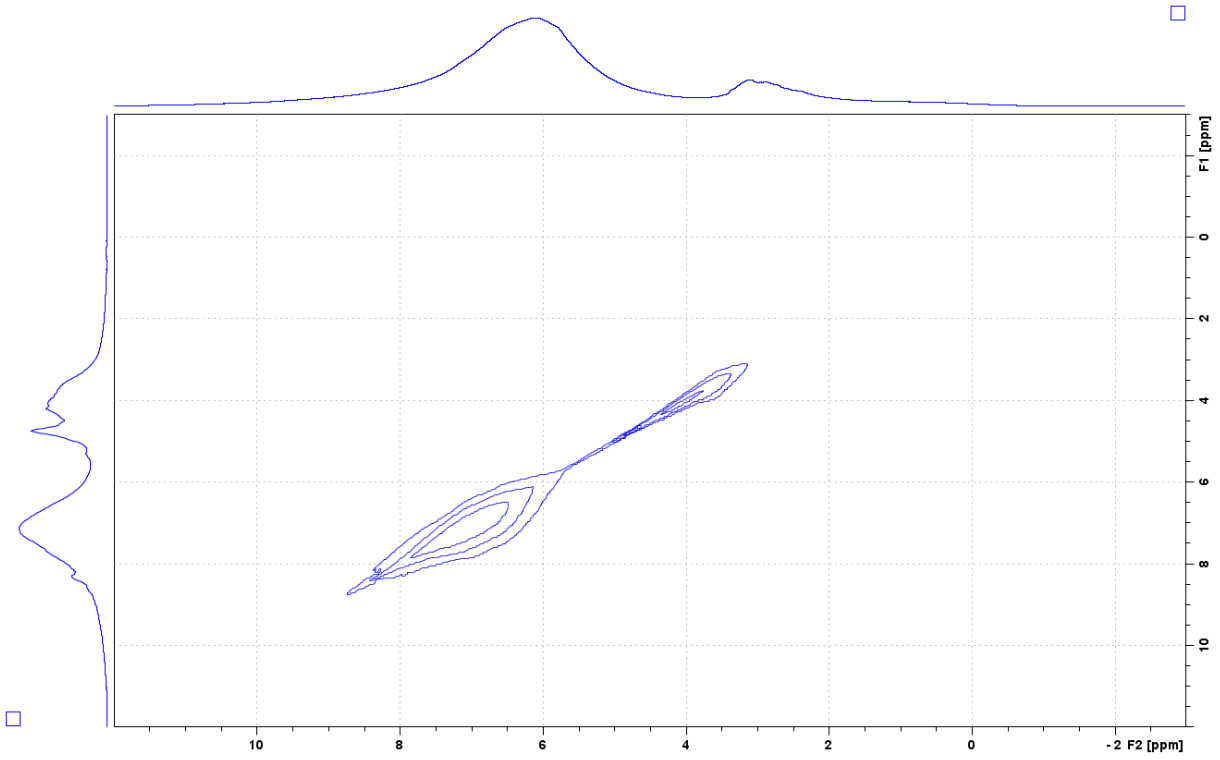

Figure D6: The third NOESY 2D spectrum of the second NOESY series with an external reference ^{1}H spectrum taken at the start of the series on the F2 axis.

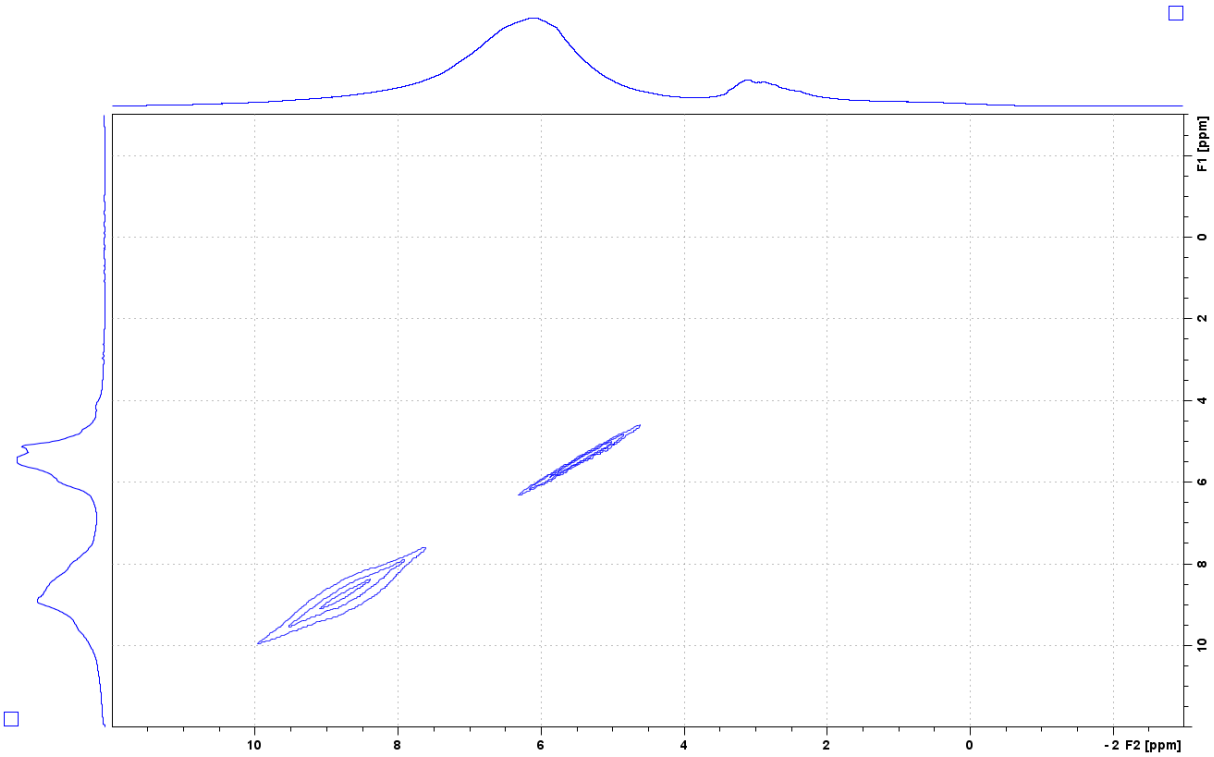

Figure D7: The fourth NOESY 2D spectrum of the second NOESY series with an external reference ^{1}H spectrum taken at the start of the series on the F2 axis.

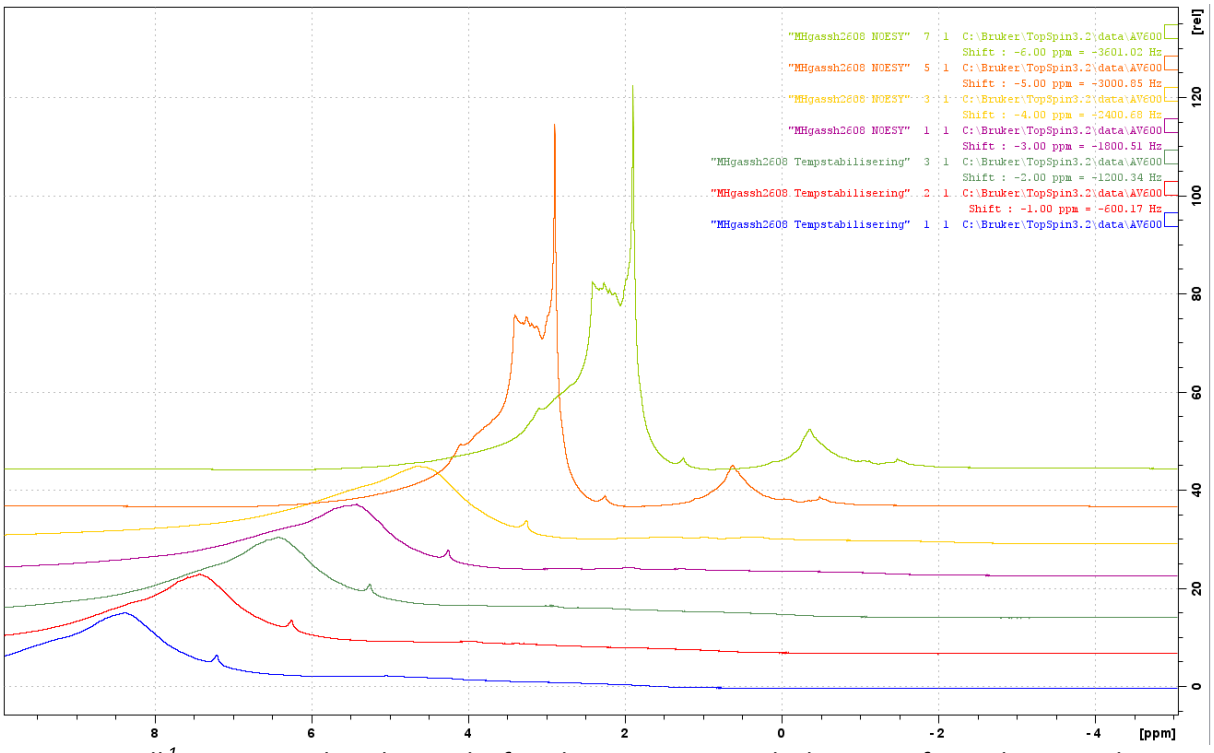

Figure D8: All ^{1}H spectra taken during the fourth NOESY series, which was performed on sample B3Fa7. From front to back, the three first spectra are verification of sample stability after insertion, whilst the following four are taken right before, between and after the three NOESY spectra, in that

order. It shows that a large change occurred somewhere between initiation and finalisation of the second NOESY experiment.

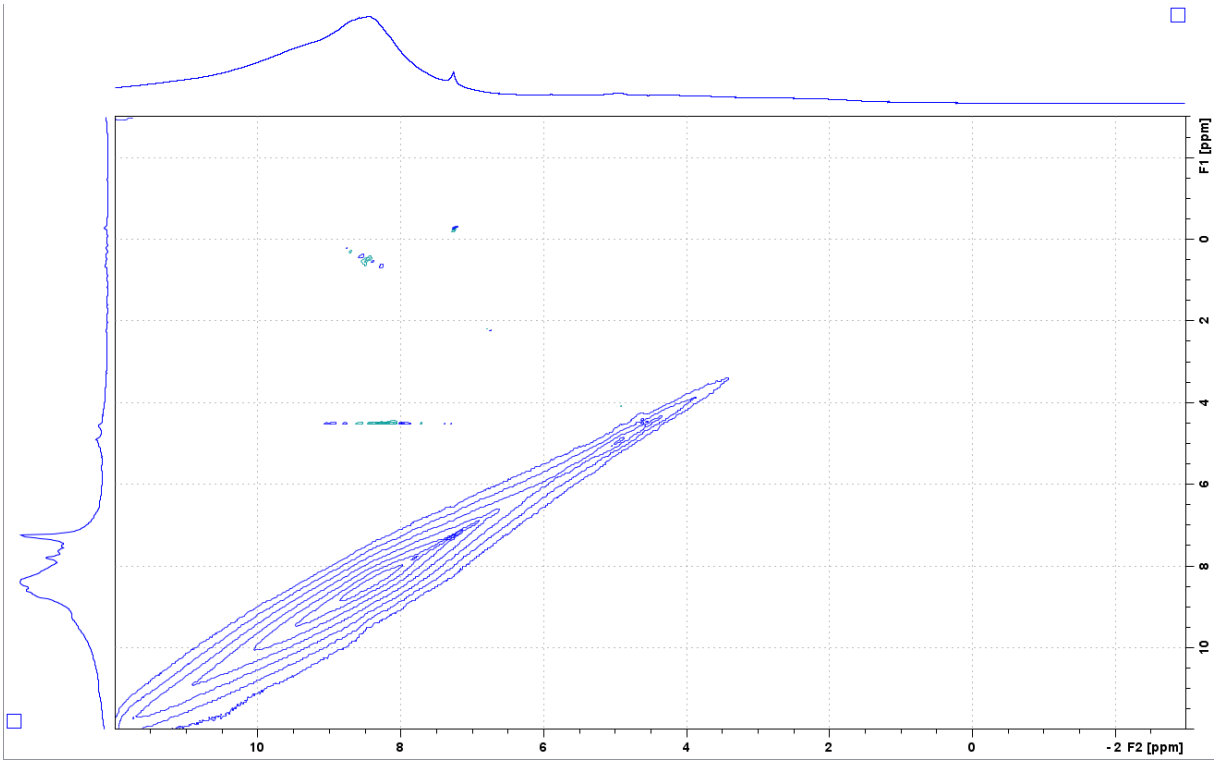

Figure D9: The first NOESY spectrum of the fourth NOESY series, performed on sample B3Fa7. An external reference ^{1}H spectrum taken right before acquisition is shown on the F2 axis. Note that the peaks lay significantly upfield of expected chemical shifts.

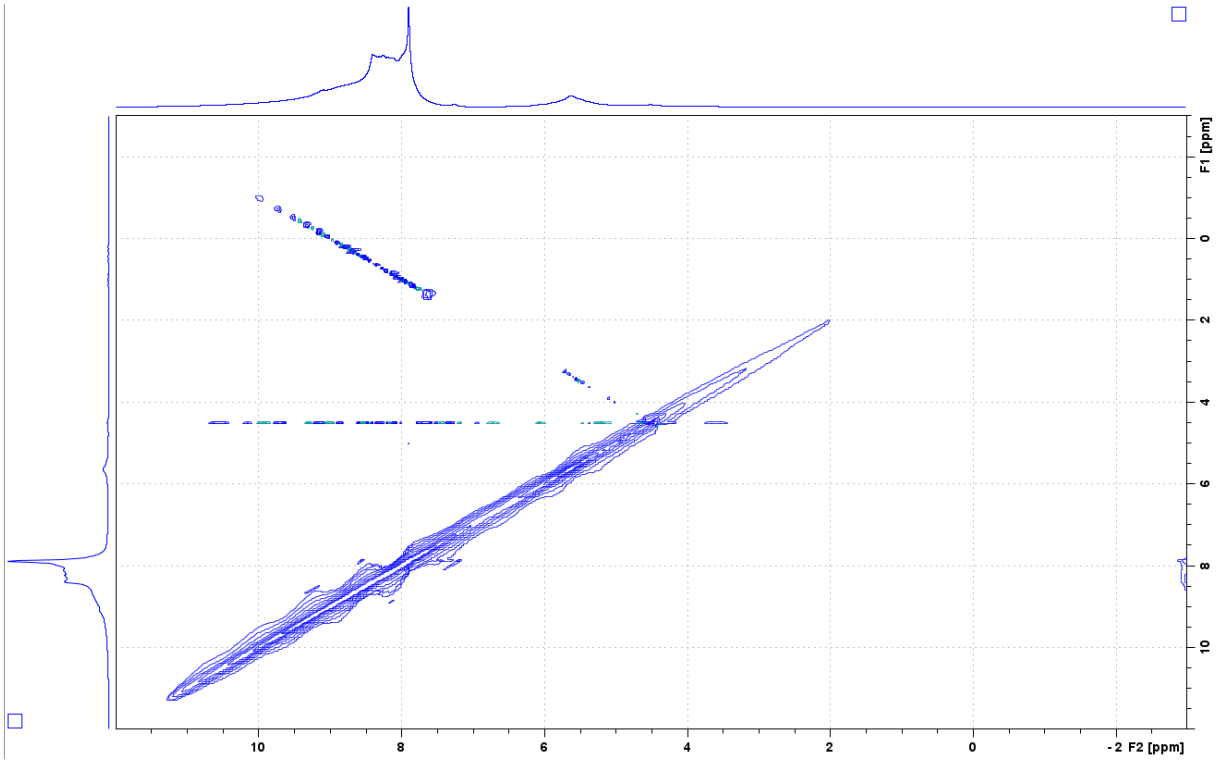

Figure D10: The third NOESY spectrum of the fourth NOESY series, performed on sample B3Fa7. An

external reference ^{1}H spectrum taken right before acquisition is shown on the F2 axis. Note that the peaks lay significantly upfield of expected chemical shifts.

Appendix E: Supporting NMR data

B2F

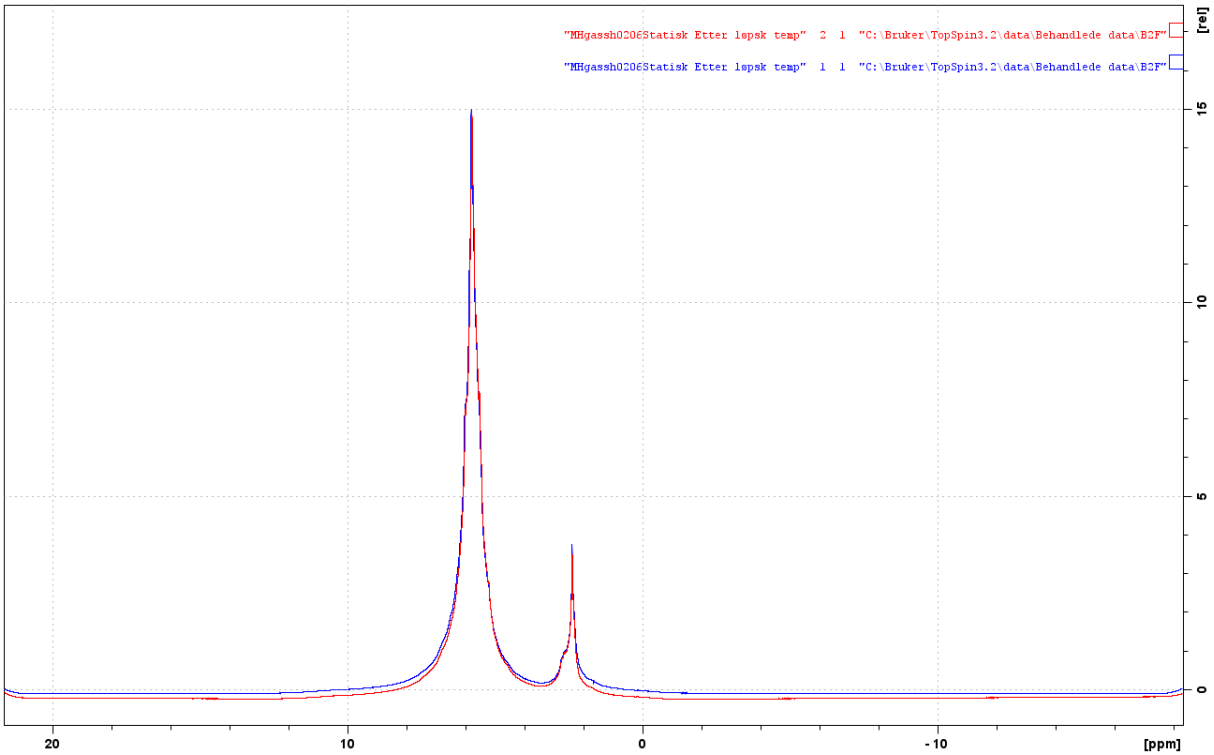

Figure E1: Two ^{1}H spectra acquired after loss of temperature control for sample B2F.

B2F4

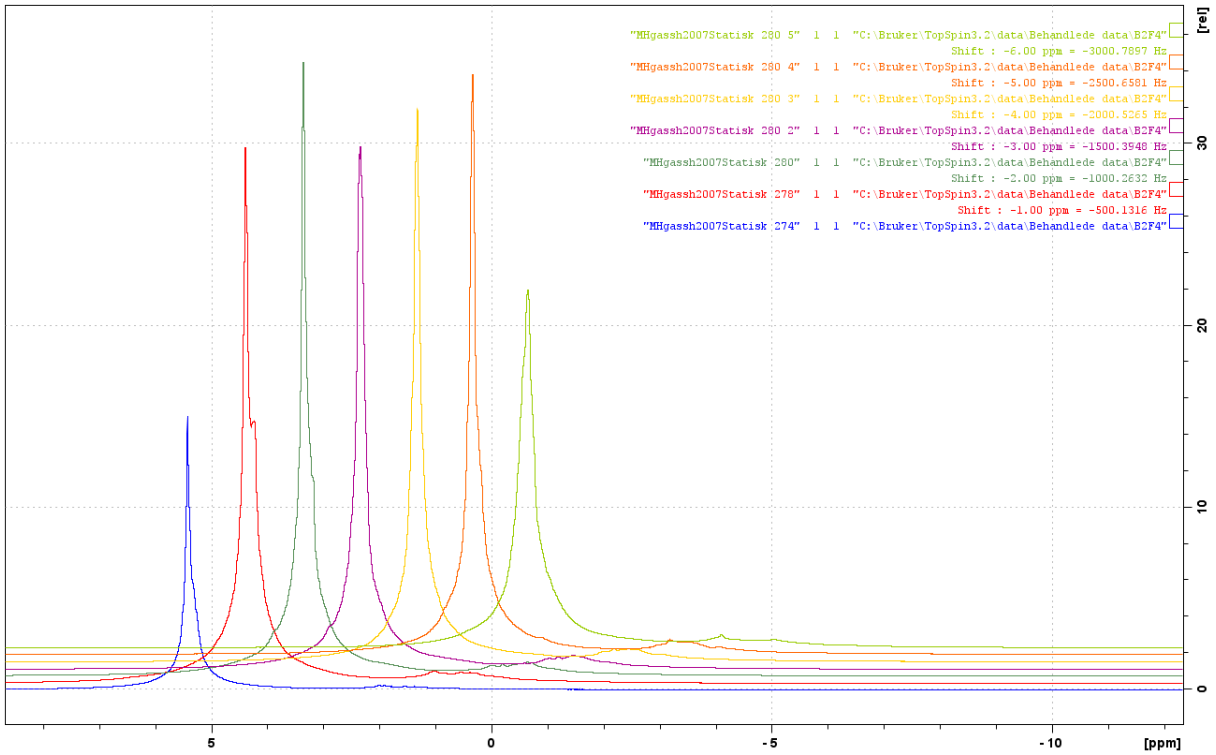

Figure E2: ^{1}H spectra with a spacing of 20 minutes acquired for sample B2F4 following insertion plotted from front to back according to time of acquisition, the first is at 274 K, the second at 278 K and the remaining at 280 K.

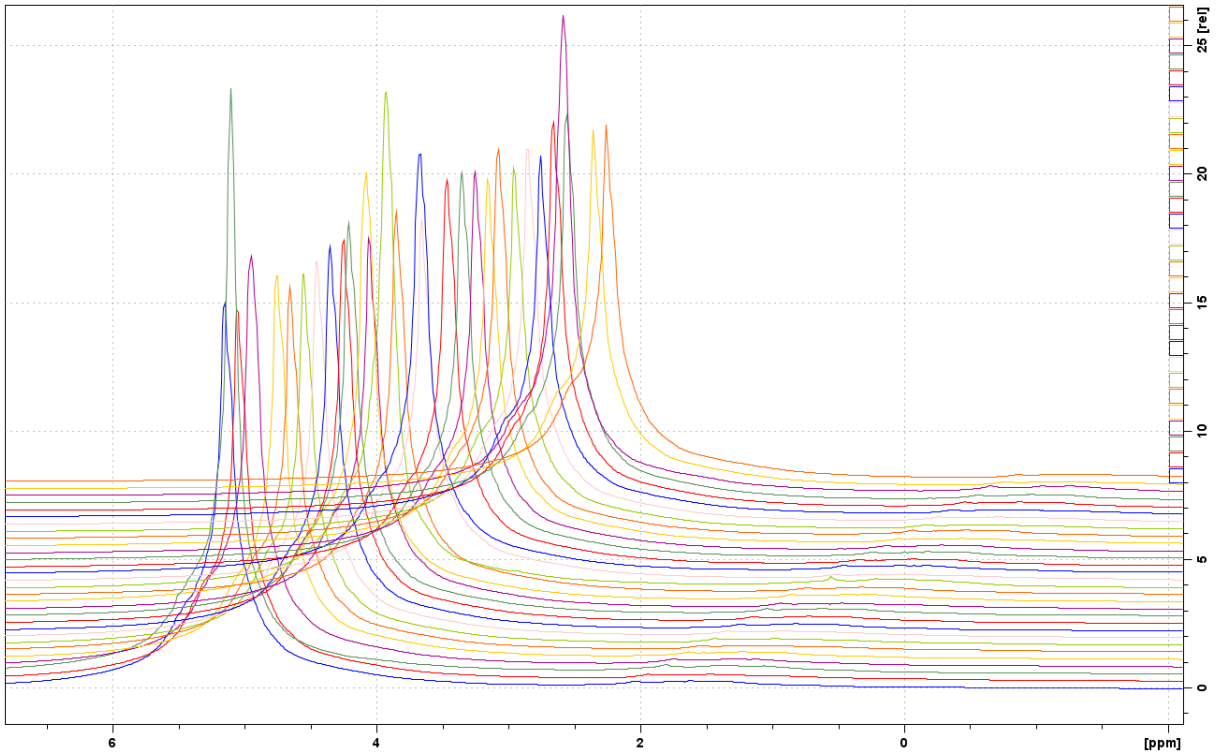

Figure E3: ^{1}H spectra with a spacing of 20 minutes acquired for sample B2F4 following loss of temperature control. Spectra are plotted from front to back according to time of acquisition, and temperature is unknown and rising.

B2F5

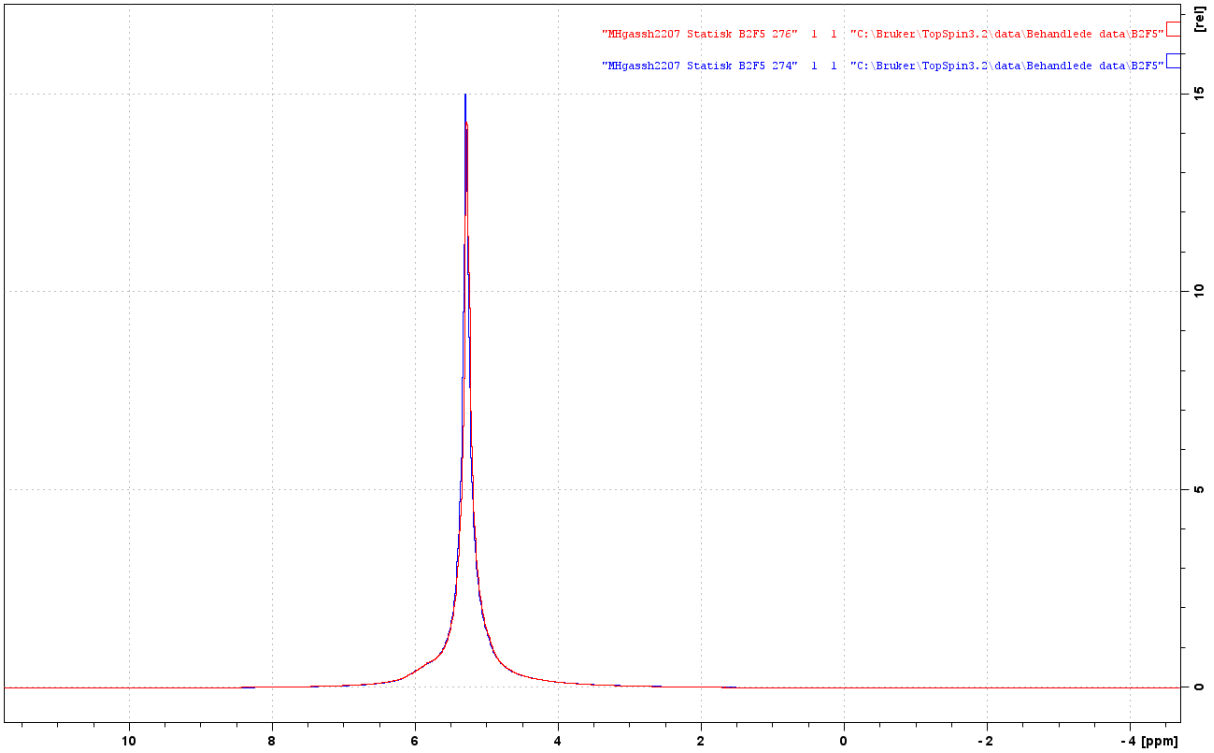

Figure E4: The two ^{1}H spectra acquired on sample B2F5 at 274 K (blue) and 776 K (red). The cyclopentane peak was nearly non-existent, and the sample was abandoned.

B2F6

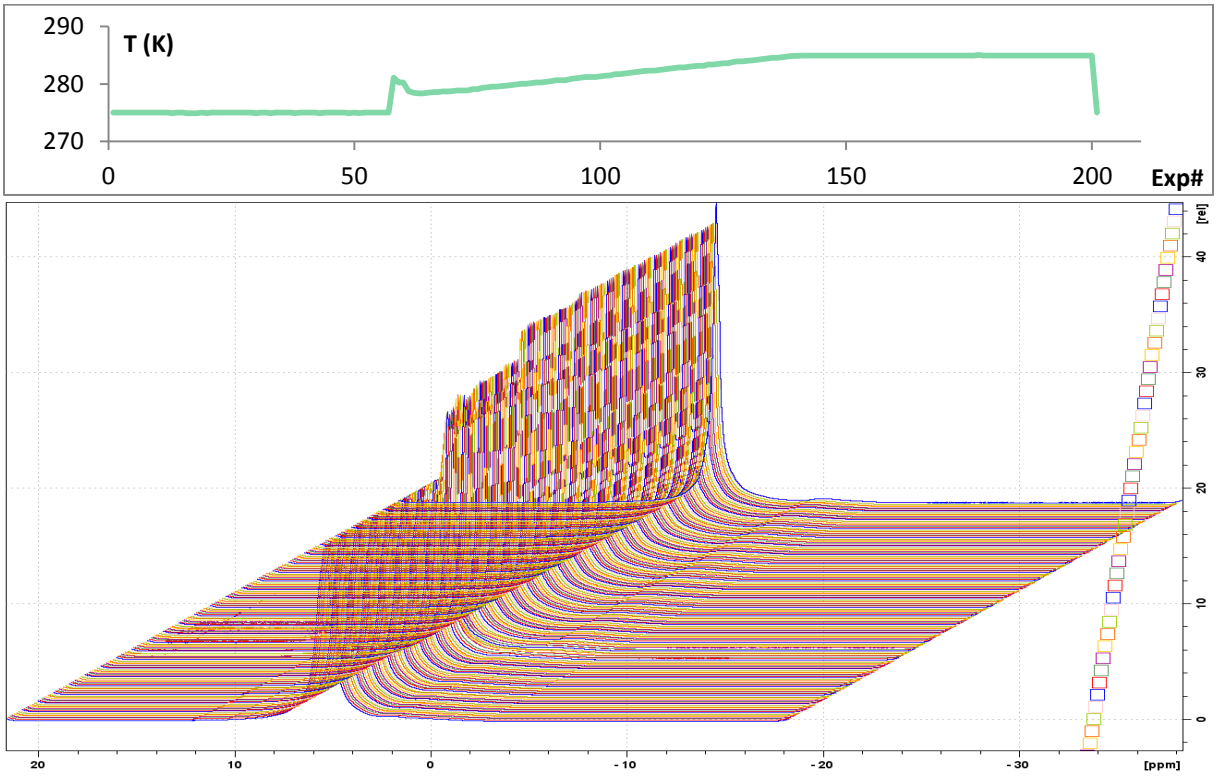

Figure E5: A ramp series of B2F6, with a spectrum acquired approximately every minute. The

temperature log is displayed on top, as a function of experiment number. Two sudden changes in the spectra can be seen, the first corresponding to experiments 61-62 thus placing it at a temperature of 278.5 K right after the temperature spike The second transition takes place during acquisition of spectra 101 and 102, placing it at a temperature of 281 K. The final spectrum in the series is acquired 12 hours after the previous, with temperature lowered to 275 K. The reason for the temperature spike is unknown, but is attributed to the spectrometer "catching up" after ignoring the set ramp program for some time.

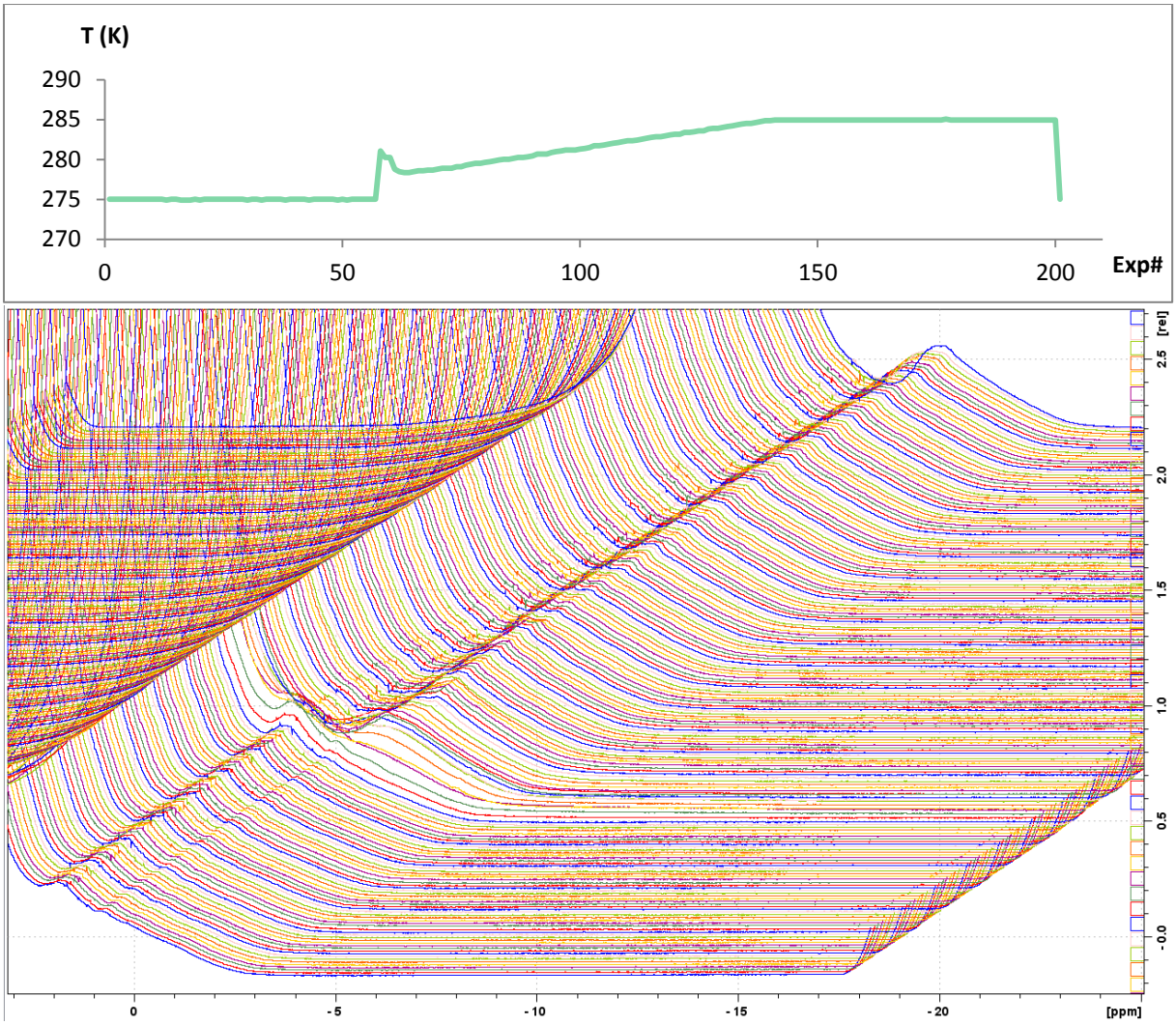

Figure E6: A ramp series of B2F6, with a spectrum acquired approximately every minute. The temperature log is displayed on top, as a function of experiment number. Two sudden changes in the spectra can be seen, the first corresponding to experiments 57-71. The change therefore coincides with the observed temperature spike at a temperature of 281 K. The second transition takes place during acquisition of spectrum 101, placing it at a temperature of 281 K in the ramping region. The final spectrum in the series is acquired 12 hours after the previous, with temperature lowered to 275 K.

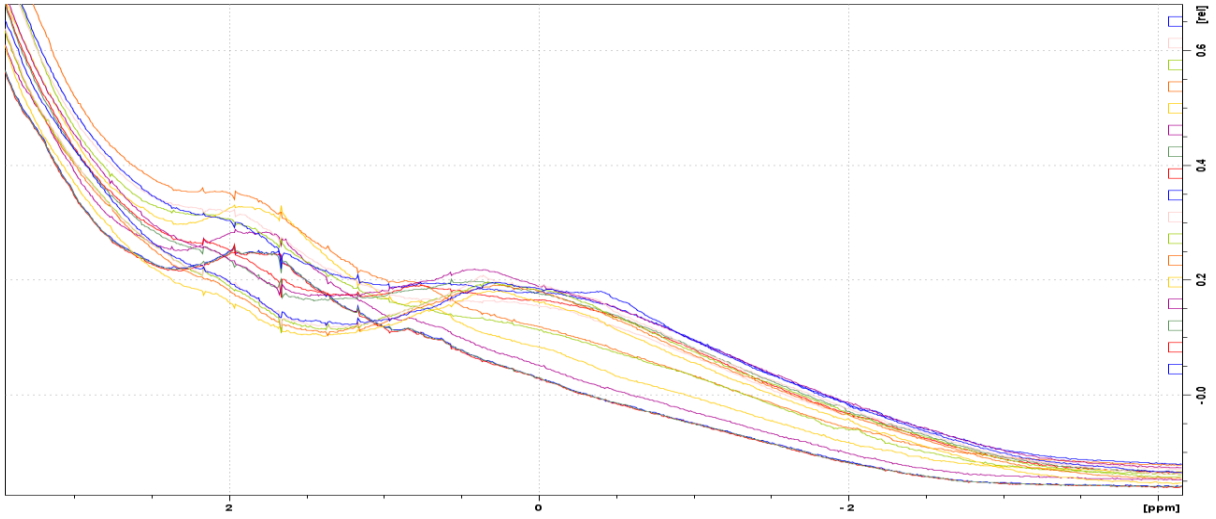

Figure E7: Focus on the change in the cyclopentane peak during and following the temperature spike at 281 K during the ramp program of sample B2F6, presented in a stacked plot.

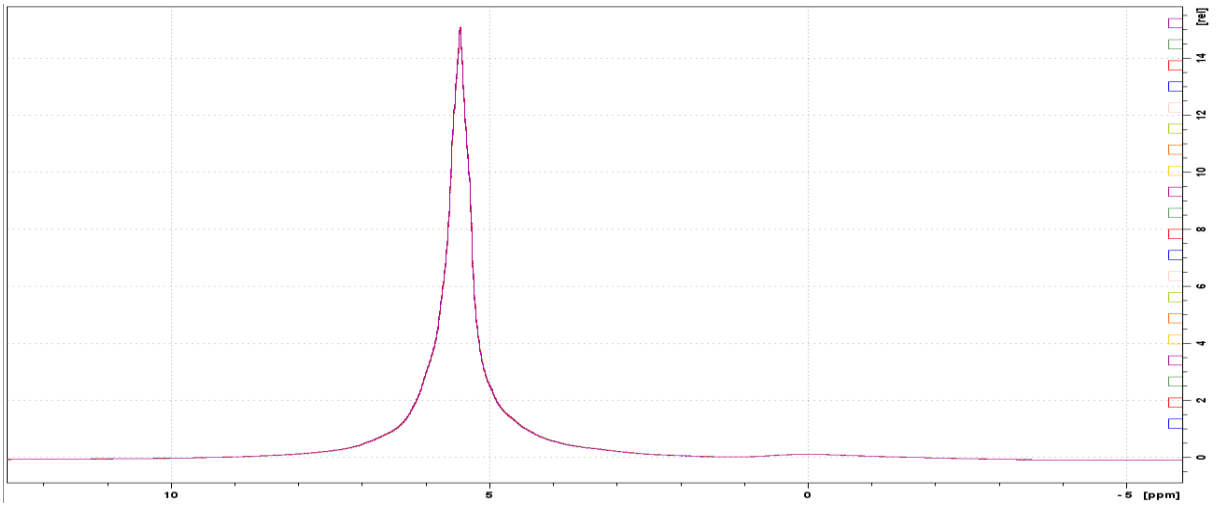

Figure E8: Attempt to reform the B2F6 hydrates at 274 K. The spectra cover a timespan of approximately 30 minutes.

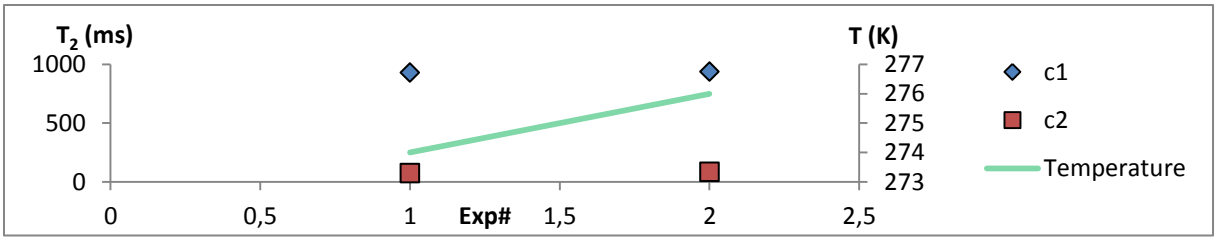

Figure E9: Two-component approach results for the B2F6 sample.

B2F7

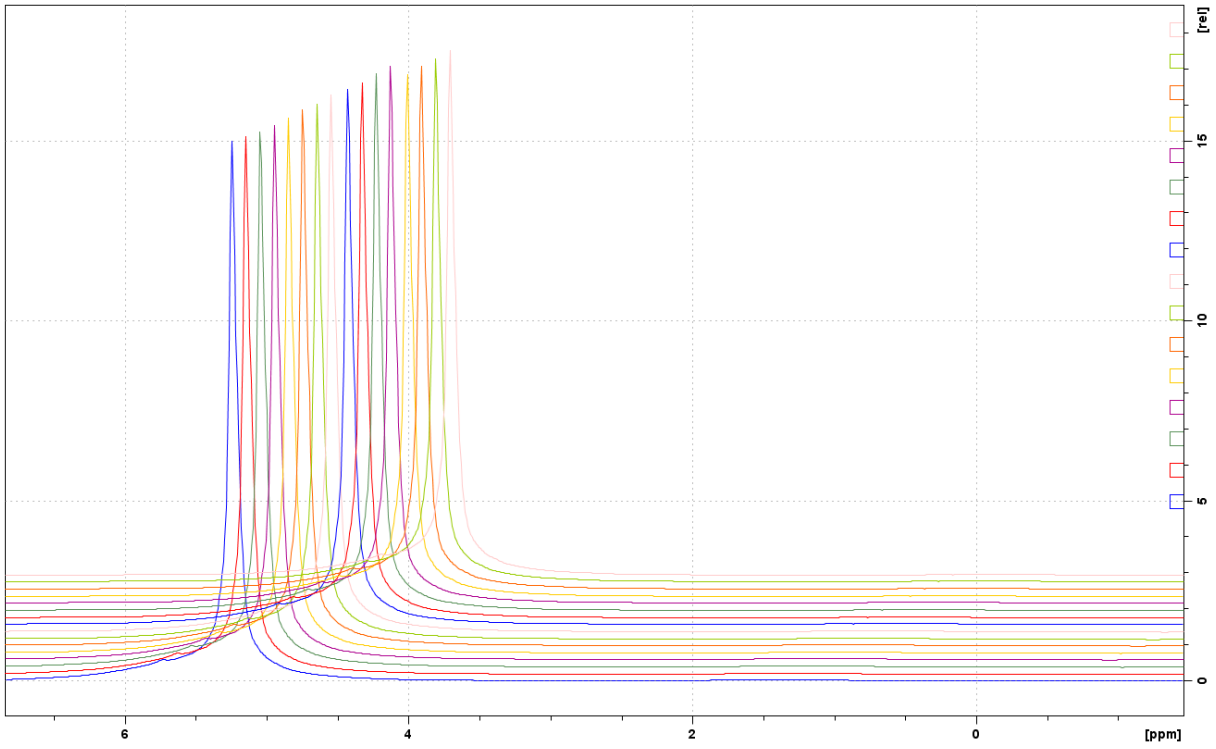

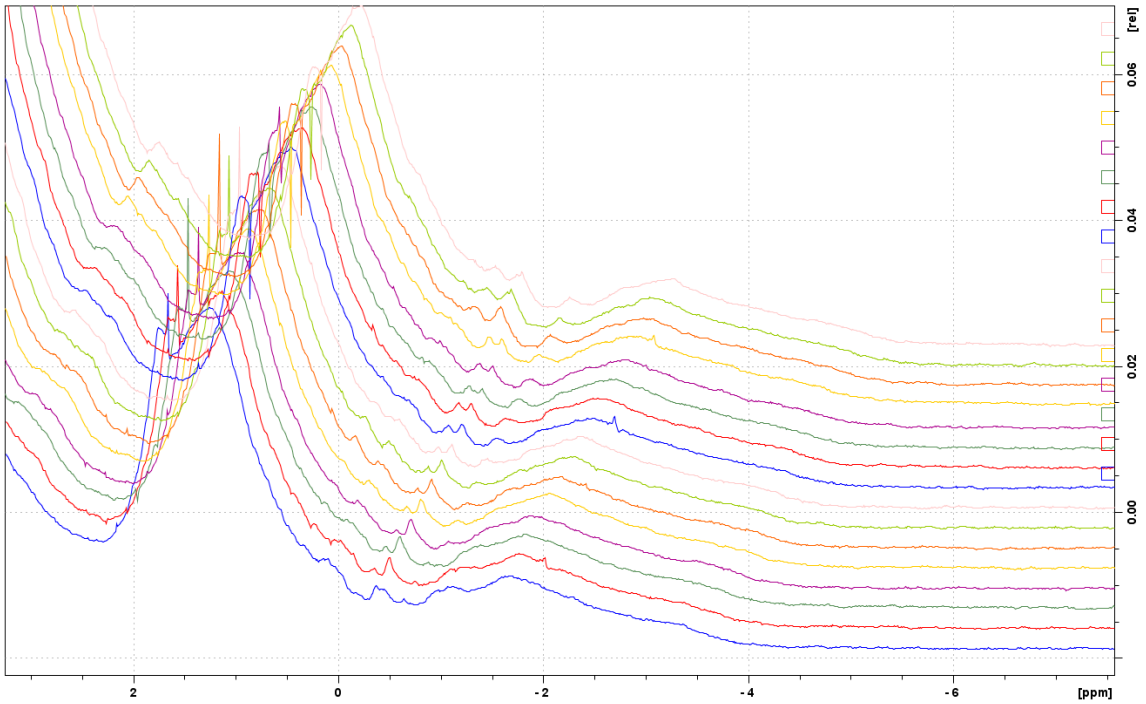

Figure E10: All ^{1}H spectra from the end of the initial acquisition series of sample B2F7, taken approximately 20 minutes apart. The spectra cover a temperature range from 274-278 K (front to back), yet no major change is found.

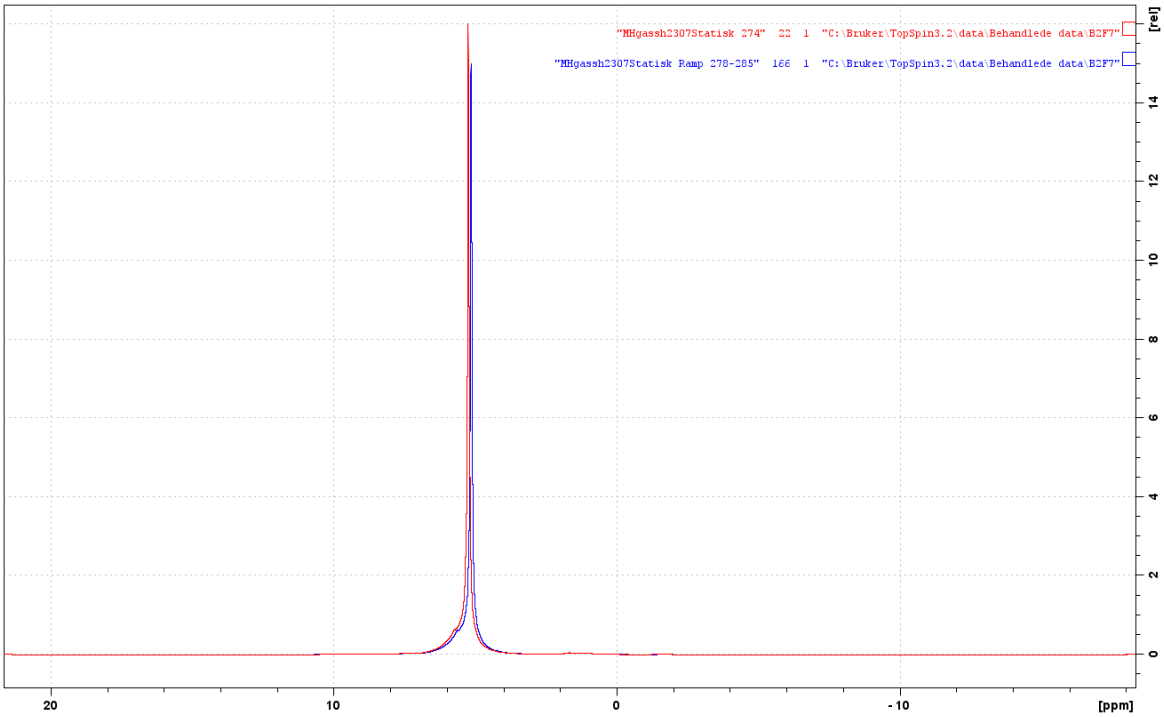

Figure E11: Comparison of the last spectrum at 274 K (red) with the last one at 285 K (blue) for sample B2F7, at which point the sample had been subjected to temperatures above the hydrate stability range for more than two hours.The cyclopentane peak is dwarfed by the water peak for both spectra. The only real difference stems from temperature dependent peak shifts, and the sample is deemed to have melted already before insertion.

B3Fa

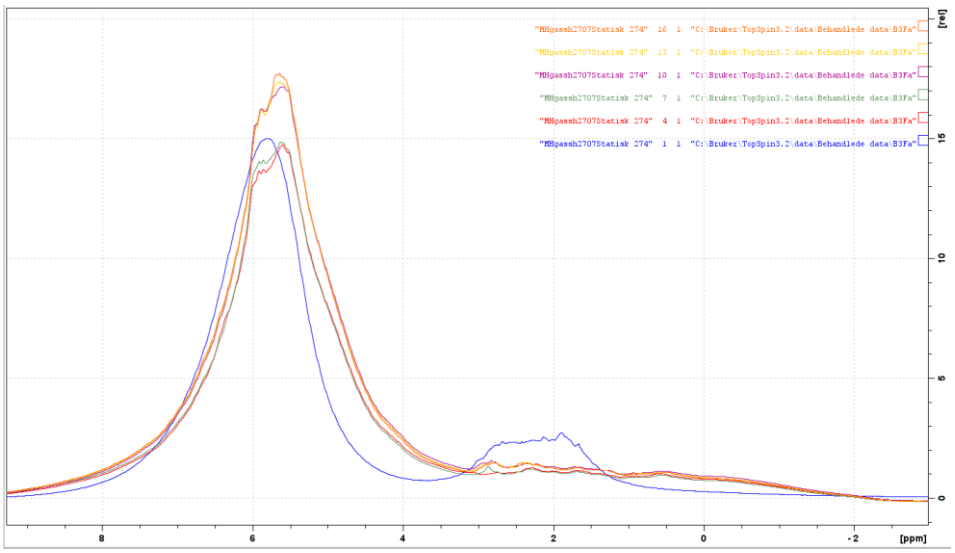

Figure E12: The ^{1}H spectra of sample B3Fa acquired at 274 K, presented in a stacked plot. The blue spectrum is the first spectra after insertion, and each spectrum is separated by 20 minutes.

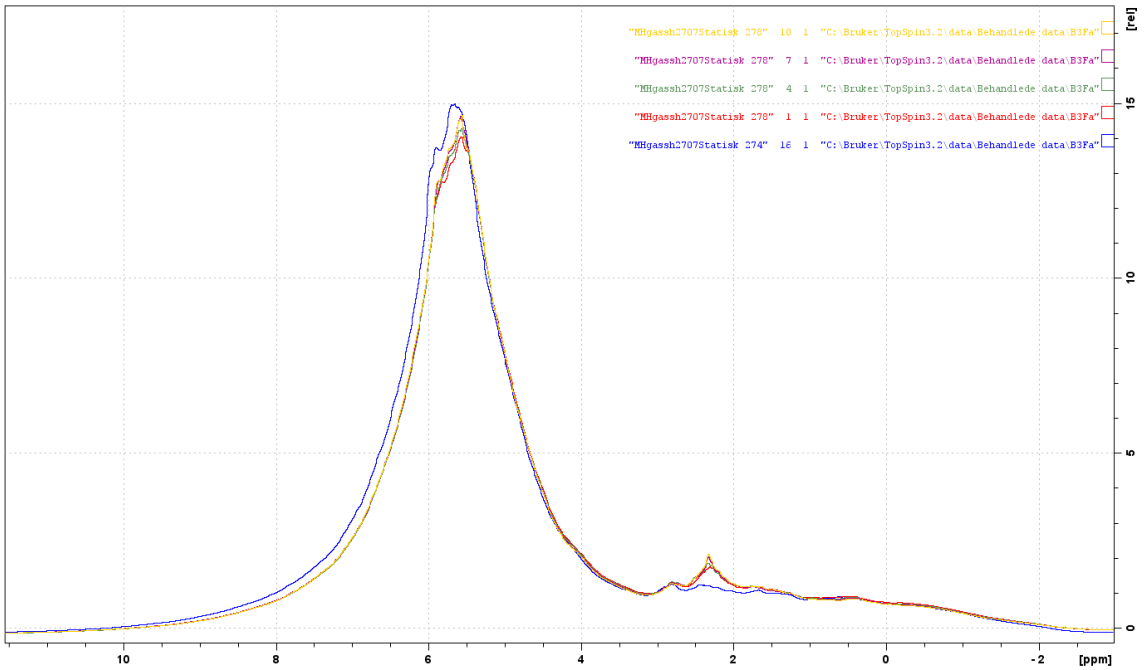

Figure E13: The ^{1}H spectra of sample B3Fa acquired at 278 K, presented in a stacked plot. The last spectrum at 274 K is included in blue. Each spectrum is separated by 20 minutes.

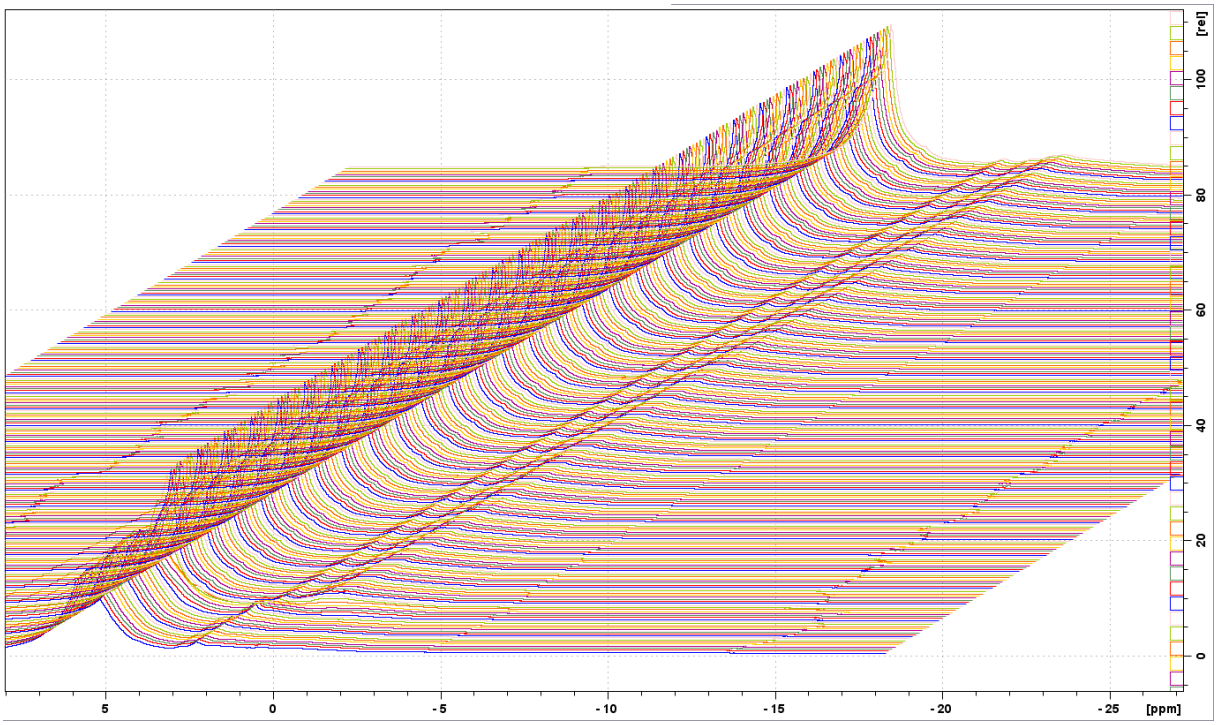

Figure E14: The results of the entire 178-185K ramp-program of sample B3Fa.

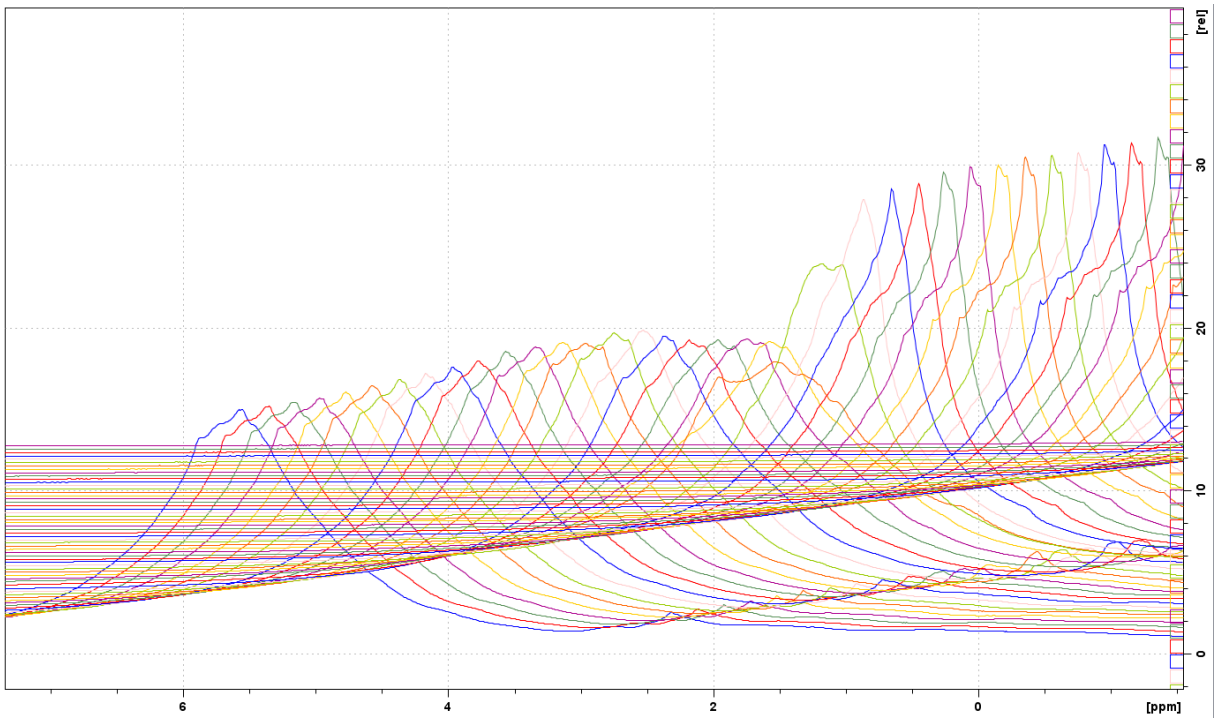

Figure E15: Changes in the water peak in during the 278-285 K ramp program of sample B3Fa.

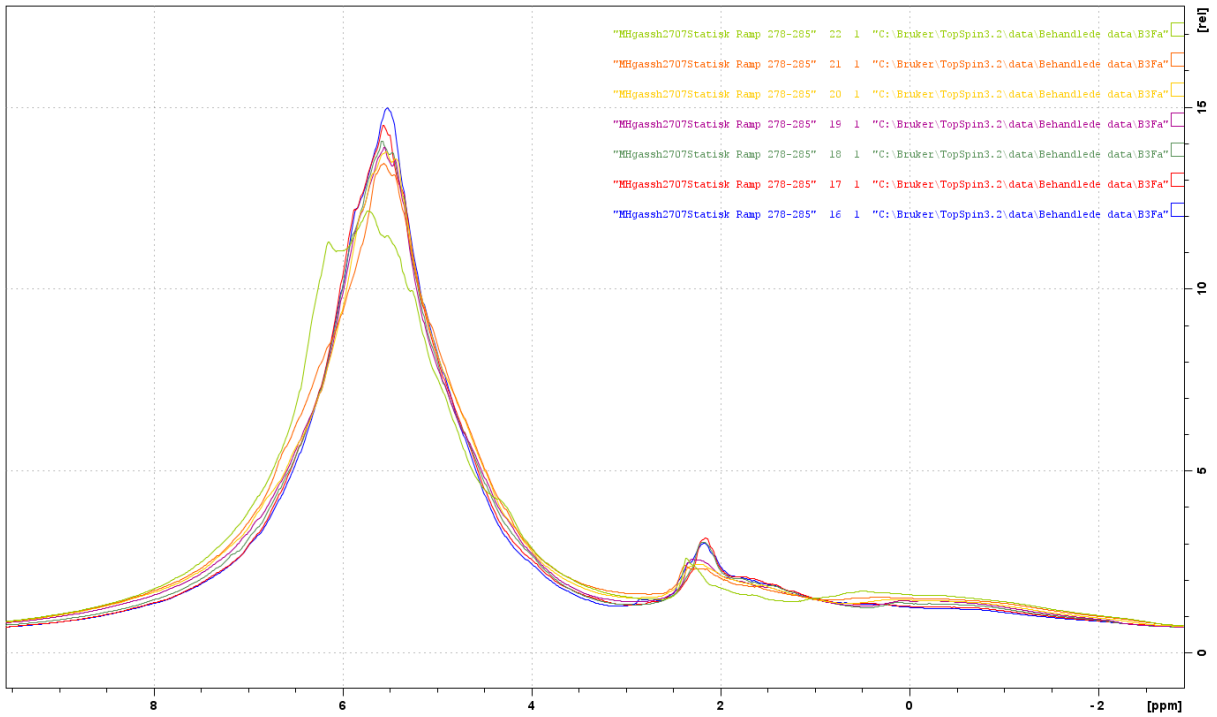

Figure E16: A stacked plot of spectra 16 through 22 from the 278-285 K ramp program of sample B3Fa show a transient water side peak as the intensity goes through a minimum.

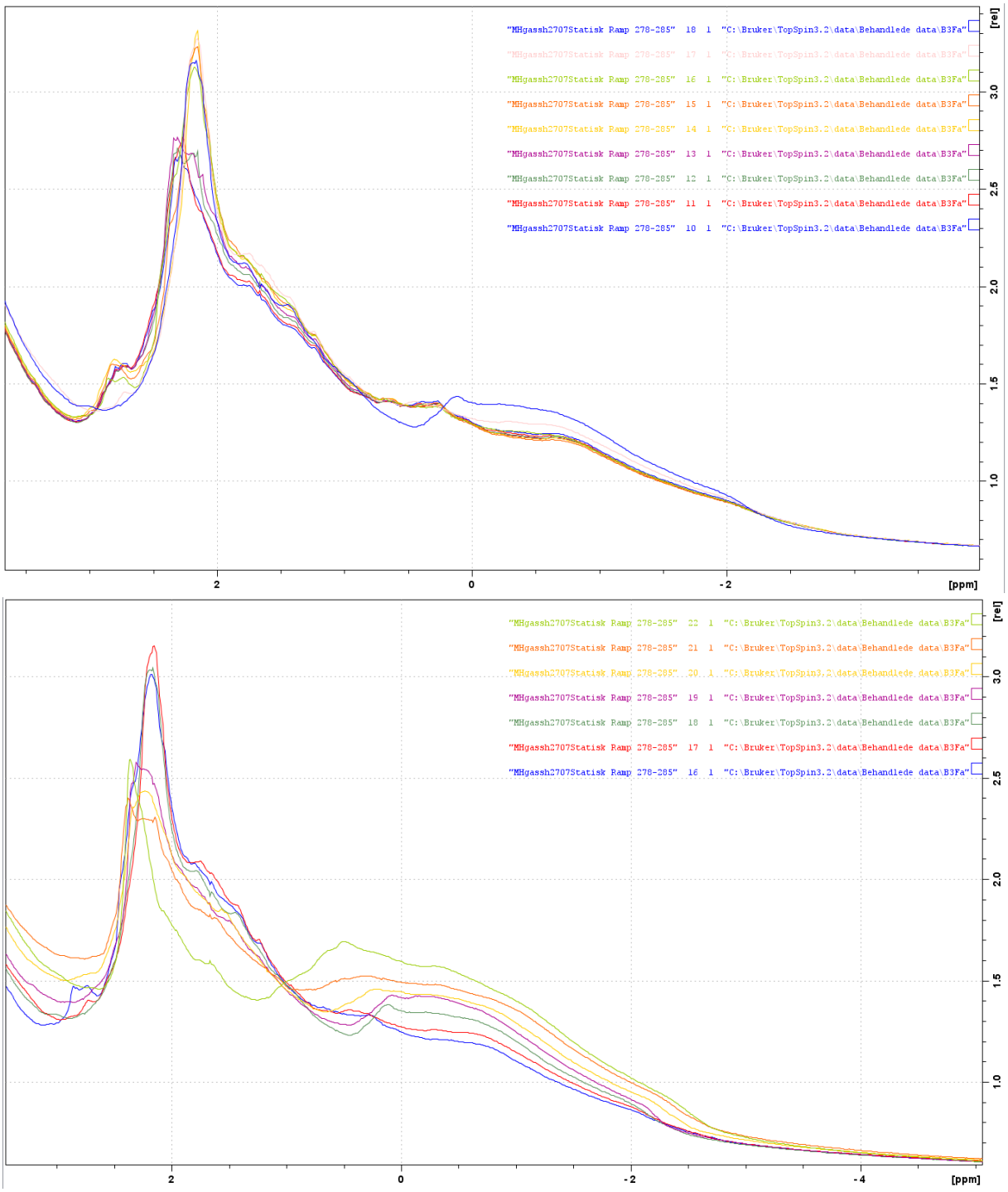

Figure E17: Close-up of the cyclopentane peak. Top: The stacked plot of spectra 10 through 18 from the 278-285 K ramp program of sample B3Fa, clearly shows the growth of the outer cyclopentane peak in spectrum 18 (blue line) when compared with the other spectra in the series. The increase can be seen starting in spectrum 17 (pink line). The upfield cyclopentane peak seems to concurrently disappear. Bottom: A stacked plot of spectra 16 through 22 shows the further growth of this peak.

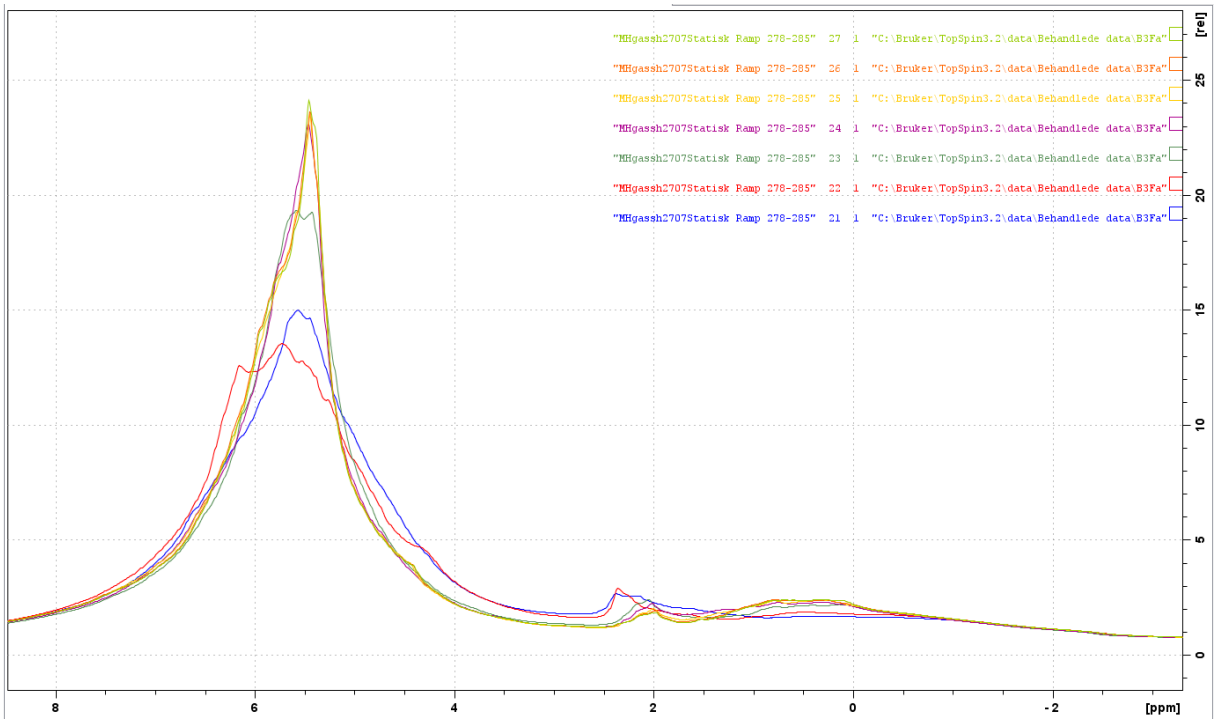

Figure E18: Sample B3Fa ramp 278-285 K. A stacked plot of the water and cyclopentane peaks in spectra 21 (blue) through 27 (olive) shows the cyclopentane peak shifting downfield as the water peak grows and stabilises.

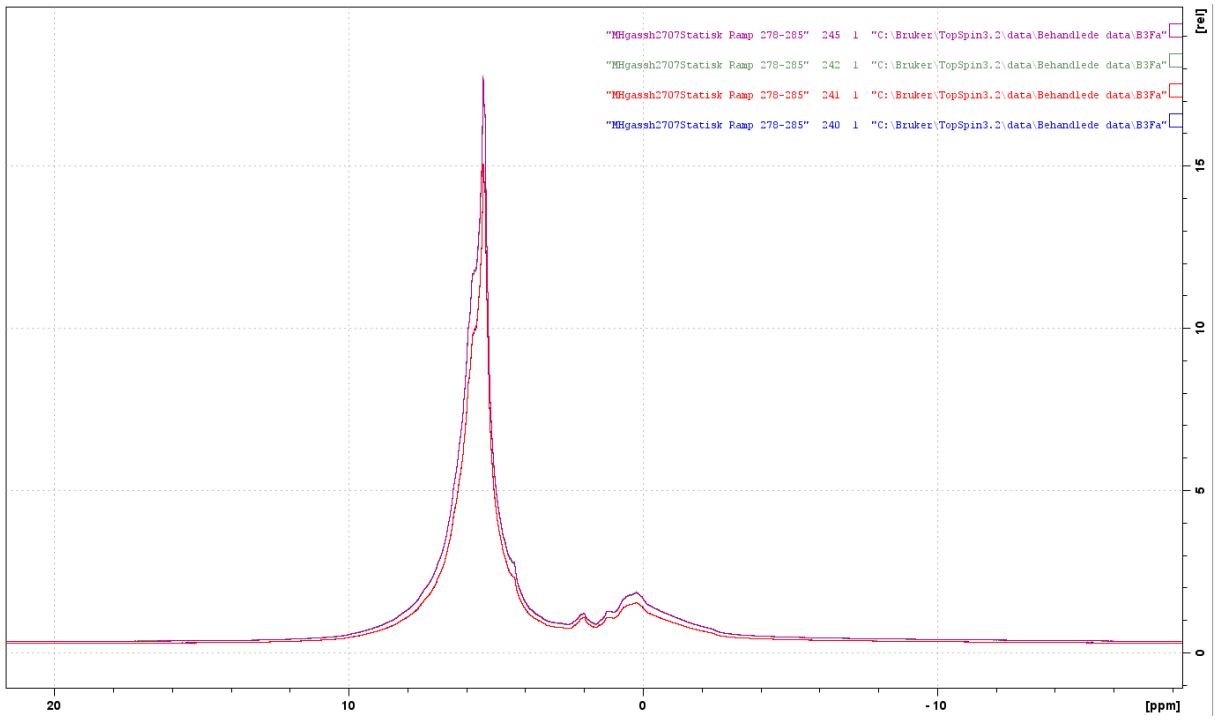

Figure E19: Sample B3Fa. The last spectrum (#240) taken as part of the 278-285 K ramp program (blue, eclipsed by red) is compared with the spectra taken half an hour to an hour later. Tuning and matching was done after acquiring the first of these (for the green and magenta, eclipsed).

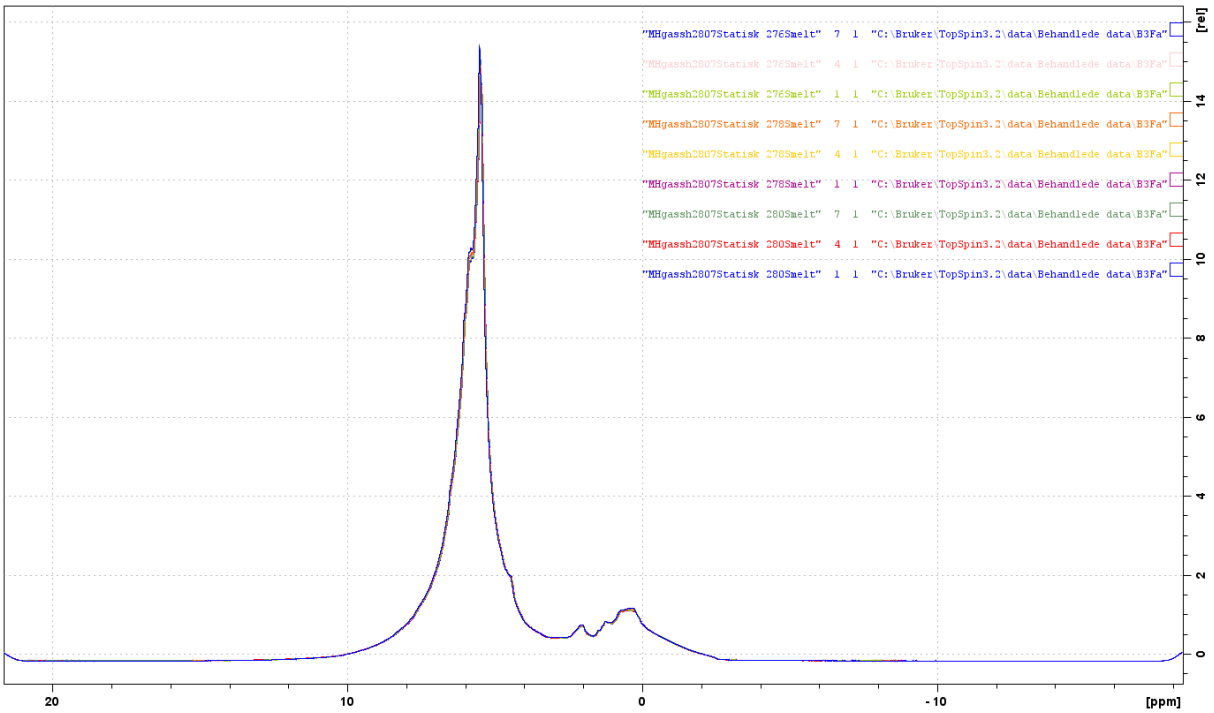

Figure E20: Nine spectra taken at 280 K, 278K and 276 K as sample B3Fa was returned to the hydrate stability range over a period of nearly 3 hours.

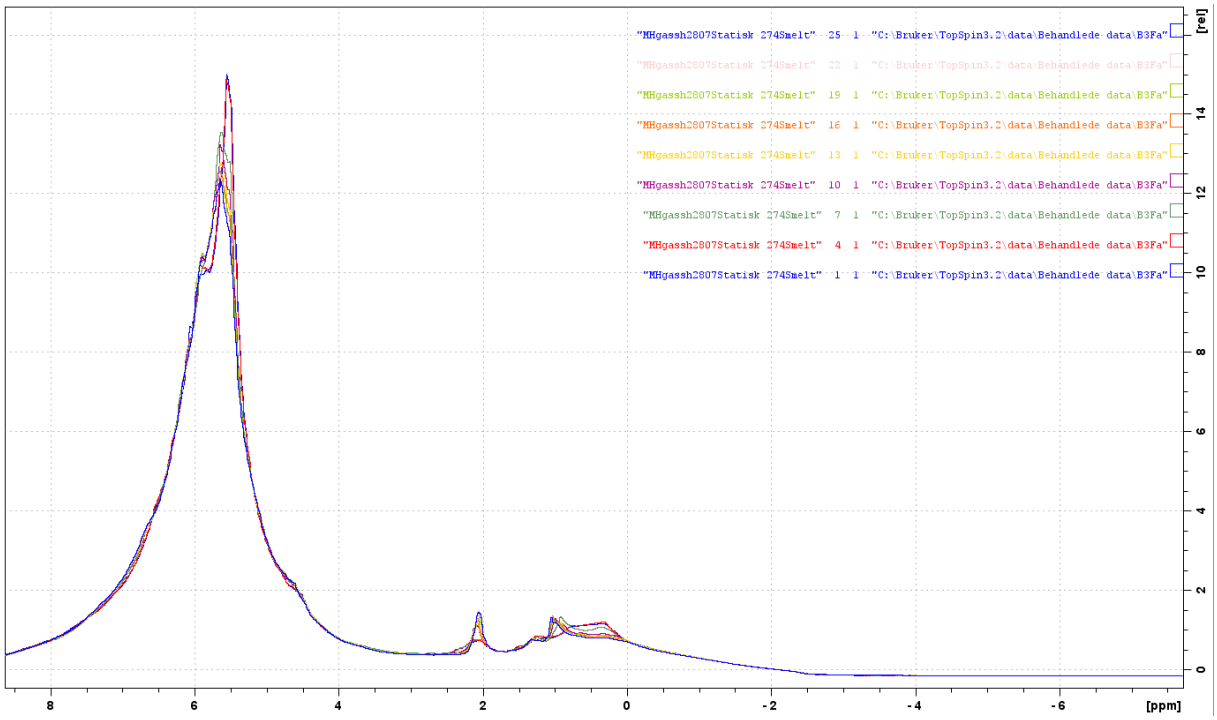

Figure E21: Nine spectra taken at 274 K after an attempt at reforming hydrates in sample B3Fa was made by reducing temperature to the hydrate stability range. Each spectrum is separated by approximately 20 minutes. Stacked plot.

The sample was then returned to freezer storage at -30 ^{o}C for three days before being reintroduced to the spectrometer, which was pre-cooled to 274 K. An initial ^{1}H spectrum was immediately acquired, followed by tuning and matching when the sample was assumed to have reached thermal

equilibrium. A ^{1}H-T_2-T_1-^{1}H program was run, before the temperature was increased first to 276 K and then to 278 K. A ^{1}H-T_2-T_1-^{1}H program was run at both temperatures.

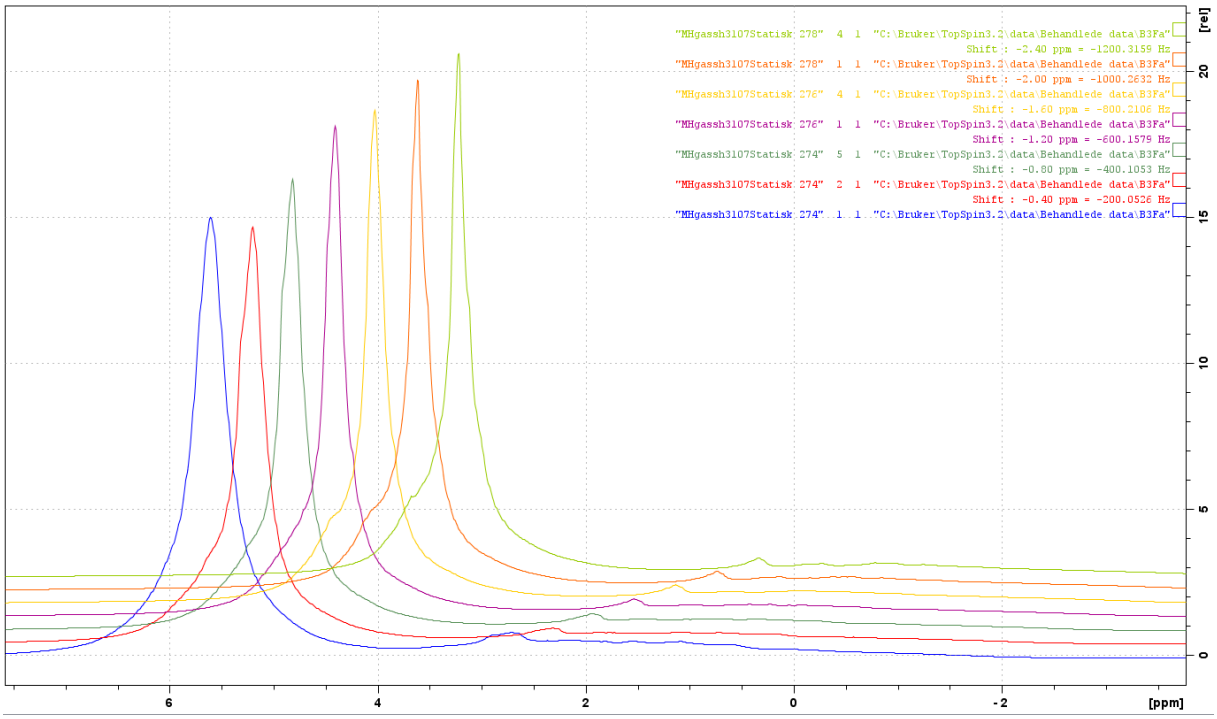

Figure E22: The spectra taken at temperatures of 274 through 278 K for the B3Fa sample after three days in freezer storage. The blue spectrum was acquired right after insertion at 274 K, and at this point the sample was neither tuned and matched nor expected to be at thermal equilibrium. Both peaks in view.

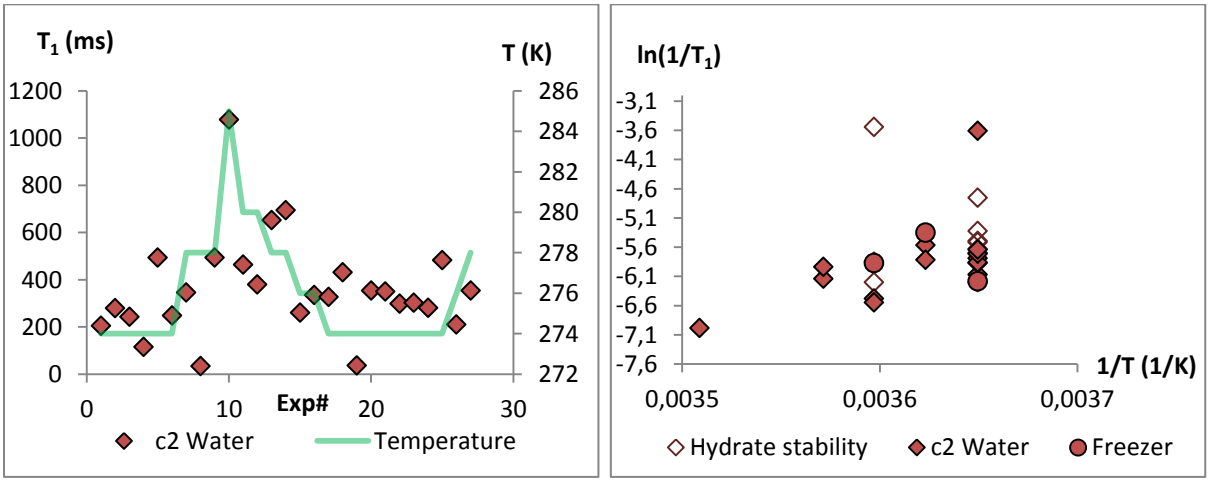

Figure E23: The water peak c2 values found from the two-component analysis of all inversion recovery experiments performed for sample B3Fa. The three last experiments were performed after the sample was removed from the spectrometer and stored at -30 °C for three days. For the inverse graph (right), the experiments performed before reaching the hydrate dissociation temperature are marked with open diamonds, while the experiments following freezer storage are marked with circles.

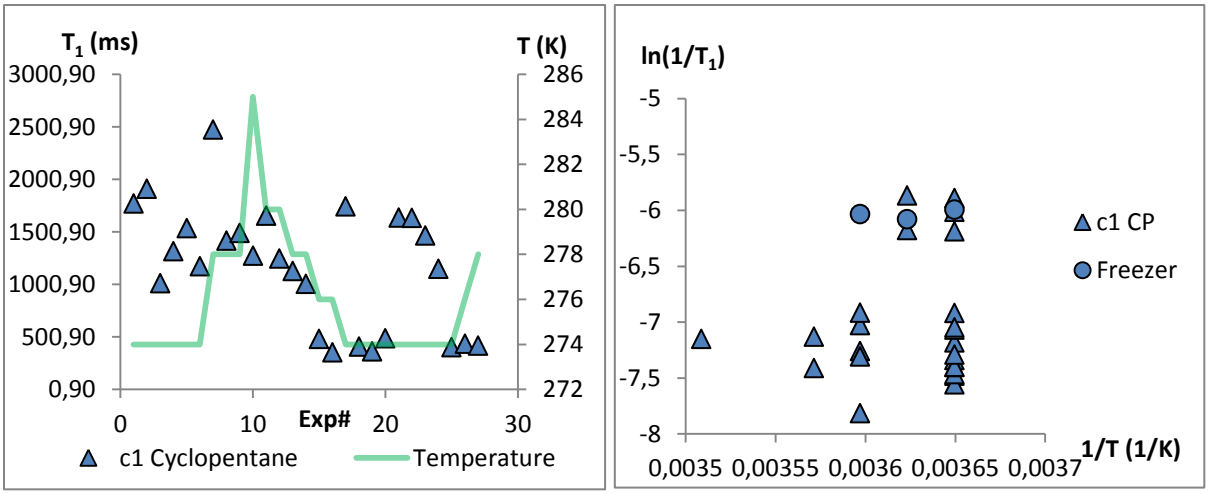

Figure E24: The cyclopentane main peak c1 values found from the two-component analysis of all inversion recovery experiments performed for sample B3Fa. The three last experiments were performed after the sample was removed from the spectrometer and stored at -30 °C for three days. For the inverse graph (right), the experiments following freezer storage are marked with circles.

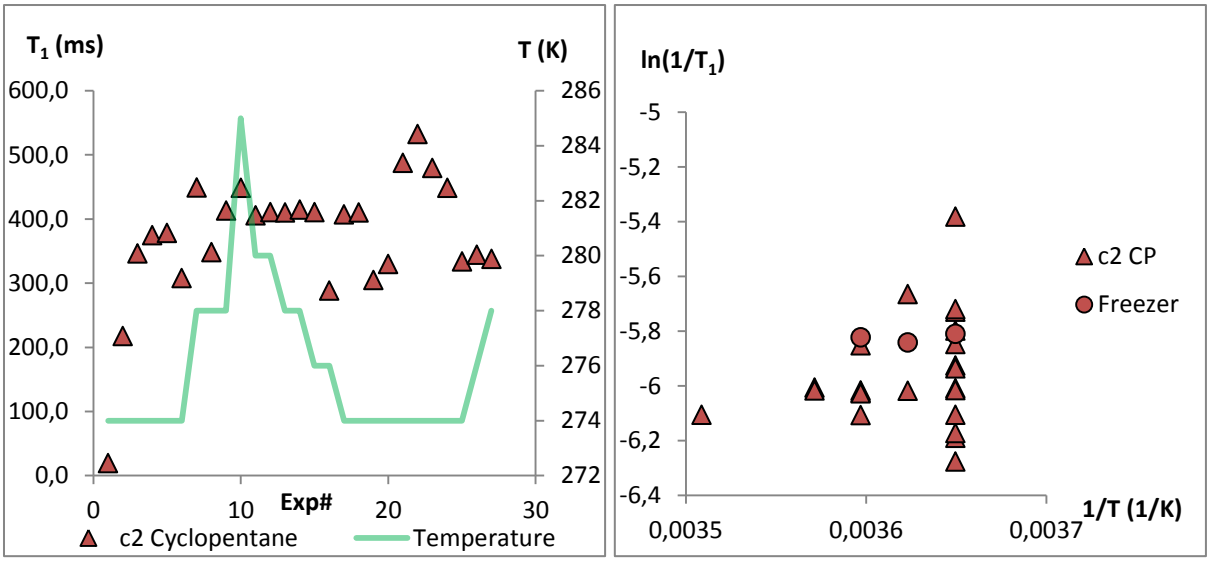

Figure E25: The cyclopentane main peak c2 values found from the two-component analysis of all inversion recovery experiments performed for sample B3Fa. The three last experiments were performed after the sample was removed from the spectrometer and stored at -30 °C for three days. For the inverse graph (right), the experiments following freezer storage are marked with circles.

Table E1: The guesses used during the calculation of T_2 values for the B3Fa sample using the T2_tilpasning3_serialProcessingRapid.m script. The values from the third iteration of the analysis was used. c1 is the guess for the first component, c2 is the guess for the second component, and c3 is the guess for the third component.

1comp	2comp1	2comp2	3comp1	3comp2	3comp3
500	500	100	1200	250	30

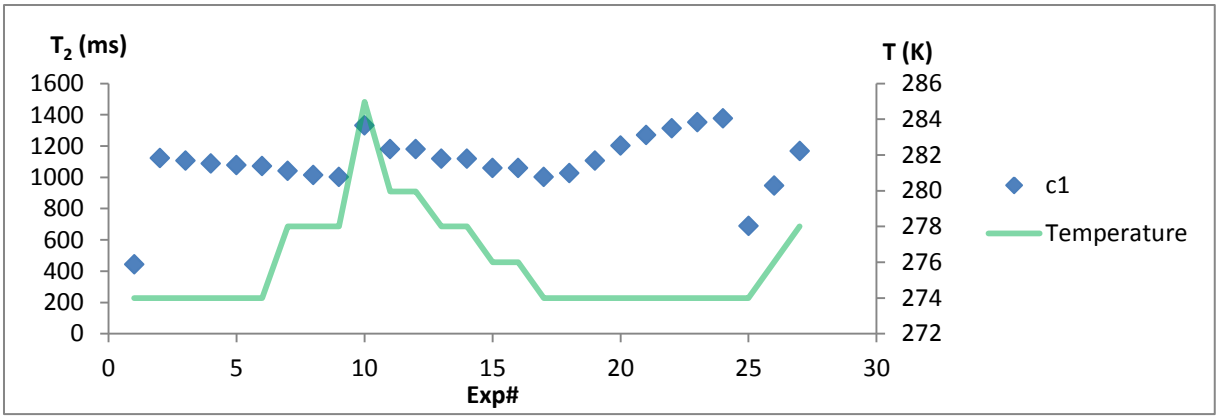

Figure E26: The results of one-component analysis of all CPMG oneshot experiments on B3Fa, plotted as T_2 in ms as a function of experiment number. The green curve is the temperature in Kelvin, plotted on the secondary vertical axis. Note that the T_2 values are high for all but the first experiment.

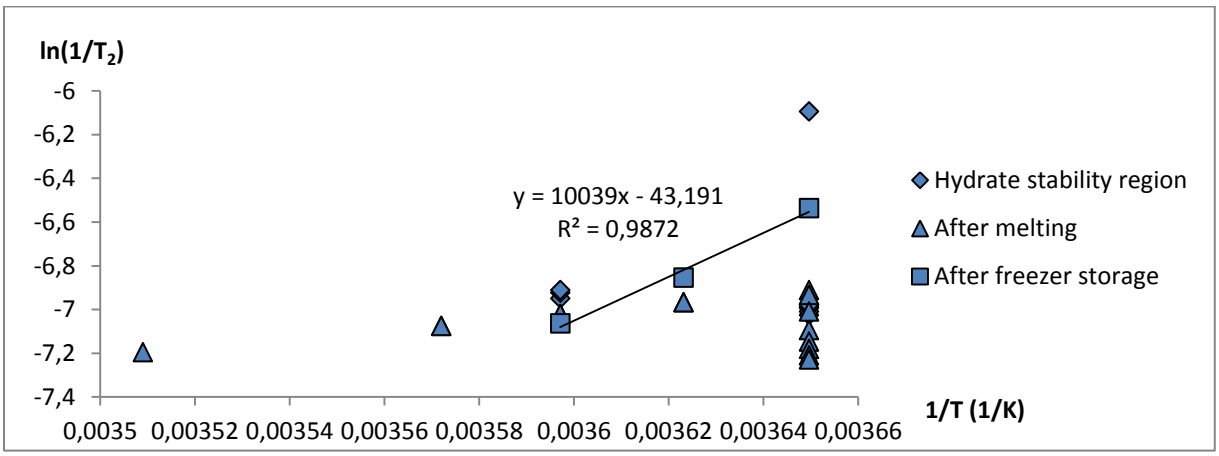

Figure E27: The results of one-component analysis of all CPMG oneshot experiments on B3Fa, plotted as plotted as $\ln((T_2)^{-1})$ as a function of T^{-1}. Experiments performed after the sample had been subjected to temperatures beyond the hydrate stability region are shown as "After melting". Measurements performed after the freezer reformation attempt is shown as squares. These are seen to form a linear range that is fitted to a regression line, the function and R^2 value of which is provided above the line.

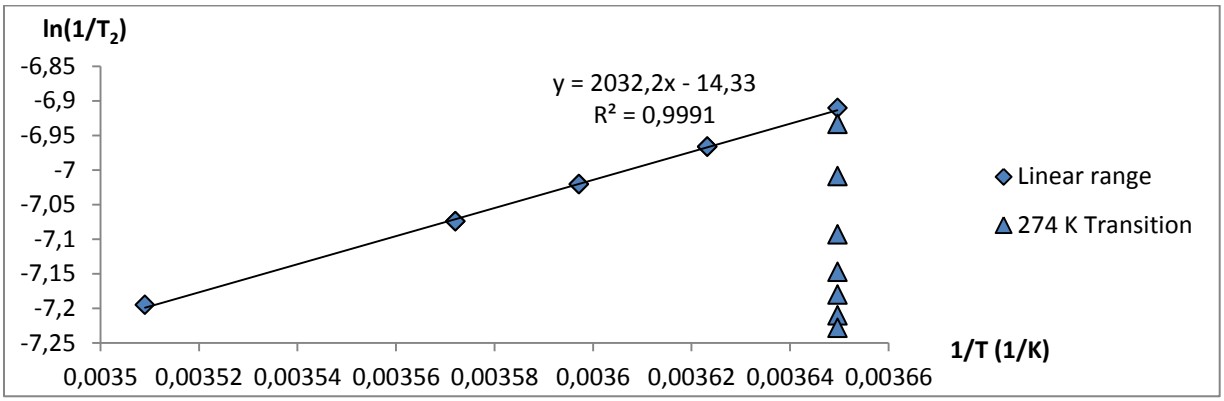

Figure E28: The one component results of the eight first experiments performed outside the range of hydrate stability for B3Fa are plotted as diamonds and fitted to a regression line, the formula and R^2 value of which is shown. The following experiments are plotted as triangles, and proceeds from top to bottom as a function of time.

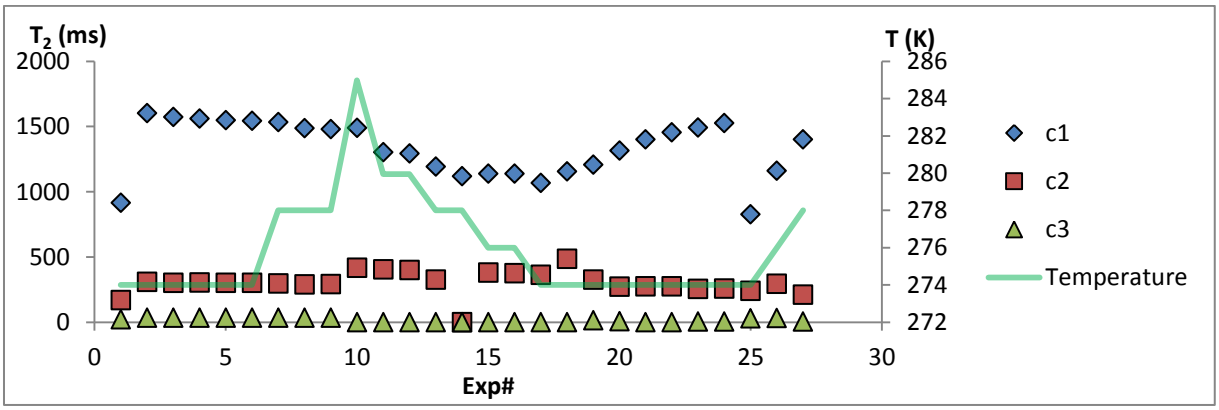

Figure E29: The results of three-component analysis of all CPMG oneshot experiments on B3Fa, plotted as T_2 in ms as a function of experiment number. The green curve is the temperature in Kelvin, plotted on the secondary vertical axis. Note that the T_2 values are high for all but the first experiment. An outlying value can be seen for c2 in experiment 14, and this value is omitted during further analyses of the results.

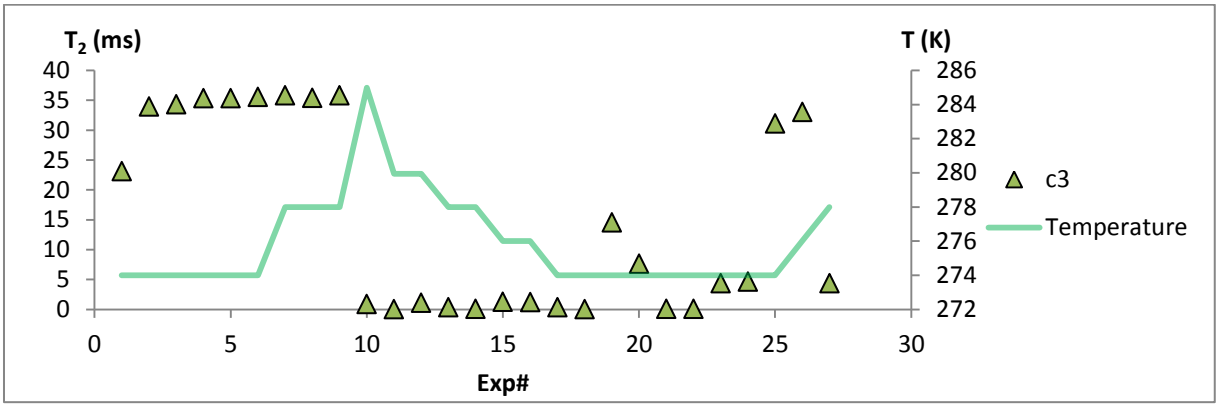

Figure E30: The c3 results of three-component analysis of all CPMG oneshot experiments on B3Fa, plotted as T_2 in ms as a function of experiment number. The green curve is the temperature in Kelvin, plotted on the secondary vertical axis.

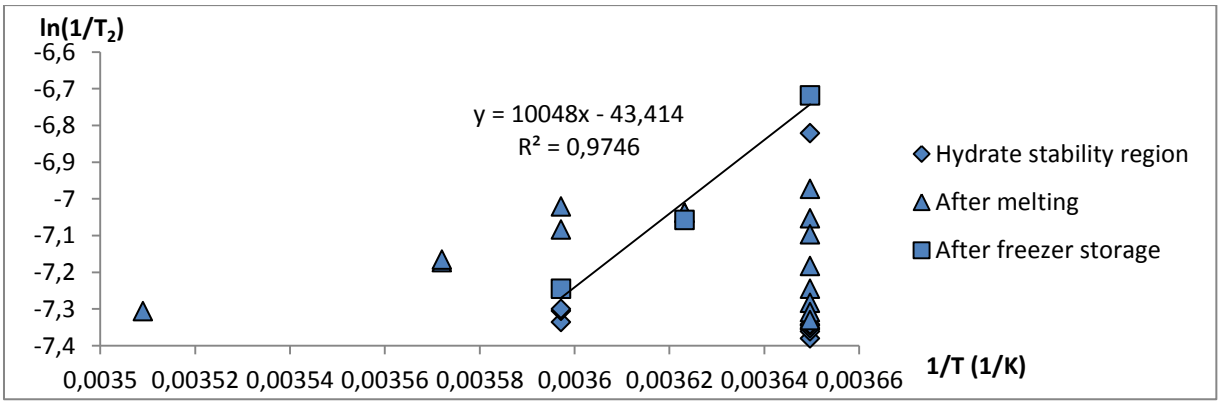

Figure E31: The c1 results of three-component analysis of all CPMG oneshot experiments on B3Fa, plotted as plotted as $ln((T_2)^{-1})$ as a function of T^{-1}. Experiments performed after the sample had been subjected to temperatures beyond the hydrate stability region are shown as "After melting". Measurements performed after the freezer reformation attempt is shown as squares. These are seen

to form a linear range that is fitted to a regression line, the function and R^2 value of which is provided above the line.

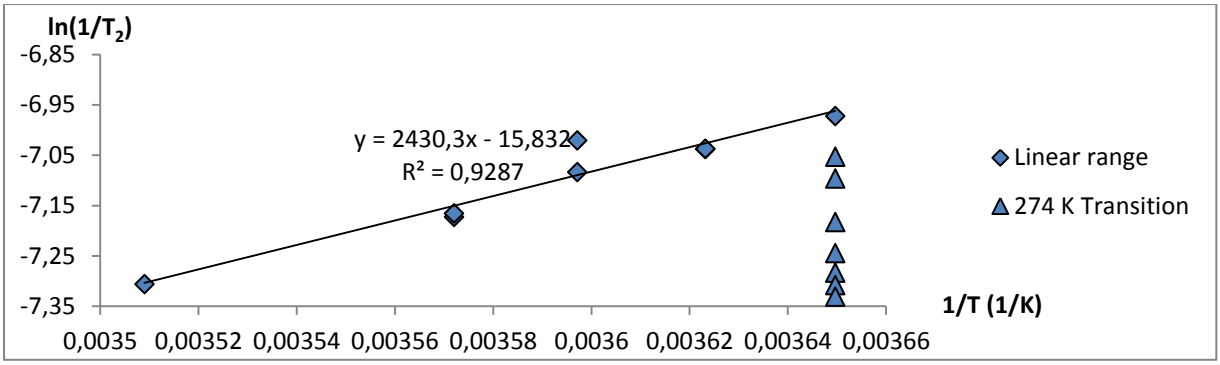

Figure E32: The c1 results of a two-component approach for the nine first experiments performed outside the range of hydrate stability for B3Fa are plotted as diamonds and fitted to a regression line, the formula and R^2 value of which is shown. The following experiments are plotted as triangles, and their ln(1/T_2) values is found to decrease as a function of time.

B3Fb

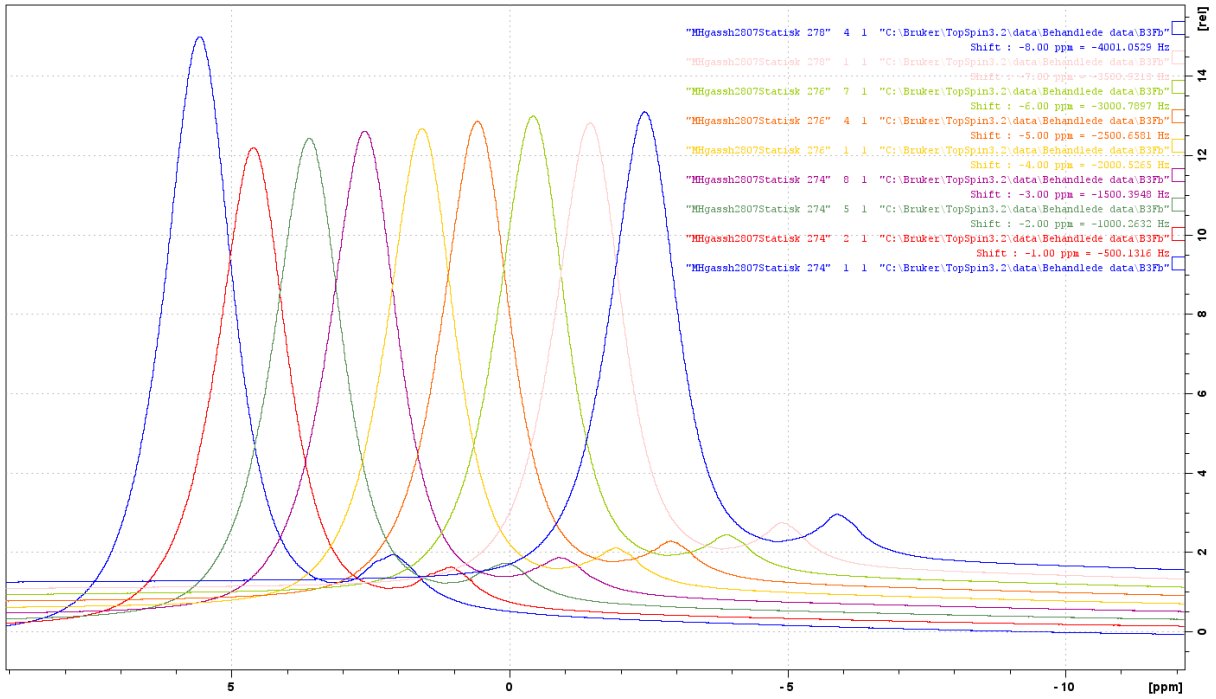

Figure E33: The ^{1}H spectra acquired on sample B3Fb before initiation of a ramp-program, plotted with horizontal and vertical offset. The first spectrum is acquired at 274 K right after insertion, closely followed by the second. The rest are acquired approximately 20 minutes apart, and comprise temperature increases of 2 K after the fourth and seventh spectra from the front. Other than the initial decrease, no significant change is observed.

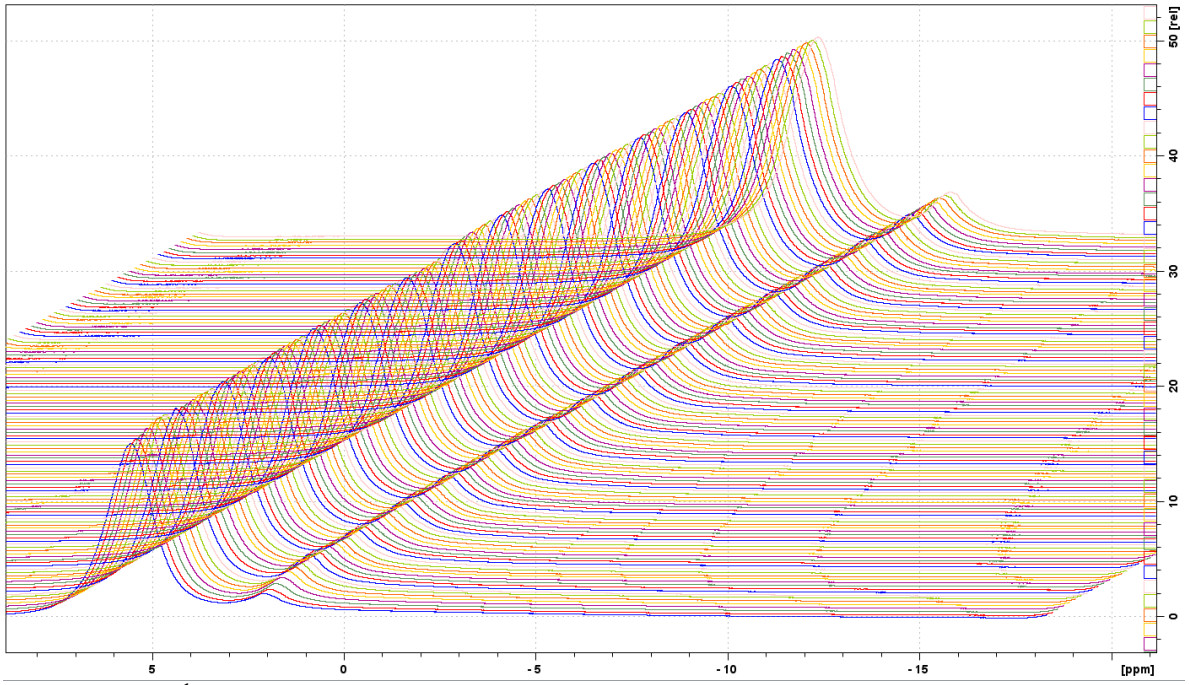

Figure E34: All ^{1}H spectra aquired during the B3Fb 278-280.5 ramp program, presented using horizontal and vertical offset. A small increase is seen in the water peak around experiment 100.

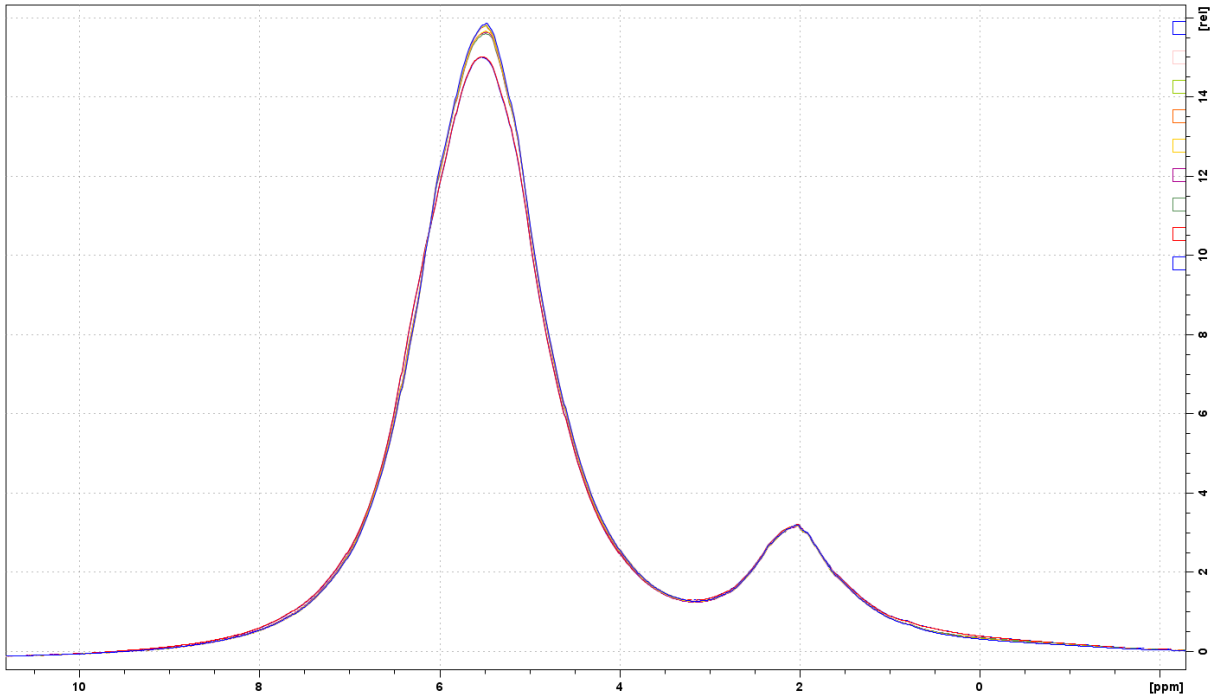

Figure E35: The change in water peak during the B3Fb ramp program was pinpointed to spectra 111 through 123. For the same spectra, the cyclopentane peak also underwent a small change, mainly by a decrease in the areas directly upfield and downfield of the peak. However, comparisons with other spectra show that this change is most likely random.

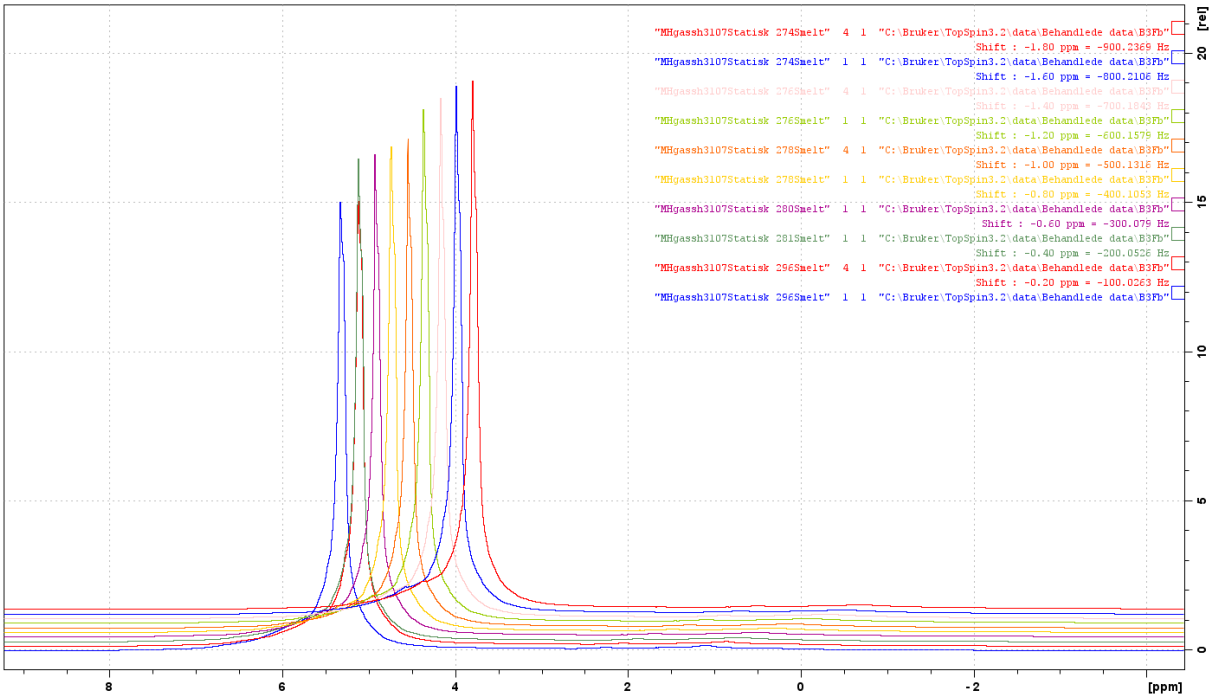

Figure E36: Both peak areas displayed for the experiments performed after reintroduction of sample B3Fb to the spectrometer after storage at room temperature for three days. The spectra are presented using horizontal and vertical offset. From front to back, the two first spectra were acquired at 295 K, followed by one at 281 K, one at 280 K, two at 278 K, two at 276 K and two at 274 K. Approximately 20 minutes separated each of the spectra, meaning the sample spent around 140 minutes within the hydrate stability region, during which time little change is observed.

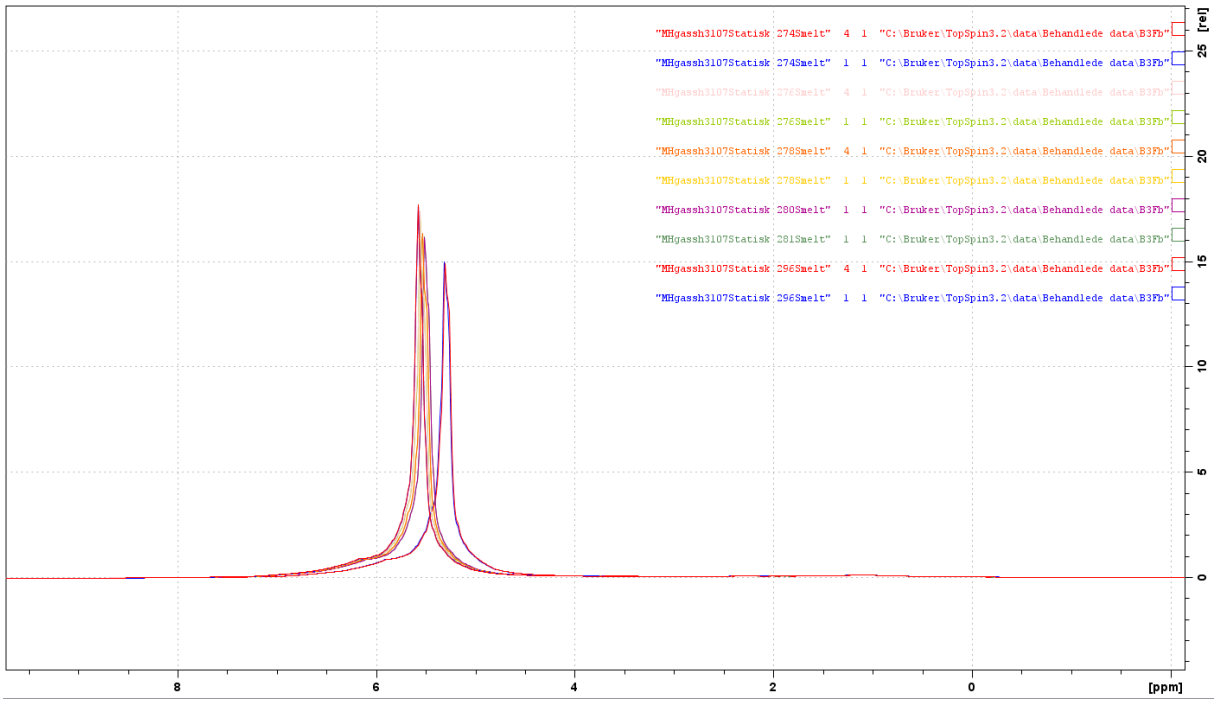

Figure E37: Stacked plot of both peak areas displayed for the experiments preformed after reintroduction of sample B3Fb to the spectrometer after storage at room temperature for three days. The two first spectra were acquired at 295 K, followed by one at 281 K, one at 280 K, two at 278 K, two at 276 K and two at 274 K. Approximately 20 minutes separated each of the spectra, meaning the

sample spent around 140 minutes within the hydrate stability region. The temperature dependent shift of the water peak is evident, but no other change can be seen.

Table E2: The guessrange utilised in analysis of the first experiment series of B3Fb.

Exprange	1comp	2comp1	2comp2	3comp1	3comp2	3comp3
All	1000	1000	200	1000	300	50

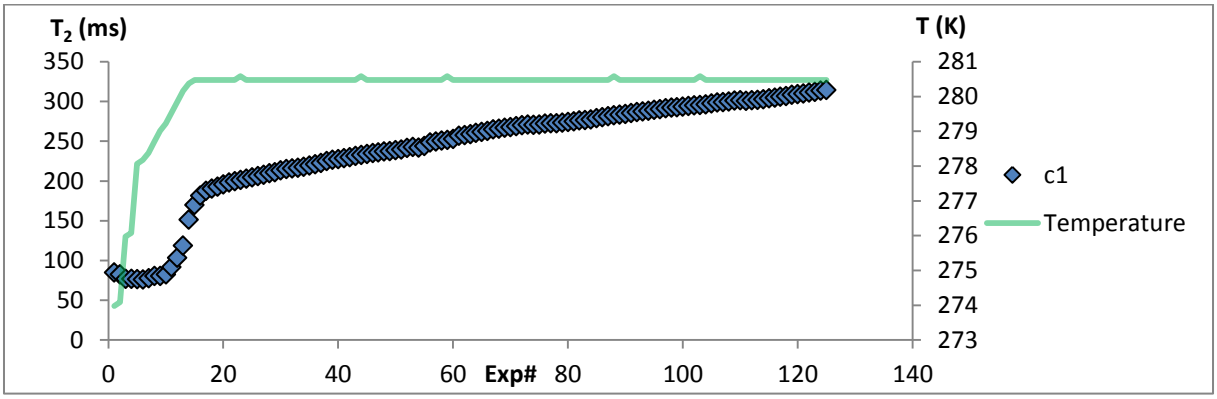

Figure E38: The T_2 results for all experiments in the first B3Fb analysis series using the one-component approach, plotted as a function of experiment number. The T_2 values can be seen to lie considerably lower than those observed for other series.

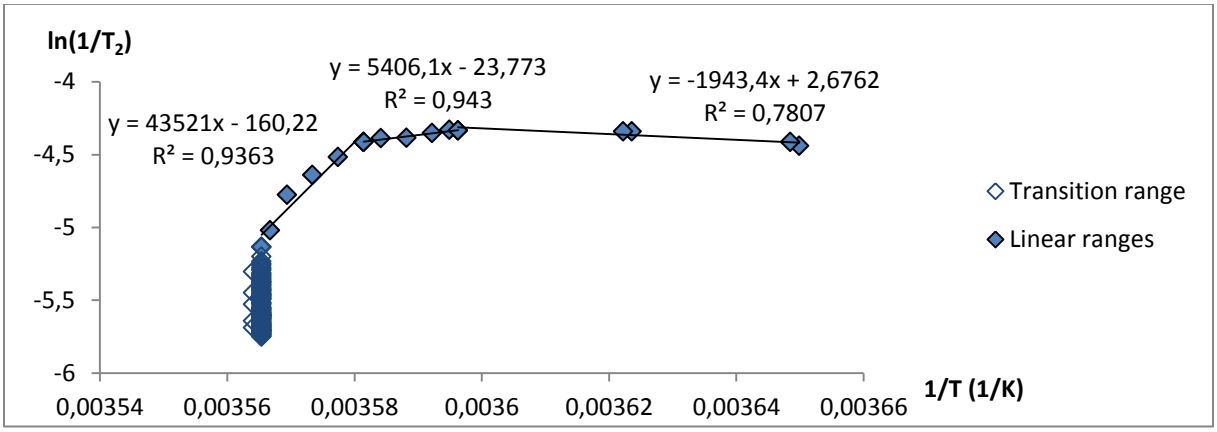

Figure E39: The T_2 results for all experiments in the first B3Fb analysis series using the one-component approach, plotted as $\ln(1/T_2)/(1/T)$. All regions of different slope are fitted to regression lines, with functions and R^2 values provided above their respective lines. The 280.5 K transition range is marked as such.

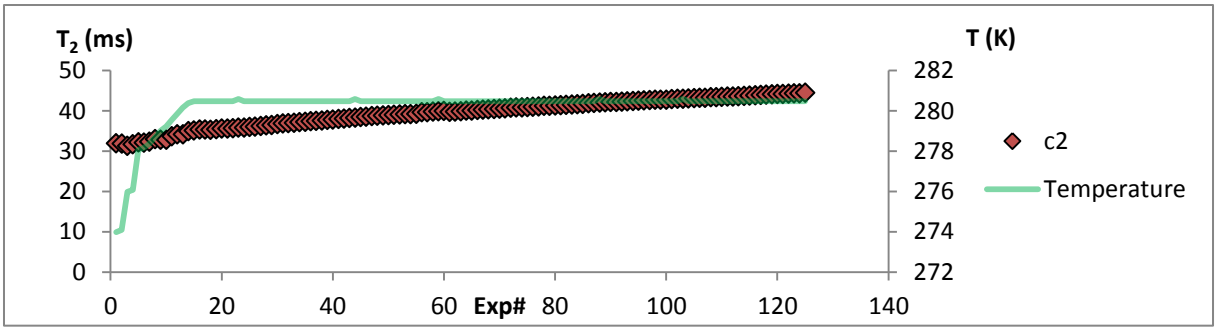

Figure E40: The c2 T_2 results for all experiments in the first B3Fb analysis series using the two-component approach, plotted as a function of experiment number.

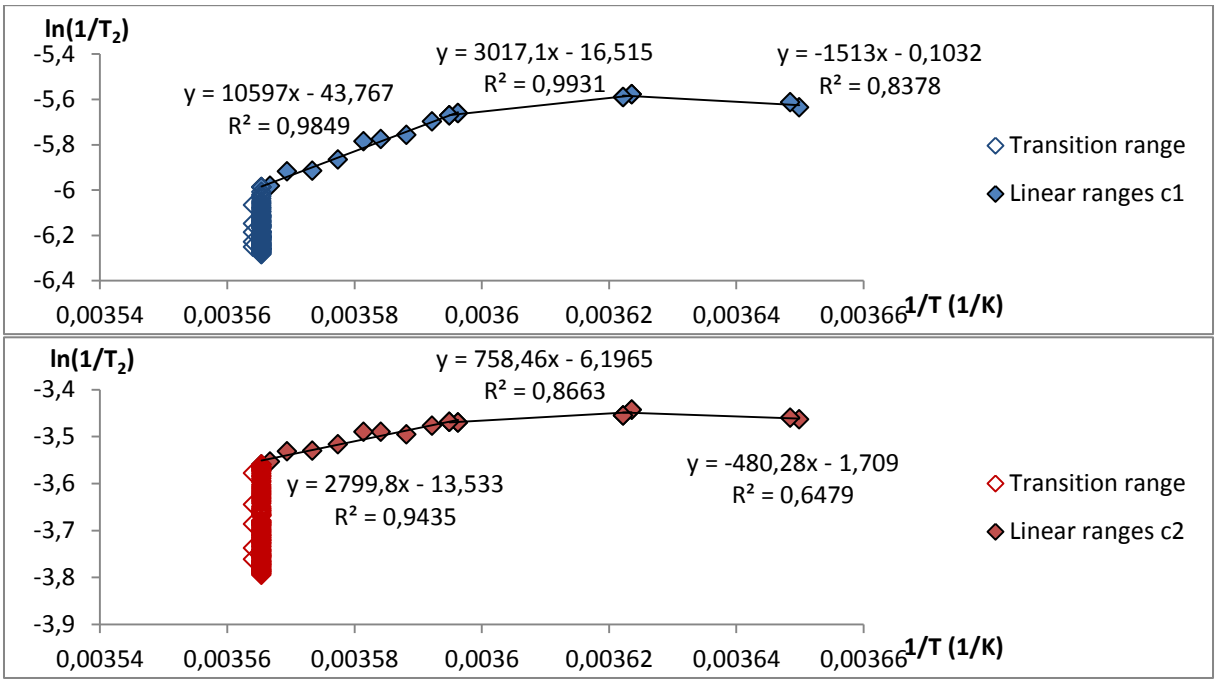

Figure E41: The T_2 results for all experiments in the first B3Fb analysis series using the two-component approach, plotted as $ln(1/T_2)/(1/T)$. All regions of different slope are fitted to regression lines, with functions and R^2 values provided above their respective lines. The 280.5 K transition range is marked as such.

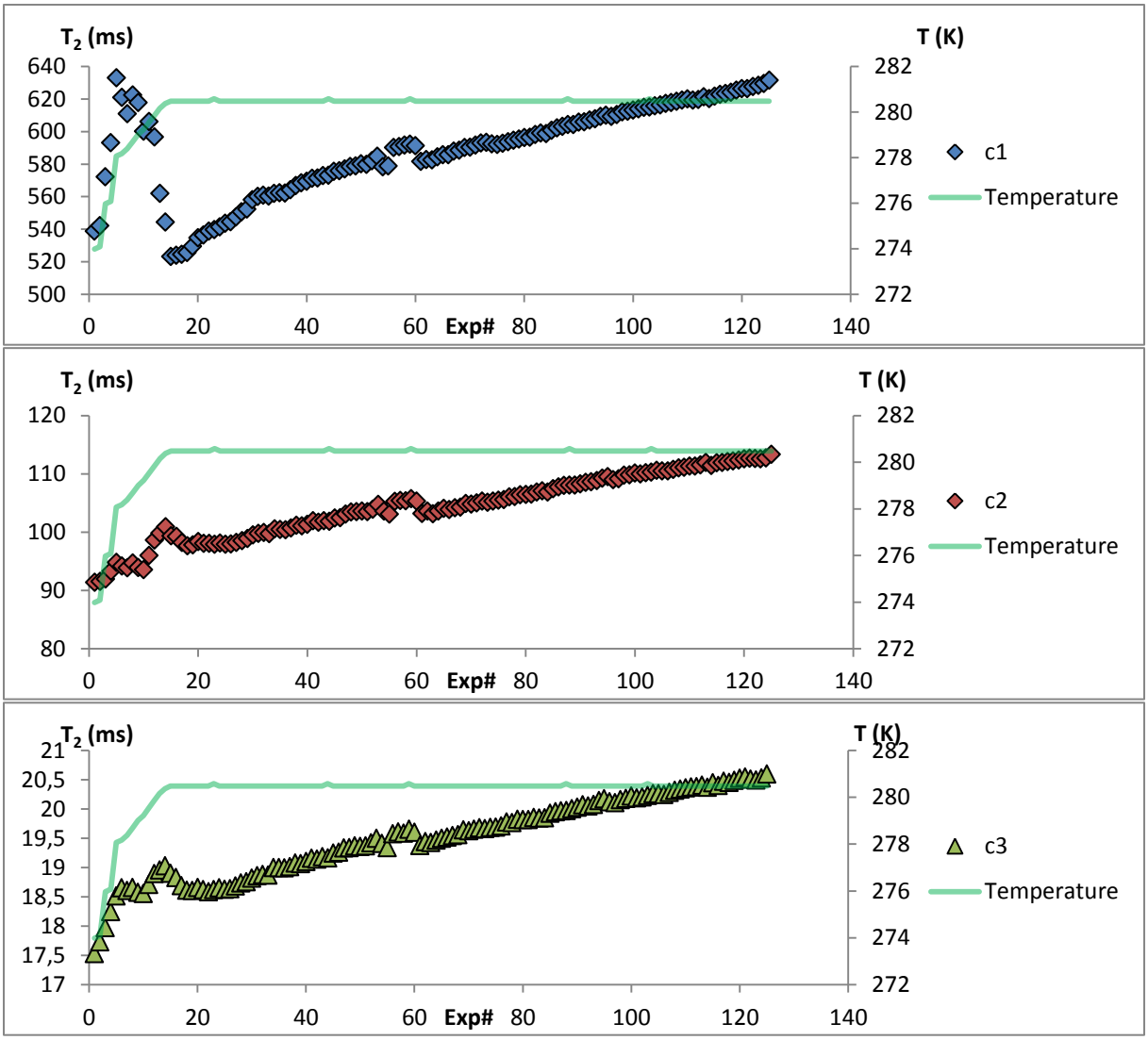

Figure E42: The T_2 results for all experiments in the first B3Fb analysis series using the three-component approach, plotted as a function of experiment number. All components are shown in separate plots.

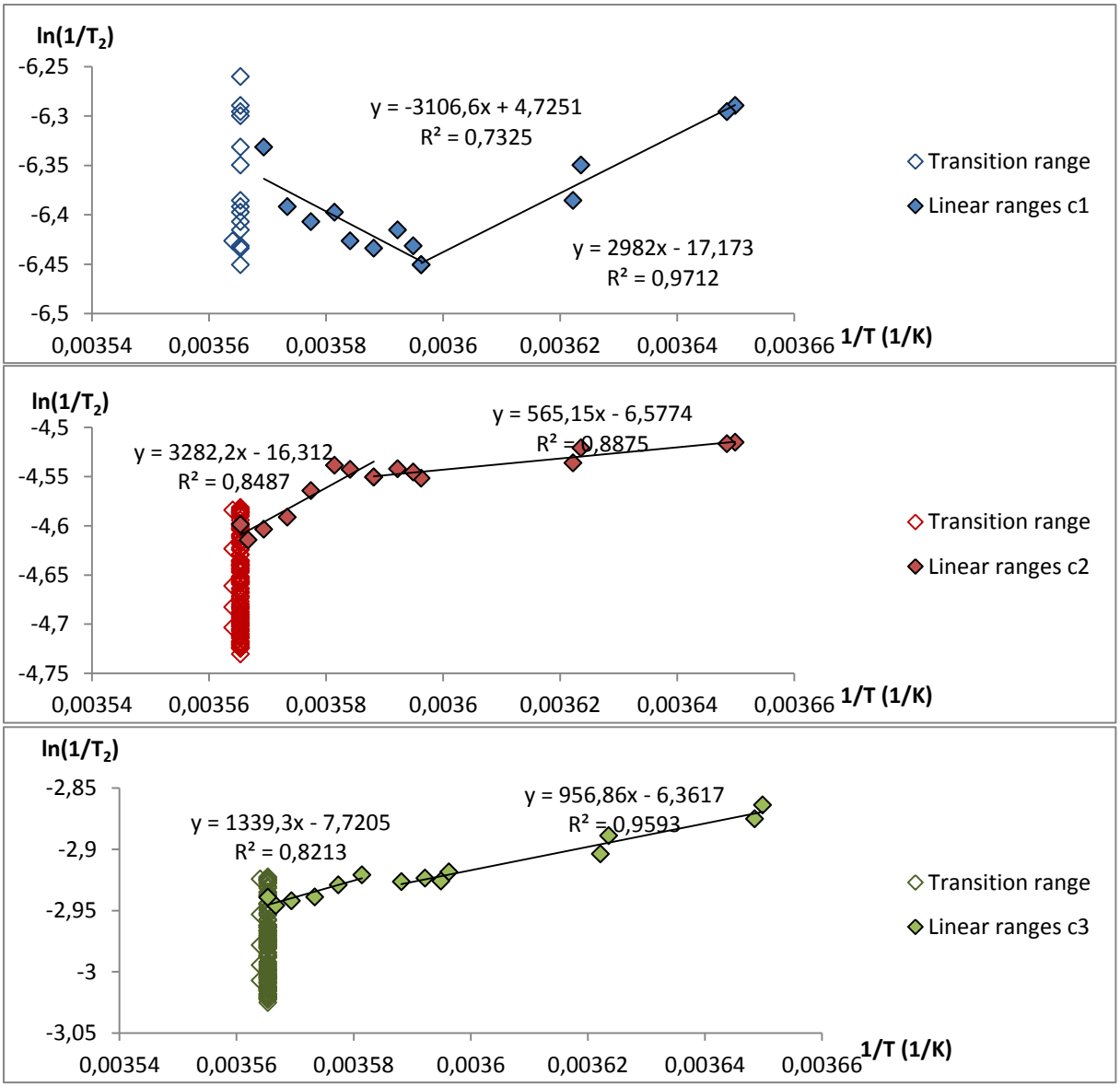

Figure E43: The T_2 results for all experiments in the first B3Fb analysis series using the three-component approach, plotted as $ln(1/T_2)/(1/T)$. All regions of different slope are fitted to regression lines, with functions and R^2 values provided above their respective lines. The 280.5 K transition range is marked as such.

Table E3: The guessrange utilised in analysis of the second experiment series of B3Fb.

Exprange	1comp	2comp1	2comp2	3comp1	3comp2	3comp3
All	1000	1000	200	1000	300	50

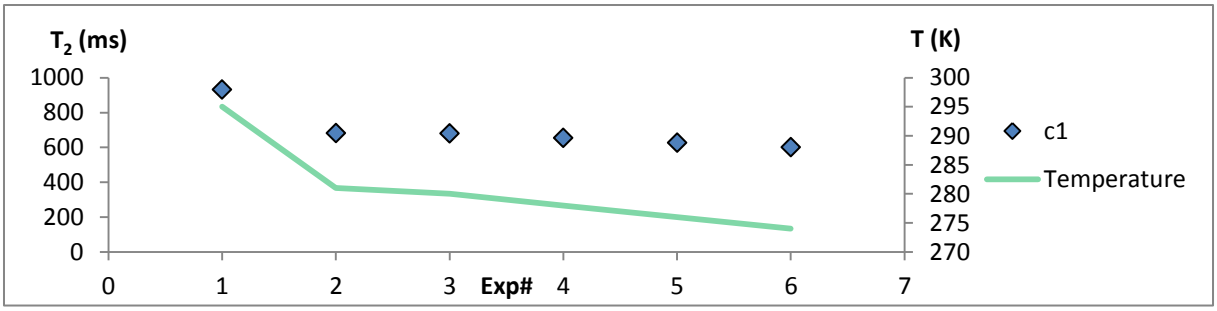

Figure E44: The T_2 results for all experiments in the second B3Fb analysis series using the one-component approach, plotted as a function of experiment number. The sample was analysed following three days at room temperature.

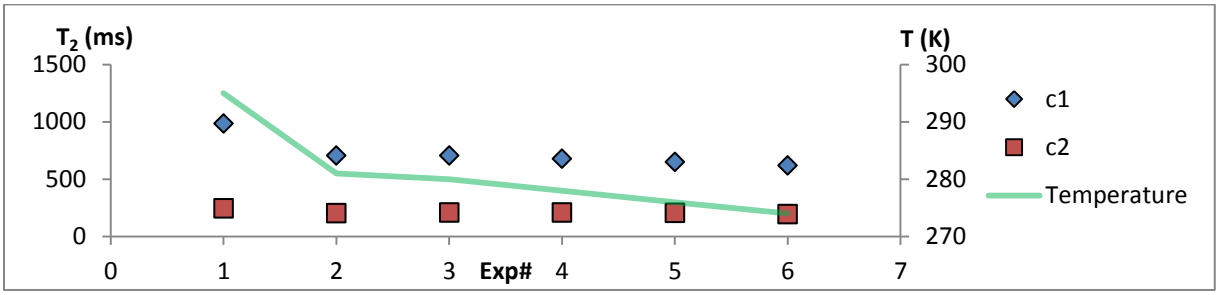

Figure E45: The T_2 results for all experiments in the second B3Fb analysis series using the two-component approach, plotted as a function of experiment number. Before the experiment series, the sample was stored at room temperature for three days. The T_2 values can be seen to lie lower than those observed for other samples, yet higher than the final values during the previous experiment series on the sample.

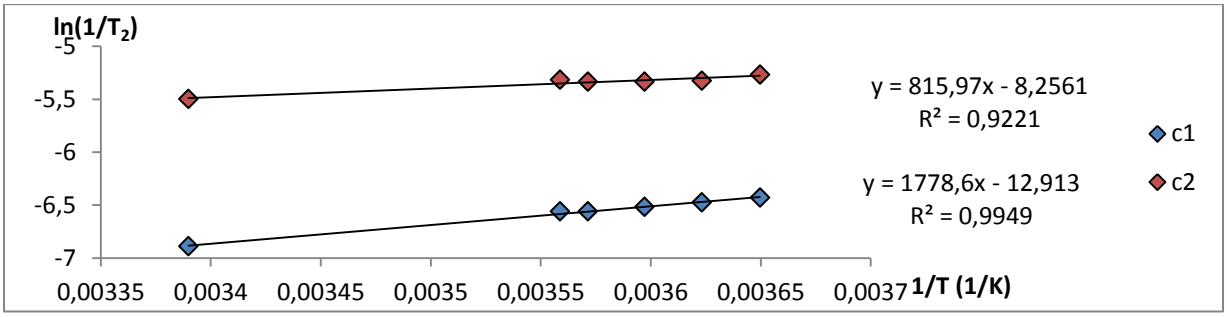

Figure E46: The T_2 results for all experiments in the second B3Fb analysis series using the two-component approach, plotted as $\ln(1/T_2)$ as a function of 1/T. The results are fitted to regression lines, the functions and R^2 values of whose are shown.

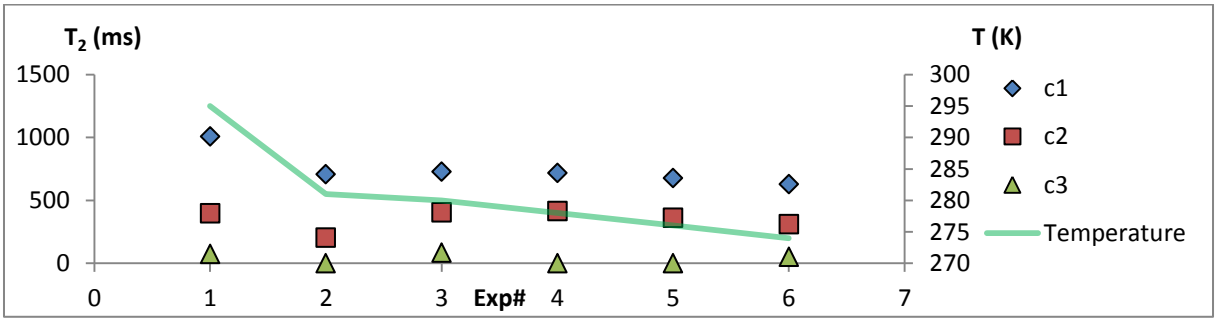

Figure E47: The T_2 results for all experiments in the second B3Fb analysis series using the three-

component approach, plotted as a function of experiment number. The sample was analysed following three days at room temperature.

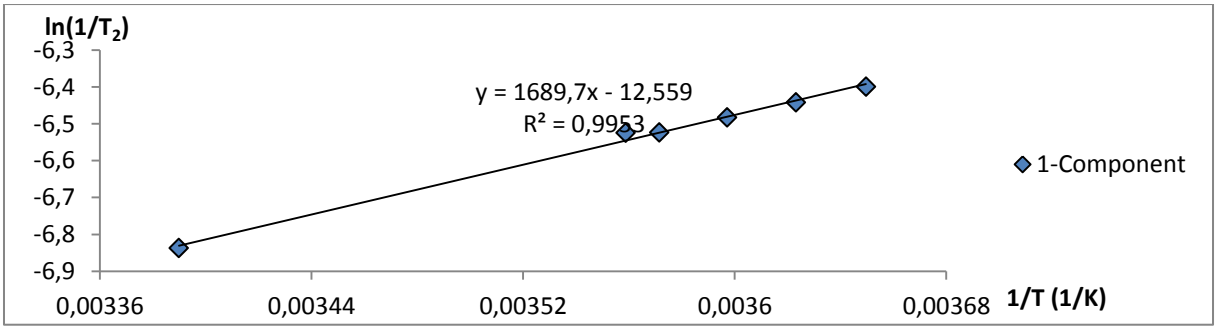

Figure E48: The T_2 results for all experiments in the second B3Fb analysis series using the one-component approach, plotted as $ln(1/T_2)/(1/T)$. Fitting to a regression line is performed, the function and R^2 value of which is also provided. The results were acquired after the sample was stored at room temperature for three days.

B3Fc

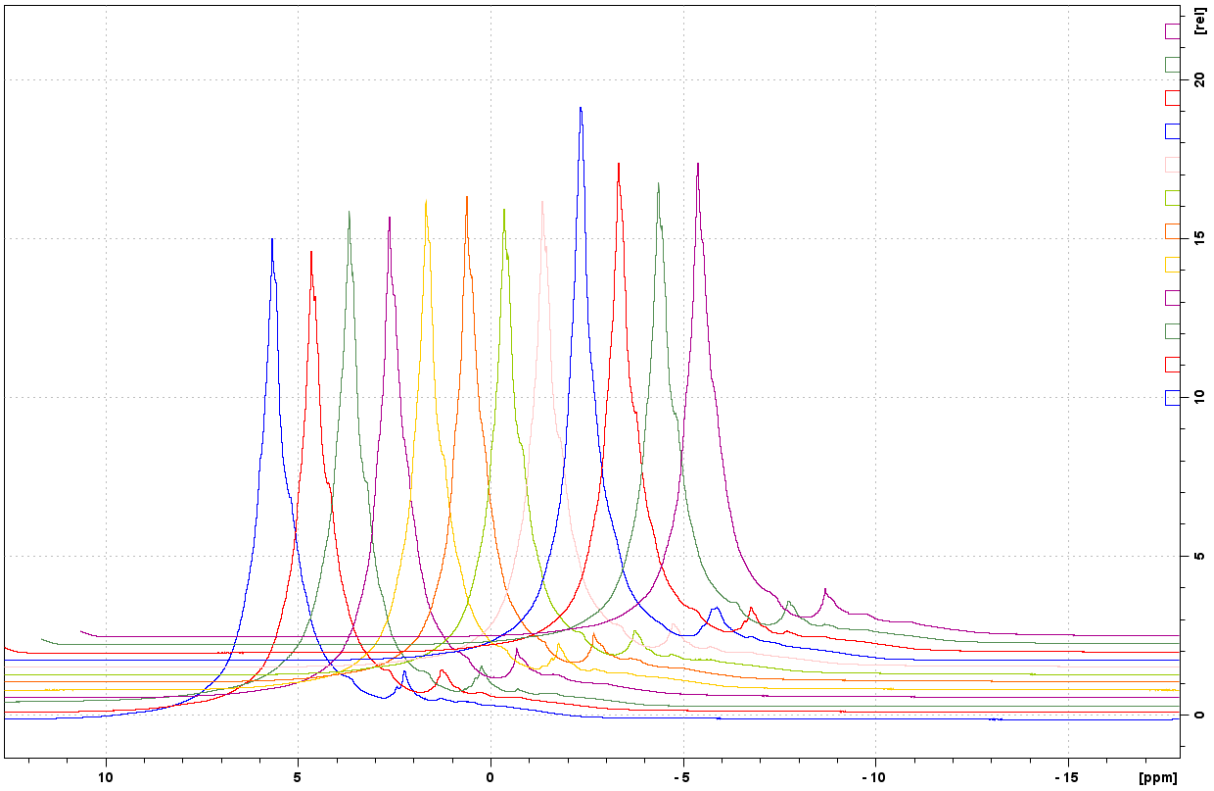

Figure E49: All ^1H spectra acquired on sample B3Fc leading up to the ramp program, presented using horizontal and vertical offset. From front to back, the temperatures are as follows: Five spectra at 274 K, four spectra at 276 K and three spectra at 278 K.

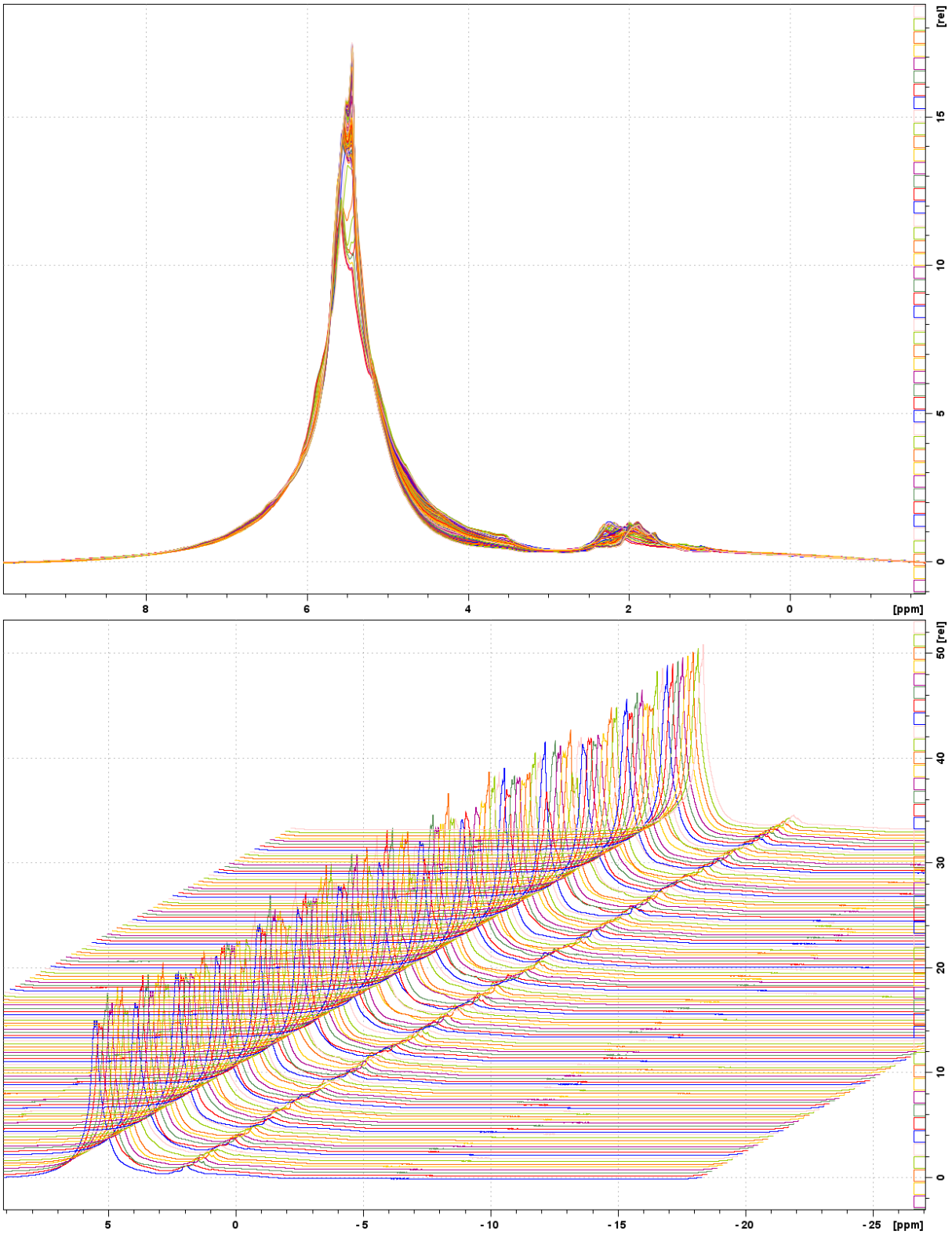

Figure E50: All ^{1}H spectra acquired during the sample B3Fc ramp program, presented in a stacked plot (top) and using horizontal and vertical offset (bottom). The water peak fluctuates before stabilising towards the end of the experiment, as does the cyclopentane peaks.

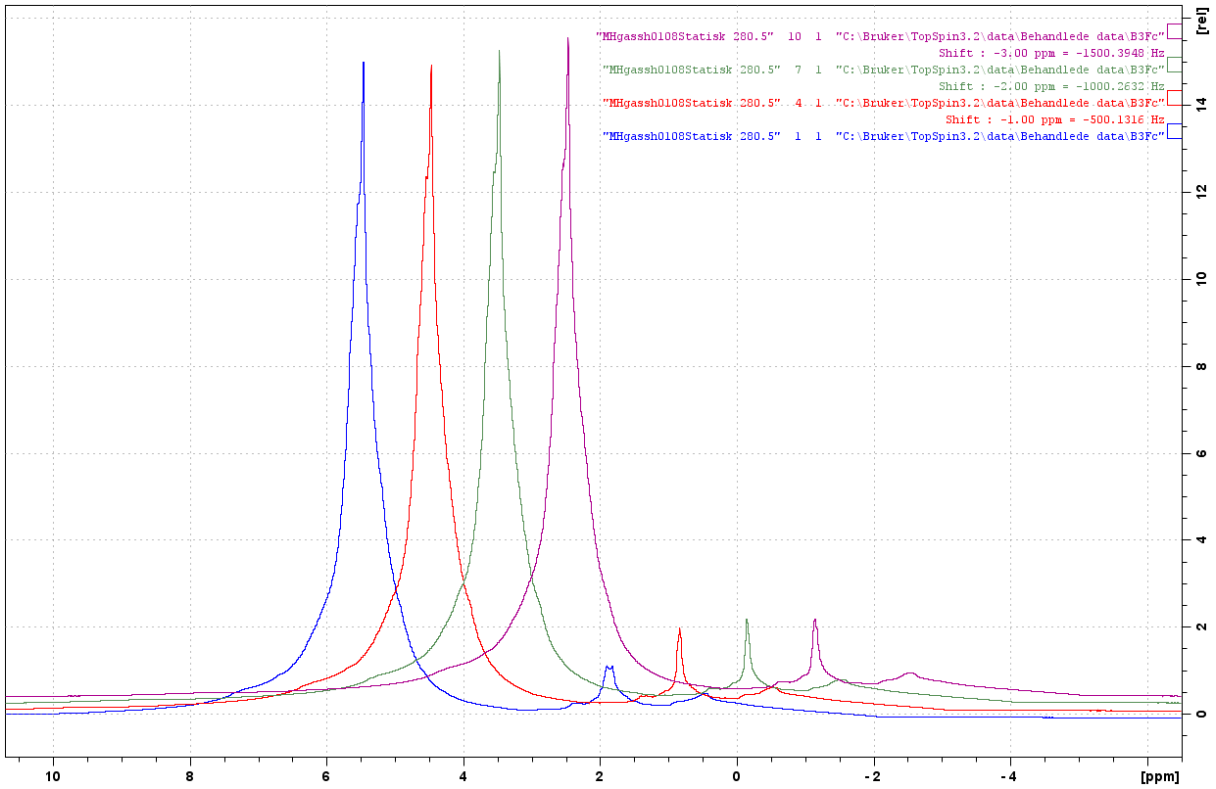

Figure E51: Four spectra aquired at 280.5 K after the sample B3Fc ramp program, presented using vertical and horizontal offset.

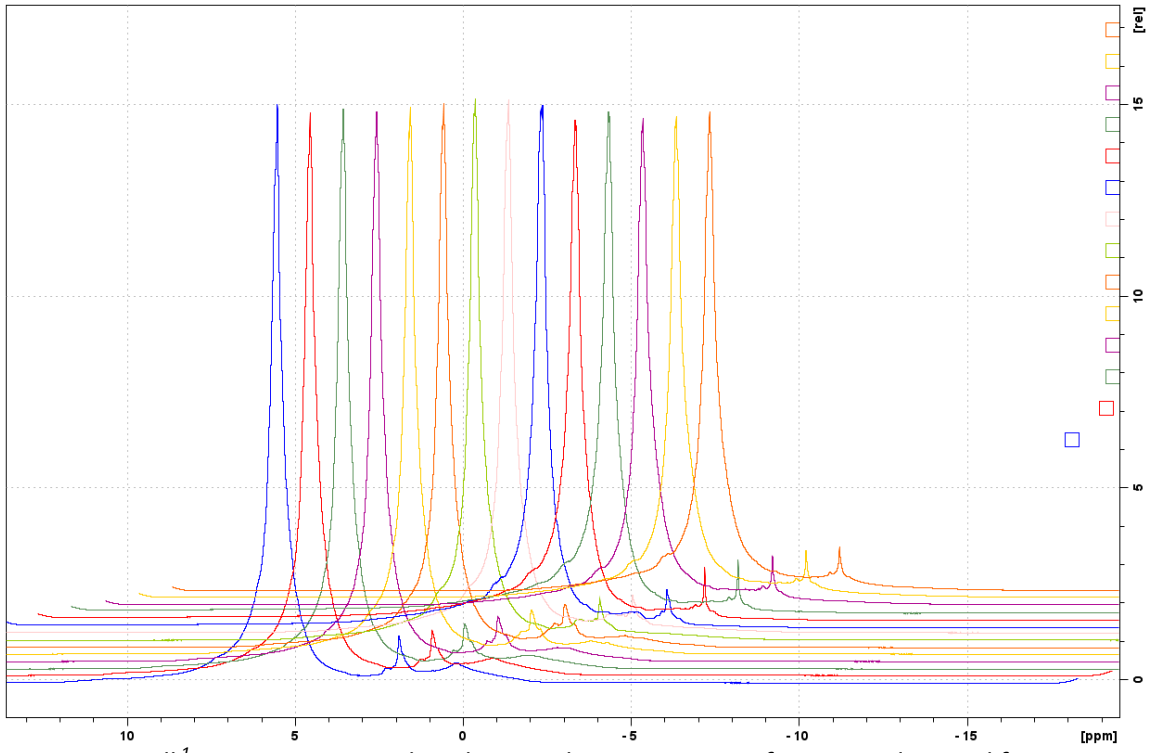

Figure E52: All ^{1}H spectra acquired as the sample temperature of B3Fc was lowered from 280.5 K back into the hydrate stability region, presented using horizontal and vertical offset. From front to back, the first six spectra were acquired at 279 K, with the following five spectra acquired at a temperature of 274 K. The remaining three were acquired at 273 K. The spectra was taken 20 minutes apart, covering a timespan of approximately five hours.

TableE4: The guessrange utilised in analysis of sample B3Fc results.

Exprange	1comp	2comp1	2comp2	3comp1	3comp2	3comp3
All	1000	1000	200	1000	300	50

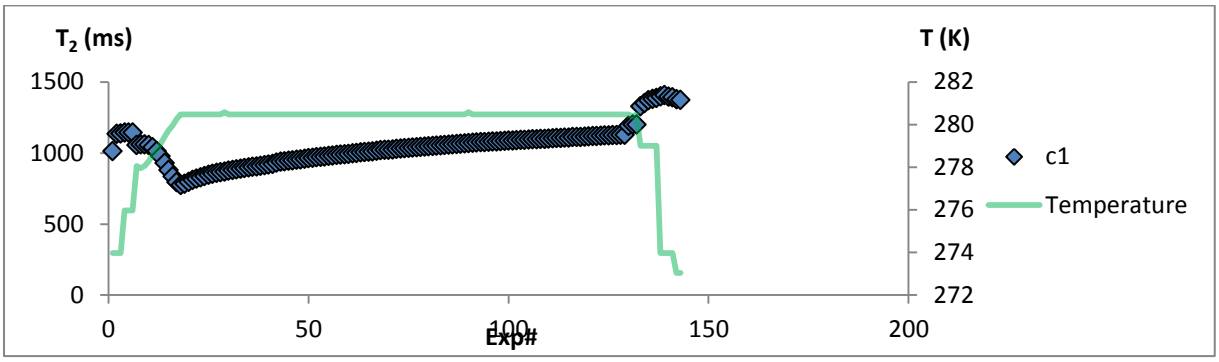

Figure E53: The T_2 results for all experiments for sample B3Fc using the one-component approach, plotted as a function of experiment number.

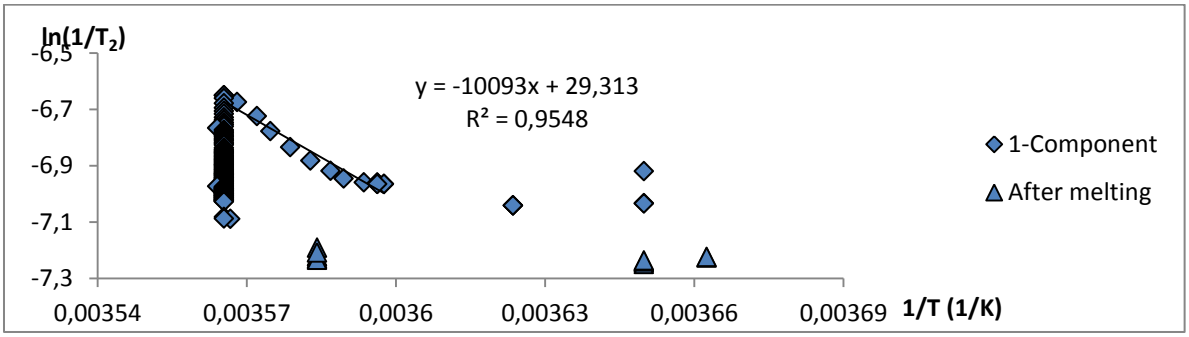

Figure E54: The T_2 results for all experiments of sample B3Fc using the one-component approach, plotted as $ln(1/T_2)/(1/T)$. Points acquired after the temperature was lowered from 280.5 K are marked as 'After melting'. The linear range fitted to a regression line.

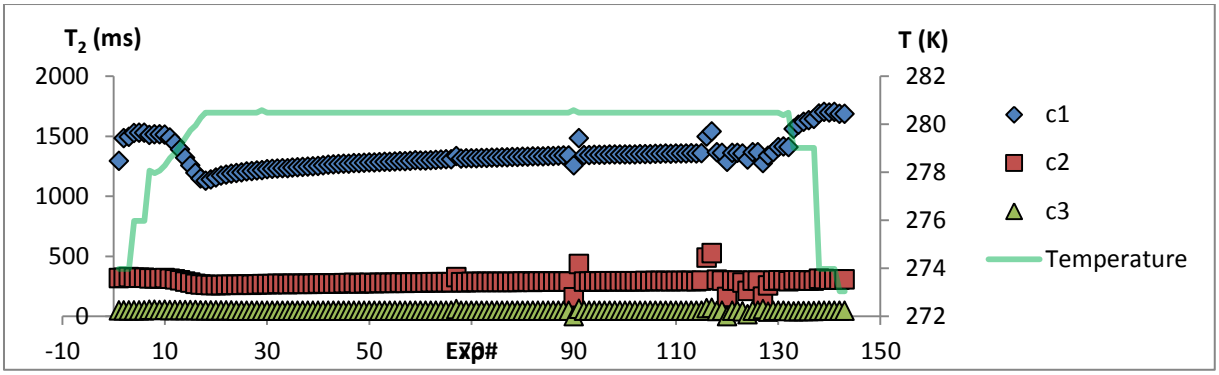

Figure E55: The T_2 results for all experiments for sample B3Fc using the three-component approach, plotted as a function of experiment number.

B3Fa2

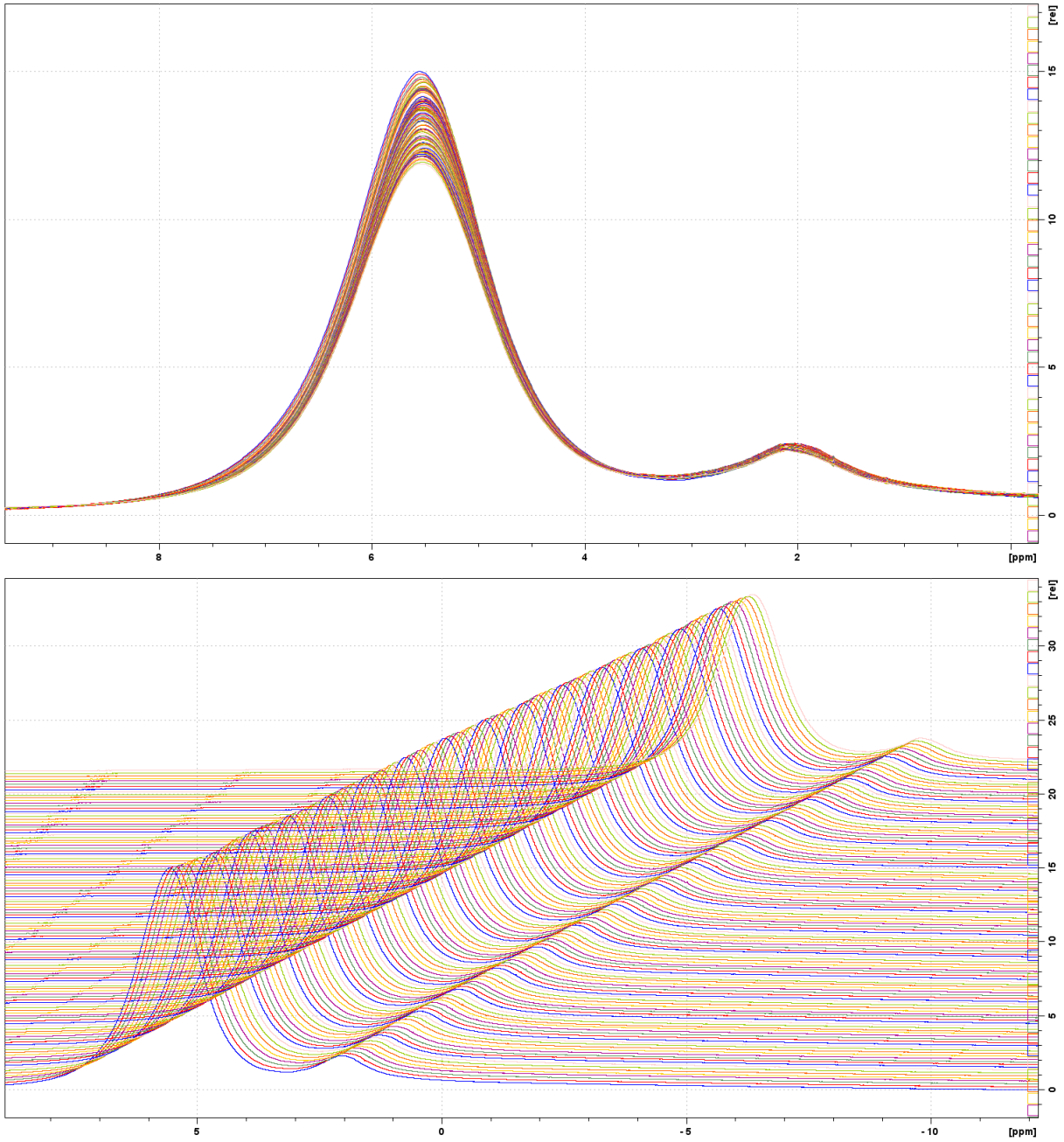

Figure E56: The results of all 120 ^{1}H experiments during and after temperature ramping of sample B3Fa2. a) Stacked plot of all results. The first acquisition gives rise to the upper, blue line in the water peak, and the peak intensity of remaining spectra falls of as a function of time and/or temperature. b) Spectra presented with horizontal and vertical offset.

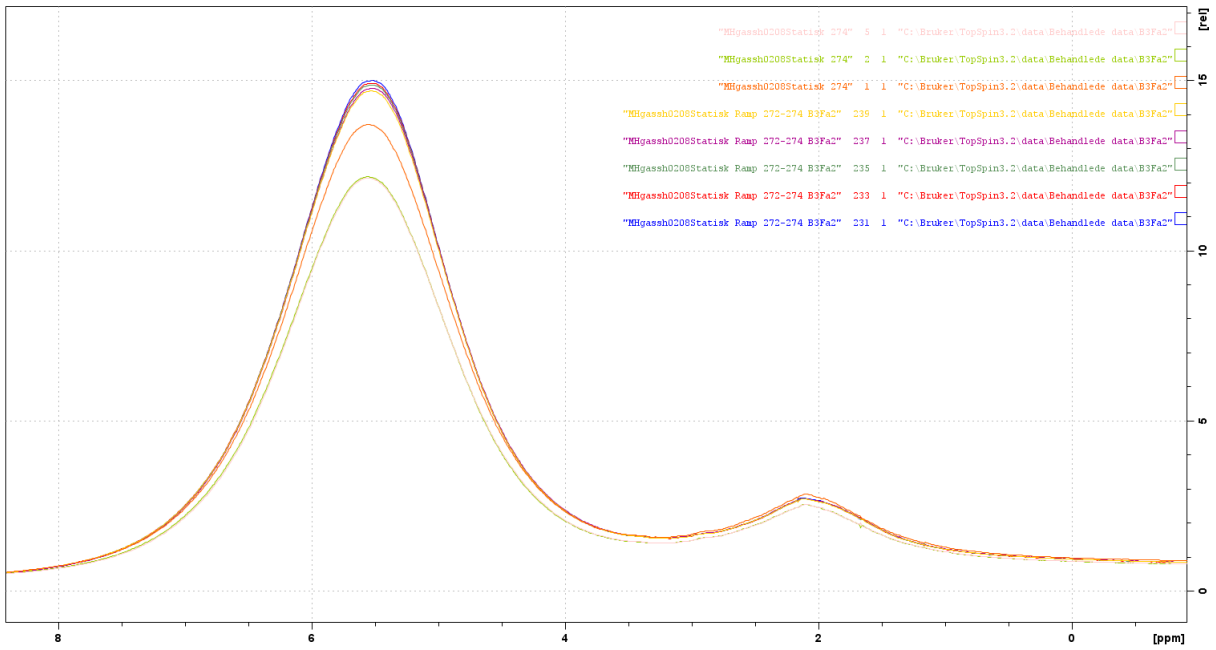

Figure E57: The initial ^{1}H spectrum taken after the ramp program (orange) and two following spectra, 21 minutes apart (lime and pink), is shown in comparison with the final five spectra during the continuous ramp acquisition. All spectra were acquired at 274 K for sample B3Fa2.

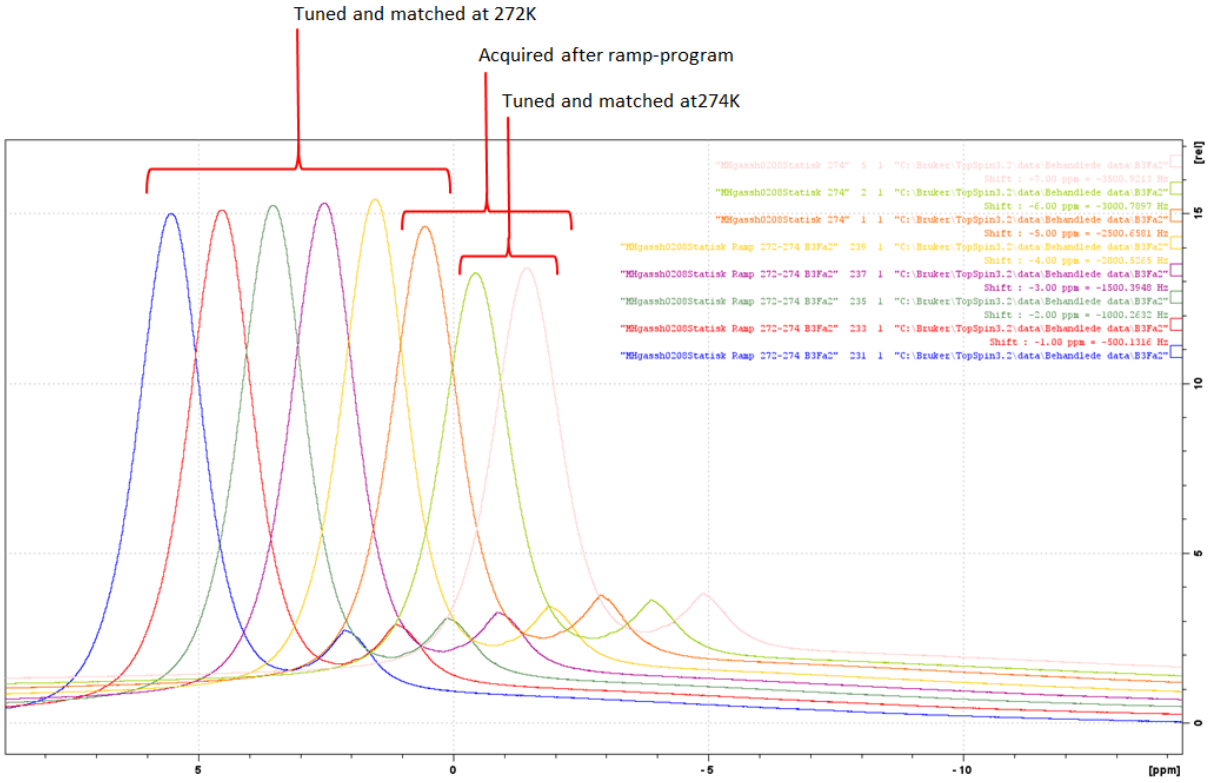

Figure E58: The same spectra as above is presented using horizontal and vertical offset. The relevant properties of each peak are marked.

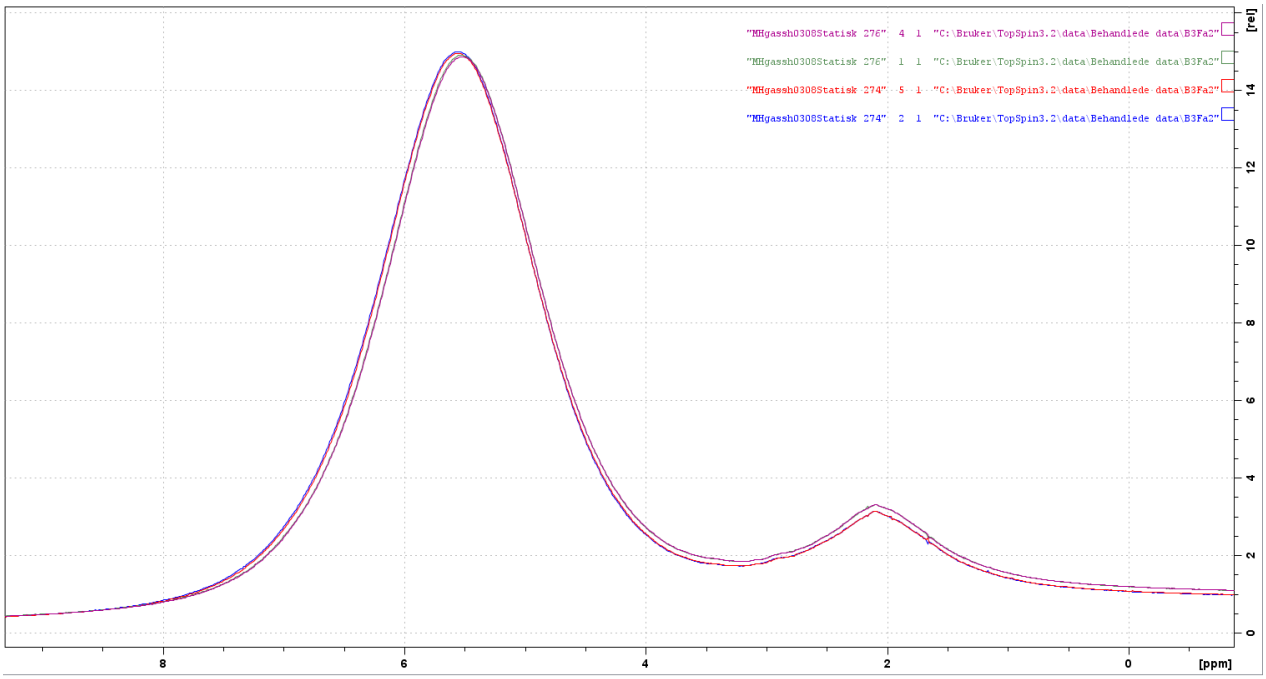

Figure E59: The first (green) and second (indigo) ^{1}H spectra acquired at 276 K are compared with the results at 274 K (red and blue). The four spectra cover a time span of approximately one hour.

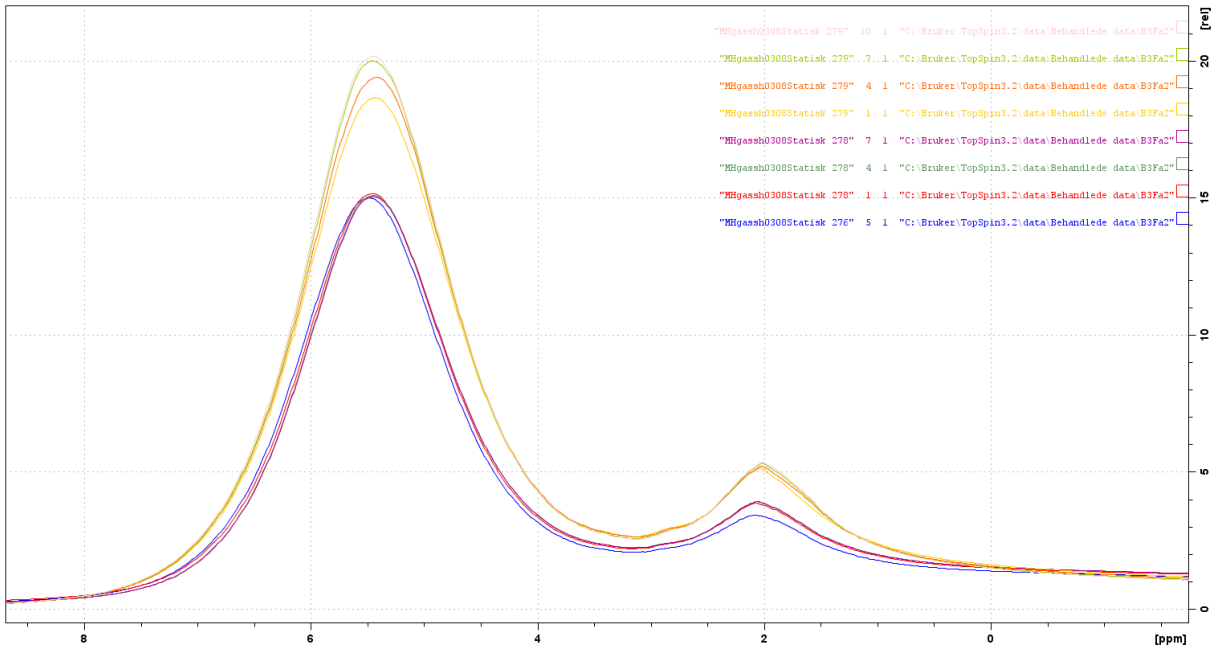

Figure E60: Stacked plot of the spectra at 278 K (red, green and indigo) and 279 K (yellow, orange, lime and pink). The blue line represents the spectrum at 276 K, provided for reference. The spectra were acquired approximately 20 minutes apart. From sample B3Fa2

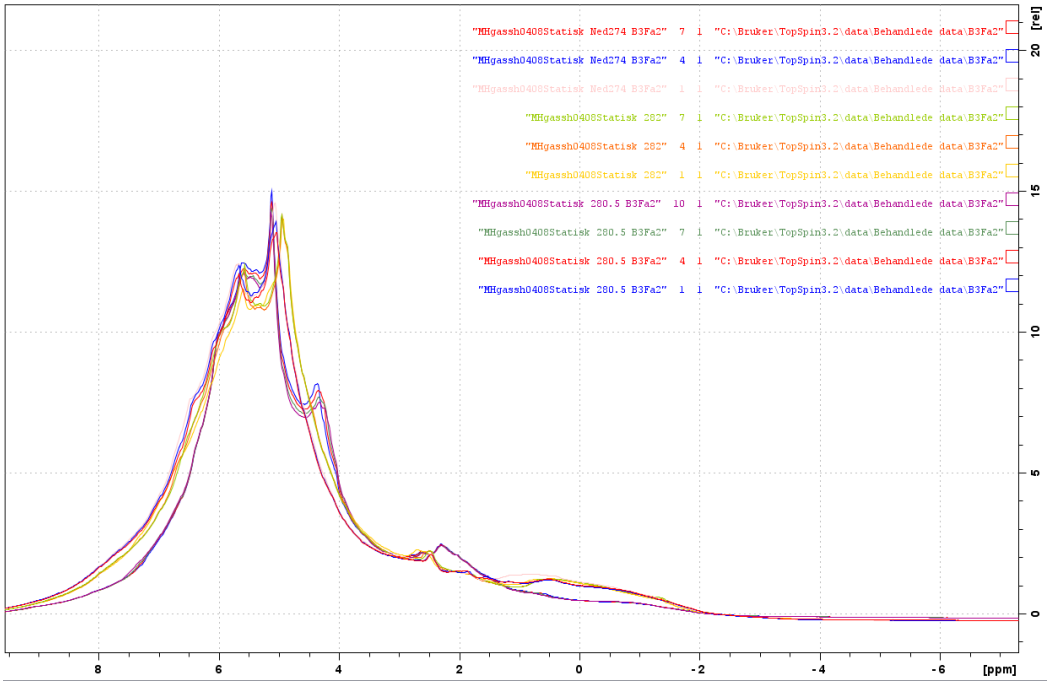

Figure E61: All spectra acquired after the last spectrum of the ramping program. The downfield water peak disappears at 282 K, and further growth in intensity of the downfield cyclopentane peak at the cost of the upfield one is also observed.

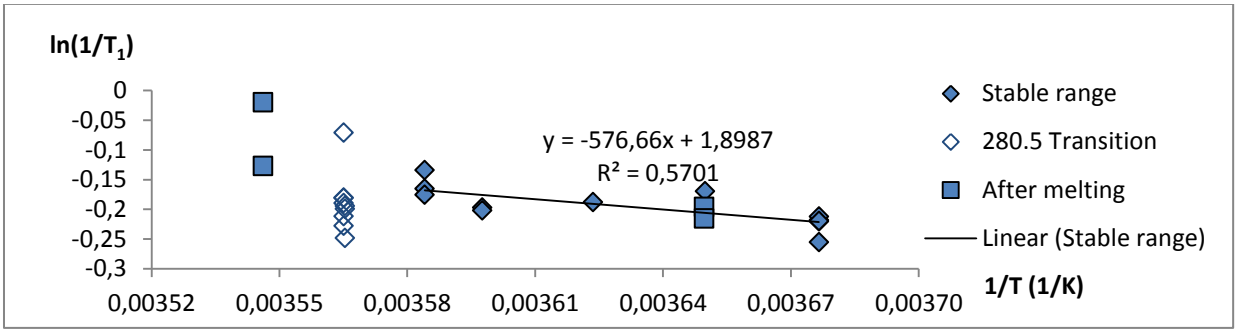

Figure E62: The component 1 results of two-component analysis of the water peak in all B3Fa2 measurements, presented as $ln(1/T_1)$ as a function inverse temperature. The transition range and post-melting measurements are marked. Linear regression is performed on the stable range.

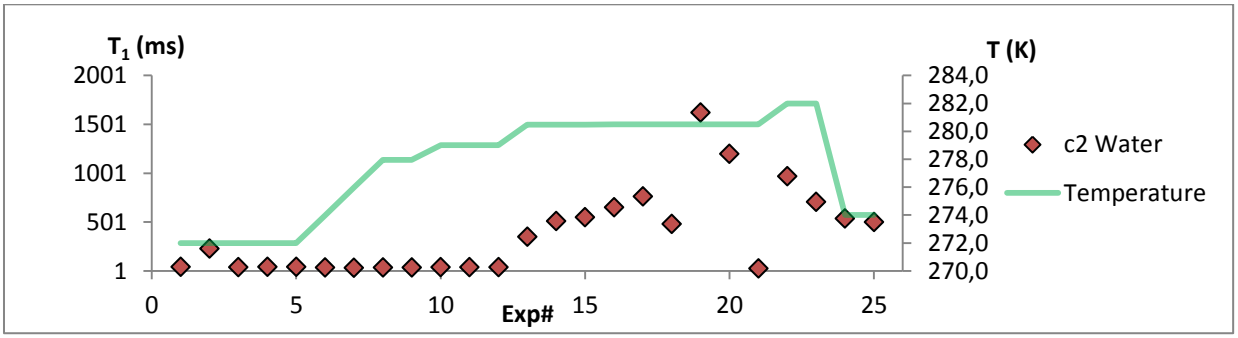

Figure E63: The component 2 results of two-component analysis of the water peak in all B3Fa2 T_1 measurements plotted as a function of experiment number. The temperature in Kelvin is plotted on the secondary axis.

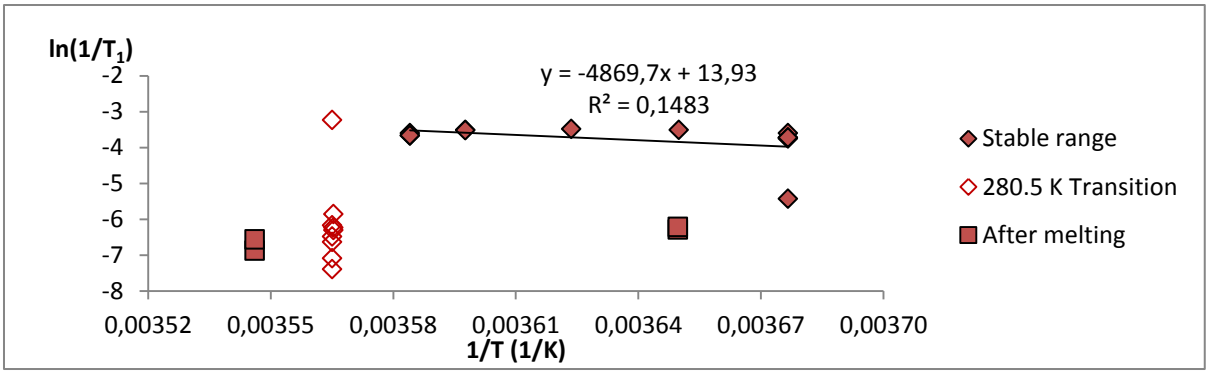

Figure E64: The component 2 results of two-component analysis of the water peak in all B3Fa2 measurements, presented as ln(1/T_1) as a function inverse temperature. The transition range and post-melting measurements are marked. Linear regression is performed on the stable range, which might also be split in two parts. The presence of one outlying value is noted. As this result is the second of five measurements at 282 K, the deviation is unlikely to be due to an on-going process in the sample.

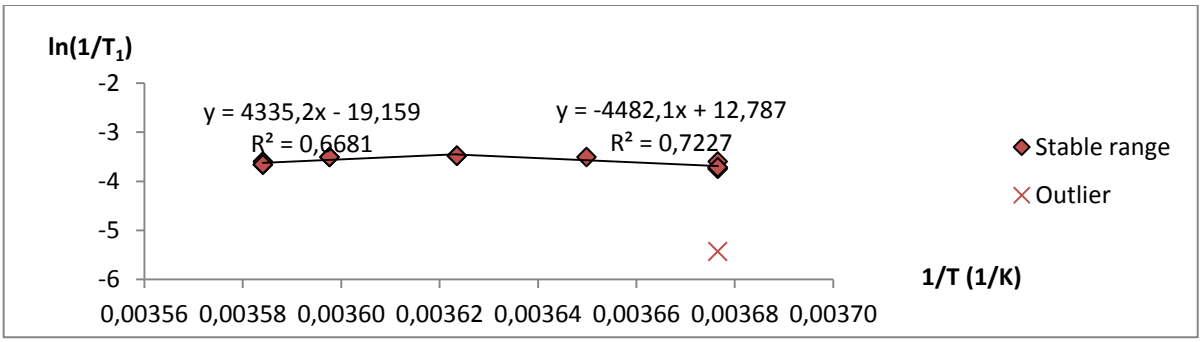

Figure E65: The stable range in Fig. E64 is split into two parts, with the outlier marked and removed from the linear regression analysis.

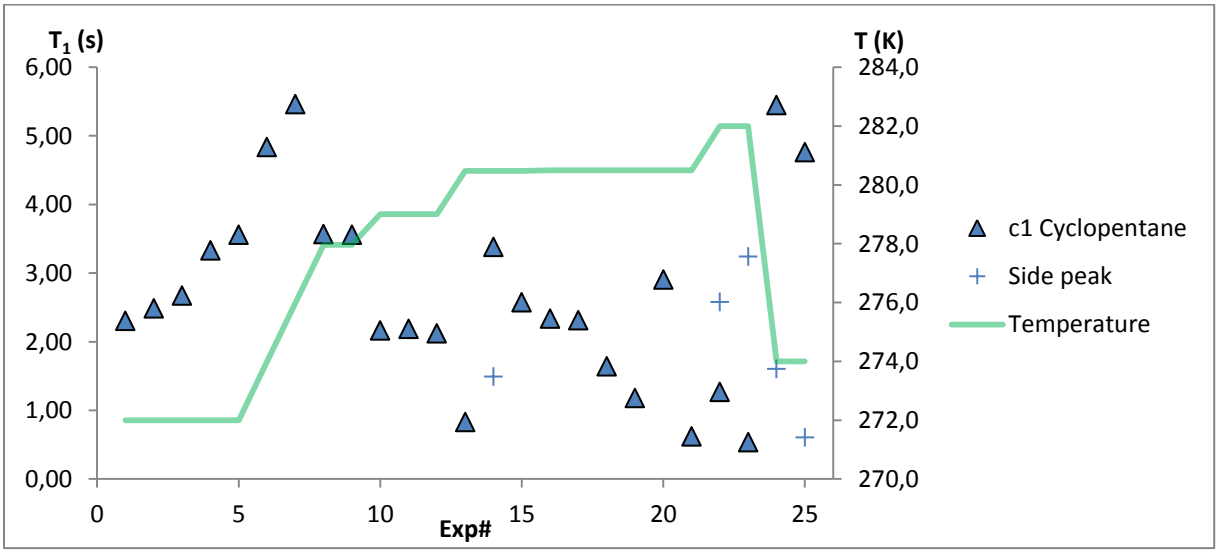

Figure E66: The component 1 results of two-component analysis of the cyclopentane peak in all B3Fa2 T_1 measurements plotted as a function of experiment number. The temperature in Kelvin is plotted on the secondary axis. The results of the side peak are included.

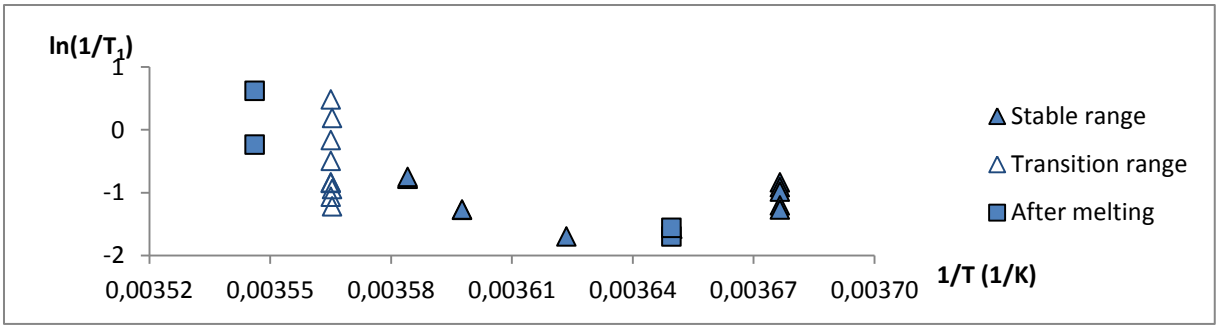

Figure E67: The component 1 results of two-component analysis of the cyclopentane peak in all B3Fa2 measurements, presented as ln(1/T_1) as a function inverse temperature. The transition range and post-melting measurements are marked. Side peaks are not included in the plot.

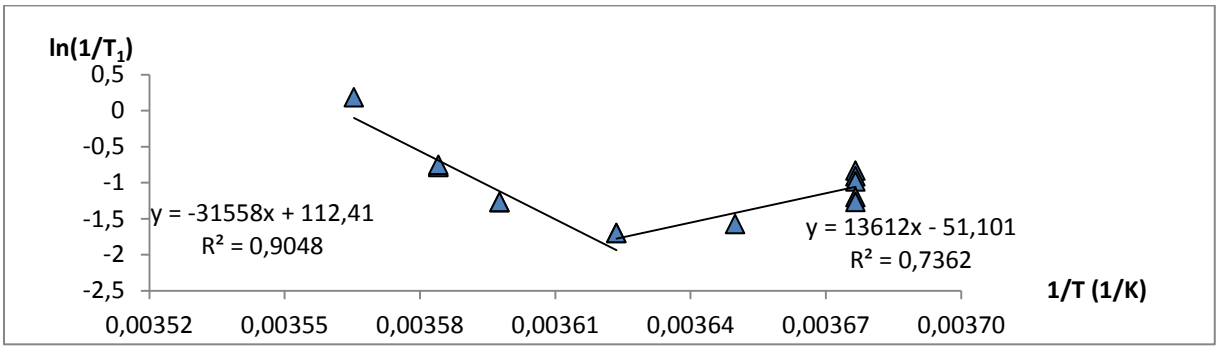

Figure E68: The stable range from Fig. E67 is plotted along with the first measurement at 280.5 K, and linear regression analysis is performed on two separate parts of the results possibly making up linear ranges. The regression functions with R^2 values are shown besides their respective lines.

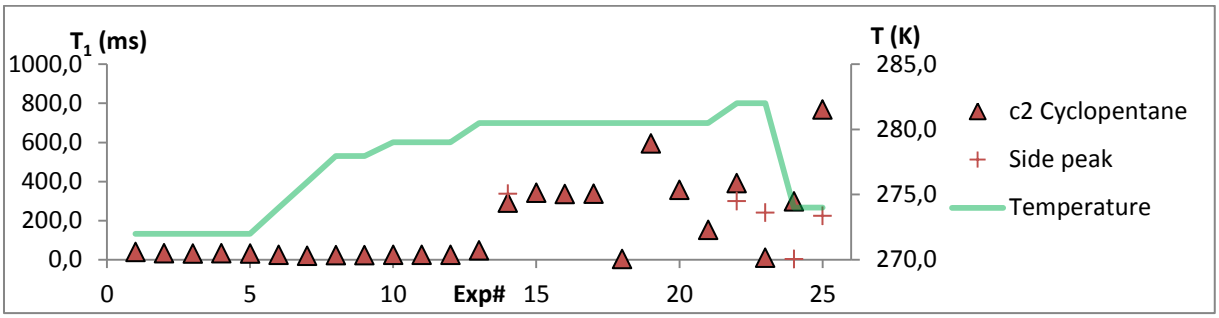

Figure E69: The component 2 results of two-component analysis of the cyclopentane peak in all B3Fa2 T_1 measurements plotted as a function of experiment number. The temperature in Kelvin is plotted on the secondary axis. The results of the side peak are included.

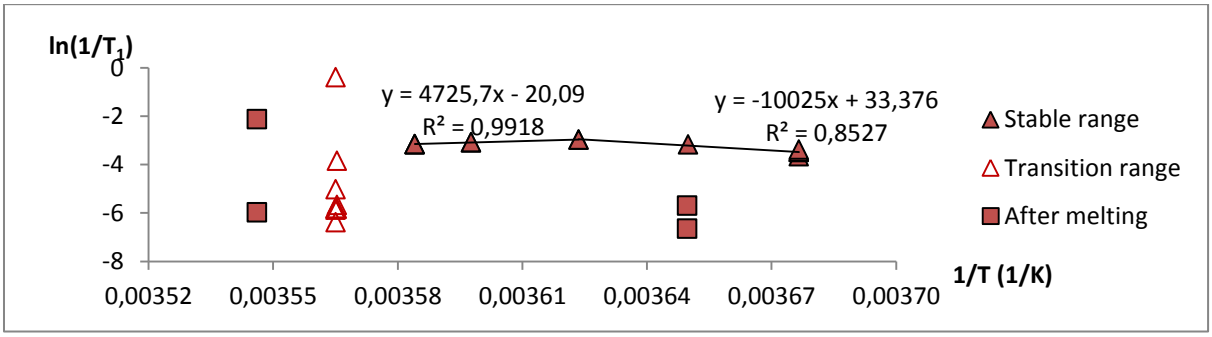

Figure E70: The component 2 results of two-component analysis of the cyclopentane peak in all B3Fa2 measurements, presented as ln(1/T_1) as a function inverse temperature. The transition range and

post-melting measurements are marked. Linear regression analysis is performed on the stable ranges. Side peaks are not included in the plot.

Table E5: The guess parameters used in the calculation of T_2 values using the appropriate MATLAB script. c1 is the guess for the first component, c2 is the guess for the second component, and c3 is the guess for the third component. One-, two- and three-component analysis is done separately, using different values. The experiment range denotes the experiments to which a given set of guesses were applied to, with each experiment given a specific number within the B3Fa2 experiment series.

Experiment range	One-component	Two-component		Three-component		
	c1	c1	c2	c1	c2	c2
1-126	100	250	50	400	100	50
127-137	100	300	50	600	100	50
138-143	1000	1000	100	1000	200	50
143-253	1200	1200	100	1200	300	50

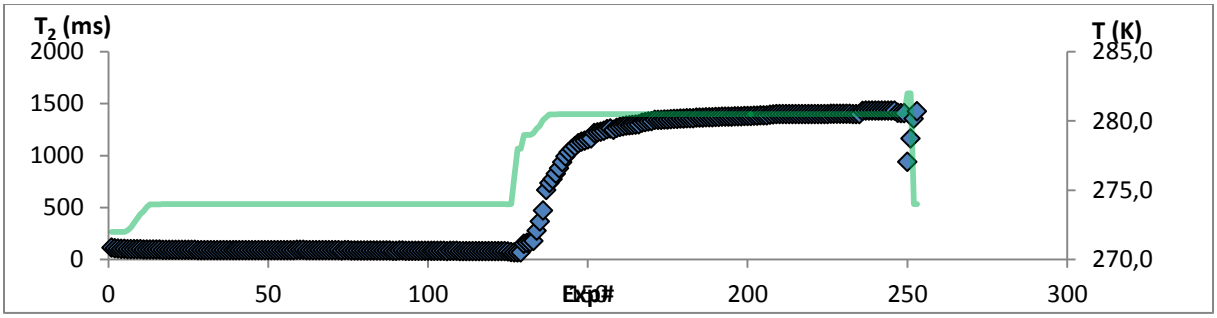

Figure E71: The results of one-component analysis of all CPMG oneshot experiments on B3Fa2, plotted as T_2 in ms as a function of experiment number. The green curve is the temperature in Kelvin, plotted on the secondary vertical axis.

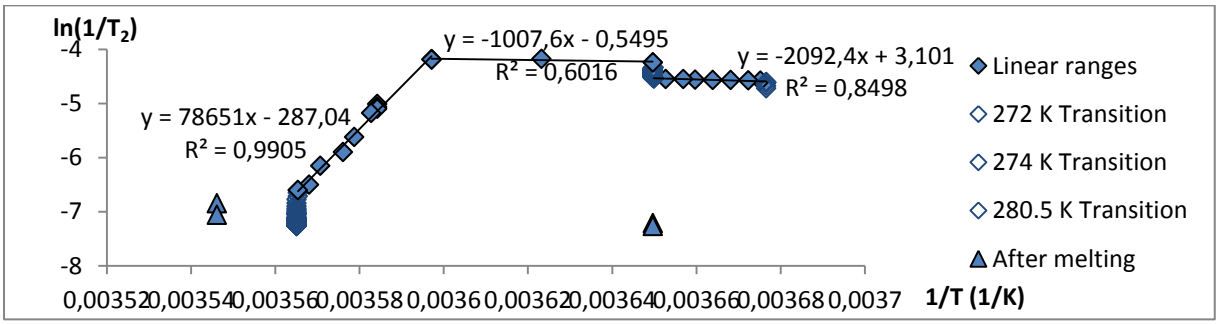

Figure E72: The results of one-component analysis of all CPMG oneshot experiments on B3Fa2, plotted as plotted as $\ln((T_2)^{-1})$ as a function of T^{-1}. Three linear ranges are identified and separately fitted to regression lines, the functions and R^2 values of whose are provided above their respective lines. The three ranges of rapid change are designated as transitions, marked with open diamonds. These results are not factored into regression. Experiments performed after the last transition is shown as "After melting", and is not included in the regressions.

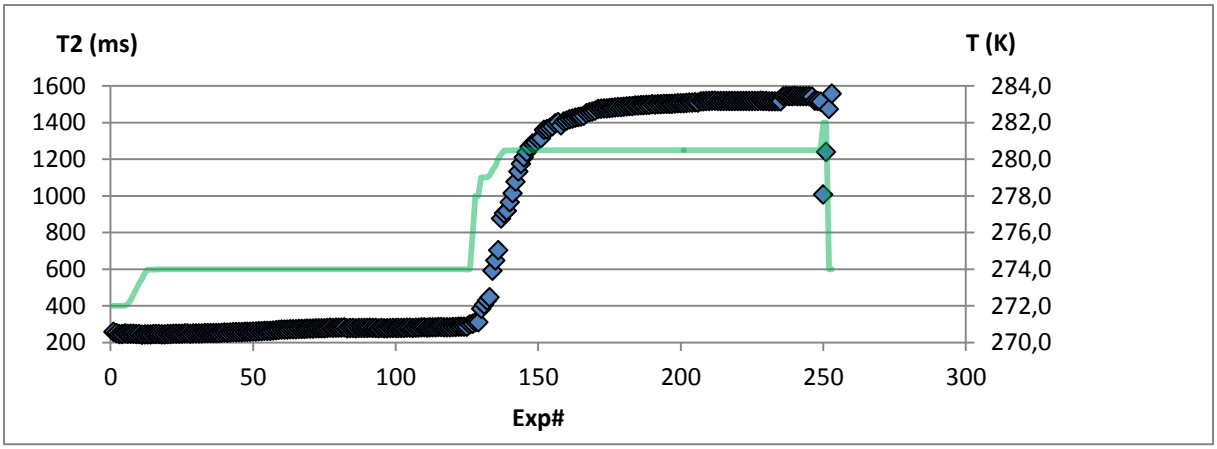

Figure E73: The plot of component 1 for the two-component analysis of all CPMG oneshot experiments on B3Fa2, plotted as T_2 in ms as a function of experiment number. The green curve is the temperature in Kelvin, plotted on the secondary vertical axis.

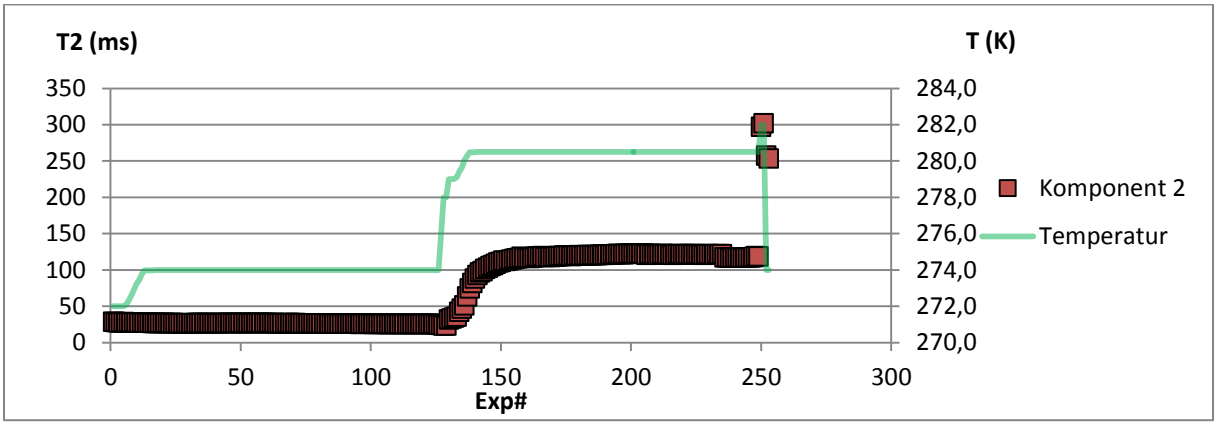

Figure E74: The plot of component 2 for the two-component analysis of all CPMG oneshot experiments on B3Fa2, plotted as T_2 in ms as a function of experiment number. The green curve is the temperature in Kelvin, plotted on the secondary vertical axis.

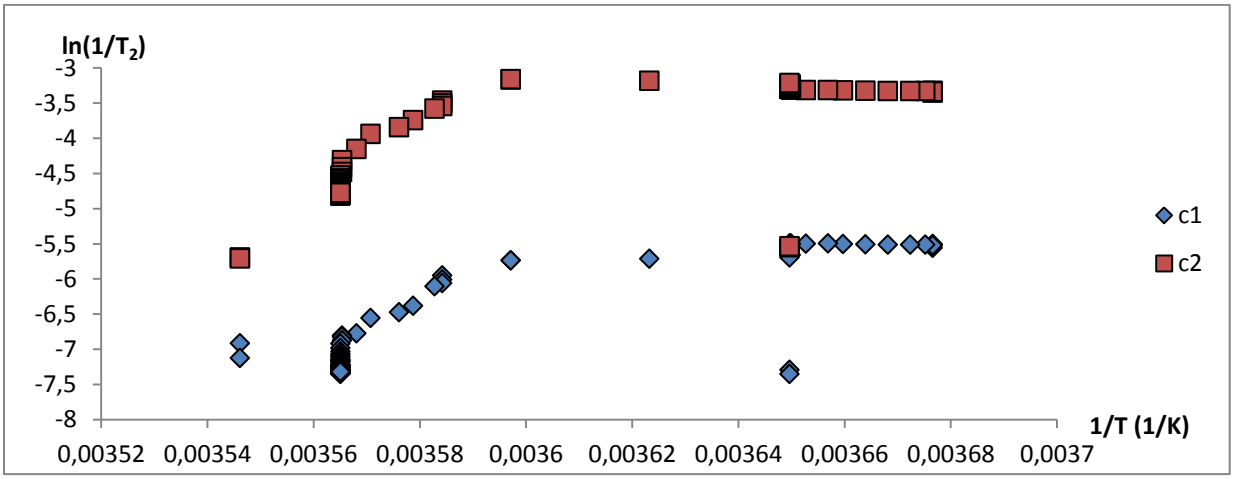

Figure E75: The results of two-component analysis of all CPMG oneshot experiments on B3Fa2, plotted as $ln(T_2)^{-1}$ function of T^{-1}. Component 1 is plotted using blue diamonds and component 2 is plotted using red squares.

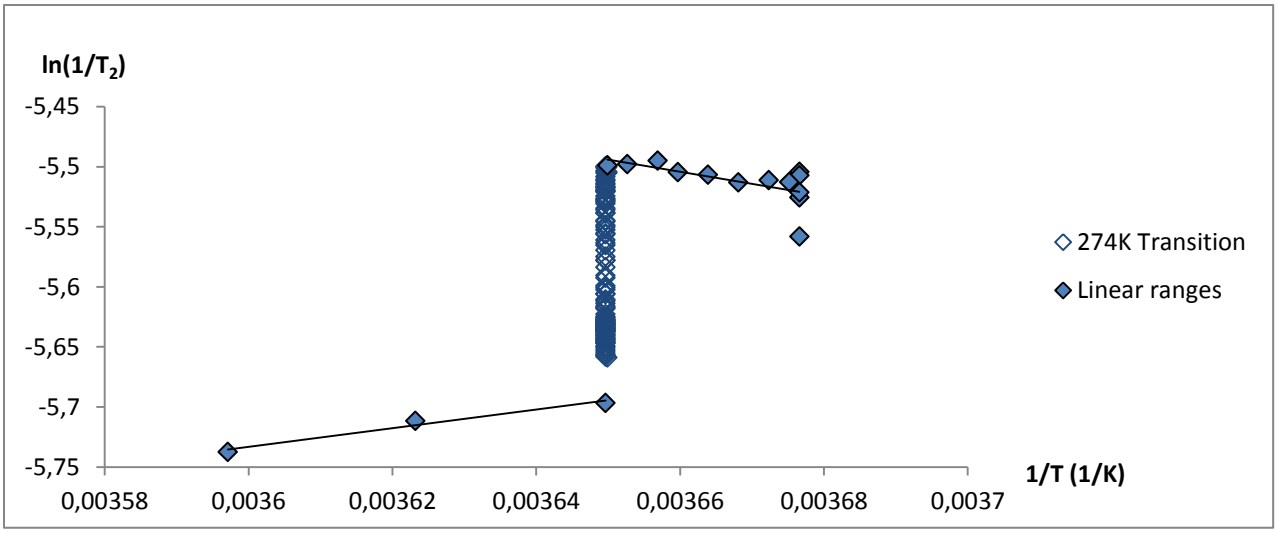

Figure E76: Close-up of the lower temperature range of c1 in the 2-component experiment from Fig. E86.

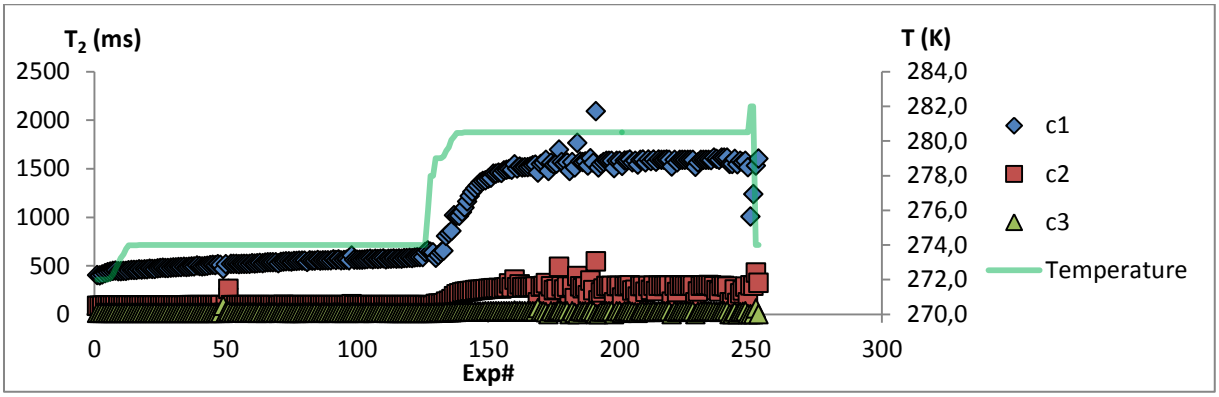

Figure E77: The results of three-component analysis of all CPMG oneshot experiments on B3Fa2, plotted as T_2 in ms as a function of experiment number. c1 is the results for component 1, c2 is the results for component 2, while c3 is the result for component 3. The green curve is the temperature in Kelvin, plotted on the secondary vertical axis.

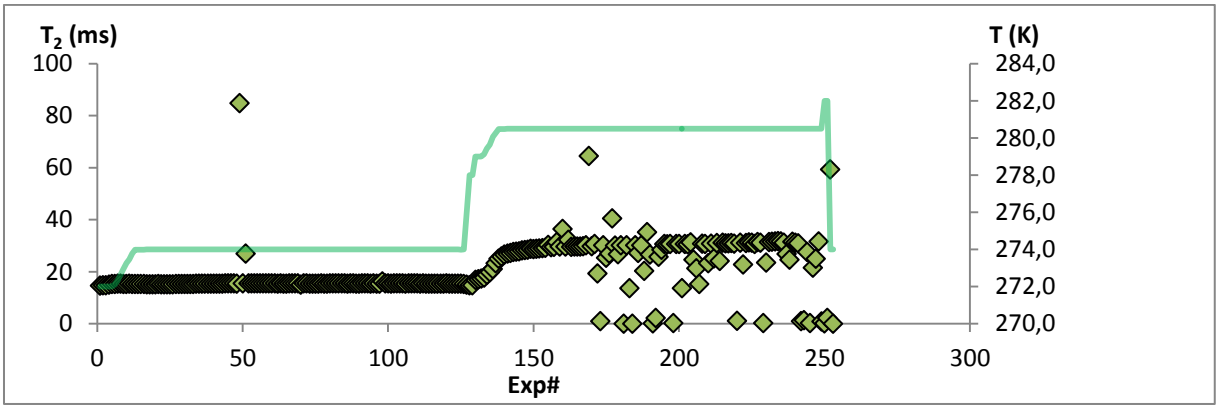

Figure E78: The plot of component 3 for the three-component analysis of all CPMG oneshot experiments on B3Fa2, plotted as T_2 in ms as a function of experiment number. The green curve is the temperature in Kelvin, plotted on the secondary vertical axis.

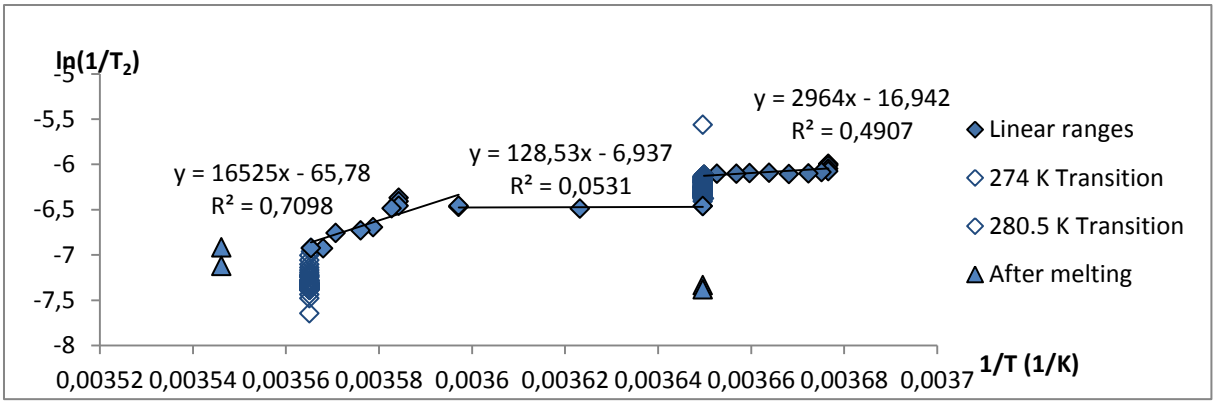

Figure E79: The results of component 1 from three-component analysis of all CPMG oneshot experiments on B3Fa2, plotted as $ln((T_2)^{-1})$ as a function of T^{-1}. Three linear ranges are identified and separately fitted to regression lines, the functions and R^2 values of whose are provided above their respective lines. The two ranges of rapid change are designated as transitions and marked with open diamonds. These results are not factored into regression. Experiments performed after the last transition is shown as "After melting", and is not included in regression.

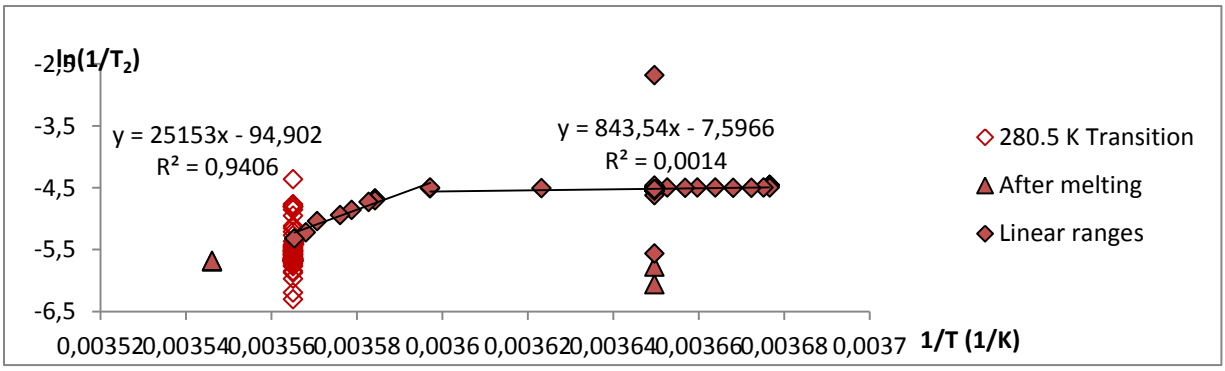

Figure E80: The results of component 2 from three-component analysis of all CPMG oneshot experiments on B3Fa2, plotted as plotted as $ln((T_2)^{-1})$ as a function of T^{-1}. Two linear ranges are identified and separately fitted to regression lines, the functions and R^2 values of whose are provided above their respective lines. Transition values are marked with open diamonds, and are not factored into the regression. Experiments performed after the last transition is shown as "After melting", but is not included in the regression.

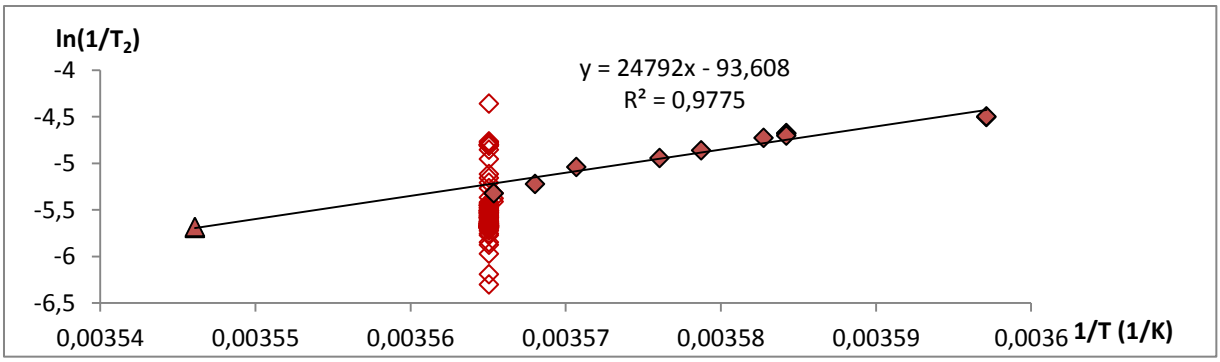

Figure E81: A close-up of the upper temperature linear range (diamonds). The two overlapping T_2 measurements at 282 K are presented as triangles and included in the linear regression analysis, the equation and R^2 value of which is presented above the line. The 280.5 K transition range is shown (open diamonds), but not factored into the regression.

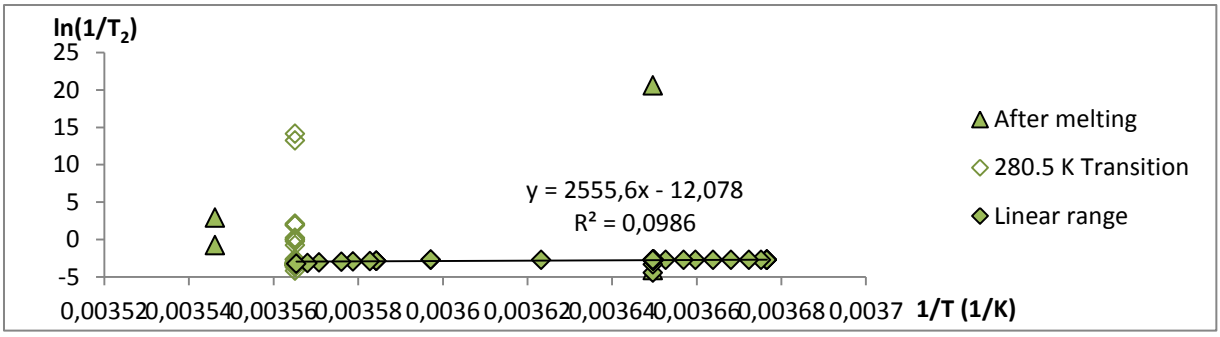

Figure E82: The results of component 3 from three-component analysis of all CPMG oneshot experiments on B3Fa2, plotted as $ln((T_2)^{-1})$ as a function of T^{-1}. The apparent presence of one continuous linear range can be seen, although the scale of the graph is not conductive to proper determination. Transition values are marked with open diamonds, and are not factored into the regression. Experiments performed after the last transition is shown as "After melting", and is not included in the regression.

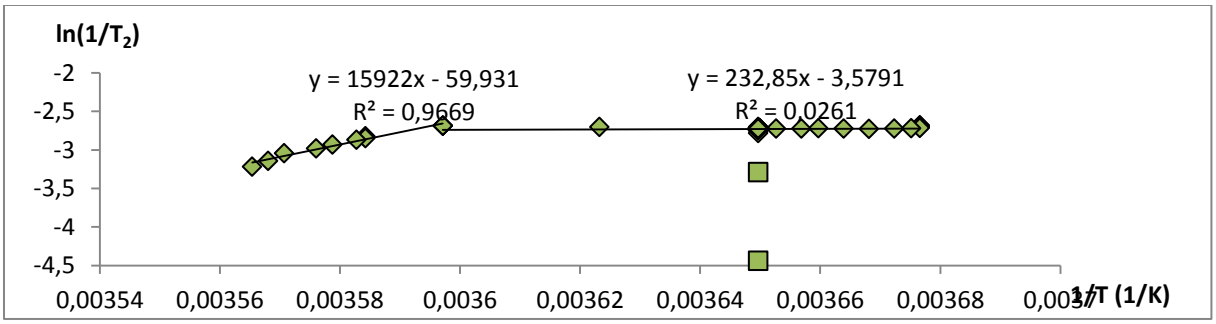

Figure E83: The "linear range" of c3 values from Fig. E82 is plotted, which show the presence of two different linear ranges. Both of these are subjected to linear regression analysis, the results of which are displayed over the respective lines. The two anomalous measurements (squares) at 274 K are excluded from the analysis.

B3Fa6

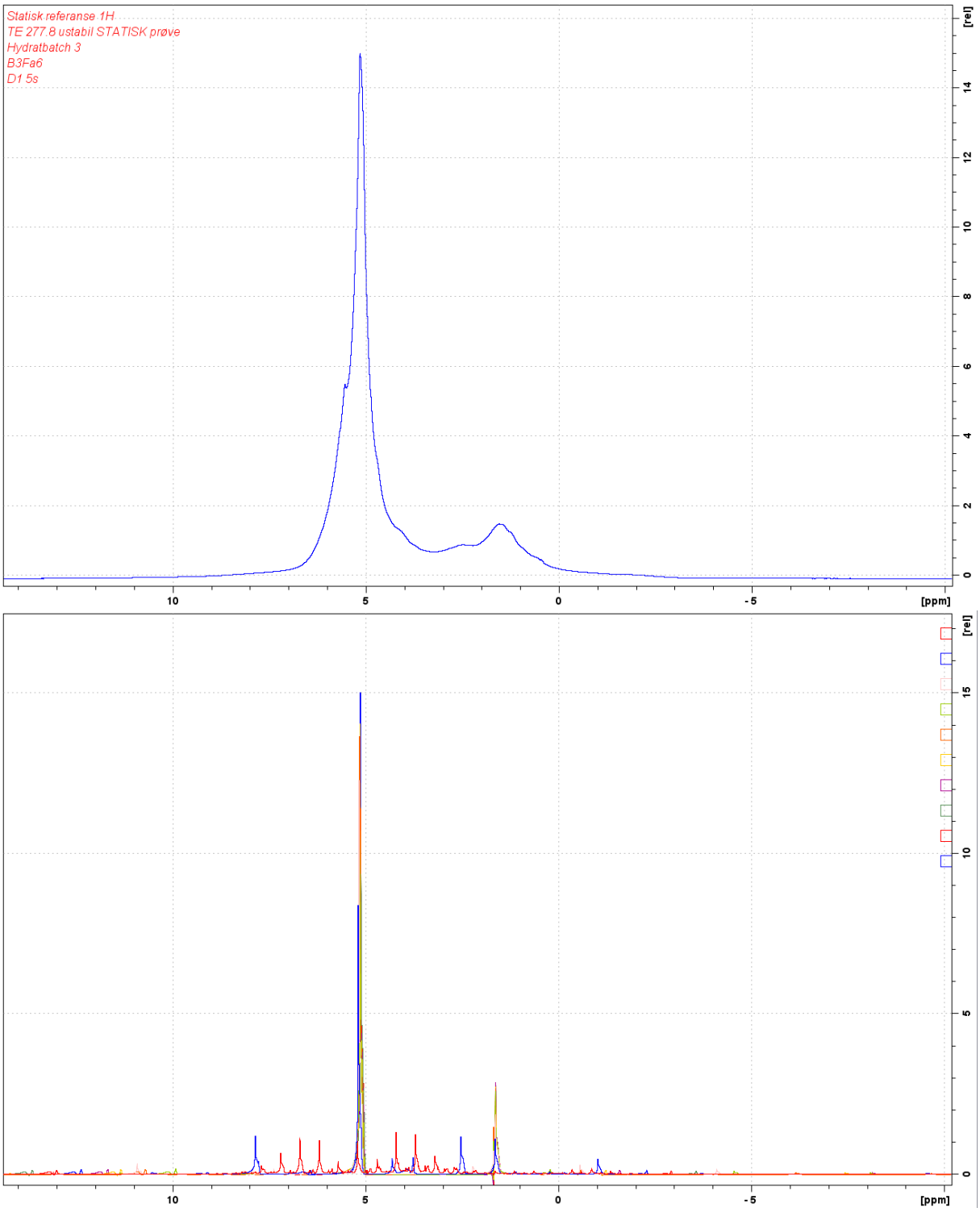

Figure E84: ^{1}H MAS experiments performed at 271.5 K for sample B3Fa6 (bottom). The spinning sidebands can be seen to move as a function of spin rate, whilst the two biggest peaks remain constant for all samples. An up-scaled non-spinning spectrum acquired at the same temperature is shown as a reference (top).

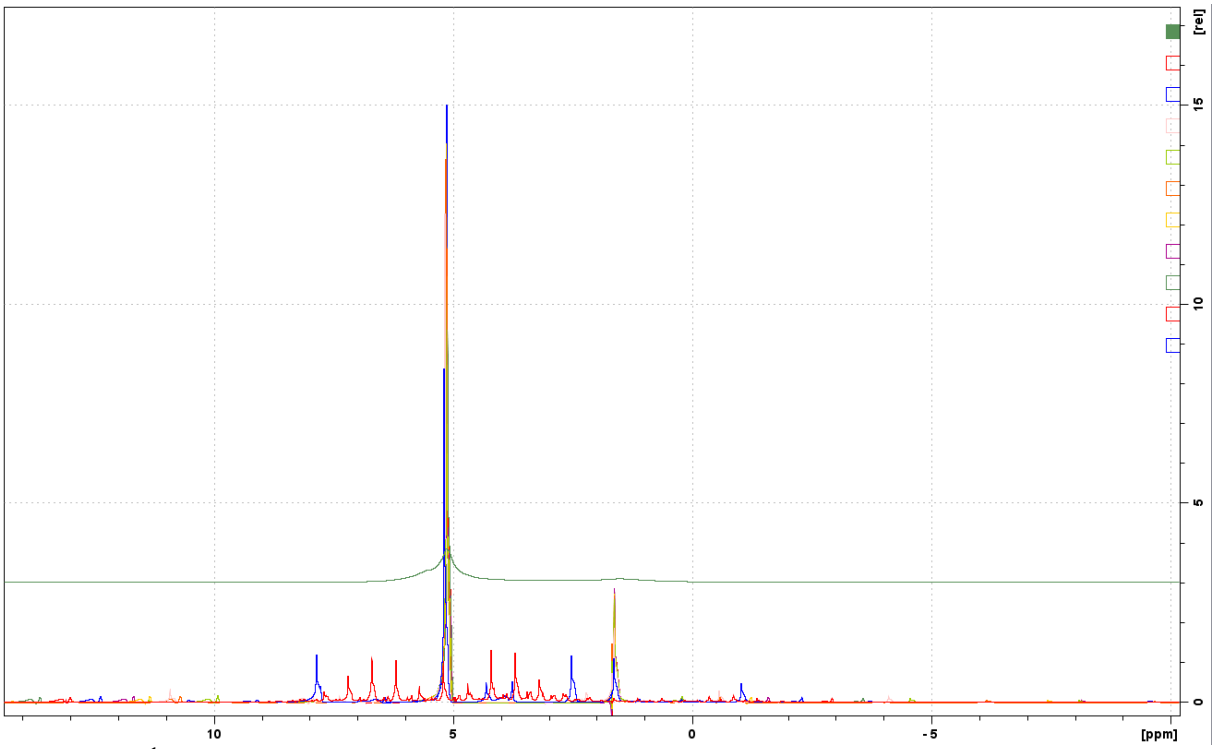

Figure E85: ^{1}H MAS experiments performed at 271.5 K for sample B3Fa6. A non-spinning spectrum (green) is shown as a reference. The spinning sidebands can be seen to move as a function of spin rate, whilst two peaks remain constant for all samples.

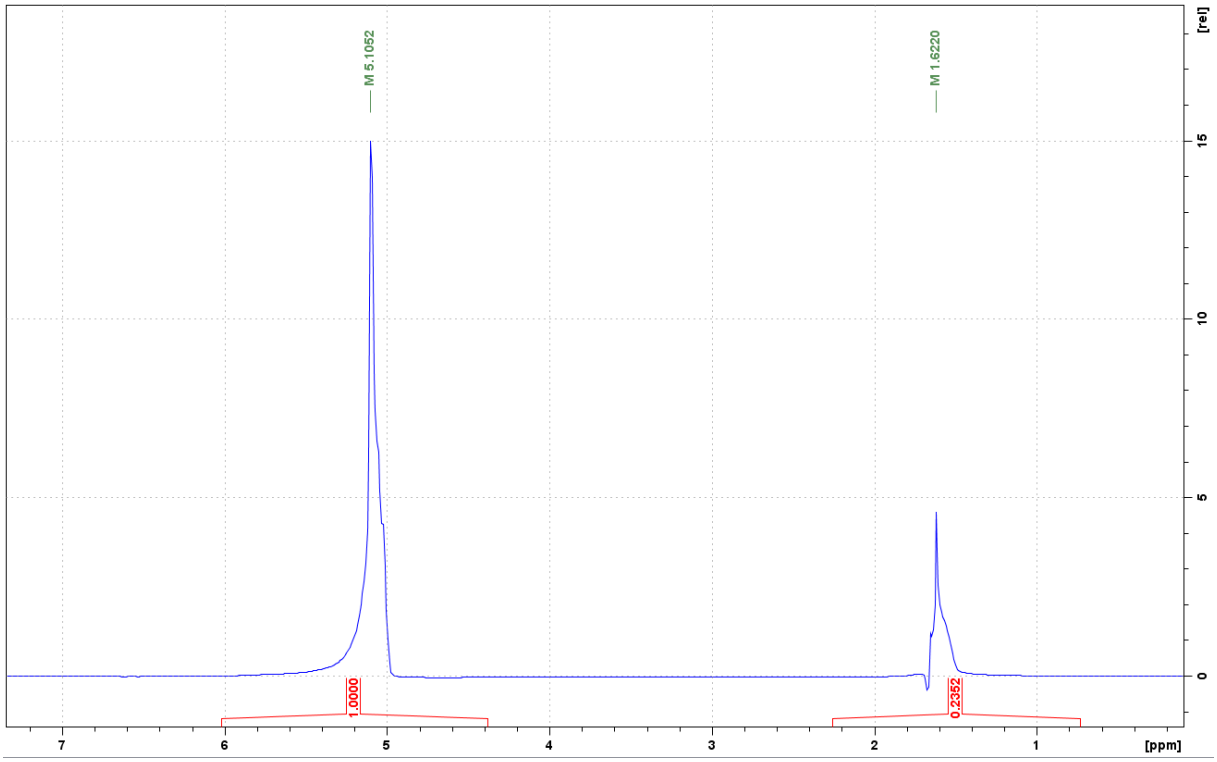

Figure E86: Peak chemical shifts and intensities found by MAS NMR at 271.5 K for sample B3Fa6.

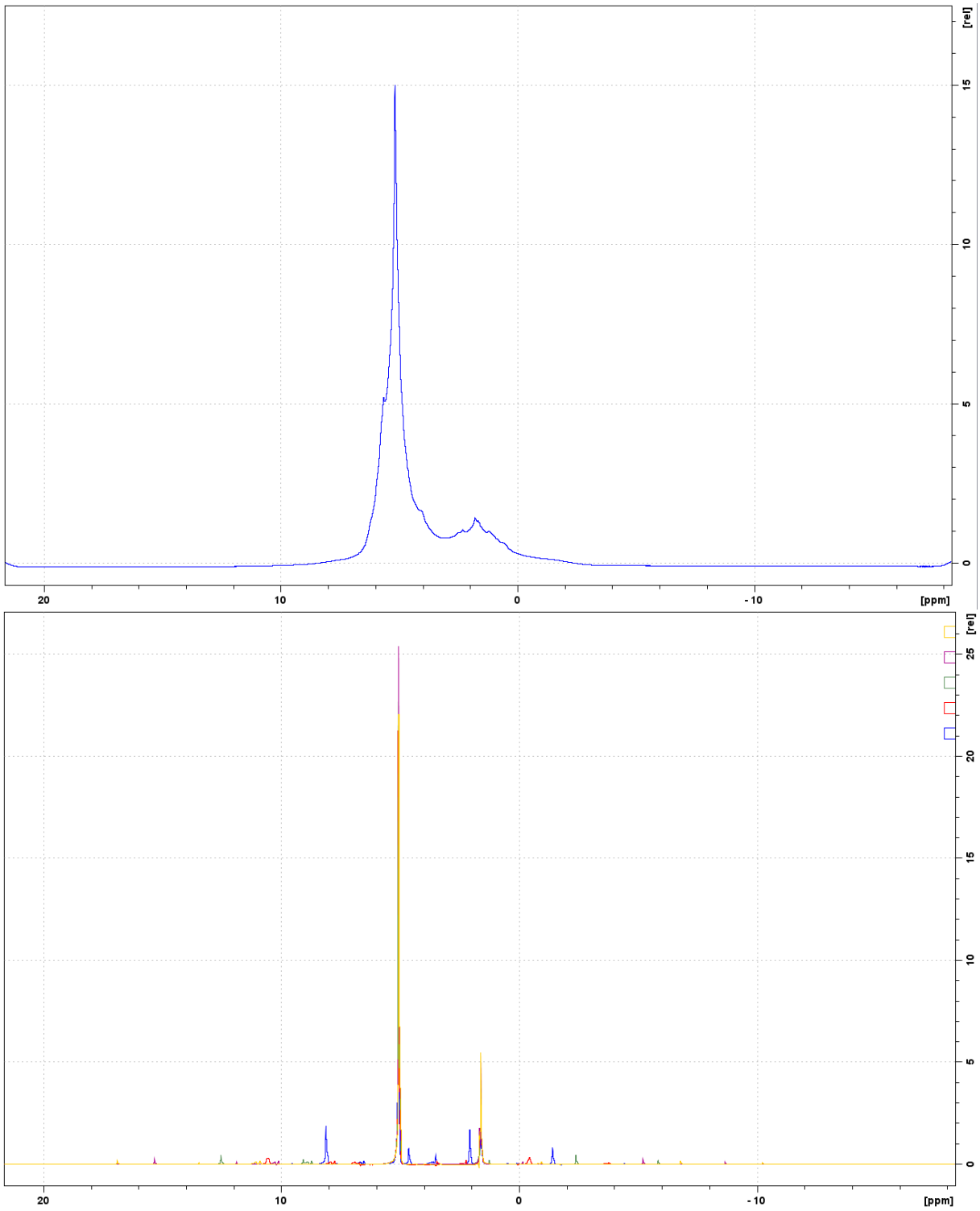

Figure E87: ^{1}H MAS experiments performed at 278 K for sample B3Fa6 (bottom). The spinning sidebands can be seen to move as a function of spin rate, whilst the two biggest peaks remain constant for all samples. An up-scaled non-spinning spectrum acquired at the same temperature is shown as a reference (top).

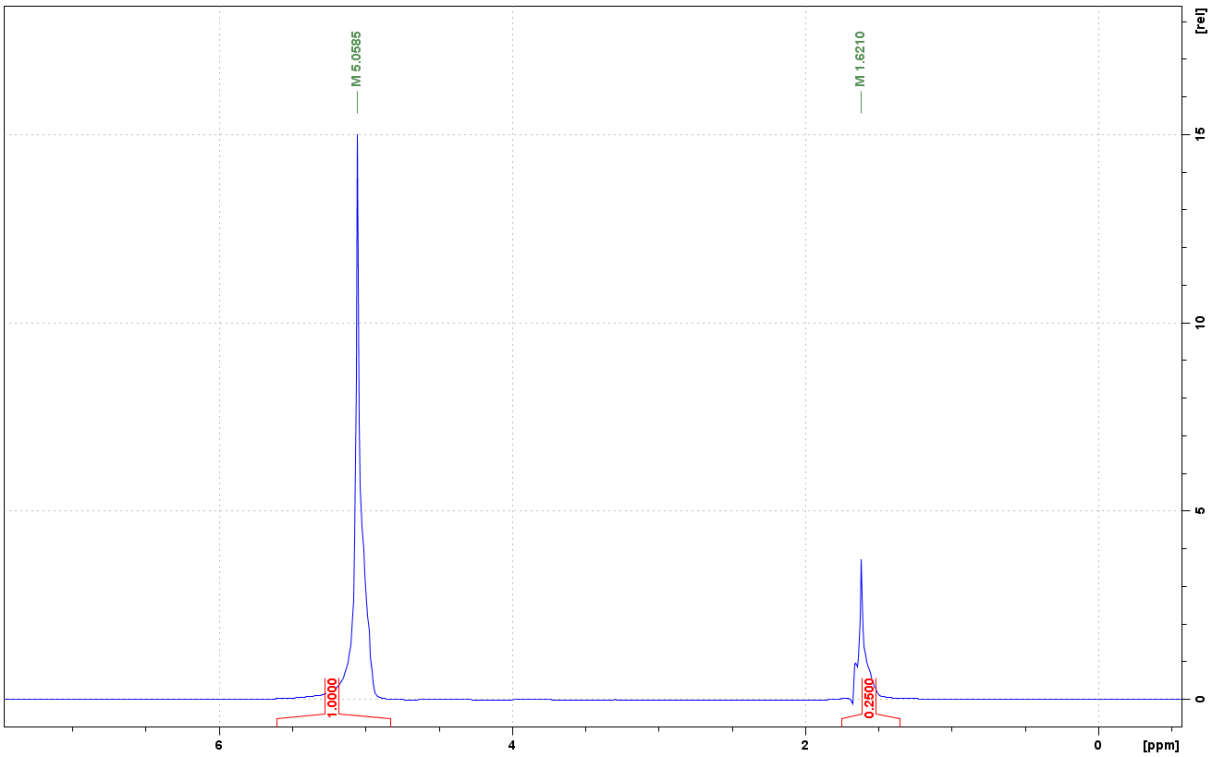

Figure E88: Peak chemical shifts and intensities found by MAS NMR at 278 K for sample B3Fa6.

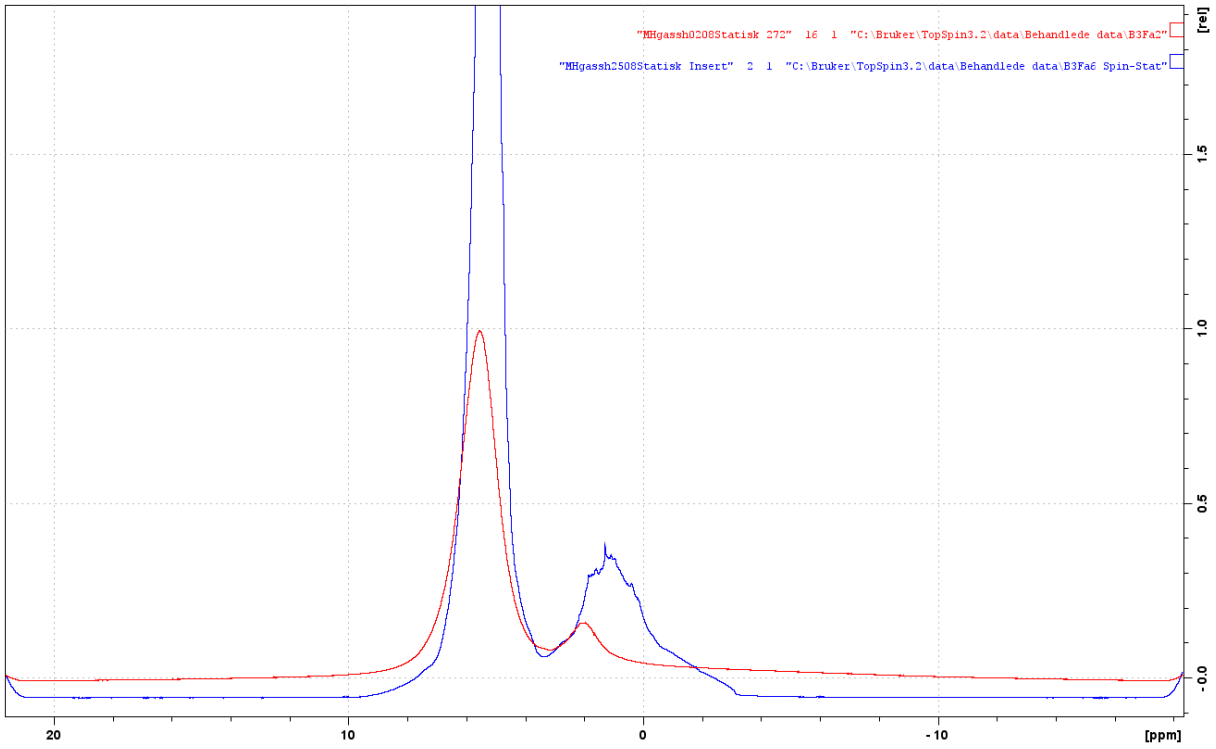

Figure E89: The ^{1}H spectrum of sample B3Fa6 acquired after insertion at 270 K (blue) compared with the last spectrum obtained for sample B3Fa2 at 272 K (red). Note that these spectra was acquired using the same acquisition parameters and receiver gain. The sample hydrate contents are 0.0727 and 0.0705 g, respectively. Also noteworthy is the baseline differences; evidence that the broad peak of interest has deteriorated or was never present for this sample.

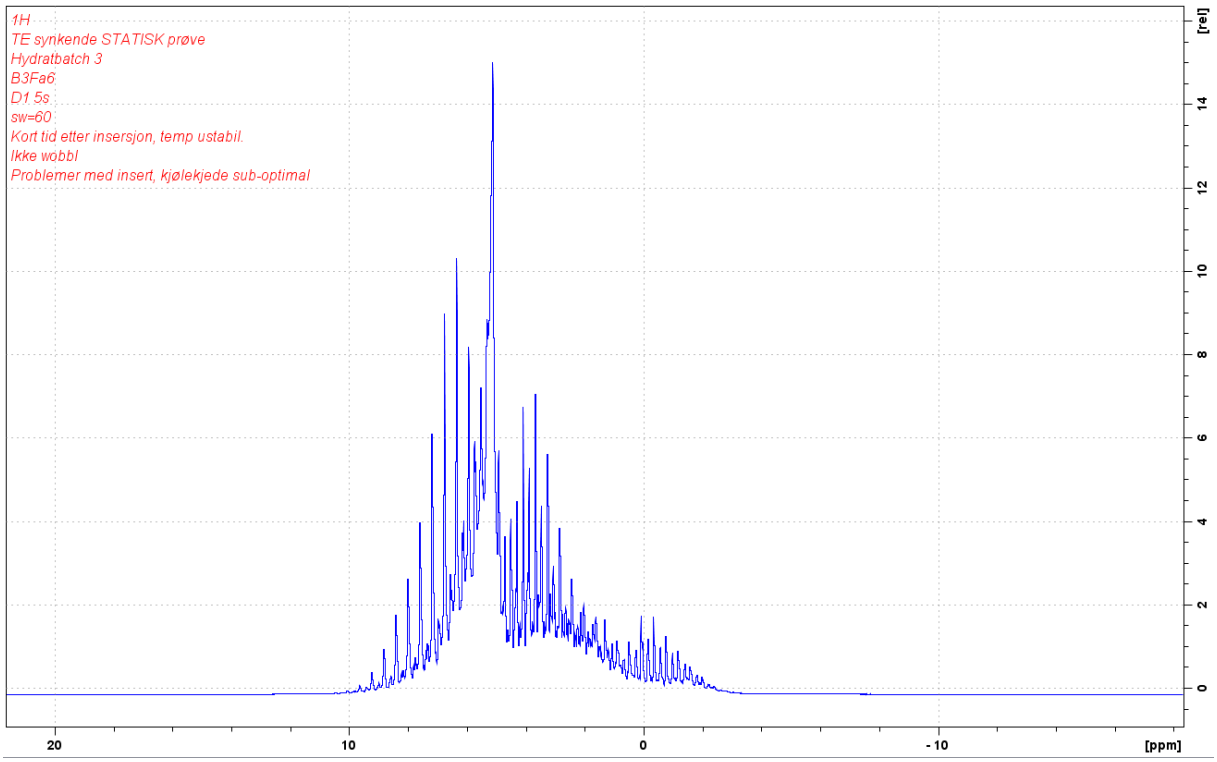

Figure E90: The first attempt at acquiring a non-spinning spectrum for sample B3Fa6.

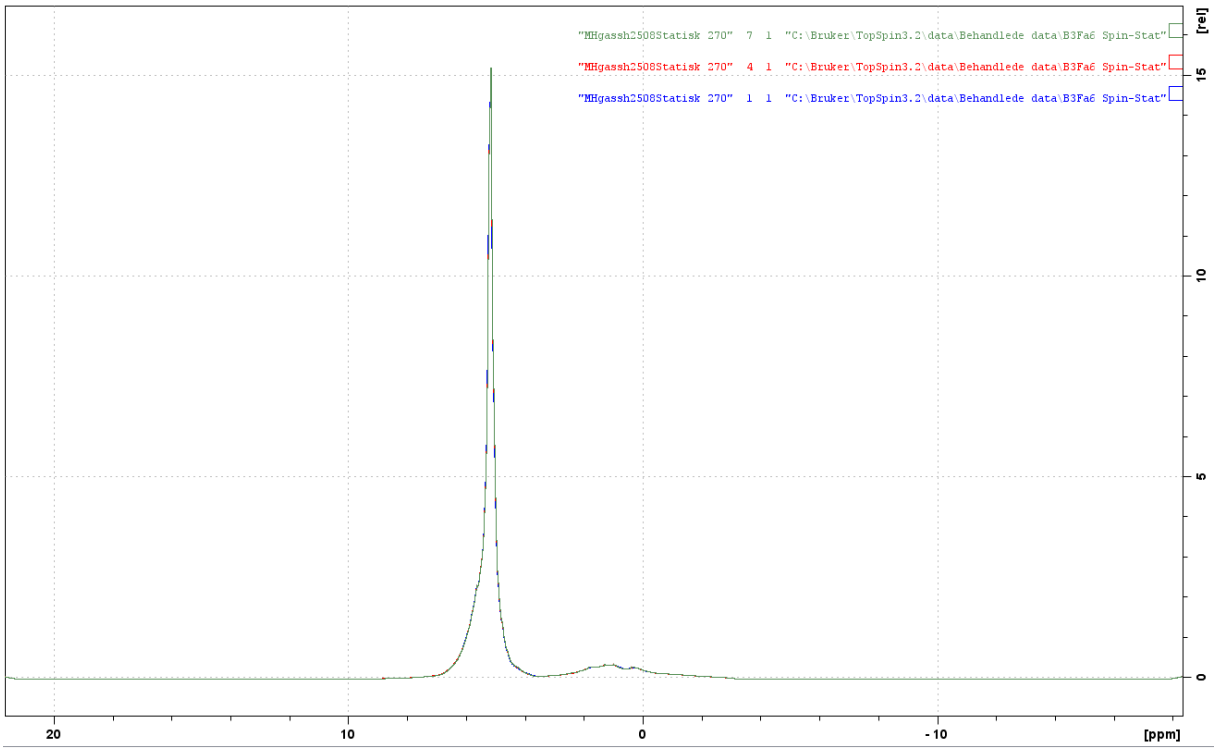

Figure E91: Three spectra acquired at 270 K for the B3Fa6 sample before MAS experiments, spanning a time of approximately 45 minutes.

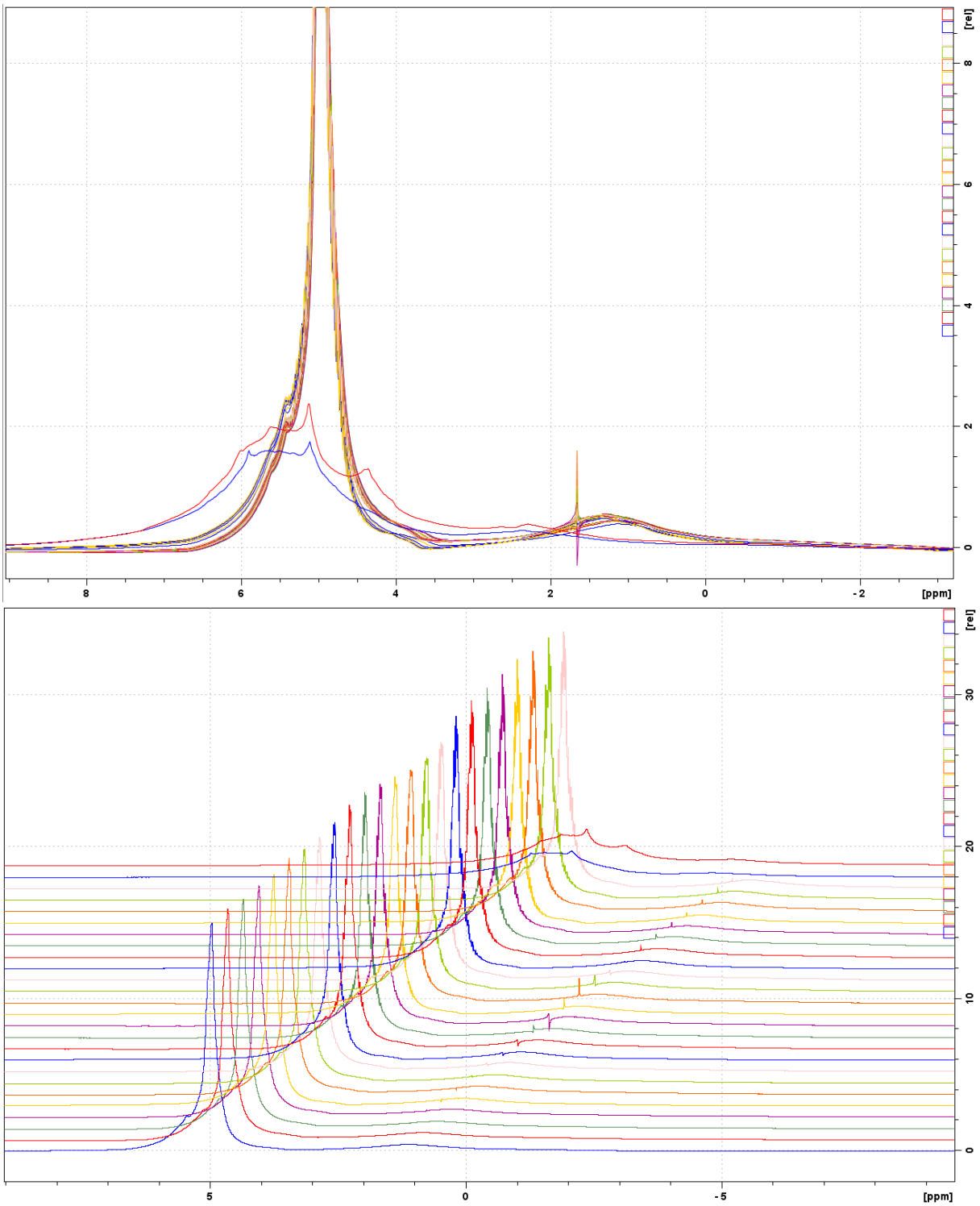

Figure E92: Top: Stacked plot. Bottom: Horizontal and vertical offset. Every tenth spectrum in the ramp series of B3Fa6, starting at experiment 1, plotted. The last experiment in the series is also provided (rearmost blue), as it constitutes the results of a rapid change, occurring within 5 minutes. The final spectrum shown (rearmost red) was acquired four hours after the end of the ramp series. The fuzzy appearance of some spectra is due to the sample spinning at a rate of approximately 10 Hz, even though the spectrometer operated in non-spinning mode.

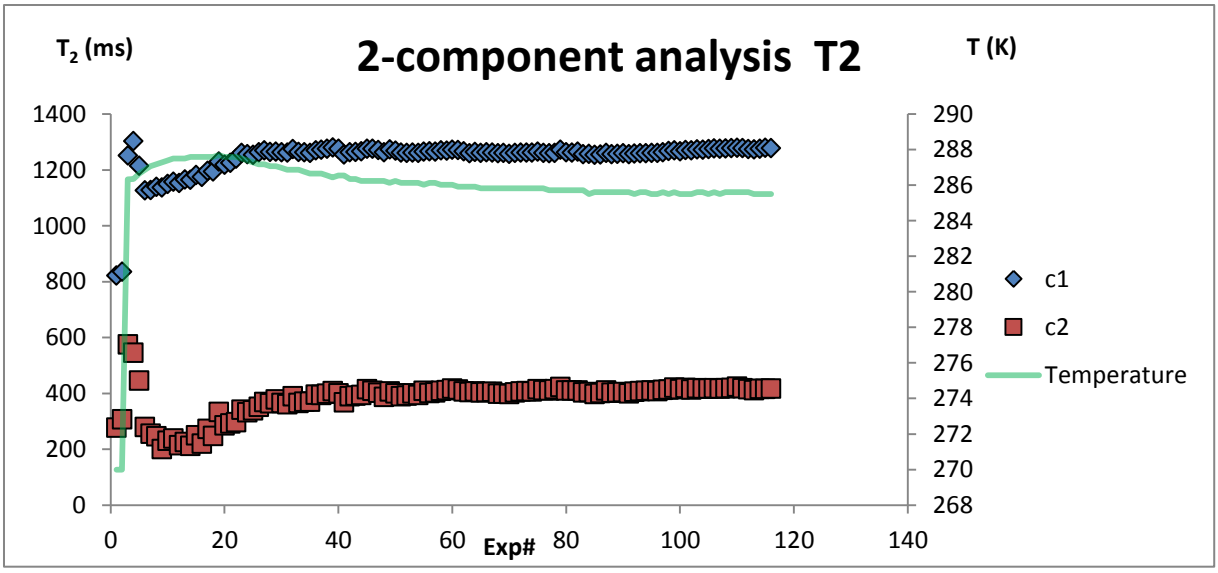

Figure E93: The T_2 values of sample B3Fa6 was found to already be high during initial acquisition.

B3Fb2

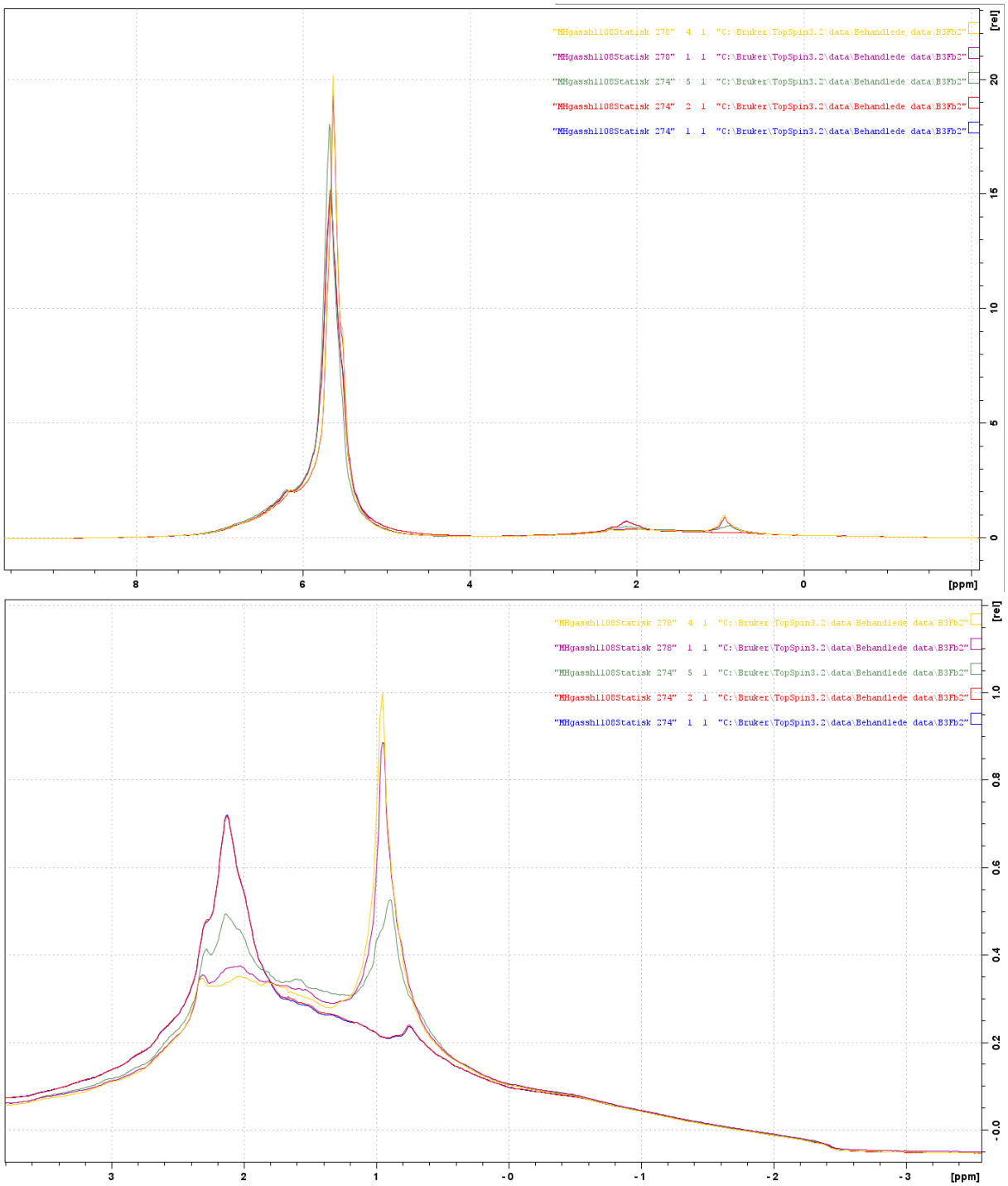

Figure E94: Sample B3Fb2. Top: Both peaks. Bottom: Cyclopentane peaks. During the five first spectra, no signs of stabilisation could be seen. Instead, a new downfield cyclopentane peak was seen to emerge while the upfield one dwindled.

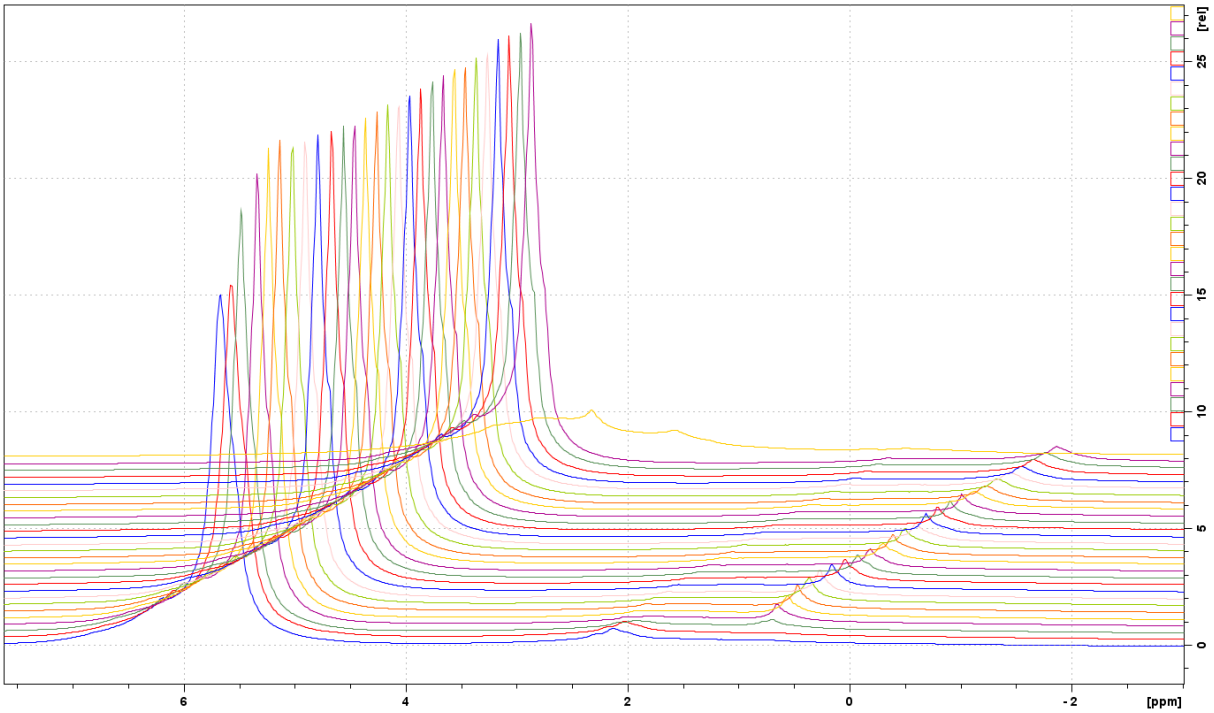

Figure E95: The first 5 spectra of sample B3Fb2 is plotted, along with every 10th spectra of the ramping series and the final spectrum. Top: Both peaks. Bottom: Cyclopentane peaks.

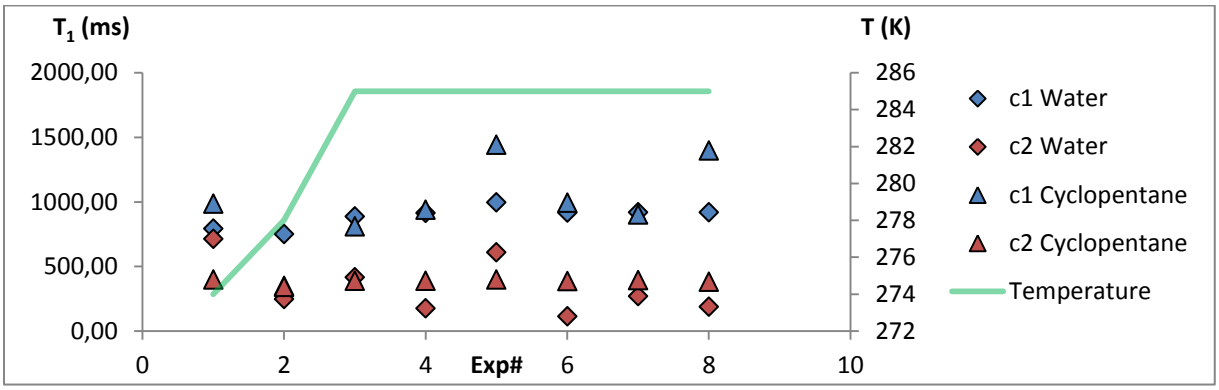

Figure E96: T_1 data from the two component analysis of sample B3Fb2. Both peaks seem to assign the same values to the two components, but with a large difference in spread.

Table E6: The utilised guessrange for the T_2 analysis. The Exp.range denotes which experiments were subjected to which guesses.

Exp.range	1comp	2comp1	2comp2	3comp1	3comp2	3comp3
1-20	400	400	80	600	150	50
21-All	500	500	100	1200	250	30

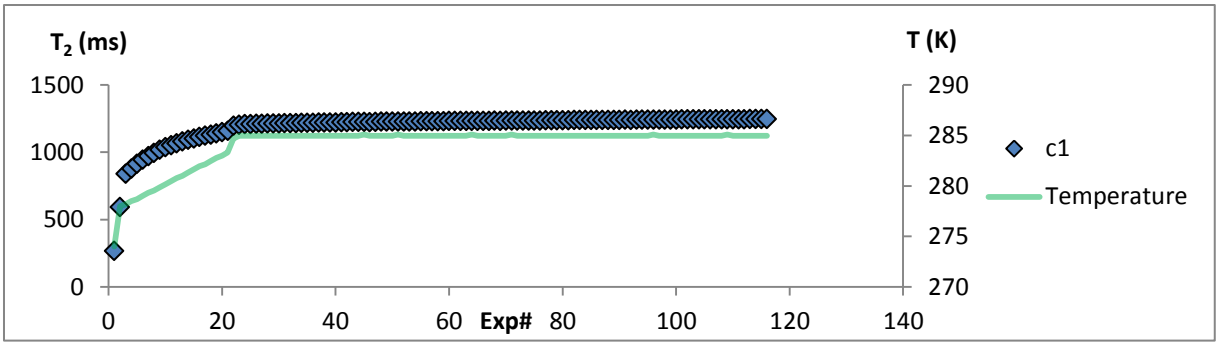

Figure E97: One-component T_2 analysis of all experiments on sample B3Fb2.

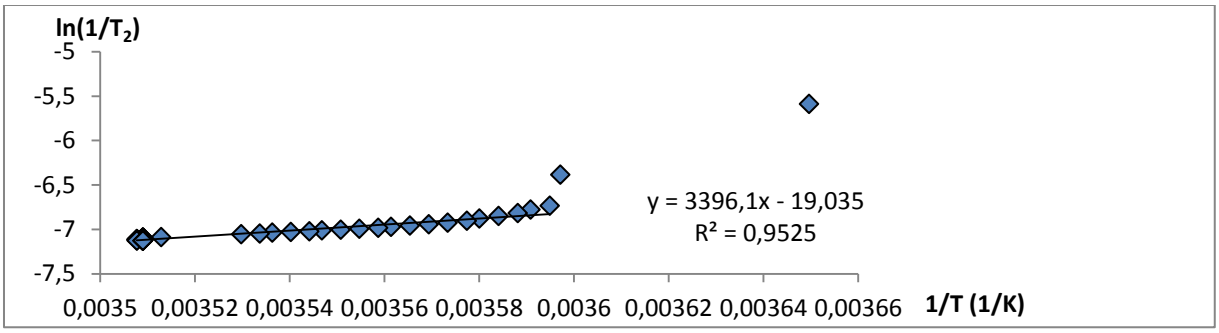

Figure E98: One-component logarithmic inverse T_2 versus inverse temperature in Kelvin for all experiments on sample B3Fb2. Linear regression is performed where applicable. Two or three different slopes might be present.

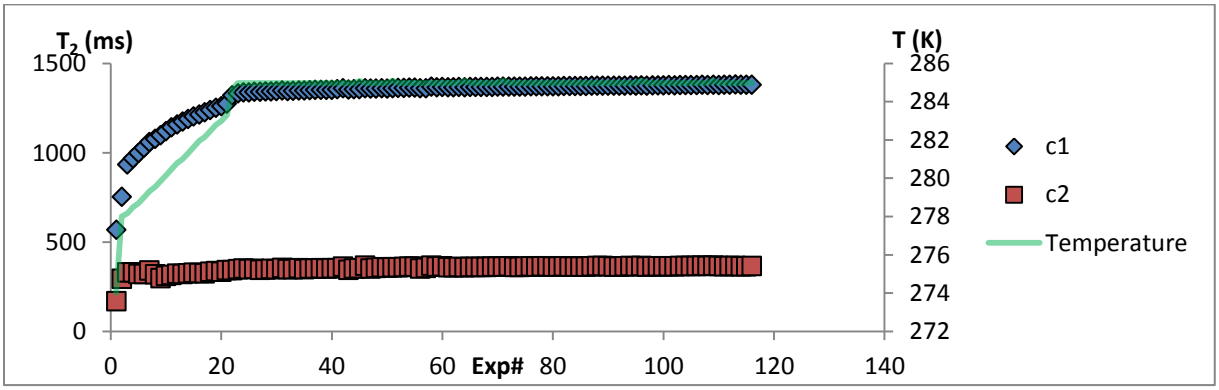

Figure E99: Two-component T_2 analysis of all experiments on sample B3Fb2.

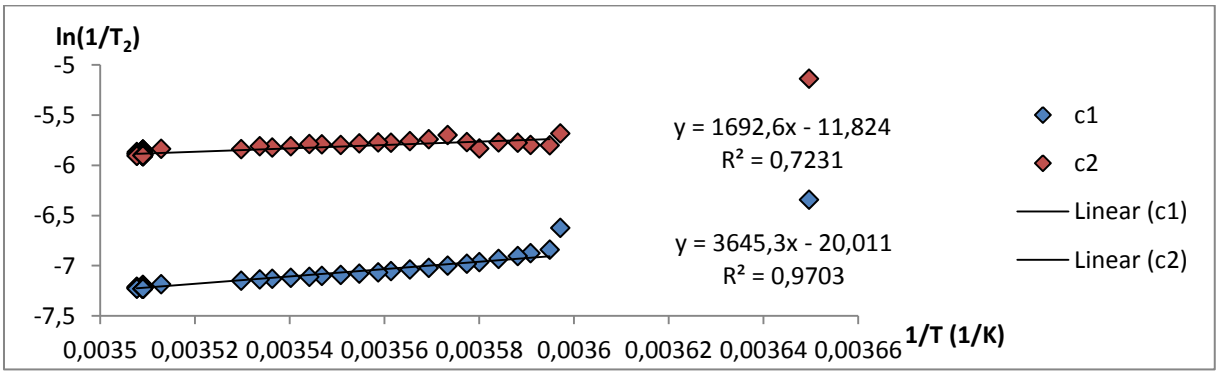

Figure E100: Two-component logarithmic inverse T_2 versus inverse temperature in Kelvin for all experiments on sample B3Fb2. Linear regression is performed where applicable. Two or three different slopes might be present.

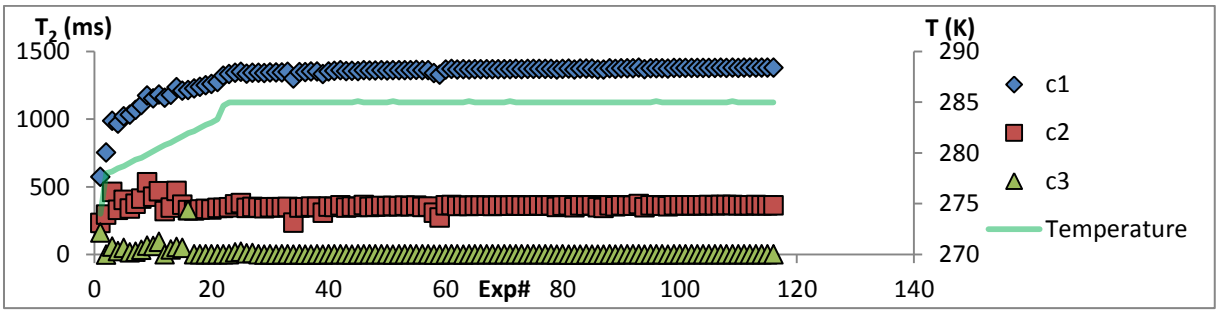

Figure E101: Three-component T_2 analysis of all experiments on sample B3Fb2.

B3Fb3

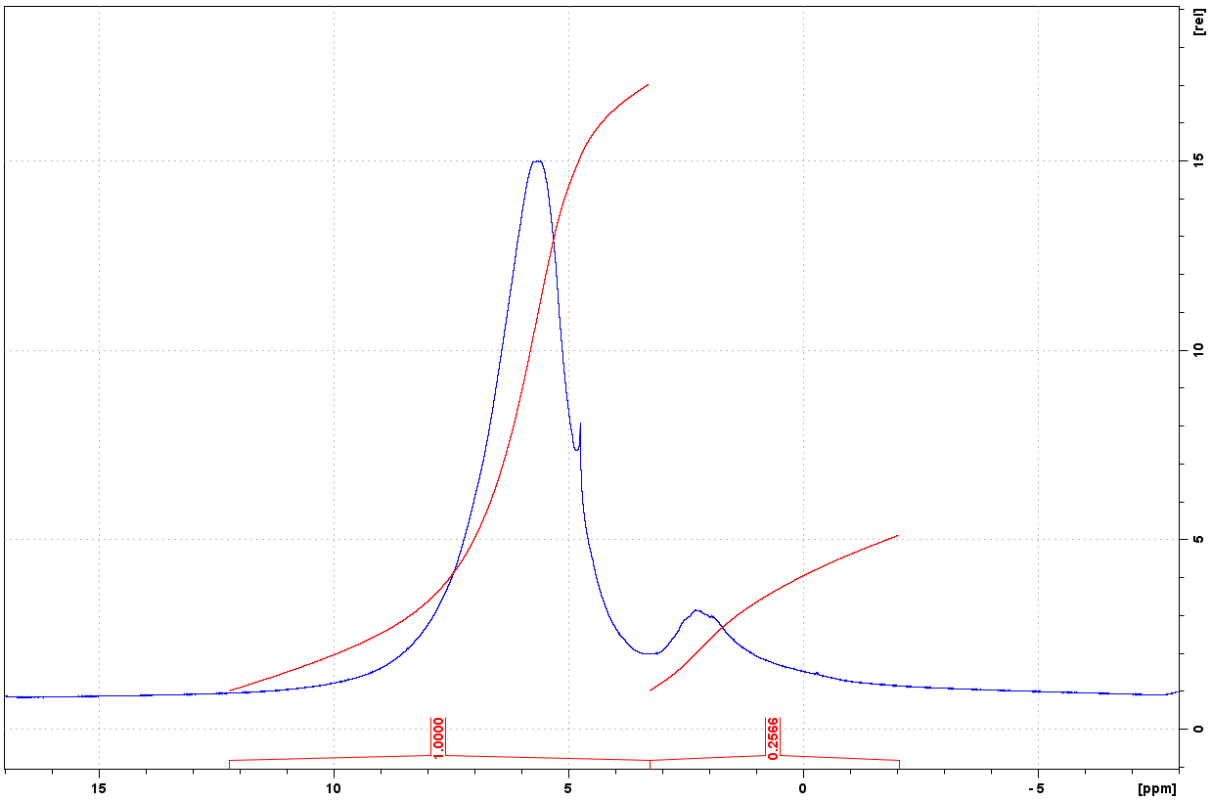

Figure E102: Integrated spectrum ofthe last spectrum acquired on sample B3Fb3.

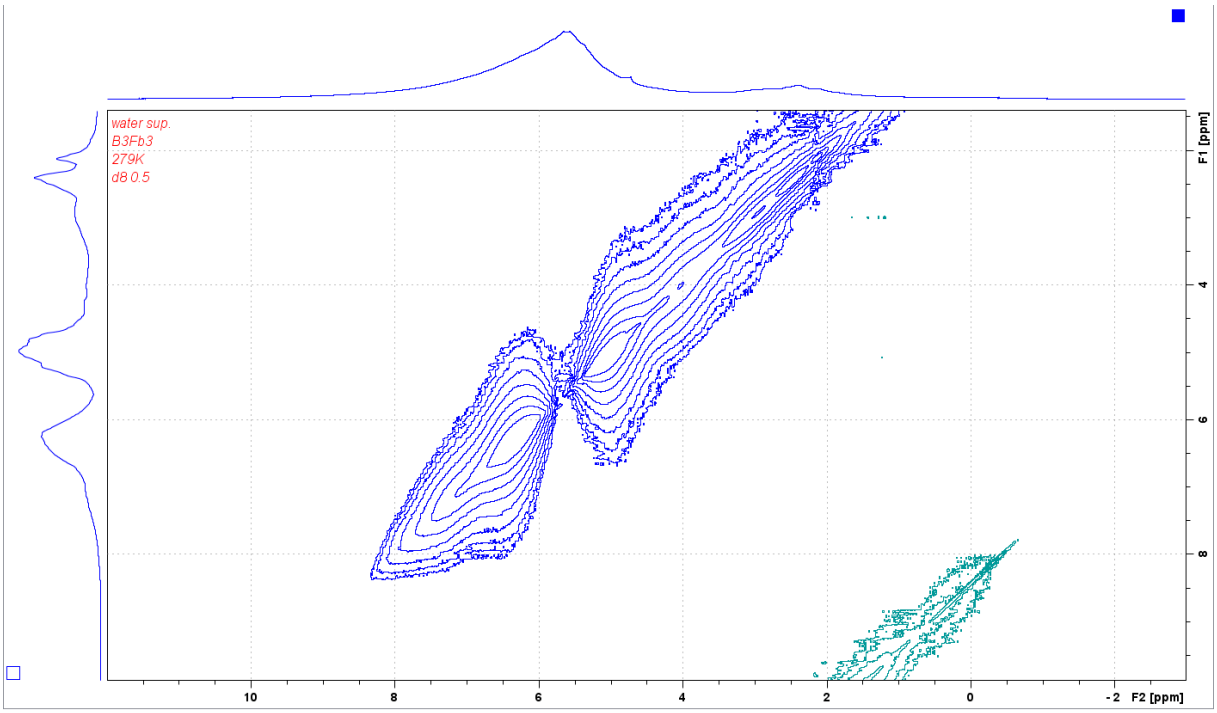

Figure E103: The 2D spectrum of the NOESY experiment utilising water suppression for the B3Fb3 sample. The function merely cleaves the broad water peak, as evident in the spectrum on the F1 axis.

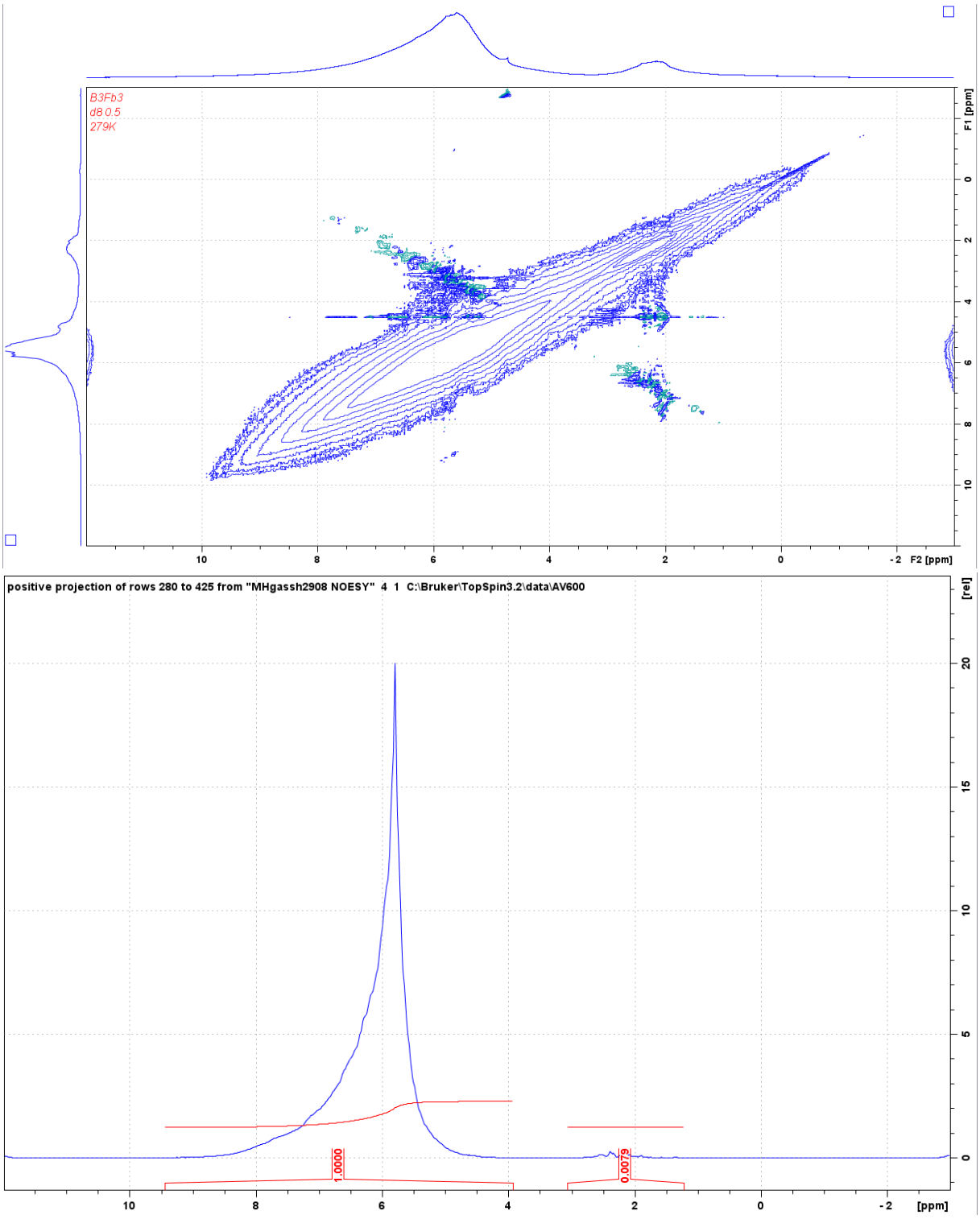

Figure E104: The 2D spectrum of the first regular NOESY experiment (top) on the B3Fb3 sample, using a mixing time of 0.5 s. A projection of the cross peak area is also provided (bottom).

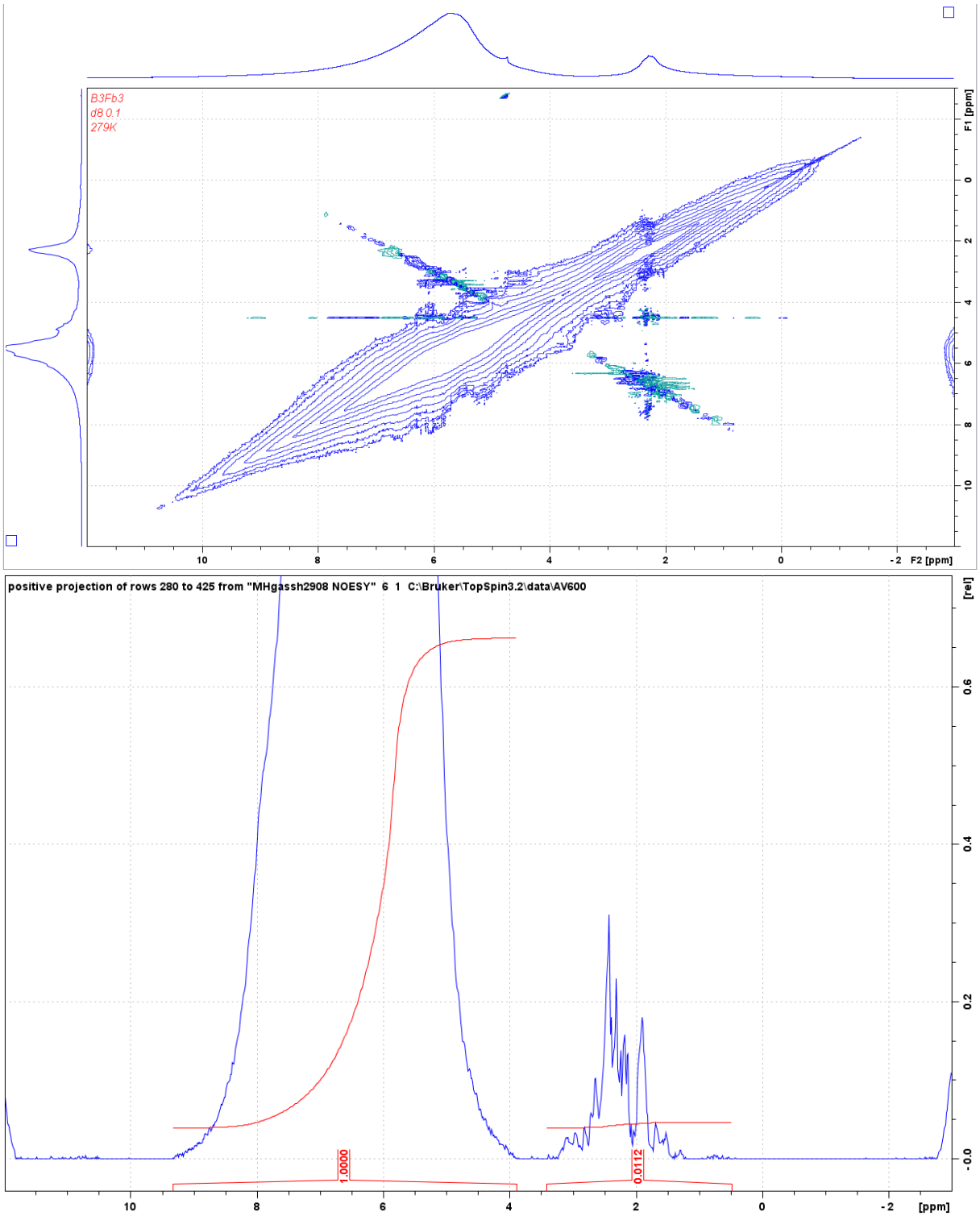

Figure E105: The 2D spectrum of the second NOESY experiment (top) on the B3Fb3 sample, using a mixing time of 0.3 s. A projection of the cross peak area is also provided (bottom).

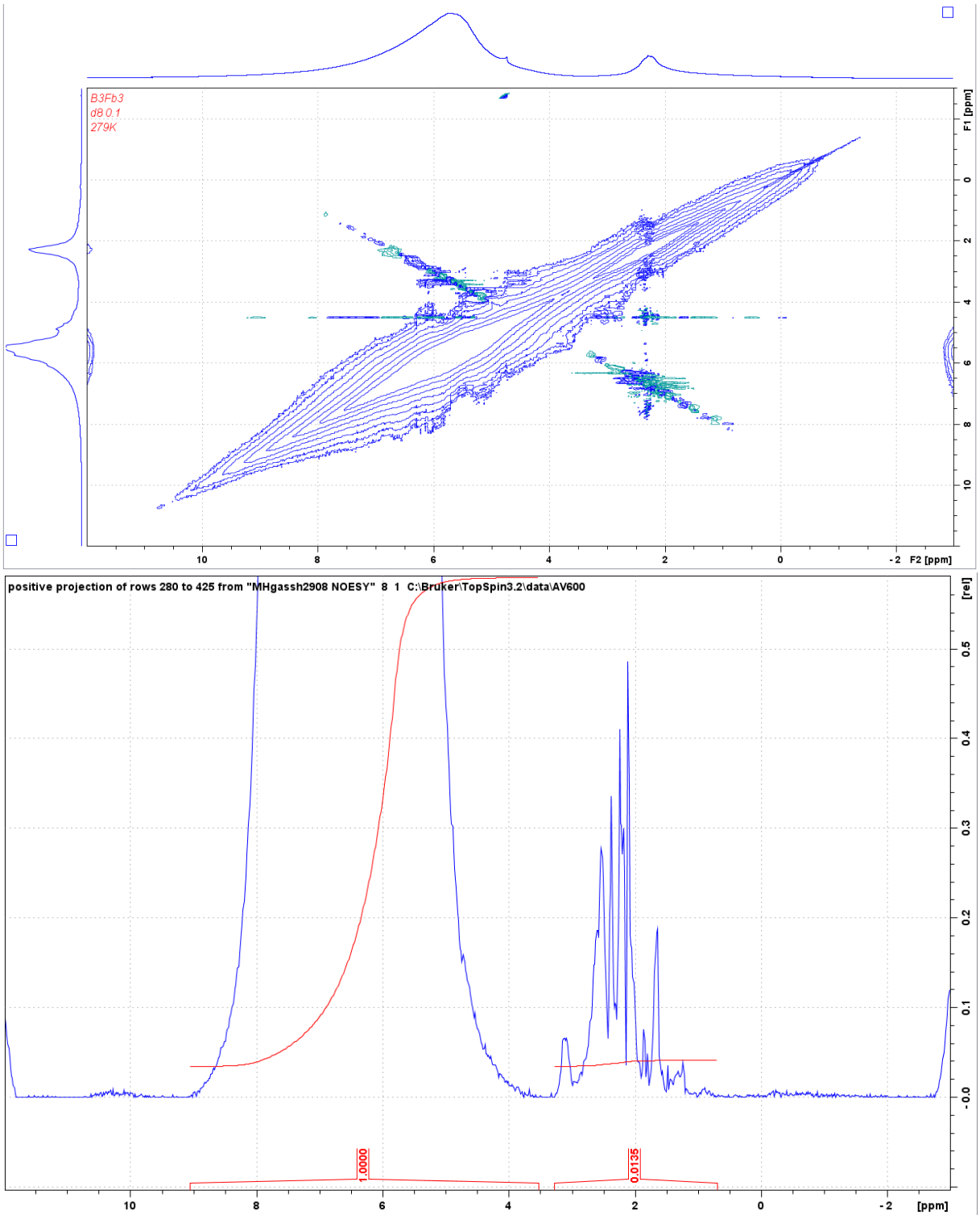

Figure E106: The 2D spectrum of the third NOESY experiment (top) on the B3Fb3 sample, using a mixing time of 0.1 s. A projection of the cross peak area is also provided (bottom).

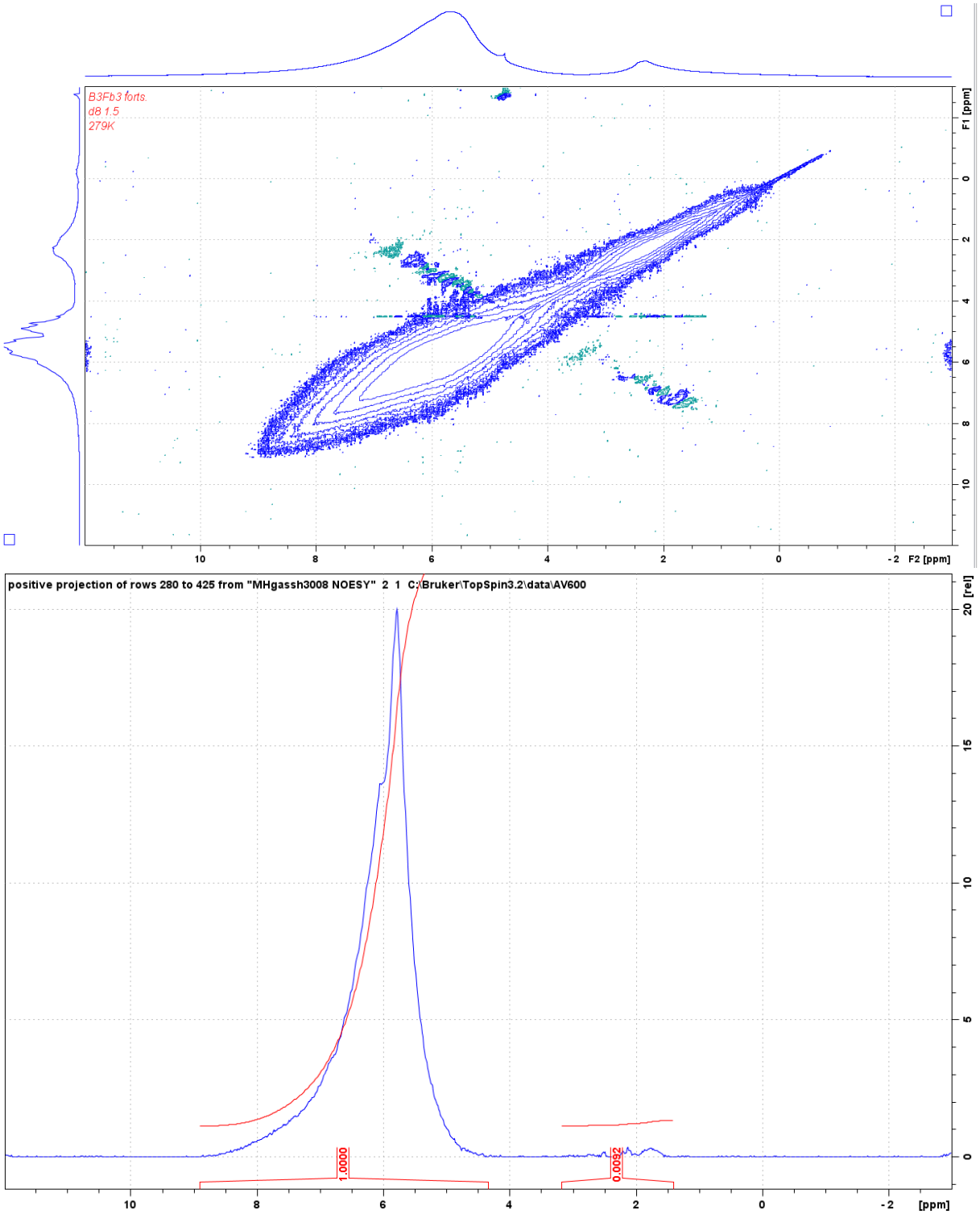

Figure E107: The 2D spectrum of the fourth NOESY experiment (top) on the B3Fb3 sample, using a mixing time of 1.5 s. A projection of the cross peak area is also provided (bottom).

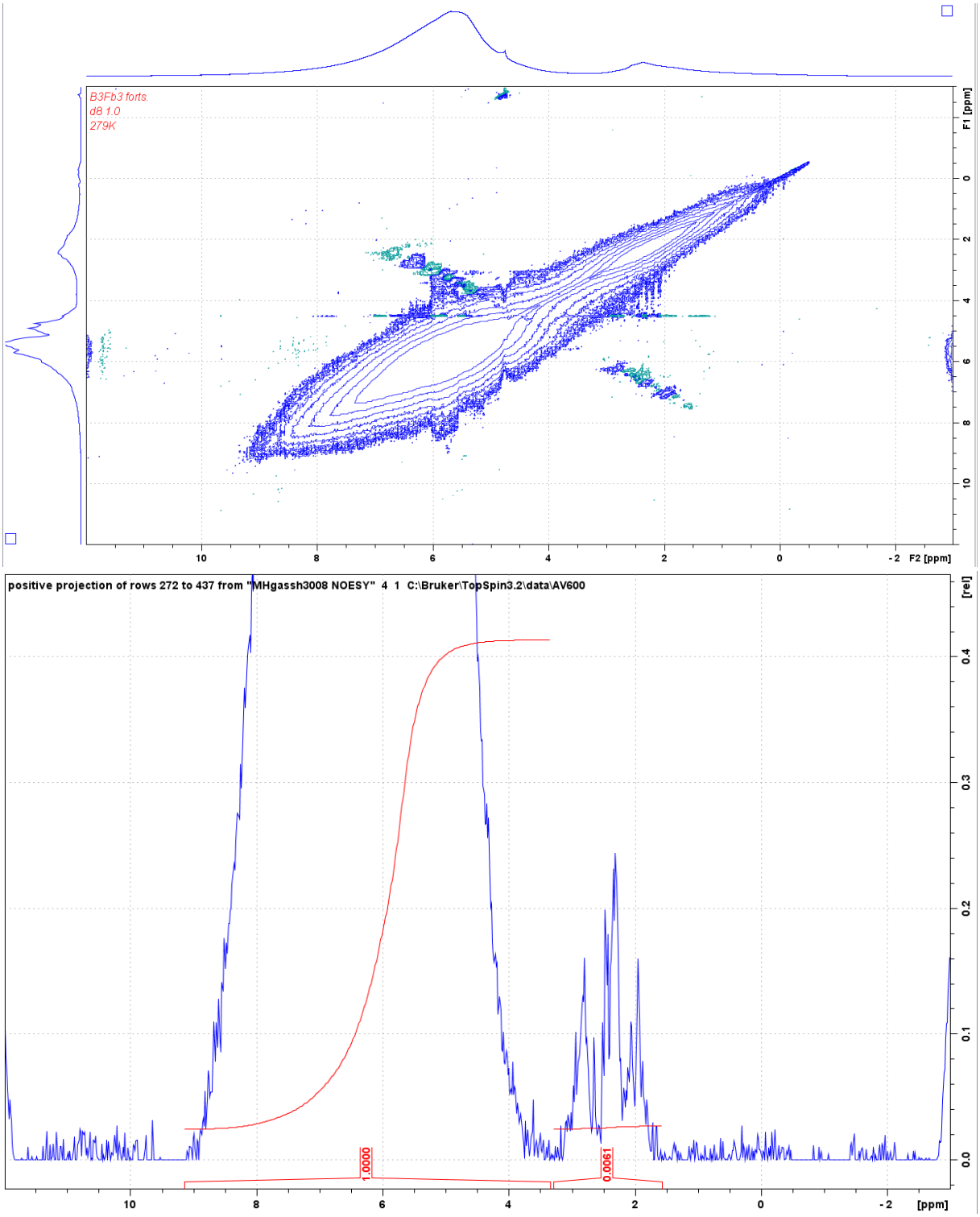

Figure E108: The 2D spectrum of the fifth NOESY experiment (top) on the B3Fb3 sample, using a mixing time of 1.0 s. A projection of the cross peak area is also provided (bottom).

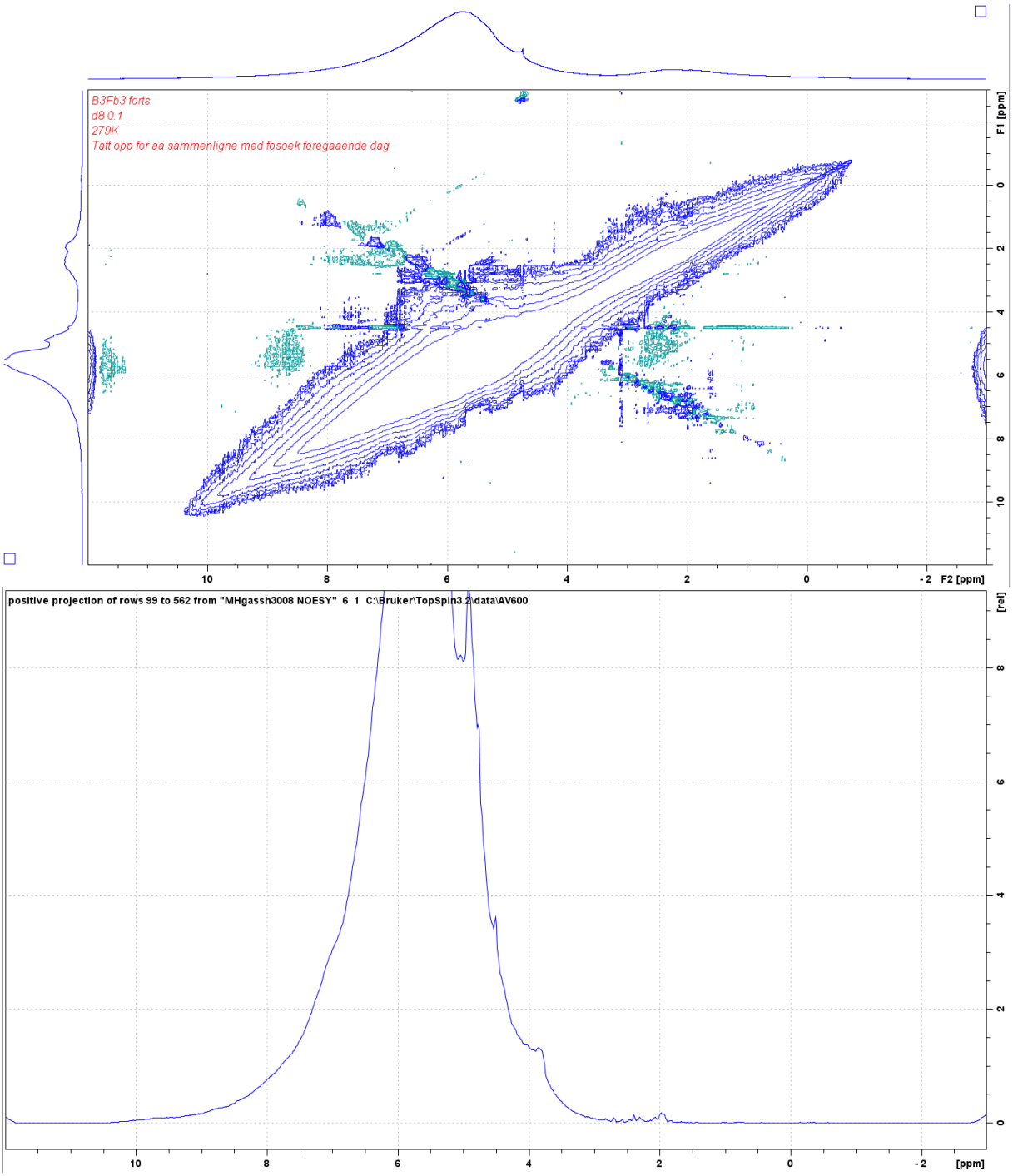

Figure E109: The 2D spectrum of the sixth NOESY experiment (top) on the B3Fb3 sample, using a mixing time of 0.1 s. A projection of the cross peak area is also provided (bottom).

References

1. Sloan, E.D. and C.A. Koh, *Clathrate hydrates of natural gases*. 3rd ed. Chemical industries, ed. J.G. Speight. 2008, Boca Raton: Taylor & Francis Group.
2. Friebolin, H., *Basic one- and two-dimensional NMR spectroscopy*. 5th ed. 2013, Weinheim: Wiley-VCH Verlag GmbH & Co. KGaA.
3. Carrol, J., *Natural gas hydrates: A guide for engineers*. 2nd ed. 2009, Oxford: Elsevier.

4. Engineering, H.W.i.o.p. *What are gas hydrates?* 2015 [cited 2015 28/09]; Available from: http://www.pet.hw.ac.uk/research/hydrate/images/hydrates/structures_large.jpg.
5. Hester, K.C. and P.G. Brewer, *Clathrate Hydrates in Nature.* Annual Review of Marine Science, 2009. **1**: p. 303-327.
6. Sum, A.K., C.A. Koh, and E.D. Sloan, *Clathrate Hydrates: From Laboratory Science to Engineering Practice.* Industrial & Engineering Chemistry Research, 2009. **48**(16): p. 7457-7465.
7. Alavi, S., R. Susilo, and J.A. Ripmeester, *Linking microscopic guest properties to macroscopic observables in clathrate hydrates: Guest-host hydrogen bonding.* The Journal of Chemical Physics, 2009. **130**(17): p. 174501.
8. Christiansen, R.L. and E.D. Sloan, *Mechanisms and Kinetics of Hydrate Formation.* Annals of the New York Academy of Sciences, 1994. **715**(1): p. 283-305.
9. Hammerschmidt, E.G., *Formation of Gas Hydrates in Natural Gas Transmission Lines.* Industrial & Engineering Chemistry, 1934. **26**(8): p. 851-855.
10. *Gas Production from Methane Hydrate Layers Confirmed*. 2012; Available from: http://www.jogmec.go.jp/english/news/release/release0110.html.
11. Kvenvolden, K.A. and G.E. Claypool, *Gas hydrates in oceanic sediment*, in *Open-File Report*. 1988.
12. Mozurkewich, G., H.I. Ringermacher, and D.I. Bolef, *Effect of demagnetization on magnetic resonance line shapes in bulk samples: Application to tungsten.* Physical Review B, 1979. **20**(1): p. 33-38.
13. Slater, J.C.N., Frank H, *Electromagnetism*. 2 ed. 1969, New York: Dover Publications.
14. Martin, B.T., G.C. Chingas, and O.M. McDougal, *Origin and correction of magnetic field inhomogeneity at the interface in biphasic NMR samples.* Journal of Magnetic Resonance, 2012. **218**: p. 147-152.
15. Balevicius, V. and K. Aidas, *Temperature Dependence of 1H and 17O NMR Shifts of Water: Entropy Effect.* Applied Magnetic Resonance, 2007. **32**(3): p. 363-376.
16. Titman, J. *Essential techniques in solid-state NMR*. [cited 2014 2/9]; Available from: http://www.solidstatenmr.org.uk/lectures_files/pdfs/EssentialTechniques.pdf.
17. Totland, C., et al., *Water Structure and Dynamics at a Silica Surface: Pake Doublets in H-1 NMR Spectra.* Langmuir, 2011. **27**(8): p. 4690-4699.
18. McDonald, P.J., et al., *Surface relaxation and chemical exchange in hydrating cement pastes: A two-dimensional NMR relaxation study.* Physical Review E, 2005. **72**(1): p. 9.
19. Totland, C., *Electronic relaxation*. 2015.
20. Bloembergen, N. and L.O. Morgan, *Proton Relaxation Times in Paramagnetic Solutions. Effects of Electron Spin Relaxation.* The Journal of Chemical Physics, 1961. **34**(3): p. 842-850.
21. Ronczka, M. and M. Müller-Petke, *Optimization of CPMG sequences to measure NMR transverse relaxation time T2 in borehole applications.* Geosci. Instrum. Method. Data Syst., 2012. **1**(2): p. 197-208.
22. Seland, J.G., *The CMPG oneshot experiment*. 2015.
23. Resing, H.A., *NUCLEAR MAGNETIC RESONANCE RELAXATION OF MOLECULES ADSORBED ON SURFACES.* Advances in Molecular Relaxation Processes, 1968. **1**(2): p. 109-&.
24. Ernst, R.R., G. Bodenhausen, and A. Wokaun, *Principles of nuclear magnetic resonance in one and two dimensions*. 1986, Oxford: Claredon Press.
25. *NMR tutorial - Relaxation*. Available from: http://www.chemie.uni-hamburg.de/nmr/insensitive/tutorial/en.lproj/relaxation.html.
26. Geppert, T., et al., *FAST NOESY FOR MICROMOLECULES WITHOUT COMPROMISE IN DISTANCE ACCURACY.* Journal of Magnetic Resonance Series B, 1995. **107**(1): p. 91-93.
27. Fleyfel, F., et al., *Interpretation of carbon-13 NMR of methane/propane hydrates in the metastable/nonequilibrium region.* The Journal of Physical Chemistry, 1993. **97**(25): p. 6722-6725.

28. Fleyfel, F., et al., *C-13 NMR OF HYDRATE PRECURSORS IN METASTABLE REGIONS*, in *International Conference on Natural Gas Hydrates*, E.D. Sloan, J. Happel, and M.A. Hnatow, Editors. 1994, New York Acad Sciences: New York. p. 212-224.
29. Kini, R.A., S.F. Dec, and E.D. Sloan, *Methane plus propane structure II hydrate formation kinetics.* Journal of Physical Chemistry A, 2004. **108**(44): p. 9550-9556.
30. Ripmeester, J.A. and C.I. Ratcliffe, *Low-temperature cross-polarization magic angle spinning C-13 NMR og solid methane hydrates - structure, cage occupancy, and hydration number.* Journal of Physical Chemistry, 1988. **92**(2): p. 337-339.
31. Subramanian, S., et al., *Evidence of structure II hydrate formation from methane plus ethane mixtures.* Chemical Engineering Science, 2000. **55**(11): p. 1981-1999.
32. Davidson, D.W., et al., *LABORATORY ANALYSIS OF A NATURALLY-OCCURRING GAS HYDRATE FROM SEDIMENT OF THE GULF OF MEXICO.* Geochimica Et Cosmochimica Acta, 1986. **50**(4): p. 619-623.
33. Gupta, A., et al., *NMR investigation of methane hydrate dissociation.* Journal of Physical Chemistry C, 2007. **111**(5): p. 2341-2346.
34. Dec, S.F., *Clathrate Hydrate Formation: Dependence on Aqueous Hydration Number.* Journal of Physical Chemistry C, 2009. **113**(28): p. 12355-12361.
35. Dec, S.F., *Clathrate Hydrate Formation: Dependence on Aqueous Hydration Number (vol 113, pg 12355, 2009).* Journal of Physical Chemistry C, 2012. **116**(10): p. 6504-6504.
36. Yutaek, S., K. Seong-Pil, and J. Wonho, *Structure and composition analysis of natural gas hydrates: 13C NMR spectroscopic and gas uptake measurements of mixed gas hydrates.* Journal of Physical Chemistry A, 2009. **113**(35): p. 9641-9649.
37. Uchida, T., et al., *Two-step formation of methane-propane mixed gas hydrates in a batch-type reactor.* Aiche Journal, 2004. **50**(2): p. 518-523.
38. Kumar, R., et al., *Structure and kinetics of gas hydrates from methane/ethane/propane mixtures relevant to the design of natural gas hydrate storage and transport facilities.* Aiche Journal, 2008. **54**(8): p. 2132-2144.
39. Uchida, T., et al., *Spectroscopic measurements on binary, ternary, and quaternary mixed-gas molecules in clathrate structures.* Industrial & Engineering Chemistry Research, 2007. **46**(14): p. 5080-5087.
40. Alavi, S., et al., *Experimental and computational 13C NMR studies of guest molecule conformations in large cages of structure H clathrate hydrates*, in *7th International Conference on Gas Hydrates*. 2011: Edinburgh.
41. Jacobs, D.M., M.D. Zeidler, and O. Kanert, *Proton magnetic relaxation studies of various guest molecules in clathrate hydrates.* Journal of Physical Chemistry A, 1997. **101**(29): p. 5241-5249.
42. Albayrak, C., et al., *NMR Relaxation of Tetrahydrofuran in Clathrate Hydrate.* Berichte der Bunsengesellschaft für physikalische Chemie, 1989. **93**(10): p. 1119-1122.
43. Beckmann, P.A., *Spectral densities and nuclear spin relaxation in solids.* Physics Reports, 1988. **171**(3): p. 85-128.
44. Garg, S.K., D.W. Davidson, and J.A. Ripmeester, *NMR behavior of the clathrate hydrate of tetrahydrofuran. I. Proton measurements.* Journal of Magnetic Resonance (1969), 1974. **15**(2): p. 295-309.
45. Gao, S.Q., W.G. Chapman, and W. House, *NMR and viscosity investigation of clathrate hydrate formation and dissociation.* Industrial & Engineering Chemistry Research, 2005. **44**(19): p. 7373-7379.
46. Nelson, H., et al., *Deuteron magnetic resonance and dielectric studies of guest reorientation and water dynamics in six clathrate hydrates containing ring-type guests.* Journal of Non-Crystalline Solids, 2015. **407**: p. 431-440.
47. Jacobs, D.M., M.D. Zeidler, and O. Kanert, *Proton Magnetic Relaxation Studies of Various Guest Molecules in Clathrate Hydrates.* The Journal of Physical Chemistry A, 1997. **101**(29): p. 5241-5249.

48. Karanjkar, P.U., J.W. Lee, and J.F. Morris, *Calorimetric investigation of cyclopentane hydrate formation in an emulsion.* Chemical Engineering Science, 2012. **68**(1): p. 481-491.
49. Nakajima, M., R. Ohmura, and Y.H. Mori, *Clathrate Hydrate Formation from Cyclopentane-in-Water Emulsions.* Industrial & Engineering Chemistry Research, 2008. **47**(22): p. 8933-8939.
50. Dyadin, Y.A., et al., *Clathrate formation in water-cyclic ether systems at high pressures.* Journal of inclusion phenomena and molecular recognition in chemistry, 1991. **10**(1): p. 39-56.
51. Udachin, K.A., C.I. Ratcliffe, and J.A. Ripmeester, *Single Crystal Diffraction Studies of Structure I, II and H Hydrates: Structure, Cage Occupancy and Composition.* Journal of Supramolecular Chemistry, 2002. **2**(4–5): p. 405-408.
52. Bloembergen, N., E.M. Purcell, and R.V. Pound, *Relaxation Effects in Nuclear Magnetic Resonance Absorption.* Physical Review, 1948. **73**(7): p. 679-712.
53. Abragam, A., *The Principles of Nuclear Magnetism*. 1961, Oxford: Oxford University Press.
54. Geil, B., T.M. Kirschgen, and F. Fujara, *Mechanism of proton transport in hexagonal ice.* Physical Review B, 2005. **72**(1): p. 014304.
55. Udachin, K.A., C.I. Ratcliffe, and J.A. Ripmeester, *Structure, Composition, and Thermal Expansion of CO2 Hydrate from Single Crystal X-ray Diffraction Measurements†.* The Journal of Physical Chemistry B, 2001. **105**(19): p. 4200-4204.
56. Udachin, K.A., et al., *Single Crystals of Naturally Occurring Gas Hydrates: The Structures of Methane and Mixed Hydrocarbon Hydrates.* Angewandte Chemie International Edition, 2007. **46**(43): p. 8220-8222.
57. Shuqiang, G., W.G. Chapman, and W. House, *Application of low field NMR T2 measurements to clathrate hydrates.* Journal of Magnetic Resonance, 2009. **197**(2): p. 208-212.
58. Hirasaki, G.J., S.W. Lo, and Y. Zhang, *NMR properties of petroleum reservoir fluids.* Magnetic Resonance Imaging, 2003. **21**(3-4): p. 269-277.
59. Gao, S., W. House, and W.G. Chapman, *NMR/MRI Study of Clathrate Hydrate Mechanisms.* The Journal of Physical Chemistry B, 2005. **109**(41): p. 19090-19093.
60. Fukushima, E. and S.B.W. Roeder, *Experimental pulse NMR. A nuts and bolts approach*. Experimental pulse NMR. A nuts and bolts approach. 1981: Addison-Wesley. xiii+539.
61. Dec, S.F., *Surface Transformation of Methane-Ethane sI and sII Clathrate Hydrates.* Journal of Physical Chemistry C, 2012. **116**(17): p. 9660-9665.
62. Moudrakovski, I.L., et al., *Facilitating guest transport in clathrate hydrates by tuning guest-host interactions.* The Journal of Chemical Physics, 2015. **142**(7): p. 074705.
63. Hahn, E.L., *Spin Echoes.* Physical Review, 1950. **80**(4): p. 580-594.
64. Hartmann, S.R. and E.L. Hahn, *Nuclear Double Resonance in the Rotating Frame.* Physical Review, 1962. **128**(5): p. 2042-2053.
65. Jeener, J., et al., *Investigation of exchange processes by two-dimensional NMR spectroscopy.* The Journal of Chemical Physics, 1979. **71**(11): p. 4546-4553.
66. Drobny, G., et al., *Fourier transform multiple quantum nuclear magnetic resonance.* Faraday Symposia of the Chemical Society, 1978. **13**(0): p. 49-55.
67. Ripmeester, J.A. and C.I. Ratcliffe, *On the contributions of NMR spectroscopy to clathrate science.* Journal of Structural Chemistry, 1999. **40**(5): p. 654-662.
68. Alavi, S., P. Dornan, and T.K. Woo, *Determination of NMR Lineshape Anisotropy of Guest Molecules within Inclusion Complexes from Molecular Dynamics Simulations.* ChemPhysChem, 2008. **9**(6): p. 911-919.
69. Davidson, D.W., *Motion of molecules engaged in clathrate hydrates.* Acta Crystallographica, Section A (Crystal Physics, Diffraction, Theoretical and General Crystallography), 1969. **a25**: p. S47-S47.
70. *Sigma-Aldrich search results - D2O*. [cited 2015 10/10]; Available from: http://www.sigmaaldrich.com/catalog/search?term=d2o&interface=All&N=0&mode=match%20partialmax&lang=en&region=NO&focus=product.

71. *Labscoop chemical products - cyclopentane-D10*. [cited 2015 10/10]; Available from: http://www.labscoop.com/p/BOC-Sciences-Cyclopentane-D10/2846492.
72. *Sigma-Aldrich search results - cyclopentane*. [cited 2015 11/10]; Available from: http://www.sigmaaldrich.com/catalog/search?term=cyclopentane&interface=All&N=0&mode=match%20partialmax&lang=en&region=NO&focus=product.
73. Sefidroodi, H., E. Abrahamsen, and M.A. Kelland. *Evidence of a memory effect in the formation and reformation of cyclopentane hydrate*. in *7th International conference on gas hydrates*. 2011. Edinburgh, Scotland.
74. Dirdal, E.G., et al.
75. Abdulkader, B.M.H., *Cyclopentane hydrate for hydrate wetting studies*, in *Department of chemistry*. 2013, University of Bergen: Bergen.
76. Corak, D., et al., *Effect of subcooling and amount of hydrate former on formation of cyclopentane hydrates in brine.* Desalination, 2011. **278**(1–3): p. 268-274.
77. Nerdal, W., *Temperature accuracy for the AV500*. 2015.
78. Decatur, J. *NOESY on the 400 and 500 using Topspin*. 2007 [cited 2015 23/10]; Available from: http://www.columbia.edu/cu/chemistry/groups/nmr/noesy.pdf.